Nonlinear Dynamics of Complex Systems

Lead Guest Editor: Viorel-Puiu Paun
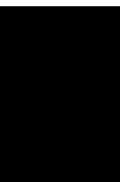Guest Editors: Frédéric Magoulès and Alina Gavriluț

Nonlinear Dynamics of Complex Systems

Nonlinear Dynamics of Complex Systems

Lead Guest Editor: Viorel-Puiu Paun
Guest Editors: Frédéric Magoulès and Alina Gavriluț

Contents

WILEY | Hindawi

Research Article

Flow, Wind, and Stochastic Connectivity Modeling Infectious Diseases

C. Udriste [ID],[1,2] I. Tevy [ID],[2] and A. S. Rasheed[2,3]

[1]*Academy of Romanian Scientists, Ilfov 3, 050044 Bucharest, Romania*
[2]*University Politehnica of Bucharest, Department of Mathematics & Informatics, Splaiul Independentei 313, 060042 Bucharest, Romania*
[3]*Ministry of Higher Education and Scientific Research, Baghdad, Iraq*

Correspondence should be addressed to C. Udriste; udriste@mathem.pub.ro

We study in this paper the trends of the evolution of different infections using a SIR flow (first-order ODE system), completed by a differential inclusion, a geodesic motion in a gyroscopic field of forces, and a stochastic SIR perturbation of the flow (Itô ODE system). We are interested in mathematical analysis, bringing new results on studied evolutionary models: infection flow together with a differential inclusion, bounds of evolution, dual description of disease evolution, log-optimal and rapid path, epidemic wind (geometric dynamics), stochastic equations of evolution, and stochastic connectivity. We hope that the paper will be a guideline for strategizing optimal sociopolitical countermeasures to mitigate infectious diseases.

1. Introduction

All topics in this paper are based on dynamics induced by flows and differential inclusions, dynamical systems of geometric origin, nonholonomic dynamical systems, and stochastic differential equations. Their combination reflects the mathematical complexity of the studied problems.

The mathematical literature that helped us to do this study is classified as follows: stochastic modeling of geometric structures [1–4], infectious disease flow [5–7], differential inclusions [8], geometric dynamics on Riemannian manifolds [9, 10], nonholonomic optimization [11, 12], and nonholonomic spaces [13].

The original results can be summarized by properties of infectious disease flow, Maple simulations for COVID-19 in Romania, infectious disease differential inclusion, bounds of disease evolution, dual description of disease evolution, epidemic wind generated by the flow and the geometry of the space, and computation of optimal striking time for stochastic connectivity.

The Maple simulations for COVID-19, with Romanian data, are more suggestive than what could be done according

to the model related to the works [3, 5–7]. Our results on the asymptotic behavior of infectious disease flow and bounds of disease evolution via extremum problems are finer than those presented by M. W. Hirsch, S. Smale, R. L. Devaney in their book [6], Chapter 11. The Pfaff evolution, the epidemic wind, and finding the optimal striking time for stochastic connectivity via an extremum problem are totally original ideas, suggested by our recent papers. Particularly, the Pfaff evolution underlines that we can study the infectious disease system like a Carnot group.

Although the epidemic differential inclusion and epidemic wind appear to have been created ad hoc, it explains the pandemic spread in the sense that any two points on the globe can be joined by an epidemic trajectory. This is not true if we stop with the explanations only at the epidemic flow. The same idea is underlined by stochastic connectivity.

1.1. Disease Infection Data. The evolution of disease infections in each region has been modeled recently via a stochastic susceptible-infected-recovered (SSIR) model [3, 5–7] with the following data:

Evolution parameter: t is the daily-time parameter.

States: (1) $S(t)$ denotes the total susceptible population at time t; (2) $I(t)$ denotes the number of active infections at time t; (3) $R(t)$ denotes the total number of recoveries and deaths at time t; (4) $dS(t), dI(t)$, and $dR(t)$ denote the change in the states at time t; (5) dW_t is an incremental Wiener process (Brownian motion), which models the randomness in the evolution.

Constant parameters: (1) β (measured by $[\beta] = (\text{people} \times \text{time})^{-1}$) is a constant denoting the growth rate, which factors the rise in the number of infections, due to interactions between susceptible and infected populations. This parameter is a lumped constant which is meant to account for (a) the population size, (b) reproduction number of infectious diseases, and (c) exposure factor (which depends on mobility, precautionary measures, etc.); (2) γ (measured by $[\gamma] = (\text{time})^{-1}$) is the rate of outcomes, that is, the rate at which the infections are neutralized, which may be due to recovery or death. It is assumed that recovered persons would not spread the infections again (at least for a window of a month); (3) σ is a parameter used to model the randomness in the evolution, which may cause local deviations from the typical (exponential) trends; (4) P_{total} is the population of the region, and S_0 and I_0 are the initial number of susceptible individuals and active infections.

2. Infectious Disease Flow

The susceptible-infected-recovered (SIR) model, with three different states, was selected [3,5–7] to describe the evolution of different infections in a region of the world. On $\mathbb{R}_+^3$, the infectious disease Cauchy problem is

$$
\begin{aligned}
\dot{S}(t) &= -\beta S(t) I(t), \\
\dot{I}(t) &= (\beta S(t) - \gamma) I(t), \\
\dot{R}(t) &= \gamma I(t), \\
S(0) &= S_0, \\
I(0) &= I_0, \\
R(0) &= R_0, \\
S_0 + I_0 + R_0 &= P_{\text{total}}.
\end{aligned}
\tag{1}
$$

Since the initial differential system is equivalent to the symmetric system

$$
\frac{dS}{-\beta S} = \frac{dI}{\beta S - \gamma} = \frac{dR}{\gamma},
\tag{2}
$$

automatically two first integrals $Se^{(\beta/\gamma)R} = c_1$ and $S + I + R = c_2$ appear, and hence the general solution is $Se^{(\beta/\gamma)R} = c_1, S + I + R = c_2$ (spiral curve in a plane). In other words, the infectious disease nonlinear differential system is compartmental and proves the mass conservation property [5–7]. The family of field surfaces has the general equation $\phi(Se^{(\beta/\gamma)R}, S + I + R) = c$, where $\phi(c_1, c_2)$ is an arbitrary C^1

function. The vortex lines of a SIR vector field are plane curves.

Given an initial condition $S(0), I(0), R(0)$ summing to P_{total}, it follows $c_1 = S_0 e^{(\beta/\gamma)R_0}$ and $c_2 = P_{\text{total}} = S_0 + I_0 + R_0$. Also, the previous differential system has a straight line of equilibrium points $I = 0, S + R = P_{\text{total}}$ (particularly, $S = 0, I = 0, R = P_{\text{total}}$ and $S = (\gamma/\beta), I = 0, R = P_{\text{total}} - (\gamma/\beta)$ are two equilibrium points). The general theory shows that a nonisolated equilibrium point can be stable but not asymptotically stable.

2.1. Open Problems

(1) Investigate whether there are monomial connections ∇ on $\mathbb{R}_{++}^3$ of components

$$
\Gamma_{ij}^k = c_{ij}^k (x^1)^{a_1} (x^2)^{a_2} (x^3)^{a_3}, \quad c_{ij}^k > 0, x^i \in \mathbb{R}_{++}, a_i \in \mathbb{R},
\tag{3}
$$

so that the SIR vector field is convex with respect to ∇.

(2) Convolution is a very powerful technique in applications. Transforming the usual product into a convolution (product), let us replace the initial Cauchy problem with a convolution problem

$$
\begin{aligned}
\dot{S}(t) &= -\beta S(t) * I(t), \\
\dot{I}(t) &= (\beta S(t) - \gamma) * I(t), \\
\dot{R}(t) &= \gamma I(t), \\
S(0) &= S_0, \\
I(0) &= I_0, \\
R(0) &= R_0, \\
S_0 + I_0 + R_0 &= P_{\text{total}},
\end{aligned}
\tag{4}
$$

where the convolution (product) is defined by $(f * g)(t) = \int_0^t f(\tau)g(t - \tau)d\tau$. Applying the Laplace transform, study the solution of this convolution problem.

2.2. Maple Simulations for COVID-19.

We denote $S = x, I = y, R = z, t = \text{days}$assume values $\beta = 7.5 \times 10^{-3}$ and $\gamma = 0.06$ (hypothetical data used for research purpose). Romanian media, 06.05.2020: P_{total} = Romania population = 19,410 million; $x0$ = quarantined + nonquarantined = 19,389; $y0$ = infected = 13,837; $z0$ = recovered 5.454 + deceased 858 = 6,312 (real data normalized by 1,000).

The graph $t, x(t)$ admits a limit point $x = \overline{x} = \lim_{t \to \infty} x(t) \geq 0$; the graph $t, y(t)$ has a maximum point and a limit point $y = \overline{y} = \lim_{t \to \infty} y(t) = 0$. The graph $t, z(t)$ has a limit point $z = \overline{z} = \lim_{t \to \infty} z(t) \geq 0$. Of course, $\overline{x} + \overline{z} = P_{\text{total}}$. See Figures 1–3.

(i) with(DEtools):
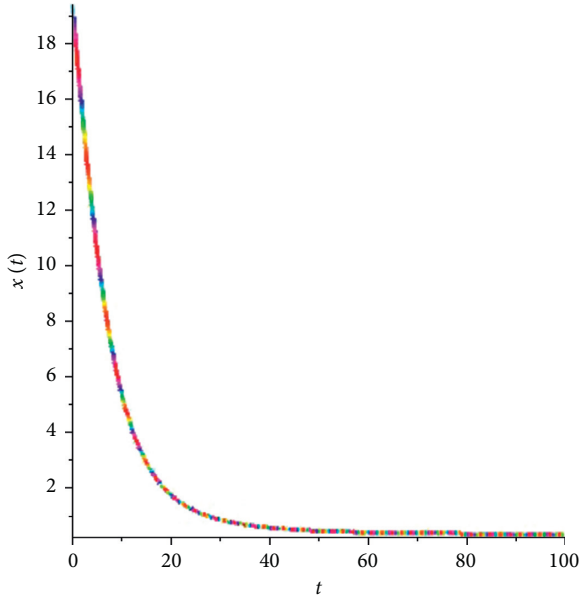
FIGURE 1: Susceptible population evolution $t, x(t)$.

phaseportrait([$D(x)(t) = -7.5 * 10^{(-3)} * x(t) * y(t)$, $(D(y))(t) = (7.5 * 10^{(-3)} * x(t) - 0.6e - 1) * y(t)$, $(D(t))(t) = 0.6e - 1 * y(t)$], $[x(t), y(t), z(t)]$, $t = 0 \, .. \, 100$, $[[x(0) = 19.389, \, y(0) = 13.837, \, z(0) = 6.312]]$, stepsize $= 0.5e - 1$, scene $= [t, \quad x(t)]$, linecolour $= \sin((1/2) * t * Pi)$, method $=$ classical [foreuler]);

(ii) phaseportrait([$D(x)(t) = -7.5 * 10^{(-3)} * x(t) * y(t)$, $(D(y))(t) = (7.5 * 10^{(-3)} * x(t) - 0.6e - 1) * y(t)$, $(D(t))(t) = 0.6e - 1 * y(t)$], $[x(t), y(t), z(t)]$, $t = 0, ..., 100$, $[[x(0) = 19.389, \, y(0) = 13.837, \, z(0) = 6.312]]$, stepsize $= 0.5e - 1$, scene $= [t, \quad y(t)]$, linecolour $= \sin((1/2) * t * Pi)$, method $=$ classical [foreuler]);

(iii) phaseportrait([$D(x)(t) = -7.5 * 10^{(-3)} * x(t) * y(t)$, $(D(y))(t) = (7.5 * 10^{(-3)} * x(t) - 0.6e - 1) * y(t)$, $(D(t))(t) = 0.6e - 1 * y(t)$], $[x(t), y(t), z(t)]$, $t = 0, ..., 100$, $[[x(0) = 19.389, \, y(0) = 13.837, \, z(0) = 6.312]]$, stepsize $= 0.5e - 1$, scene $= [t, \quad z(t)]$, linecolour $= \sin((1/2) * t * Pi)$, method $=$ classical [foreuler]).

Remark 1. Let us animate the surface $Se^{(\beta/\gamma)R} = c_1$ with respect to the parameter $a = (\beta/\gamma)$ (Figure 4).

(i) with(plots);

(ii) animate(plot3d,
[$x * \exp(a * z), x = 1, \ldots, 10, z = 1, \ldots, 10$],
$a = 0.125, \ldots, 1$).

2.3. Parametrization by S. It would be more natural to parameterize the previous general solution by "raw material" S; namely,

$$S = S,$$

$$I = \frac{\gamma}{\beta} \ln(c_2 S) - S,$$

$$R = -\frac{\gamma}{\beta} \ln(c_1 S),$$

(5)

where $c_1 S < 1 < c_2 S$ and $(\gamma/\beta) \ln(c_2/c_1) = P_{total}$. If the social constants β, γ and the state S are so that $I > 0$, then there are infections; otherwise, there are not. So, trying to influence the transmission constants β, γ we can limit the number of infections. In fact, the state I exists, if and only if $S_1 \leq S \leq S_2$ and then $I(S_1) = I(S_2) = 0$.

If we start with the equilibrium points $S_0 = P_{total}, I_0 = 0$, and $R_0 = 0$, we find

$$I = \frac{\gamma}{\beta} \ln\left(\frac{S}{S_0}\right) + S_0 - S,$$

$$R = -\frac{\gamma}{\beta} \ln\left(\frac{S}{S_0}\right), \quad S < S_0.$$

(6)

The more interesting case holds for $S_0 > (\gamma/\beta)$. Then, the ODE for $S(t)$ becomes

$$\dot{S}(t) = \beta S(t)^2 - \beta S_0 S(t) - \gamma S(t) \ln\left(\frac{S(t)}{S_0}\right),$$

(7)

or changing the variable as $S(t) = S_0 u(t)$,

$$\dot{u}(t) = \beta S_0 \left(u(t)^2 - u(t)\right) - \gamma u(t) \ln u(t), \quad u(t) < 1.$$

(8)

The solution of this ODE is written in the form

$$t + c = \int \frac{du}{\beta S_0 (u^2 - u) - \gamma u \ln u}.$$

(9)

The denominator of the integrand has three roots $0, u_0$, and 1. Using the qualitative approximation

$$t + c = k \int \frac{du}{u(u - u_0)(u - 1)}, \quad u_0 < u < 1,$$

(10)

we find the implicit solution

$$\frac{u^{1/u_0} (1 - u)^{1/(1 - u_0)}}{(u - u_0)^{1/u_0 (1 - u_0)}} = ce^{t/k}.$$

(11)

The constant c is determined from the initial condition $u(0) = 1 - \varepsilon$. The initial condition $u(0) = 1$ would give us the equilibrium point $u(t) \equiv 1$.

Let us observe that $u(t) \longrightarrow u_0$ for $t \longrightarrow \infty$. Hence, the final state $I = 0, S = S_1$ appears for $t \longrightarrow \infty$.

We fix $\beta = 1, \gamma = 3, S_0 = 5$. From the graphs $S, I(S)$ and $(S, F(S) = S^2 - 5S - 3S \ln(S/5))$, in Figure 5, we can read the following: when S is decreasing from S_0 to S_1, the function I is increasing from 0 to a maximum for $S = \beta/\gamma$ and then decreasing again to 0. In other words, when the epidemic goes out, that is, $I = 0$ again, and the variable S stops at $S_1 > 0$, then we talk about an uncontaminated population.
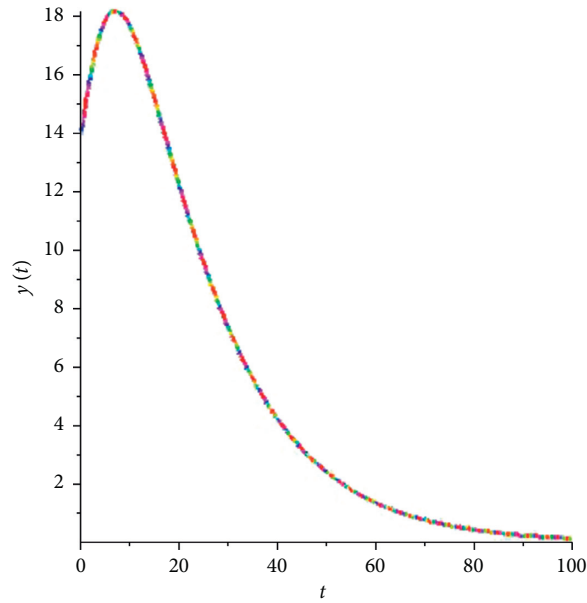
FIGURE 2: Active infection evolution $t, y(t)$.
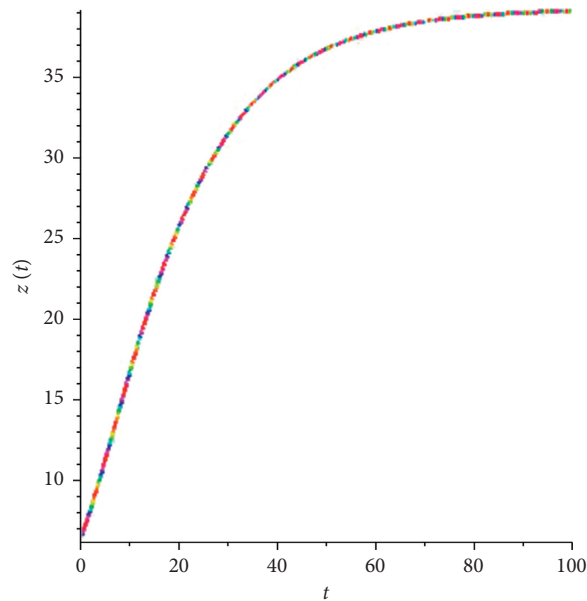
FIGURE 3: Number of recoveries and deaths' evolution $t, z(t)$.

Maple simulation (Figure 5):

(i) plot([3 * ln((1/5) * x) + 5 − x, x² − 5 * x − 3 * x * ln((1/5) * x)], x = 0.. 6, color = ["red", "green"]).

2.4. Asymptotic Behavior of Infectious Disease Flow

Theorem 1. *For positive initial conditions* (S_0, I_0, R_0)*, the limit value* $\overline{S} + \overline{I} = \lim_{t \longrightarrow \infty} (S(t) + I(t))$ *exists and is* $P_{total} - \overline{R}$.

Proof. Suppose $S(t) \leq (\gamma/\beta)$.

Because $S(t)$ is monotonically decreasing $(\dot{S}(t) = -\beta S(t)I(t) \leq 0)$ and nonnegative, it has a limit $\overline{S} = \lim_{t \longrightarrow \infty} S(t)$, with $0 \leq \overline{S} \leq (\gamma/\beta)$.

Since $I(t)$ is monotonically decreasing $(\dot{I}(t) = (\beta S(t) - \gamma)I(t) \leq 0)$ and nonnegative, it has a limit $\overline{I} = \lim_{t \longrightarrow \infty} I(t)$, with $\overline{I} \geq 0$.

On the other hand, $R(t)$ is monotonically increasing $(\dot{R}(t) = \gamma I(t) \geq 0)$ and nonnegative. But $S(t) + I(t) + R(t) = P_{total}$ shows that $R(t)$ has a limit $\overline{R} \geq 0$. For t large enough, we have $S(t) \approx \overline{S}, I(t) \approx \overline{I}$, and $R(t) \approx \overline{R}$. Then, the differential

$a = 1.0000$

Animate SR first integral
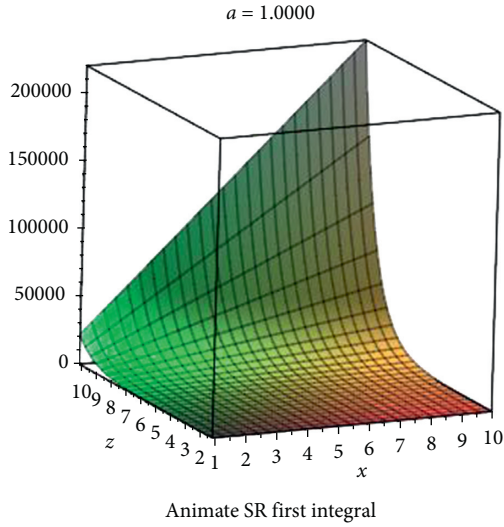
Figure 4: Animate SR first integral.
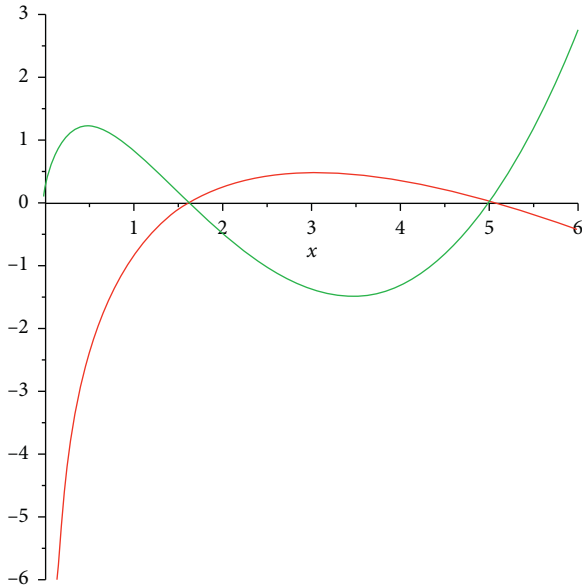
Figure 5: Intersection $I(S) \cap F(S)$.

system consisting of the first equation and third equation converges to the linear system corresponding to the linearization at the point $(\overline{S}, \overline{I})$; that is,

$$\dot{S} = -\beta\overline{I}(S(t) - \overline{S}) - \beta\overline{S}(I(t) - \overline{I}),$$
$$\dot{R}(t) = \gamma\overline{I}(I(t) - \overline{I}).$$

(12)

The matrix of this linear system has the eigenvalues $\lambda_1 = -\beta\overline{I} < 0$ and $\lambda_2 = \gamma\overline{I} > 0$. Consequently, $(\overline{S}, \overline{I})$ render this system unstable, and then the trajectory $S(t), I(t), R(t)$ diverges. This contradicts $S(t) + I(t) + R(t) = P_{total}$.

Suppose $S(t) > (\gamma/\beta)$. Similarly, it follows the existence of $(\overline{S}, \overline{I}, \overline{R})$, satisfying $(\gamma/\beta) \leq \overline{S}$, $\overline{I} \geq 0$, and $\overline{R} \geq 0$. □

Theorem 2. *For the infectious disease flow, one has* $\overline{I} = \lim_{t\to\infty} I(t) = 0$ *(see equilibrium point).*

Proof. We use the second differential equation $dI(t)/I(t) = (d/dt)\ln I(t) = \beta S(t) - \gamma$. Let $\mathcal{S}$ be the primitive of function $S(t)$. Since $\int_0^b \beta S(t) - \gamma dt = \ln(I(b)/I(0))$, we find $\beta(\mathcal{S}(b) - \mathcal{S}(0)) - \gamma b = \ln(I(b)/I(0))$. At limit, when $b \to \infty$, we must have $\overline{I} = I(\infty) = 0$ (see equilibrium point). □

Remark 2. Let $\mathcal{S}$, $\mathcal{I}$, and $\mathcal{R}$ be the primitives of functions $S(t)$, $I(t)$, and $R(t)$. Then, $\mathcal{S}(t) + \mathcal{I}(t) + \mathcal{R}(t) = tP_{total}$.

Theorem 3. *Let $\mathcal{S}$, $\mathcal{I}$, and $\mathcal{R}$ be the primitives of functions $S(t)$, $I(t)$, and $R(t)$. For positive initial conditions (S_0, I_0, R_0), the limit values*

$$\overline{S} = \lim_{t\to\infty} S(t),$$
$$\overline{\mathcal{I}} = \lim_{t\to\infty} \mathcal{I}(t),$$
$$\overline{R} = \lim_{t\to\infty} R(t)$$

(13)

are related by

$$-\beta(\overline{\mathcal{I}} - \mathcal{I}(0)) = \ln\frac{\overline{S}}{S(0)},$$
$$\overline{R} - R(0) = \gamma(\overline{\mathcal{I}} - \mathcal{I}(0)).$$

(14)

Proof. Let us consider the first differential equation

$$\frac{dS(t)}{S(t)} = \frac{d}{dt}\ln S(t) = -\beta I(t)dt.$$

(15)

It follows $-\beta\int_0^\infty I(t)dt = \ln(\overline{S}/S(0))$, and hence $-\beta(\overline{\mathcal{I}} - \mathcal{I}(0)) = \ln(\overline{S}/S(0))$.

Integrating the third differential equation, we find

$$\overline{R} - R(0) = \gamma(\overline{\mathcal{I}} - \mathcal{I}(0)).$$

(16)

Since (S, I, R) represent the evolution of disease infections, the initial conditions $S_0 \geq 0, I_0 \geq 0, R_0 \geq 0$, and $S_0 + I_0 + R_0 = P_{total}$ are perfectly suited for biological applications. Suppose these initial conditions. The monotony of the state functions $S(t), I(t), R(t)$ is described by the signum of derivatives: either $\dot{S} \leq 0, \dot{I} > 0, \dot{R} \geq 0$ which show that $S(t)$ is decreasing and $I(t)$ and $R(t)$ are increasing $\forall t > 0$ or $\dot{S} \leq 0, \dot{I} \leq 0, \dot{R} \geq 0$ which show that $S(t), I(t)$ are decreasing and $R(t)$ is increasing $\forall t > 0$. □

2.5. Covering All the Manifold by a Differential Inclusion.
As any flow, the infectious disease flow does not cover all the manifold $\mathbb{R}^3_+$, and so there are pairs of points that cannot be joined by a flow trajectory. The natural question arises: what mathematical construction allows us to cover all the manifold?

The infectious disease vector field $X = I(-\beta S, \beta S - \gamma, \gamma)$ determines an orthogonal distribution generated by two linearly independent vector fields $Y = (\beta S - \gamma, \beta S, 0)$ and $Z = (0, -\gamma, \beta S - \gamma)$, orthogonal to X.

The three vector fields X, Y, Z determine the differential inclusion

$$\frac{d}{dt}\begin{pmatrix} S \\ I \\ R \end{pmatrix} \in \{X, Sp\{Y, Z\}\}, \tag{17}$$

which can be used to understand and suitably interpret the spreading of the disease, in the sense that any two points on $\mathbb{R}_+^3$ can be joined by a piecewise solution of the differential inclusion.

3. Bounds of Disease Evolution

Let us select the best values of state variables when we evolve along the solution of the disease flow. The aim is to manage correctly a pandemic since the values of certain parameters can be chosen subject to some conditions expressing their ranges and interrelationships. The choice determines the values of a number of other variables on which the desirability of the end result depends, such as cost, weight, speed, bandwidth, and reliability.

3.1. Extrema Constrained by Equalities. A basic problem we discuss at the beginning of this paper is as follows: "find $\max f(S, I, R) = I$ subject to $Se^{(\beta/\gamma)R} = c_1, S + I + R = c_2$."

The constraints satisfy the condition of nondegenerate constraint qualification.

To solve this problem, we attach the Lagrange function

$$F = I + \lambda\left(Se^{(\beta/\gamma)R} - c_1\right) + \mu(S + I + R - c_2). \tag{18}$$

Since

$$dF = dI + \lambda\left(e^{(\beta/\gamma)R}dS + S\frac{\beta}{\gamma}e^{(\beta/\gamma)R}dR\right) + \mu(dS + dI + dR), \tag{19}$$

the critical points of the function F are given by the algebraic system

$$\frac{\partial F}{\partial S} = \lambda e^{(\beta/\gamma)R} + \mu = 0,$$

$$\frac{\partial F}{\partial I} = 1 + \mu = 0,$$

$$\frac{\partial F}{\partial R} = \lambda S\frac{\beta}{\gamma}e^{(\beta/\gamma)R} + \mu = 0, \tag{20}$$

$$Se^{(\beta/\gamma)R} = c_1,$$

$$S + I + R = c_2.$$

It follows the critical points

$$S = \frac{\gamma}{\beta},$$

$$R = -\frac{\gamma}{\beta}\ln \lambda,$$

$$I = c_2 - \frac{\gamma}{\beta} - \frac{\gamma}{\beta}\ln \lambda, \tag{21}$$

$$\lambda = \frac{\gamma}{\beta c_1},$$

$$\mu = -1.$$

On the other hand,

$$d^2F = \lambda\left(2\frac{\beta}{\gamma}e^{(\beta/\gamma)R}dSdR + S\left(\frac{\beta}{\gamma}\right)^2 e^{(\beta/\gamma)R}dR^2\right). \tag{22}$$

The associated matrix

$$\begin{pmatrix} 0 & \lambda\frac{\beta}{\gamma}e^{(\beta/\gamma)R} \\ \lambda\frac{\beta}{\gamma}e^{(\beta/\gamma)R} & \lambda S\left(\frac{\beta}{\gamma}\right)^2 e^{(\beta/\gamma)R} \end{pmatrix}, \tag{23}$$

with respect to $\{dS, dR\}$, is negative definite. The function F is concave. Hence, all critical points are maximum points. The maximum value of objective function I is

$$I_{\max} = c_2 - \frac{\gamma}{\beta} - \frac{\gamma}{\beta}\ln \lambda. \tag{24}$$

The introduction of Lagrange multipliers λ, μ as additional variables looks artificial but it makes it possible to apply to the constrained-extremum problem the same first-order condition used in the free-extremum problem (but for more complex function F). Note also that λ, μ have a certain specific meaning: if the solution is regarded as

$$S^*(c_1, c_2), I^*(c_1, c_2), R^*(c_1, c_2), \lambda^*(c_1, c_2), \mu^*(c_1, c_2), \tag{25}$$

then the marginal variations are

$$\frac{\partial}{\partial c_1}I\left(S^*(c_1, c_2), I^*(c_1, c_2), R^*(c_1, c_2)\right) = \lambda^*(c_1, c_2),$$

$$\frac{\partial}{\partial c_2}I\left(S^*(c_1, c_2), I^*(c_1, c_2), R^*(c_1, c_2)\right) = \mu^*(c_1, c_2). \tag{26}$$

Maple Simulations: we denote $S = x, I = y, R = z$. Let us find the extrema of some functions constrained by the spiral curve.

(i) with (optimization);

The Minimize command automatically selects the most appropriate solver.

(ii) Minimize(x, $x * \exp(z) = 1, x + y + z = 2$, assume = nonnegative); 0.158594339562640796, [$x =$ HFloat$(0.1585943395626408), y =$ HFloat$(0.0), z =$ HFloat(1.8414056604373585)]

(iii) Minimize(y, $x * \exp(z) = 10, x + y + z = 50$, assume = nonnegative); 39.9999999999999858, [$x =$ HFloat$(10.0), y =$ HFloat$(39.9999999999999$ $86), z =$ HFloat(0.0)]

(iv) Minimize(z, $x * \exp(z) = 10, x + y + z = 50$, assume = nonnegative); 0., [$x =$ HFloat$(1.0), y =$ HFloat$(0.9999999999999998), z =$ HFloat(0.0)]

(v) Minimize(y, $x * \exp(z) = a, x + y + z = b$, assume = nonnegative); 0., [$a =$ HFloat$(1.1097167$ $915216666), b =$ HFloat$(1.2345190270116868), x =$ HFloat$(0.5722702360103161), y =$ HFloat$(0.0), z =$ HFloat(0.6622487910013707)]

(vi) Minimize(y, $x * \exp(10 * z) = a, x + y + z = b$, assume = nonnegative); 0., [$a =$ HFloat$(1.4613$ $527630961411), b =$ HFloat$(1.458647134440591), x =$ HFloat$(1.4584481765262327), y =$ HFloat$(0.0), z =$ HFloat$(1.9895791435813165e - 4)$]

(vii) Minimize($x^2 + y^2 + z^2$, $x * \exp(10 * z) = 1, x + y +z = 2$, assume = nonnegative); 1.99415568473971461, [$x =$ HFloat$0.9413968463983702 y =$ HFloat $1.052564103608946, z =$ HFloat0.0060390499926835095]

3.2. Extrema Constrained by Field Lines.

To simplify, we use standard notations in mathematics $S = x^1, I = x^2, R = x^3$. Then, infectious disease Cauchy problem on $\mathbb{R}^3_+$ is written

$$
\begin{aligned}
\dot{x}^1(t) &= -\beta x^1(t)x^2(t), \\
\dot{x}^2(t) &= \left(\beta x^1(t) - \gamma\right)x^2(t), \\
\dot{x}^3(t) &= \gamma x^2(t), \\
x^1(0) &= x_0^1, \\
x^2(0) &= x_0^2, \\
x^3(0) &= x_0^3, \\
x_0^1 + x_0^2 + x_0^3 &= P_{\text{total}}.
\end{aligned}
\tag{27}
$$

To find bounds of significant functions connected to this flow, we use the technique of optimization of an objective function constrained by a field line $x = xt, x_0, t \in 0, \infty, x_0 = x_0^1, x_0^2, x_0^3$.

Let us start with finding the maximum for the total susceptible population $x^1(t)$: find$\max f(x^1, x^2, x^3) = x^1$ with the restriction $x = x(t, x_0)$.

Since the component $x^1(t)$ is a decreasing function, the maximum is reached at the starting point x_0.

Let us show that we do not have constrained critical points that produce an extremum. We set the critical point condition $\langle \nabla f, X \rangle = 0$. In this case, $\nabla f = (1, 0, 0)$ and hence $-\beta x^1(t)x^2(t) = 0$.

We eliminate $x^2 = 0$, since this condition leads to an equilibrium point of the dynamical system. Also, the solution $x^1 = 0$ is not convenient. Indeed, a critical point of the form $\overline{x} = (\overline{x}^1 = 0, \overline{x}^2 > 0, \overline{x}^3 \geq 0)$ cancels the expression Hess $f(X, X)(\overline{x}) + \langle \nabla f, D_X X \rangle(\overline{x})$ whose sign at the point $\overline{x}$ would decide the property of extremum: $\langle \nabla f, D_X X \rangle(\overline{x}) \equiv 0$, that is, $\beta x^1 x^2 - \beta^2 (x^1)^2 + \beta \gamma x^1 \equiv 0$.

Since $\ddot{x}^1(t) = \beta x^1(t)x^2(t)(\beta x^2(t) - x^1(t) + \gamma)$, the function $x^1(t)$ is convex on the subset $\beta x^2(t) - x^1(t) + \gamma \geq 0$.

Proposition 1. *The maximum of the total susceptible population is reached at the starting point x_0.*

Let us find now the maximum for the number of active infections $x^2(t)$: determine $\max f(x^1, x^2, x^3) = x^2$ constrained by $x = x(t, x_0)$.

We set the critical point condition $\langle \nabla f, X \rangle = 0$. In this case, $\nabla f = (0, 1, 0)$. It follows the relation $\beta x^1(t) - \gamma x^2(t) = 0$. The convenient solution (critical point) is $\overline{x} = (\overline{x}^1 = (\gamma/\beta) \geq 0, \overline{x}^2 > 0, \overline{x}^3 \geq 0)$.

The sufficient condition Hess $f(X, X)(\overline{x}) + \langle \nabla f, D_X X \rangle(\overline{x}) < 0$ is equivalent to $\langle \nabla f, D_X X \rangle(\overline{x}) < 0$ or $-\beta^2 \overline{x}^1 \overline{x}^2 + (\beta \overline{x}^1 - \gamma)^2 < 0$.

Theorem 4. *Suppose that on an evolution field line there exists a point $\overline{x}$ satisfying*

$$
\left(\frac{\beta^2}{\gamma^2} - 1\right)^2 < \frac{\beta^3}{\gamma^3}\overline{x}^2.
\tag{28}
$$

Then, the number of active infections has an upper bound at this point.

To find the minimum for the number of recoveries and deaths $x^3(t)$, we use the problem: determine $\min f(x^1, x^2, x^3) = x^3$ constrained by $x = x(t, x_0)$.

Since the function $x^3(t)$ is increasing, the minimum is reached at the starting point x_0.

Let us show that we do not have constrained critical points that produce an extremum. We set the critical point condition $\langle \nabla f, X \rangle = 0$. In this case, $\nabla f = (0, 0, 1)$. It follows the relation $\gamma x^2(t) = 0$. We have no convenient solution (critical point) since $x^2 = 0$ leads to an equilibrium point of the dynamical system.

On the subset $x^1 \geq (\gamma/\beta)$, the function $x^3(t)$ is convex. Indeed, we have $\ddot{x}^3(t) = \gamma(\beta x^1(t) - \gamma)x^2(t)$.

Proposition 2. *The minimum number of recoveries and deaths is reached at the starting point x_0.*

4. Dual Description of Disease Evolution

A vector field determines a flow (collinearity condition) and a Pfaff equation (orthogonality condition) [9]. By duality, the nonlinear ODEs in infectious disease flow are transformed into an infectious disease Pfaff equation

$$
\omega = -\beta S I dS + (\beta S - \gamma)I dI + \gamma I dR = 0.
\tag{29}
$$

Since $\omega \wedge d\omega = \beta\gamma I^2 dS \wedge dI \wedge dR$, this Pfaff equation is noncompletely integrable (it represents a nonholonomic surface, i.e., a collection of integral curves). The integral curves are orthogonal to infectious disease field lines. Since any two points in $\mathbb{R}_+^3$ are joined by an integral curve of this Pfaff equation, the dual evolution of infectious disease shows that all parts of the world will be infected.

Simplifying by I, we obtain an equivalent infectious disease Pfaff equation

$$\beta S dS - (\beta S - \gamma) dI - \gamma dR = 0. \tag{30}$$

The normal vector field to this distribution is $N = (\beta S, -(\beta S - \gamma), -\gamma)$. Two independent vector fields tangent to the distribution are

$$X = \frac{\partial}{\partial S} + \frac{\beta S}{\gamma} \frac{\partial}{\partial R},$$

$$Y = \frac{\partial}{\partial I} - \left(\frac{\beta S - \gamma}{\gamma}\right) \frac{\partial}{\partial R}. \tag{31}$$

It follows

$$[X, Y] = Z = -\frac{\beta}{\gamma} \frac{\partial}{\partial R},$$

$$[X, Z] = 0, \tag{32}$$

$$[Y, Z] = 0,$$

and hence the vector fields X, Y, Z determine a *Carnot group* (in a future paper we shall study the infectious disease system like a Carnot group).

Proposition 3. *For $t \in [0, b]$, one has*

$$\beta S^2(b) + 2\gamma R(b) \geq \beta S^2(0) + 2\gamma R(0). \tag{33}$$

Proof. For $t \in [0, b]$, we consider the curve $c(t) = S(t), I(t), R(t)$. Integrating the Pfaff form and selecting $I(t)$ in a convenient way, it follows

$$\frac{\beta}{2}\left(S^2(b) - S^2(0)\right) + \gamma(R(b) - R(0)) = \int_{c(t)} (\beta S - \gamma) dI = \int_0^b \beta S(t) - \gamma \dot{I}(t) dt$$

$$= \int_0^b \beta S(t) - \gamma^2 I(t) dt \geq 0. \tag{34}$$

□

4.1. Log-Optimal and Rapid Path.

To find bounds of significant functions for disease distribution, we can use the technique of optimization of an objective function with nonholonomic constraints [11, 12]. One of these functions is the "volume" (SIR product) of disease states.

To find bounds for the function $g(S, I, R) = \ln|SIR|$ (logarithm of "volume"), we use the problem "determine max $g(S, I, R)$ constrained by the Pfaff equation of evolution."

The critical point condition is

$$\eta = \frac{dS}{S} + \frac{dI}{I} + \frac{dR}{R} + \lambda(-\beta SIdS + (\beta SI - \gamma I)dI + \gamma I dR) \equiv 0. \tag{35}$$

It follows

$$\lambda(\beta SI) = \frac{1}{S},$$

$$\lambda(\beta SI - \gamma I) = -\frac{1}{I}, \tag{36}$$

$$\lambda(\gamma I) = -\frac{1}{R},$$

or

$$\lambda = \frac{1}{S^2 I} = -\frac{1}{(\beta S - \gamma)I^2} = -\frac{1}{\gamma RI}. \tag{37}$$

Consequently, the critical point set is described by

$$(\beta S - \gamma)I = S^2,$$

$$S^2 = \gamma R, \tag{38}$$

$$S + I + R = P_{\text{total}},$$

that is,

$$S = \frac{1}{2}\left(\beta I + \sqrt{(\beta^2 I - 4\gamma)I}\right),$$

$$R = \left(\frac{\beta}{\gamma} S - 1\right)I, \tag{39}$$

$$S + I + R = P_{\text{total}},$$

subject to the condition $\beta^2 I - 4\gamma \geq 0$. This algebraic system has a solution since the curve\

$$S = \frac{1}{2}\left(\beta I + \sqrt{(\beta^2 I - 4\gamma)I}\right),$$

$$I = I, \tag{40}$$

$$R = \left(\frac{\beta}{\gamma} S - 1\right)I,$$

is transversal to the plane $S + I + R = P_{\text{total}}$. Indeed, the tangent vector to the curve has the components

$$T: \frac{\partial S}{\partial I} = \frac{1}{2}\left(\beta + \frac{\beta^2 I - 2\gamma}{\sqrt{(\beta^2 I - 4\gamma)I}}\right),$$

$$\frac{\partial I}{\partial I} = 1, \quad (41)$$

$$\frac{\partial R}{\partial I} = \frac{\beta}{\gamma}S - 1$$

the normal vector to the plane has the components $N = (1, 1, 1)$, and the scalar product $\langle T, N \rangle$ is different from zero.

5. Epidemic Wind

The geometric data of the world [9, 10] change the epidemic flow into an epidemic wind. This is a new idea that we are adding to the spread of infections.

So far, predictive mathematical models for epidemics were treated as flows. Now, we add a more complex idea, namely, to look at the evolution of an epidemic as a wind created ad hoc by the epidemic flow and the "geometry of the world." These are fundamental to understand the course of the epidemics and to plan effective control strategies for answering the question: how can we explain an exponentially growing number of patients all over the world who were diagnosed with COVID-19?

The time has come for us to treat the epidemics like winds (geometric dynamics and geodesic motion in a gyroscopic field of forces) [9, 10], producing chaotic dynamics. The geometric dynamics is generated by primordial data: flow and geometry of the space.

The infectious disease autonomous flow on $\mathbb{R}_+^3$ is

$$\dot{S}(t) = -\beta S(t)I(t),$$

$$\dot{I}(t) = (\beta S(t) - \gamma)I(t), \quad (42)$$

$$\dot{R}(t) = \gamma I(t).$$

On the Riemannian manifold $(\mathbb{R}_+^3, \delta_{ij})$, the flow and the metric determine the least squares autonomous Lagrangian

$$2L = (\dot{S}(t) + \beta S(t)I(t))^2 + (\dot{I}(t) - (\beta S(t) - \gamma)I(t))^2 + (\dot{R}(t) - \gamma I(t))^2. \quad (43)$$

We attach an integral action

$$C(S(\cdot), I(\cdot), R(\cdot)) = \int_{t_0}^{t_1} L(S(t), I(t), R(t), \dot{S}(t), \dot{I}(t), \dot{R}(t)) dt. \quad (44)$$

A geometric dynamics [9, 10] appears, described by the Euler-Lagrange ODEs

$$\frac{\partial L}{\partial S} - \frac{d}{dt}\frac{\partial L}{\partial \dot{S}} = 0,$$

$$\frac{\partial L}{\partial I} - \frac{d}{dt}\frac{\partial L}{\partial \dot{I}} = 0, \quad (45)$$

$$\frac{\partial L}{\partial R} - \frac{d}{dt}\frac{\partial L}{\partial \dot{R}} = 0.$$

Explicitly, the epidemic wind is described by the second-order differential system

$$\beta I(t)(\dot{S}(t) - \dot{I}(t)) + 2\beta(S(t) - \gamma)I(t)^2 - \frac{d}{dt}(\dot{S}(t) + \beta S(t)I(t)) = 0,$$

$$\beta S(t)(\dot{S}(t) - \dot{I}(t)) + \gamma \dot{I}(t) - \gamma \dot{R}(t) + 2\beta^2 S(t)^2 I(t)^2 - \beta \gamma S(t)I(t) + \gamma^2 I(t)$$

$$- \frac{d}{dt}(\dot{I}(t) - \beta S(t)I(t) + \gamma I(t)) = 0, \quad (46)$$

$$\frac{d}{dt}(\dot{R}(t) - \gamma I(t)) = 0.$$

Adding all three ODEs, we obtain an ODE whose last term is $-(\ddot{S}(t) + \ddot{I}(t) + \ddot{R}(t))$. Furthermore, the last second-order ODE is equivalent to the first-order ODE

$$\dot{R}(t) - \gamma I(t) = c_1. \quad (47)$$

Theorem 5. *The geometric dynamics (wind) represented by previous second-order ODEs is decomposable into the infectious disease flow and transversal to flow spiral trajectories.*

Proof. We give the proof in generic coordinates. The subset of solutions corresponding to the initial values $x(t_0) = x_0, \dot{x}(t_0) = X(x(t_0))$ are solutions reducible to solutions of the infectious disease flow. The subset of solutions corresponding to the initial values $x(t_0) = x_0, \dot{x}(t_0) = W \neq \lambda X(x(t_0)), \lambda > 0$, are transversal to the solutions of the infectious disease flow. The converse is also true.

Based on the existence and uniqueness theorem, each solution $x = x(t)$ of any second-order prolongation of the

first-order ODE system has the property: $\dot{x}(t_0) = X(x(t_0))$ implies $\dot{x}(t) = X(x(t)), \forall t \in I$.

In generic coordinates, the attached Hamiltonian to the wind is

$$H = \frac{1}{2}\langle \dot{x} - X(x), \dot{x} + X(x)\rangle = \frac{1}{2}\|\dot{x}\|^2 - f(x), \qquad (48)$$

where $f(x) = (1/2)\|X(x)\|^2$ (kinetic energy). The maximal solutions of infectious disease wind are split into three categories of curves: (1) curves characterized by $H = 0$ (flow trajectories); (2) curves satisfying $H = \text{const} > 0$; (3) curves characterized by $H = \text{const} < 0$. The transversal curves in category (2) can have the images throughout, but the curves in category (3) have the images only in the set $f(x) \geq -H$.

The solutions of infectious disease wind are highly sensitive to initial conditions. In other words, small differences in initial conditions, such as those due to rounding errors in numerical computation, can yield widely diverging outcomes for infectious disease wind, rendering long-term prediction of its behavior impossible in general. A single field line and an infinity of transverse curves start from a fixed point.

In a flow, the starting point is fixed, but the endpoint is the one that results. In geometric dynamics, the initial conditions are in the form of point-direction point-endpoint The solution we find optimizes the objective function of the smallest squares (the best approximation of flow in the sense of a convenient Riemannian metric). Small disturbances of the initial direction or of the endpoint can produce dramatic changes in the solution, which highlight the complexity of the problem.   □

Remark 3. In our sense, any wind is strongly dependent on the Riemannian manifold $M, g_{ij}(x)$. The best selection of

the Riemannian manifold adapted to infectious disease wind is after constant curvature: (1) curvature 0, Euclidean manifold $\mathbb{R}^3$, $g_{ij}(x) = \delta_{ij}$, used in the previous explanations; (2) curvature -1, hyperbolic manifold ($\mathbb{H}^3$, $g_{ij}(x) = (\delta_{ij}/x^{32})$); (2) curvature 1, sphere $S^3 = \left\{x = (x^1, x^2, x^3, x^4) \in \mathbb{R}^4 \|\|x\|^2 = 1\right\}$, with the metric induced by the Euclidean metric on $\mathbb{R}^4$.

6. Stochastic Connectivity

Stochastic differential equations are widely used to model epidemic infections, molecular dynamics, biophysical dynamics, climate dynamics, engineering systems, and so on, under random fluctuations.

Let us write the flow in Pfaff terminology and let us replace the parameter β by a control $u(t)$. We use $W^a(t), t \geq 0, a = 1, 2, 3$, as independent Wiener processes. Starting from the (nonlinear control system) infectious disease Cauchy problem

$$\begin{aligned}
dS(t) &= -u(t)S(t)I(t)dt, \\
dI(t) &= (u(t)S(t) - \gamma)I(t)dt, \\
dR(t) &= \gamma I(t)dt, \\
S(0) &= S_0, \qquad\qquad (49) \\
I(0) &= I_0, \\
R(0) &= R_0, \\
S_0 + I_0 + R_0 &= P_{\text{total}},
\end{aligned}$$

on $\mathbb{R}^3_+$, a stochastic perturbation is defined by stochastic differential equation system,

$$\begin{aligned}
dS(t) &= -u(t)S(t)I(t)dt + \sigma_a^1(t, S(t), I(t), R(t), u(t))dW^a(t), \\
dI(t) &= (u(t)S(t) - \gamma)I(t)dt + \sigma_a^2(t, S(t), I(t), R(t), u(t))dW^a(t), \\
dR(t) &= \gamma I(t)dt - \sigma_a^3(t, S(t), I(t), R(t), u(t))dW^a(t), \\
S(0) &= S_0, \qquad\qquad\qquad\qquad\qquad\qquad\qquad\qquad\qquad\qquad\qquad (50) \\
I(0) &= I_0, \\
R(0) &= R_0, \\
S_0 + I_0 + R_0 &= P_{\text{total}},
\end{aligned}$$

where the functions $u(t)S(t)I(t), u(t)S(t)$ $I(t) - \gamma I(t), \gamma I(t)$ are *drift coefficients* and $\sigma_a^i(t, S(t), I(t), R(t), u(t)), i = 1, 2, 3; a = 1, \ldots, d$, are *diffusion coefficients*.

If $S_0 + I_0 + R_0 = P_{\text{total}}$ and $\sigma_a^1 + \sigma_a^2 = \sigma_a^3$, then the stochastic perturbation satisfies $dS(t) + dI(t) + dR(t) = 0$; that is, we have again a first integral $S(t) + I(t) + R(t) = P_{\text{total}}$.

Suppose that the control $u(t)$ is piecewise smooth and has values in a bounded and closed set $U = [\delta, m] \subset (0, \infty)$, where m will be selected at the end of this section by an extremum problem, determining the optimal striking time.

The set of such controls, denoted by $\mathcal{U}$, is called the set of admissible controls.

We explore how stochastic noise can be used to find connectivity properties generated by the underlying deterministic infectious disease dynamics and randomness.

Definition 1. A strong solution $c(t) = (S(t), I(t), R(t))$ of this stochastic differential system with the initial condition (S_0, I_0, R_0) is an adapted continuous process, such that, for all $t \geq 0$, it satisfies the stochastic integral system

$$S(t) - S_0 = - \int_0^t u(s)S(s)I(s)\mathrm{d}s + \int_0^t \sigma_a^1(s, S(s), I(s), R(s), u(s))\mathrm{d}W^a(s),$$

$$I(t) - I_0 = \int_0^t u(s)S(s) - \gamma I(s)\mathrm{d}s + \int_0^t \sigma_a^2(s, S(s), I(s), R(s), u(s))\mathrm{d}W^a(s), \qquad (51)$$

$$R(t) - R_0 = \int_0^t \gamma I(s)\mathrm{d}s - \int_0^t \sigma_a^3(s, S(s), I(s), R(s), u(s))\mathrm{d}W^a(s), a.s.$$

However, there is a number of subtle points involved: first, the existence of the integrals requires some degree of regularity on $c(t) = (S(t), I(t), R(t))$ and on the functions $u(t), \sigma = (\sigma_a^i)$ (matrix); in particular, it must be the case that, for all $t \geq 0$, with probability one, $\int_0^t \|\sigma(s)\|^2 \mathrm{d}s < \infty$.

Second, the solution is required to exist for all $t < \infty$ with probability one.

Properties of Itô integral are that, for all $G, H \in \mathbb{L}^2(0, T)$, we have

$$\mathbb{E}\left(\int_0^T G\mathrm{d}W \right) = 0,$$

$$\mathbb{E}\left(\left(\int_0^T G\mathrm{d}W \right)^2 \right) = \mathbb{E}\left(\int_0^T G^2\mathrm{d}t \right), \qquad (52)$$

$$\mathbb{E}\left(\left(\int_0^T G\mathrm{d}W \right)\left(\int_0^T H\mathrm{d}W \right) \right) = \mathbb{E}\left(\int_0^T GH\mathrm{d}t \right).$$

Definition 2. A weak solution $c(t) = (S(t), I(t), R(t))$ of the SDE with the initial condition (S_0, I_0, R_0) is a continuous stochastic process defined on some probability space

$(\Omega, \mathfrak{F}, P)$, such that, for some Wiener processes $W^a(t)$ and some admissible filtration $\mathfrak{F}$, the process $c(t)$ is adapted and satisfies the associated stochastic integral system.

The drift coefficients are uniformly Lipschitz functions. The basic result, due to Itô, is that, for uniformly Lipschitz functions σ, the SDE has strong solutions and that, for each initial value $c(0) = (S(0), I(0), R(0))$, the solution is unique.

Without loss of generality, we consider that the amplitudes of error are constants; that is, $\sigma_a^i(t, S(t), I(t), R(t), u(t)) = \sigma_a^i$.

Definition 3. Let $u(t) = u(S(t), I(t), R(t))$ be a feedback bounded control. A stochastic process $c(t) = (S(t), I(t), R(t))$, which satisfies the SDE system, is called an admissible stochastic process.

Theorem 6. *Let* $P = (S_P, I_P, R_P)$ *and* $Q = (S_Q, I_Q, R_Q)$ *be two points in the set* $[0, 1]^3 \subset \mathbb{R}_+^3$. *Denote* $D(Q, r)$ *as the Euclidean sphere of radius* r, *centered at* Q. *Then, for any* $\varepsilon > 0$ *and* $r > 0$, *there exists a striking time* $t < \infty$ *and an admissible stochastic process* $c(t)$, *satisfying the boundary conditions*

$$(S(0), I(0), R(0)) = (S_P, I_P, R_P), (\mathbb{E}[S(t)], \mathbb{E}[I(t)], \mathbb{E}[R(t)]) = (S_Q, I_Q, R_Q), \qquad (53)$$

such that

$$\mathbb{P}(c(t) \in D(Q, r)) \geq 1 - \varepsilon. \qquad (54)$$

Proof. We start with the nonnegative random variable $\|c(t) - Q\|^2$. Markov inequality shows that

$$\mathbb{P}\left(\|c(t) - Q\|^2 \geq r^2 \right) \leq \frac{1}{r^2} \mathbb{E}\left[\|c(t) - Q\|^2 \right], \qquad (55)$$

or, equivalently,

$$\mathbb{P}\left(\|c(t) - Q\|^2 \leq r^2 \right) \geq 1 - \frac{1}{r^2} \mathbb{E}\left[\|c(t) - Q\|^2 \right]. \qquad (56)$$

The stochastic integral variant of the previous SDE system is

$$S(t) = - \int_0^t u(s)S(s)I(s)\mathrm{d}s + \sigma_a^1 W^a(t) + S_P,$$

$$I(t) = \int_0^t (u(s)S(s) - \gamma) I(s)\mathrm{d}s + \sigma_a^2 W^a(t) + I_P, \qquad (57)$$

$$R(t) = \int_0^t \gamma I(s)\mathrm{d}s - \sigma_a^3 W^a(t) + R_P.$$

It is well-known that the expectation $\mathbb{E}$ has the properties

$$\mathbb{E}[W^a(t)] = 0,$$

$$\mathbb{E}\left[(W^a(t))^2 \right] = t \qquad (58)$$

$$\mathbb{E}[W^a(t)W^b(t)] = 0, \quad a \neq b.$$

If two random variables $X, Y: \Omega \longrightarrow \mathbb{R}$ are independent, then $\mathbb{E}[XY] = \mathbb{E}[X]\mathbb{E}[Y]$, provided that $\mathbb{E}[|X|] < \infty$ and $\mathbb{E}[|Y|] < \infty$.

The boundary conditions produce

$$\mathbb{E}[S(t)] = S_Q \Rightarrow \int_0^t \mathbb{E}[-u(s)S(s)I(s)]\mathrm{d}s + S_P = S_Q,$$

$$\mathbb{E}[I(t)] = I_Q \Rightarrow \int_0^t \mathbb{E}[(u(s)S(s) - \gamma)I(s)]\mathrm{d}s + I_P = I_Q,$$

$$\mathbb{E}[R(t)] = R_Q \Rightarrow \int_0^t \mathbb{E}[\gamma I(s)]\mathrm{d}s + R_P = R_Q.$$

$$(59)$$

Moreover, $S_P + I_P + R_P = 1$ implies $S_Q + I_Q + R_Q = 1$.

We use the advantages of Itô integral and the independence of Wiener processes $W^a(t)$. We find

$$
\begin{aligned}
\mathbb{E}\left[\|c(t) - Q\|^2\right] &= \mathbb{E}\left[\left(S(t) - S_Q\right)^2\right] + \mathbb{E}\left[\left(I(t) - I_Q\right)^2\right] + \mathbb{E}\left[\left(R(t) - R_Q\right)^2\right] \\
&= \mathbb{E}\left[\left(-\int_0^t u(s)S(s)I(s)\mathrm{d}s + \sigma_a^1 W^a(t) + S_P - S_Q\right)^2\right] \\
&\quad + \mathbb{E}\left[\left(\int_0^t (u(s)S(s) - \gamma)I(s)\mathrm{d}s + \sigma_a^2 W^a(t) + I_P - I_Q\right)^2\right] \\
&\quad + \mathbb{E}\left[\left(\int_0^t \gamma I(s)\mathrm{d}s - \sigma_a^3 W^a(t) + R_P - R_Q\right)^2\right] \\
&= \mathbb{E}\bigg[\int_0^t u(s)S(s)I(s)\mathrm{d}s \int_0^t u(s)S(s)I(s)u(s)\mathrm{d}s + \left(\sigma_a^1 W^a(t)\right)^2 + \left(S_P - S_Q\right)^2 \\
&\quad - 2\left(\int_0^t u(s)S(s)I(s)\mathrm{d}s\right)\sigma_a^1 W^a(t) - 2\left(\int_0^t u(s)S(s)I(s)\mathrm{d}s\right)\left(S_P - S_Q\right) + 2\sigma_a^1 W^a(t)\left(S_P - S_Q\right)\bigg] \\
&\quad + \mathbb{E}\int_0^t (u(s)S(s) - \gamma)I(s)\mathrm{d}s \int_0^t (u(s)S(s) - \gamma)I(s)\mathrm{d}s \\
&\quad + \left(\sigma_a^2 W^a(t)\right)^2 + \left(I_P - I_Q\right)^2 + 2\left(\int_0^t (u(s)S(s) - \gamma)I(s)\mathrm{d}s\right)\sigma_a^2 W^a(t) \\
&\quad + 2\left(\int_0^t (u(s)S(s) - \gamma)I(s)\mathrm{d}s\right)\left(I_P - I_Q\right) + 2\sigma_a^2 W^a(t)\left(I_P - I_Q\right) \\
&\quad + \mathbb{E}\bigg[\int_0^t \gamma I(s)\mathrm{d}s \int_0^t \gamma I(s)\mathrm{d}s + \left(\sigma_a^3 W^a(t)\right)^2 + \left(R_P - R_Q\right)^2 \\
&\quad - 2\left(\int_0^t \gamma I(s)\mathrm{d}s\right)\sigma_a^3 W^a(t) - 2\left(\int_0^t \gamma I(s)\mathrm{d}s\right)\left(R_P - R_Q\right) + 2\sigma_a^3 W^a(t)\left(R_P - R_Q\right)\bigg].
\end{aligned}
$$

$$(60)$$

This last expression is reduced to

$$
\begin{aligned}
&\mathbb{E}\left[\int_0^t u(s)S(s)I(s)\mathrm{d}s \int_0^t u(s)S(s)I(s)\mathrm{d}s\right] + t\sum_a \sigma_a^1 \sigma_a^1 - \left(S_P - S_Q\right)^2 \\
&\quad + \mathbb{E}\left[\int_0^t (u(s)S(s) - \gamma)I(s)\mathrm{d}s \int_0^t (u(s)S(s) - \gamma)I(s)\mathrm{d}s\right] + t\sum_a \sigma_a^2 \sigma_a^2 - \left(I_P - I_Q\right)^2 \\
&\quad + \mathbb{E}\left[\int_0^t \gamma I(s)\mathrm{d}s \int_0^t \gamma I(s)\mathrm{d}s\right] + t\sum_a \sigma_a^3 \sigma_a^3 - \left(R_P - R_Q\right)^2 \\
&= \mathbb{E}\left[\left(\int_0^t u(s)S(s)I(s)\mathrm{d}s\right)^2\right] + \mathbb{E}\left[\left(\int_0^t (u(s)S(s) - \gamma)I(s)\mathrm{d}s\right)^2\right] \\
&\quad + \mathbb{E}\left[\left(\int_0^t \gamma I(s)\mathrm{d}s\right)^2\right] + t\delta_{ij}\sum_a \sigma_a^i \sigma_a^j - \|P - Q\|^2.
\end{aligned}
$$

$$(61)$$

On the other hand, the Cauchy-Schwarz inequalities

$$\left(\int_0^t u(s)S(s)I(s)ds\right)^2 \le t\int_0^t (u(s)S(s)I(s))^2 ds,$$

$$\left(\int_0^t (u(s)S(s) - \gamma)I(s)ds\right)^2 \le t\int_0^t (u(s)S(s) - \gamma)^2 I^2(s)ds,$$

$$\left(\int_0^t \gamma I(s)ds\right)^2 \le t\int_0^t (\gamma I(s))^2 ds, \tag{62}$$

the properties of expectation, and the condition $u(t) \le m$ produce the estimations

$$\mathbb{E}\left[\left(\int_0^t u(s)S(s)I(s)ds\right)^2\right] \le m^2 S_Q^2 I_Q^2 t^2,$$

$$\mathbb{E}\left[\left(\int_0^t (u(s)S(s) - \gamma)I(s)ds\right)^2\right] \le (mS_Q - \gamma)^2 I_Q^2 t^2, \tag{63}$$

$$\mathbb{E}\left[\left(\int_0^t \gamma I(s)ds\right)^2\right] \le \gamma^2 I_Q^2 t^2.$$

Denoting

$$k_1^2 = m^2 S_Q^2 I_Q^2,$$

$$k_2^2 = (mS_Q - \gamma)^2 I_Q^2,$$

$$k_3^2 = \gamma^2 I_Q^2, \tag{64}$$

$$\|\sigma\|^2 = \delta_{ij} \sum_a \sigma_a^i \sigma_a^j,$$

we find

$$\mathbb{E}\left[\|c(t) - Q\|^2\right] \le (k_1^2 + k_2^2 + k_3^2)t^2 + \|\sigma\|^2 t - \|P - Q\|^2. \tag{65}$$

For any $\epsilon > 0$ and $r > 0$, the equation

$$(k_1^2 + k_2^2 + k_3^2)t^2 + \|\sigma\|^2 t - \|P - Q\|^2 - \epsilon r^2 = 0, \tag{66}$$

has a strictly positive solution

$$t_+ = \frac{-\|\sigma\|^2 + \sqrt{\|\sigma\|^4 + 4(k_1^2 + k_2^2 + k_3^2)\Lambda^2}}{2(k_1^2 + k_2^2 + k_3^2)}, \tag{67}$$

where $\Lambda^2 = \|P - Q\|^2 + \epsilon r^2$.

Denote $\|\sigma\| = c$, $k_1^2 = m^2 a^2$, and $k_2^2 = (mS - g)^2 b^2$. Using Maple routines, we find $t_{+e} = \text{extrema}_m t_+$:

(i) extrema-
$$((-c^2 + \text{sqrt}(c^4 + (4*(m^2*a^2 + (S*m - g)^2 \\ * b^2 + k3^2))*A))/(2*(m^2*a^2 + \\ (S*m - g)^2*b^2 + k3^2)),,m)$$

Answer:

$$\frac{1}{2} \frac{\left(-c^2 + \sqrt{\left((S^2 b^2 c^4 + 4AS^2 b^2 k3^2 + 4Aa^2 b^2 g^2 + a^2 c^4 + 4Aa^2 k3^2)/(S^2 b^2 + a^2)\right)}\right)(S^2 b^2 + a^2)}{S^2 b^2 k3^2 + a^2 b^2 g^2 + a^2 k3^2}. \tag{68}$$

For this optimal solution t_{+e}, we can write

$$\mathbb{E}\left[\|c(t_{+e}) - Q\|^2\right] \le \epsilon r^2 \Leftrightarrow 1 - \frac{1}{r^2}\mathbb{E}\left[\|c(t_{+e}) - Q\|^2\right] \ge 1 - \epsilon, \tag{69}$$

that is, $\mathbb{P}(c(t_{+e}) \in D(Q, r)) \ge 1 - \epsilon$. □

The previous theorem confirms that almost sure any two points in the "world" are joined by a stochastic curve. So, contamination can get anywhere from anywhere.

7. Conclusions

The most difficult thing for an epidemiological model is to predict human behavior. Infected population size estimation is a common problem in any epidemic analysis and it is the most important aspect for planning appropriate care and prevention policies. We underline that a model, even complex, is a simplification of reality, since a lot of other variables are still not completely known. An interactive approach with Maple can clarify some of these issues.

The flow models and even differential inclusion models are varied, often confusing to interpret, and are not crystal balls, especially because the ideal data are not yet available. But they are a large part of what government leaders use to make decisions, influencing how resources are allocated to health care facilities and how social distancing orders are issued to the public.

The three points of view in this paper, infectious disease flow, infectious disease wind, and stochastic connectivity, can input the biology of the virus and give positive answers to the following questions: how does it spread, how quickly

does it infect, how quickly does it lead to symptoms, and how quickly does it replicate to a level where it can jump from person to person?

The infectious disease wind is determined by the flow and by the geometry of space (created by nature or by human activities, conscious or not). All (the flow, the geometry, and the least squares technique) generate gyroscopic forces that lead to spiraling (uncontrolled) evolutions. The Riemannian structure can generate also chaos in geometric dynamics (sensitive dependence on initial conditions, and three or more dimensions). The experts in the fields of surveillance, epidemiology, and prevention of communicable disease spread, infection preventionists, must understand that infectious diseases modeled as wind and stochastic modeling of geometric structures are responsible for reading the infectious disease disasters.

Data Availability

The underlying data supporting the results of our study can be found through Prof. Emeritus Dr. Constantin Udriste.

Conflicts of Interest

The authors declare that they have no conflicts of interest.

Acknowledgments

References

[1] O. Calin and C. Udriste, *Geometric Modeling in Probability and Statistics*, Springer, Berlin, Germany, 2014.

[2] O. Calin, C. Udriste, and I. Tevy, "Stochastic sub-riemannian geodesics on grushin distribution," *Balkan Journal of Geometry and Its Applications*, vol. 19, no. 2, pp. 37–49, 2014.

[3] A. Simha, R. V. Prasad, and S. Narayana, "A simple stochastic sir model for COVID-19 infection dynamics for karnataka – learning from europe," 2020, http://arxiv.org/abs/2003.11920v1.

[4] T. Turcanu and C. Udriste, "Stochastic connectivity on a almost-Riemannian structure induced by symmetric polynomials," *Scientific Bulletin-University Politehnica of Bucharest*, vol. 81, no. 2, pp. 17–22, 2019.

[5] G. Giordano, F. Blanchini, R. Bruno et al., "Modelling the COVID-19 epidemic and implementation of population-wide interventions in Italy," *Letters*, vol. 14, 2020.

[6] M. W. Hirsch, S. Smale, and R. L. Devaney, *Differential Equations, Dynamical Systems and Introduction to Chaos*, Academic Press, Cambridge, UK, 2004.

[7] Y. Maki and H. Hideo, "Infectious disease spread analysis using stochastic differential equations for SIR model," in *Proceedings of the 4th International Conference on Intelligent Systems, Modelling and Simulation*, IEEE, Bangkok,Thailand, 2013.

[8] J.-P. Aubin and A. Cellina, *Differential Inclusions (Set-Valued Maps and Viability Theory)*, Springer-Verlag, Berlin, Germany, 1984.

[9] C. Udriste, *Geometric Dynamics*, Kluwer Academic Publishers, Amsterdam, Netherlands, 2000.

[10] C. Udriste and I. Tevy, "Geometric dynamics on Riemannian manifolds," *Mathematics*, vol. 8, no. 79, pp. 1–14, 2020.

[11] C. Udriste, O. Dogaru, M. Ferrara, and I. Tevy, "Nonholonomic optimization," in *Recent Advances in Optimization. Lecture Notes in Economics and Mathematical Systems*, A. Seeger, Ed., vol. vol 563, pp. 119–132, Springer, Berlin, Germany, 2006.

[12] C. Udriste, M. Constantinescu, I. Tevy, and O. Dogaru, "Dualities in nonholonomic optimization," *Mathematics and Computer Science*, vol. 54, no. 2, pp. 149–166, 2016.

[13] G. Vranceanu, "Sur les spaces non holonomes," *Comptes rendus de l'Académie des Sciences*, vol. 183, pp. 852–854, 1926.

WILEY | Hindawi

Research Article

On the 5G Communications: Fractal-Shaped Antennas for PPDR Applications

Mihai-Virgil Nichita [ID],[1] **Maria-Alexandra Paun** [ID],[2] **Vladimir-Alexandru Paun** [ID],[3] **and Viorel-Puiu Paun** [ID][4,5]

[1]*Doctoral School, Faculty of Applied Sciences, University Politehnica of Bucharest, 313 Splaiul Independentei, Sector 6, Bucharest RO-060042, Romania*
[2]*School of Engineering, Swiss Federal Institute of Technology (EPFL), Route Cantonale, Lausanne 1015, Switzerland*
[3]*Five Rescue Research Laboratory, 35 Quai d'Anjou, Paris 75004, France*
[4]*Physics Department, Faculty of Applied Sciences, University Politehnica of Bucharest, 313 Splaiul Independentei, Sector 6, Bucharest RO-060042, Romania*
[5]*Academy of Romanian Scientists, 54 Splaiul Independentei, Sector 5, Bucharest RO-050094, Romania*

Correspondence should be addressed to Maria-Alexandra Paun; maria_paun2003@yahoo.com

In this study, one method of using antennas based on fractals to cover few kinds of public protection and disaster relief (PPDR) communications was presented. Dedicated antenna forms, necessary for antenna design by 5G implementation, were enhanced to suit the requirements of specific applications. Employing fractal-shaped antennas have allowed us to accomplish all these actions, which request compact, conformal, and broadband high performance devices. Antennas derived from Koch's curve fractals are studied. In order to implement PPDR communications in 5G technology, frequency bandwidths of importance have been carefully selected and properly included in the antenna developments under MATLAB environment. Important information necessary for antenna designers, such as 360 degrees directivity at various frequencies, the impedance (resistance and reactance) along the bandwidth of interest, as well as voltage standing wave ratio (VSWR) along the bandwidth of interest for dipole, one-iteration, and two-iteration Koch's curves, respectively, have been obtained. The characteristic of directivity at selected frequencies is also highlighted. In order to maximize antenna parameters, this study has successfully proposed using fractal antennas, objects that use self-similarity property of fractals for optimum operation in several frequency ranges. For the studied antennas, we have obtained the following results regarding the maximum gains in dBi (which is the unit of the ratio between the gains of the antenna compared to the gain of an isotropic antenna). For the dipole antennas, the gains are 2.73 dBi and 4.76 dBi at 460 MHz and 770 MHz, respectively. The gains for one-iteration fractal Koch antenna are 6.91 dBi and 4.51 dBi at 460 MHz and 770 MHz, respectively, and finally, for two-iteration fractal Koch antenna, the gains are 4.91 dBi and 3.28 dBi at 460 MHz and 770 MHz, respectively. Moreover, the impedance along the bandwidth is approximately 360 Ohms for two-iteration fractal Koch antenna, 180 Ohms for one-iteration fractal Koch antenna, and 140 Ohms for dipole antenna, respectively.

1. Introduction

Today, the modern society needs more and more information. Apparently, individual customers, also the government, have a fabulous appetite for information repositories. Whether we talk about access to entertainment information or to PPDR (public protection and disaster relief) information, links to information sources are not allowed, from the customer's point of view, to have delays or inability to access them. At this moment, each of us has a smart communications terminal through which we access applications to facilitate our daily activities.

In this context, being an important part of the transceiver, the antennas must have a suitable design to function accordingly.

The IT&C environment has begun some time ago to develop programs for most of the actions that a person can take daily. Thus, the possibility of parallelization of activities was born. Moreover, social media applications have developed impressively over the last decade due to the fact that they have allowed people to be interconnected and to share with each other various information. Profile studies have shown that a user of 4G technology performs double information traffic compared to a user of another type of communication [1].

In the state of the art, a comparison between the results obtained by us in this study and the other authors from the scientific specialized literature is welcomed. Thus, size, shape, and gain are generally better or closer than [2, 3], as also highlighted in more depth at a thorough literature review made on this occasion in the next chapters, references cited in text where the exact comparisons are being made. Our values can be found in the results chapter.

Nowadays, mobile operators have developed infrastructures that allow for the sudden development of the IT&C environment. For this reason, customers are showing today an increasing need for denser networks, greater capacity for high mobility, ubiquitous coverage, low latency, massive number of affiliated devices, and low energy consumption, indices that begin to be decisive when it comes to value for money.

Thus, in order to optimize the production costs, in this document, it is proposed to design a fractal-shaped antenna that can be used for communications in different frequency bands.

Geometric shapes such as Sierpinski's triangle, Koch's curve, or Cantor's set can easily define antennas or antenna networks that facilitate communications across multiple frequency ranges if properly sized.

The study describes the objectives of 5G communications, the principles of fractal geometry, and how these irregular shapes can help the future of communications.

The work is organized in six chapters. In the introduction, the motivation for developing fractal-shaped antenna in the telecommunication domain is given. The second chapter talks about the emerging need for 5G technology and all the strict requirements that must be followed in order to allow for a multitude of connected devices to interact in a fast and reliable way. Furthermore, the third chapter introduces the fractal theory and gives few necessary equations. The fourth chapter is devoted to fractals antennas, from description of Koch's curve with governing equations, to enumerating the advantages of fractal-shaped antennas and then moving to fractal antennas design.

In the fifth chapter, the results obtained using our developed MATLAB programs are presented, in specific frequency bandwidth carefully chosen in order to implement PPDR communications in 5G technology. Therefore, the reader is given an overview of important information necessary for antenna designers, such as 360 degrees directivity at various frequencies, the impedance along the bandwidth of interest, as well as voltage standing wave ratio (VSWR) along the bandwidth of interest for dipole, one-iteration, and two-iteration Koch's curves, respectively. The characteristic of directivity at selected frequencies is also highlighted. The study concludes in the sixth chapter.

2. The Emerging Need for 5G

One desired issue to implement in 5G would be beamforming, the method that should point the end user equipment. Obviously, the cost for 5G infrastructure would increase because of the huge number of connected devices, fact which is contrary to actual generation of communications, as today, networks use little power to work.

Suddenly, massive MIMO concept became a backup solution to increase the bandwidth but not for a long time because of the high probability of occurrence of interference. So, a good antenna design is needed to avoid this phenomenon.

Microseconds latencies represent one major challenge for 5G. This facility emerged from the rush in which the society is at the moment. Some contemporary processors offer possibilities to achieve this objective, but the laws of physics are the ones that limit the transfers. So, the sender and the receiver should be close enough to accomplish this, and the topology should include a big number of hardware devices.

As for the bandwidths to be used, few intervals are suggested:

(i) 452.5–457.5 MHz

(ii) 462.5–467.5 MHz

(iii) 753–758 MHz

(iv) 788–791 MHz

The use of each frequency range implies the emergence of specific behaviors regarding the propagation of electromagnetic waves. Some of the most important phenomena to study are reflection and scattering, free space path loss, diffraction, or material penetration [1].

In order to offer communications for a large number of customers, it is recommended to have intelligent receivers, able to distinguish between signals intended for them, for others or noises. This would become a challenge for DSP or SDR programmers to develop the optimum software.

5G technology should be adopted even by the PPDR communications in order to improve their response time in case of an emergency [4].

Combined with fractal design techniques, the new technology should cover almost all the needs of the clients from PPDR area.

3. Fractals Theory

In 1977, the Swedish mathematician of French origins, Benoit Mandelbrot (1924–2010), published "Fractal Geometry of Nature," in order to offer a new way of describing the shape of objects such as coastlines and clouds [5].

Self-similarity is the most important property of fractals, and it implies that the fractal object must have an identical look at each iteration (most of the natural objects are self-similar). Due to the fact that a fractal object cannot be an input for an Euclidean formula, the fractal dimension must be introduced. This notion has a rational value, and it is strictly bigger than topological dimension.

According to Hausdorff, the fractal dimension is proportional to the minimum number of spheres, of given radius required to cover the measured object. Today, cubes are more reliable to use image processing [6, 7].

For a curve of length 1, $N(s) = 1$, cubes of side s are needed. Following this example, for an area $N(s) = 1/s^2$, cubes of side s are required, and for a volume, $N(s) = 1/s^3$, cubes of side s are required.

Considering d, s from R, and $N(s) = f(d)^*$sd, a set of functions, such that $N(s)$ is the number of spheres (balls) of s diameter (cubes of s side), is needed to cover the given set X. Then, there is a unique real value $d = D_H$, called the Hausdorff dimension of X, so that [7, 8]

$$d > D_H \Rightarrow N(s) \longrightarrow 0. \tag{1}$$

Thus, the Hausdorff dimension is described by

$$N(s) * sD_H. \tag{2}$$

The size of an object describes how it occupies space and how it can be measured (quantitatively). It is expressed in a rational number. We can easily calculate the geometric size of an object [9]. Generally, it is calculated using the Hausdorff dimension DH.

It starts from the formula written above, more precisely

$$N(s) = f(d)^* s^{D_H}, \tag{3}$$

where $N(s)$ is the number of cubes (or sphere), s is the length of cube's side (or spheres diameter), and D_H is the object's geometric dimension, respectively.

Fractal dimension formula: allow $N(X, s)$ to indicate the minimum series of identical figures (balls, spheres let us say) of radius s, necessary to include in the set X. Then, the theoretical fractal dimension is exactly given as

$$d(X) = \lim_{s \longrightarrow 0} \sup \frac{\log N(X, s)}{\log(1/s)}. \tag{4}$$

Observation 1: the coherent definition of fractal dimension we demonstrate here would essentially be proven if the superior limit in (4) could be superseded by a straightforward limit. No, this is not an extravagant exigency, and the "lim sup" solicitation is necessary, as there are simple sets for which the limit as $s \longrightarrow 0$ is nonexistent [8].

In concluding this topic, we specify that there are some very good methods for fast calculation of the fractal dimension, among which we list the one called the box-counting method.

Observation 2: on the engineering expectation side, the practical box-counting dimension could replace the
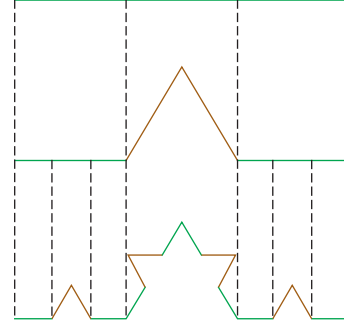
FIGURE 1: Koch curve construction based on Koch generator, orders 0, 1, and 2.

theoretical Hausdorff–Besicovitch dimension, being given by the box-counting method, facile to calculate. However, the aspect of fractal dimension calculus being nonetheless beyond the purpose of the current study, we will stop here with the details related to this topic.

Fractals used for antenna design are artificial ones like Minkowski's loop, Koch's curve, Sierpinski's carpet, and Sierpinski's gasket

4. Fractals Antennas

As we can affirm now, one of the advantages of fractal object is that it has an infinite measure of length, fitting in a finite measure of volume. Like it is known, radiation frequency is distinct for each individual electromagnetic transmitter and depends on electrical length of geometric structure. That is why, it was considered that utilizing the property of fractal geometry, we may increase the electrical length of an antenna (in direct connection with the wavelength, respectively), maintaining the identical antenna volume. We rely on mathematical observation at our disposal, namely, that we have many possibilities available to attempt as a design of same fractal antenna [10].

4.1. Fractal Geometry. Certain fractals portray replica of the entire structure at reduced scales. This property is mathematically named self-similarity, and it is helpful to project multiband antennas. Koch's snowflake is one of the particularly familiar self-similar fractals. Some other fractals fill the space, as is the case of space-packing curves, which makes them attractive in the design of little antennas. Koch's curve is one example of a space-packing curve, which has been utilized to build little antennas [11].

4.1.1. Koch's Curve. The initiator or, more precisely, the initial curve is a straight line. Specifically, in this case, the law of transformation requires that the straight line be divided into three equal parts that the central part be removed and in its place, an equilateral triangle without a base be placed (Figure 1).

At each iteration, each independent right is considered, and the transformation law is applied to it. In this case, the 4 segments each become a "new" initiator, and the support of 4
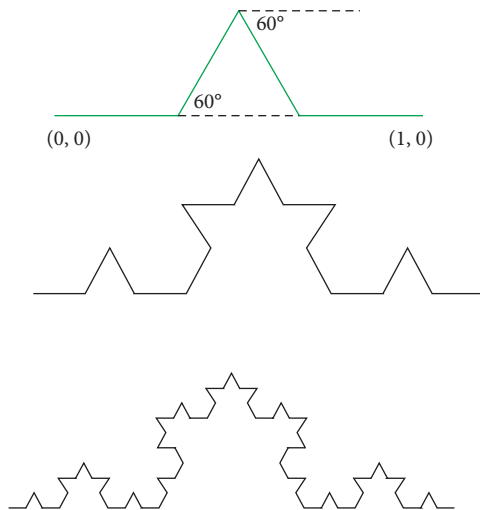
FIGURE 2: Koch curve construction based on the generator, orders 1 and 2 and length = 4/3.

"images" shrunk and is placed according to the same rule. Let us not forget that our mind must take the essence of the process and continue it to infinity because only after infinity of many steps, we obtain what is called the Koch fractal. This curve is of infinite length and has its own dimension between 1 and 2. It is a "strange" geometric object for the thinking of a person, unused to work with abstract things. It is a continuous curve, indivisible at no point, which exceeds the "nature" of a line, but does not reach the quality of being surface [11].

The proper fractal dimension: the characteristic of this Koch curve is fractal dimension: $df = \ln(4)/\ln(3) = 1.26185\ldots$.

A more concrete explanation is that to construct this curve, one starts by drawing a straight line (the blue segment in the figure). Then, divide this segment into three equal parts, and the middle segment is replaced by the two sides of an equilateral triangle of the same length as the length of the segment that is removed (the two red segments in the middle of the figure) [9]. Now repeat, take each of the four resulting segments, divide them into 3 equal parts, and replace each of the middle segments in two sides of an equilateral triangle (the red segments at the bottom of the figure).

In Figure 1, the Koch curve construction based on a specific generator is presented, namely, orders 0, 1, and 2.

The Koch curve is the limit of a curve obtained by applying this construction an infinite number of times. As proof, this construction even produces a "limit" that is the current curve, for example, the continuous image of a compact interval.

The first iteration for the Koch curve consists the fact that 4 copies of the original right segment are taken, each multiplied by $r = 1/3$. Two segments must be rotated by 60°, one clockwise and one in reverse.

In Figure 2, the Koch curve construction, based on a specific generator, is presented. Obviously, the length obtained is 4/3.

Niels Fabian Helge von Koch (1870–1924) constructed this curve in 1904 as an example of a nondifferentiable curve, which is a continuous curve that has no tangents at any point. Karl Weierstrass demonstrated the first existence of such a curve in 1872. The length of the intermediate curve at the nth iteration of the construction is $(4/3)n$, where $n = 0$ denotes the original length of the right segment. However, the length of the Koch curve is infinite. Moreover, the length of the curve between any 2 points of the curve is also infinite, with a copy of the Koch curve between any 2 of its points [12, 13].

4.2. Advantages of Fractal-Shaped Antennas. The telecommunications branch considers the antennas as a separate element of radio communications and therefore needs special attention not only in the design phase but also in the maintenance phase.

As the world becomes more and more dependent on cellular devices, there has been an increasing demand in antennas that are compact, conformal, and broadband [10]. A popular method of achieving these characteristics in an antenna is by exploiting the property of fractals.

In order to maximize antenna's length, this study suggests using fractal antennas, objects that use self-similarity property of fractals for optimum operation in several frequency ranges.

Among the advantages of fractal-shaped antennas, we can mention the following:

 (i) Very compact emplacement (a wire can be bended as a fractal, and so at the end of the process, on the same surface will fit a larger length of wire)

 (ii) Higher input resistance because of increase in length or perimeter [4]

 (iii) Low side-lobe levels and wide bandwidth

 (iv) Capable to implement beam-forming techniques due to fractals recursivity [10]

According to a public document from National Authority for Management and Regulation in Communications of Romania (ANCOM) (page 49) [14], PPDR communications would use few bandwidths to specific links. So, why do not the systems use only one antenna for all bandwidths? This can be the possibility to develop a self-reconfigurable system.

4.3. Fractal Antennas Design. The support of fractals geometry in antenna design engineering has led to a novel recently acquainted domain like fractal-electrodynamics, which has greatly influenced antenna theory. Traditional antenna design has been based on Euclidean geometries, but novel designs have come from modern fractal antenna engineering.

Fractal antennas get the benefit of geometries that cannot be acquired by classical Euclidean developments to provide accurately what consumers want.
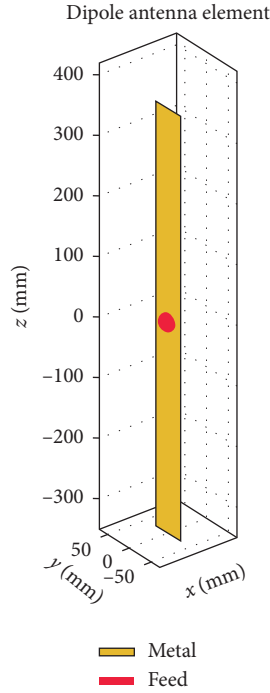
Figure 3: Dipole antenna.

First of the significant profit of fractal antenna is that we can obtain more than one single resonant band. As we said before, the fractal concept can be used to reduce antenna dimensions, such as in the case of the Koch dipole, Koch monopole, Koch loop, and Minkowski loop, for example.

The relationship that describes the radiated power for a multielement antenna is the following [13]:

$$
E \cdot E^* \sim \left(\sum_{n=1}^{N} A_n e^{i\phi_n} \right) \cdot \left(\sum_{m=1}^{N} A_n e^{i\phi_m} \right)^* = \sum_{n,m} (A_n A_m^*) e^{i(\phi_n - \phi_m)},
$$
(5)

where A_n defines the strength and orientation for each element, and ϕ_n has a connection with fractal's elements spatial distribution. We mention that every one of the elements concurs at the calculus of the entire radiated power density at a time-determined moment, through a vectorial amplitude and known phase, evidently.

A difference between antenna arrays and fractal antenna is that the order of classic antennas makes them be resonant just along one bandwidth, and fractal's disorder (made by fractal's elements) makes fractal-shaped antenna be resonant along many bandwidths (iteration 0 can be viewed as a classic antenna, and starting with a new iteration, a new bandwidth can be obtained).

Several applications can be developed based on fractal-shaped antennas due to their compact size and multiband resonance. Applications such as radars, personal cell phones, the ones from UWB branch, or 5G PPDR devices can benefit such an element which can have as a starting point any dedicated antenna (log-periodic, monopole, dipole, and patch).

5. Results

In order to implement PPDR communications in 5G technology, few bandwidths were suggested by ANCOM in Romania [14]: 452.5–457.5 MHz, 462.5–467.5 MHz, 753–758 MHz, and 788–791 MHz.

5.1. Antennas Derived from Koch's Curve Fractals. From this point of view, we designed in MATLAB R2018b a center-fed fractal-shaped antenna (Koch's curve format) to observe how well does this kind of solution fits in a 5G communication in comparison with a dipole.

By default, MATLAB generates the dipole with a length of one meter each side and 0.1 meters width. By adjusting the dimensions according to the desired bandwidths, we obtain a length of 0.75 meters each side and a width of 0.0583 meters. After making the first iteration, we observe that the antenna should be fatten in order to obtain a wider bandwidth [13]. Thus, the length obtained is 0.7 meters for one side and the width is 0.07 meters. Achieving the second iteration, it can be observed that no fatten is needed. So, the length would be the same, 0.7 meters for each side, and the width would also remain 0.0583 meters.

Figure 3 presents the dipole antenna's element, as simulated.

In Figures 4–6, the 360 degrees directivity (for dipole, one-iteration Koch's curve and two-iteration Koch's curve), at frequency value of 460 MHz and frequency value of 770 MHz, are shown in detail.

The resonant frequency can be determined using fractal dimension by dividing c ($3 \cdot 10^8$ m/s) to 4 multiplied by the effective length of fractal [10].

Figures 7 and 8 display the three-dimensional radiation pattern and phase of the dipole at 460 MHz and 770 MHz, respectively, in a color-coded fashion.

It can be observed in Figure 9 that the impedance is almost 50 Ohms along the bandwidths of interest [15].

In Figure 10, the fractal Koch antenna (iteration 1) is represented, while further on, Figure 11 depicts the Fractal Koch antenna (iteration 2).

In Figure 5, one-iteration fractal Koch antenna 360 degrees directivity is graphically represented for the two frequencies of interest, 460 and 770 MHz, respectively.

Figures 12 and 13 show the color-coded three-dimensional representation of one-iteration fractal Koch antenna radiation pattern and phase at 460 MHz and 770 MHz, respectively [16, 17].

It can be observed in Figure 14 that the impedance has zero imaginary component, so the antenna is resonant along the bandwidths of interest.

Figures 15 and 16 show the color-coded three-dimensional representation of two iterations: fractal Koch antenna radiation pattern and phase at 460 MHz and 770 MHz, respectively.

Figure 17 shows that along two of the bandwidths of interest, the antenna might not be resonant, but it still remains suitable for the two others.

(a)   (b)
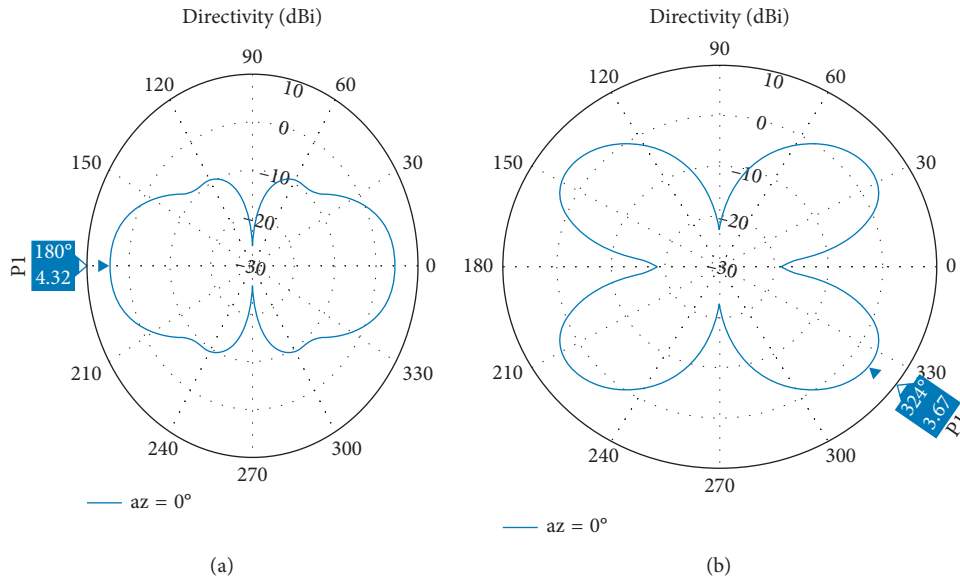
FIGURE 4: Dipole's 360 degrees directivity (more precisely, for dipole at 460 MHz left and right at 770 MHz).

(a)   (b)
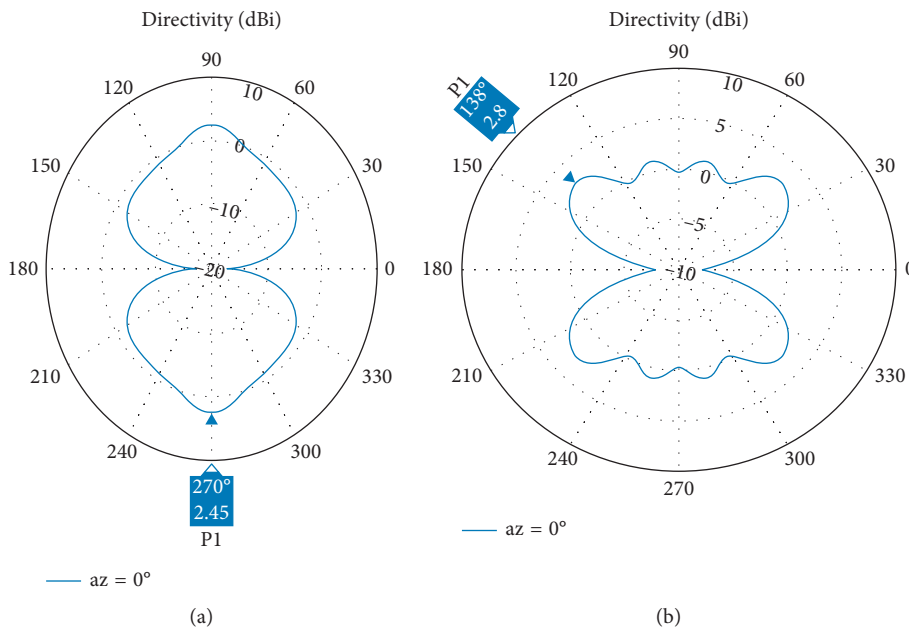
FIGURE 5: One-iteration fractal Koch antenna 360 degrees directivity (more precisely, one-iteration Koch's curve at 460 MHz left and right at 770 MHz).

In Figures 9, 14, and 17, the impedance, measured in Ohms (on the y-axis), is graphically represented along the band of interest versus frequency, measured in GHz [17], for the antenna with dipole, with one-iteration, and with two-iteration of Koch's curve. The graphics are marked with two distinct colors, resistance (blue) and reactance (red), to distinguish them.

Values for impedance, from Figures 9, 14, and 17, show that the dipole and the one-iteration Koch's curve antennas are suitable for using in the desired bandwidths, and the two-iteration Koch's curve may work poorly in the first part of the chosen spectrum, but it will certainly work properly in the second half.

The VSWR, Figure 18, it can be observed that most of the power to be delivered to the antennas is actually radiated by the antennas. For the first couple of bandwidths, the dipole and the two-iteration fractal are the most suitable, whereas for the second couple of bandwidths, the antenna from Figure 10 is better.

(a)

(b)
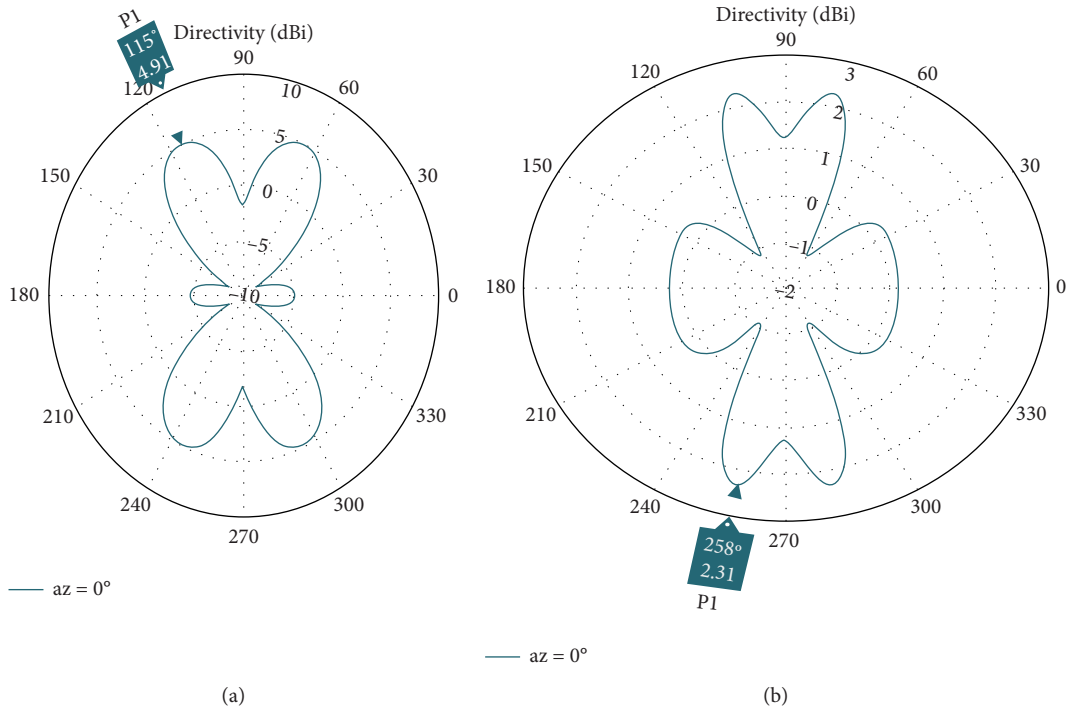
FIGURE 6: Two-iteration fractal Koch antenna 360 degrees directivity (more precisely, two-iteration Koch's curve at 460 MHz left and right at 770 MHz).
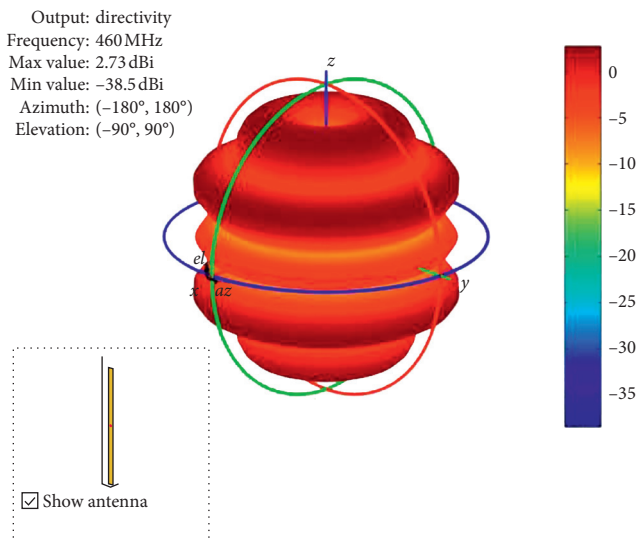
FIGURE 7: Dipole's radiation pattern and phase at 460 MHz.

In Figure 18, the magnitude, measured in dB (on the y-axis), is graphically represented along the band of interest versus frequency, measured in MHz for the antenna with dipole (iteration 0), with one-iteration, and with two-iteration of Koch's curve. The graphics are marked with three distinct colors for dipole (blue), one-iteration (brown), and two-iteration (olive) to distinguish them.

The VSWR values, from Figure 18, show that most of the power to be delivered to the antennas is actually radiated by the antennas. For the first couple of bandwidths, the dipole and the two-iteration fractal are the most suitable, whereas for the second couple of bandwidths, the resulting antenna is much better [2, 18, 19].

In Figure 19, the return loss for dipole and Koch's curve antennas have been evaluated, where the magnitude, measured in dB (on the y-axis), is graphically represented versus frequency, measured in MHz [20]. The graphics are marked with three distinct colors for dipole (blue), one-iteration (brown), and two-iteration (olive) to distinguish them.

In Figure 20, a comparison between dipole and Koch's curves antennas (one-iteration and two-iteration) is shown. Also, the graphics are marked with three distinct colors, blue, brown, and olive for dipole, one-iteration, and two-iteration, respectively.

We would like at this point to give a summary of the quantitative results we have obtained in our study. By performing the three-dimensional physical simulations of the artefacts developed, we have obtained the following numerical values for the directivity with maximum values of 2.73 dBi and 4.76 dBi for the dipole at 460 MHz and 770 MHz, respectively. At the same frequencies, the antenna radiation patterns revealed at 460 MHz maximum directivity values of 6.91 dBi for one-iteration fractal Koch antenna and 4.91 dBi for two-iteration fractal Koch antenna, while at 770 MHz, those values were 4.51 dBi for one-iteration fractal Koch antennas and 3.28 dBi for two-iteration fractal Koch antenna, respectively. Therefore, we can observe that the directivity drops by 29% for one-iteration antenna at 460 MHz and by approximately 27% at the higher frequency

Output: directivity
Frequency: 770 MHz
Max value: 4.76 dBi
Min value: −44.9 dBi
Azimuth: (−180°, 180°)
Elevation: (−90°, 90°)

☑ Show antenna
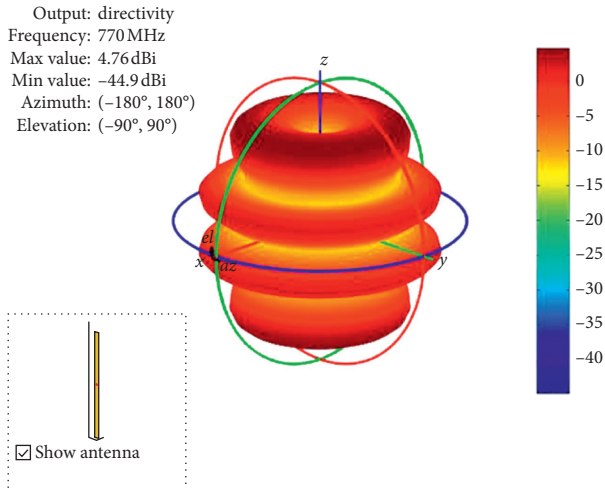
FIGURE 8: Dipole's radiation pattern and phase at 770 MHz.

Fractal Koch antenna element

■ Metal
■ Feed

FIGURE 11: Fractal Koch antenna (iteration 2).

FIGURE 9: Dipole's impedance along the bandwidth.

— Resistance
— Reactance

Output: directivity
Frequency: 460 MHz
Max value: 6.91 dBi
Min value: −24.7 dBi
Azimuth: (−180°, 180°)
Elevation: (−90°, 90°)

☑ Show antenna
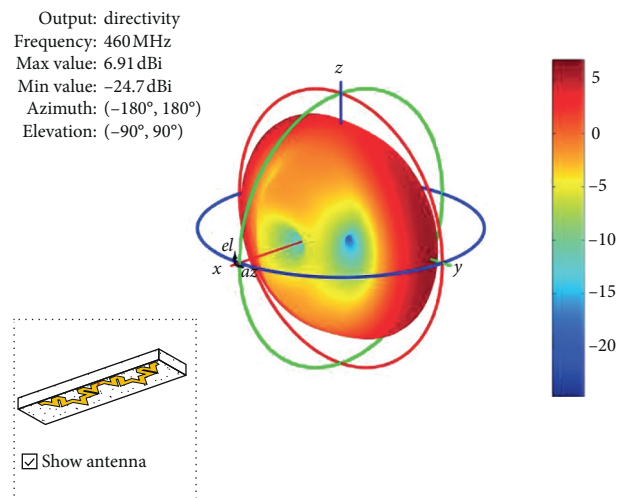
FIGURE 12: One-iteration fractal Koch antenna radiation pattern and phase at 460 MHz.

Fractal Koch antenna element

■ Metal
■ Feed

FIGURE 10: Fractal Koch antenna (iteration 1).

Output: directivity
Frequency: 770 MHz
Max value: 4.51 dBi
Min value: −31.9 dBi
Azimuth: (−180°, 180°)
Elevation: (−90°, 90°)

☑ Show antenna
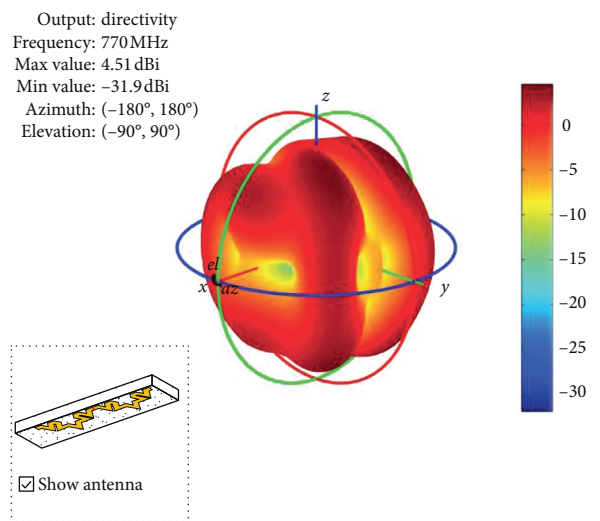
FIGURE 13: One-iteration fractal Koch antenna radiation pattern and phase at 770 MHz.
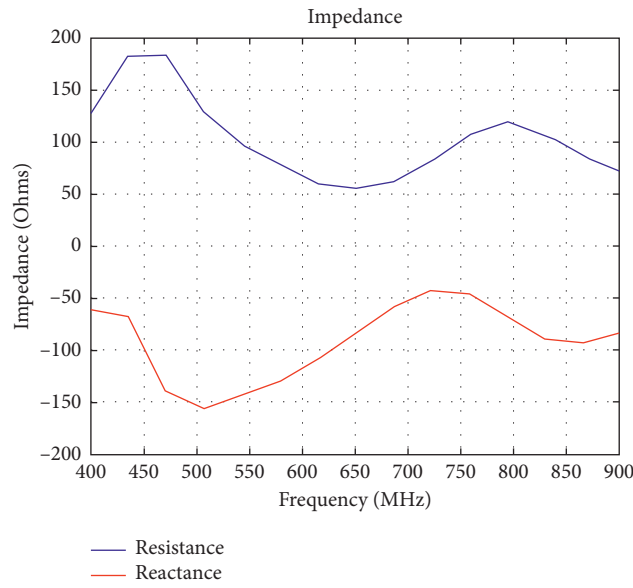
FIGURE 14: One-iteration fractal Koch antenna impedance along the bandwidth.
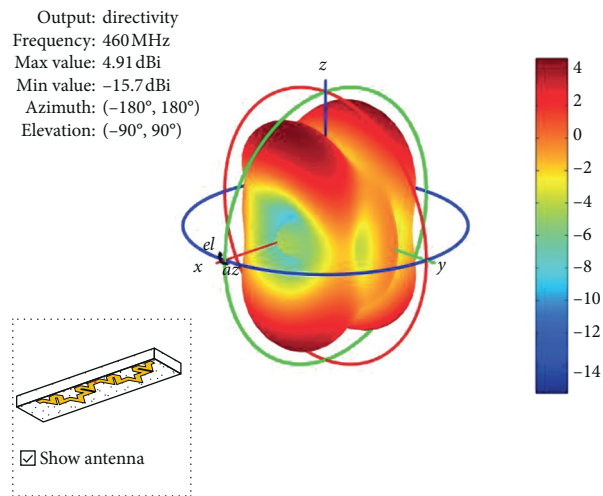
FIGURE 15: Two-iteration fractal Koch antenna radiation pattern and phase at 460 MHz.
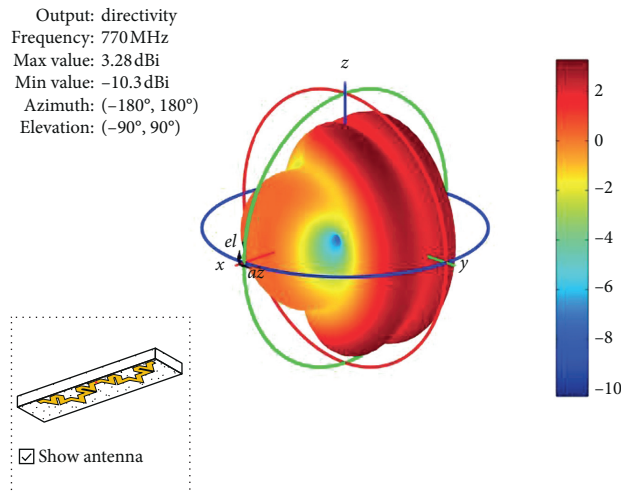
FIGURE 16: Two-iteration fractal Koch antenna radiation pattern and phase at 770 MHz.
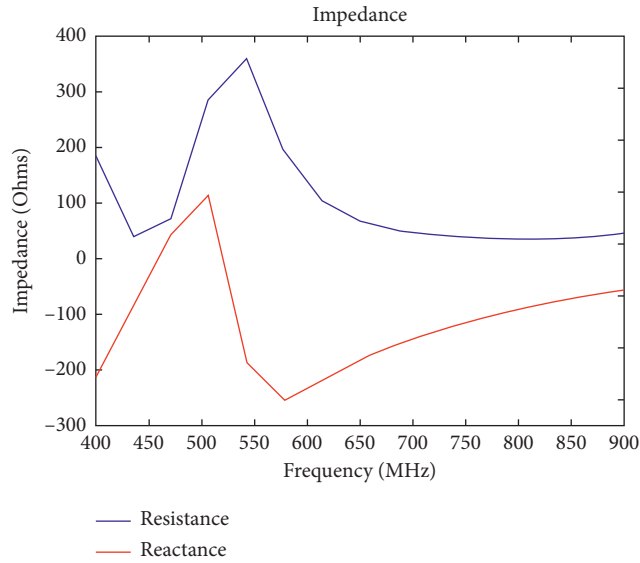
FIGURE 17: Two-iteration fractal Koch antenna impedance along the bandwidth.
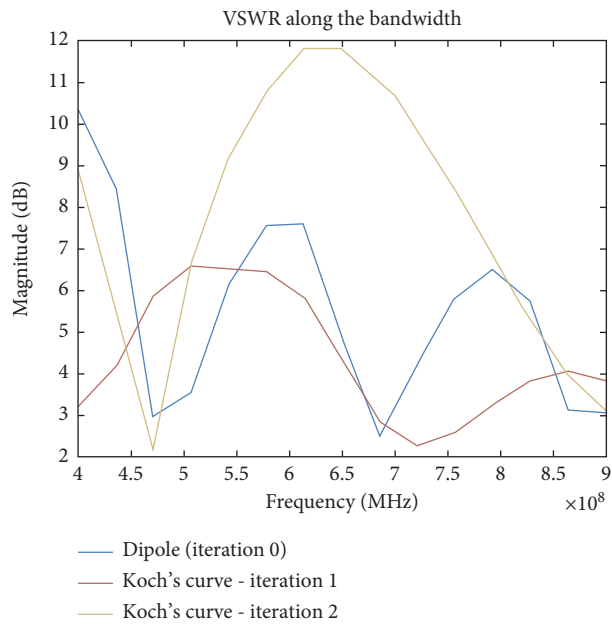
FIGURE 18: VSWR for dipole and Koch's curve antennas.

of 770 MHz. Moreover, both one-iteration and two-iteration fractal Koch antennas exhibit higher maximum directivities than dipole antennas at both frequencies studied.

The VSWR investigation produced the highest value of approximately 12 dB at 625 MHz for two-iteration fractal Koch antenna. Moreover, maximum return loss magnitudes

of approximately 8.8 dB for two-iteration Koch antenna and of 6 dB for dipole antenna are obtained at 460 MHz. Finally, the impedance along the bandwidth is approximately 360 Ohms for two-iteration fractal Koch antenna, 180 Ohms for one-iteration fractal Koch antenna, and 140 Ohms for dipole antenna, respectively.

Return loss along the bandwidth
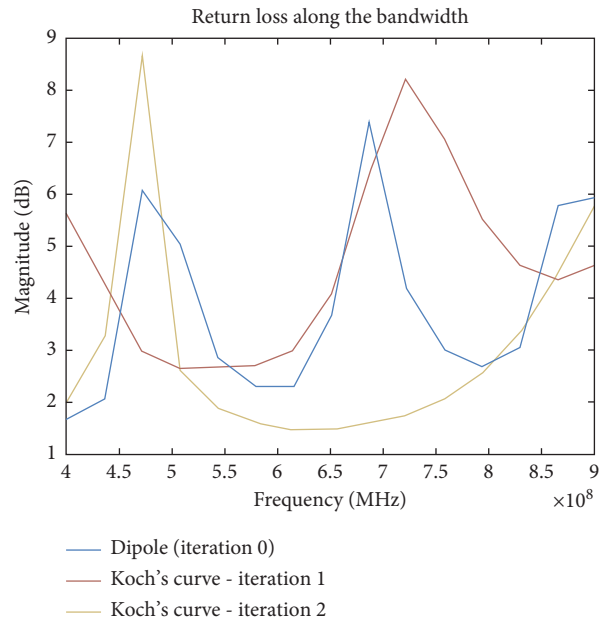
FIGURE 19: Return loss for dipole and Koch's curve antennas.

Impedance along the bandwidth
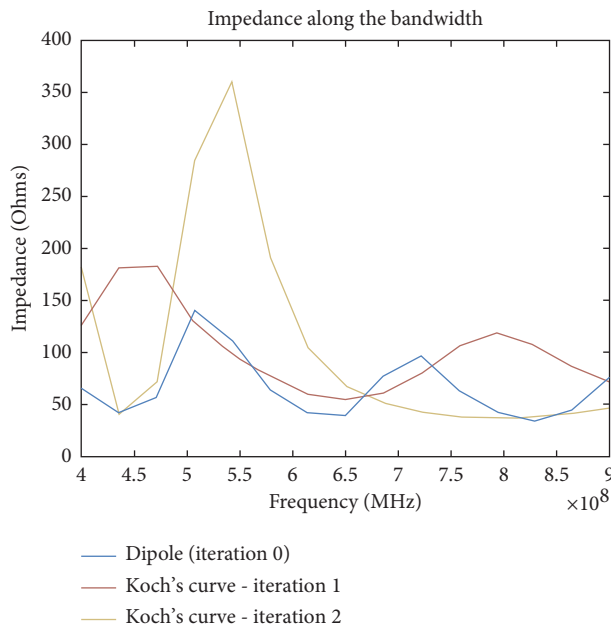
FIGURE 20: Comparison between dipole and Koch's curves antennas.

6. Conclusions

Dedicated wideband antennas can be used as starting point for fractal-shaped antennas to obtain new advantages such as compact size, multiband resonance, and providing more communication links to a single device.

One problem for the emergent technology, 5G, is the antenna because it has to transfer a huge quantity of information without filtering a little slice. This can be very challenging when a large number of users and protocols to follow are taken into account.

Only one antenna can cover technologies such as 2G, 3G, 4G, ZigBee, WLAN, and WiMax if properly designed, and it would be a shame to forget these kinds of networks when 5G would appear on the market.

Because of the need for speed, in order to improve the response times, the PPDR agencies will adopt the 5G technology as soon as possible.

In this study, two ways of using fractal-based antennas to cover few kinds of PPDR communications are presented.

The fractal shape suggested is a Koch's curve fractal-shaped antenna, which was based on a dipole. This kind of

antenna covers frequencies between 350 MHz and 800 MHz with few limitations.

All results were obtained using MATLAB R2018b software development. For the studied antennas, we have obtained the following results regarding the maximum gains in dBi (which is the unit of the ratio between the gains of the antenna compared to the gain of an isotropic antenna). For the dipole antennas, the gains are 2.73 dBi and 4.76 dBi at 460 MHz and 770 MHz, respectively. The gains for one-iteration fractal Koch antenna are 6.91 dBi and 4.51 dBi at 460 MHz and 770 MHz, respectively, and finally, for two-iteration fractal Koch antenna, the gains are 4.91 dBi and 3.28 dBi at 460 MHz and 770 MHz, respectively. Moreover, the impedance along the bandwidth is approximately 360 Ohms for two-iteration fractal Koch antenna, 180 Ohms for one-iteration fractal Koch antenna, and 140 Ohms for dipole antenna, respectively.

Signal intelligence, electronic warfare, or tactical communications can be one of those applications because properties such as wideband frequency range or compact size are desired for the ones who develop solutions for this branch.

Therefore, objectives raised for antenna design by 5G implementation can be accomplished by enhancing dedicated antenna forms. These actions can be done using fractal-shaped antennas. Much more, in the future, we intend to use an original two or three-iteration binary bionic fractal tree as the pattern in antenna to design 5th generation (5G) antennas, derived from the rules of nominal microstrip monopole antenna but together with the resonant connection device [21], integrated in the benefit of familiar fractal Koch geometry.

Data Availability

The data used to support the findings of this study cannot be accessed due to commercial confidentiality.

Conflicts of Interest

The authors declare that they have no conflicts of interest.

References

[1] M. V. Nichita, P. Ciotirnae, R. L. Luca, and V. N. Petrescu, "5G propagation: current solutions and future proposals," in *Proceedings of the 2016 12th IEEE International Symposium on Electronics and Telecommunications (ISETC)*, pp. 47–50, Timisoara, Romania, October 2016.

[2] G. Khanna and N. Sharma, "Fractal antenna geometries: a review," *International Journal of Computer Applications*, vol. 153, no. 7, pp. 29–32, 2016.

[3] N. Mohamed Mohamed, E. Antonino-Daviu, M. Cabedo-Fabrés, and M. Ferrando-Bataller, "A novel low-profile high-gain UHF antenna using high-impedance surfaces," *IEEE Antennas And Wireless Propagation Letters*, vol. 14, pp. 1014–1017, 2015.

[4] https://www.mathworks.com/help/antenna/fractal-antennas.html, website accessed on 24th of February 2020..

[5] B. Mandelbrot, *Fractal Geometry of Nature*, pp. 25–57, Freeman, New York, NY, USA, 1983.

[6] M. V. Nichita and V. P. Paun, "Fractal analysis in complex arterial network of pulmonary X-rays images," *University Politehnica of Bucharest Scientific Bulletin, Series A-Applied Mathematics and Physics*, vol. 80, no. 2, pp. 325–339, 2018.

[7] C. A. Rogers, *Hausdorff Measures*, Cambridge University Press, Oxford, UK, 1970.

[8] M. V. Nichita, M. A. Paun, V. A. Paun, and V. P. Paun, "Fractal analysis of brain glial cells. Fractal dimension and lacunarity," *University Politehnica of Bucharest Scientific Bulletin, Series A-Applied Mathematics and Physics*, vol. 81, no. 1, pp. 273–284, 2019.

[9] D. Bordescu, M. A. Paun, V. A. Paun, and V. P. Paun, "Fractal analysis of neuroimagistic. Lacunarity degree, a precious indicator in the detection of Alzheimer's disease," *University POLITEHNICA of Bucharest Scientific Bulletin, Series A-Applied Mathematics and Physics*, vol. 80, no. 4, pp. 309–320, 2018.

[10] A. Kiani, S. T. Karim, and S. B. Solak, *Fractal Antennas*, McGill University, Montreal, Canada, 2007.

[11] Y. K. Choukiker and S. K. Behera, "Wideband frequency reconfigurable Koch snowflake fractal antenna," *IET Microwaves, Antennas & Propagation*, vol. 11, no. 2, pp. 203–208, 2017.

[12] H. Rajabloo, V. Amiri Kooshki, and H. Oraizi, "Compact microstrip fractal Koch slot antenna with ELC coupling load for triple band application," *AEU - International Journal of Electronics and Communications*, vol. 73, pp. 144–149, 2017.

[13] N. S. M. Yaziz, M. K. A. Rahim, F. Zubir, N. S. Nadzir, R. Dewan, and H. A. Majid, "The improvement of first iteration log periodic fractal Koch antenna with slot implementation," *International Journal of Electrical and Computer Engineering (IJECE)*, vol. 8, no. 4, pp. 2564–2570, 2018.

[14] https://www.ancom.ro/uploads/links_files, website accessed on 14th of March 2020..

[15] Z. Borsos, V.-P. Paun, I. C. Botez, C.-M. Stoica, P. Vizureanu, and M. Agop, "Structural conductivity of carbon nanotubes," *Revista de Chimie*, vol. 59, no. 10, pp. 1169–1171, 2008.

[16] J. Anguera, A. Andújar, J. Jayasinghe et al., "Fractal antennas: an historical perspective", review, fractal fract," *MDPI*, vol. 4, no. 1, pp. 1–26, 2020.

[17] R. Tyagi and S. Kohli, "Design and development of square fractal antenna for wireless applications," *International Journal of Advanced Research in Computer Science and Software Engineering*, vol. 5, no. 5, 2015.

[18] P. Srivastava and O. P. Singh, "A review paper on fractal antenna and their geometries," in *Proceedings of the Advances in Electrical & Information Communication Technology, AEICT, 2015*, Kanpur, India, April 2015.

[19] M.-A. Paun and V.-A. Paun, "High-frequency 3-D model for the study of antennas in cochlear implants," *IEEE Transactions on Components, Packaging and Manufacturing Technology*, vol. 8, no. 7, pp. 1135–1140, 2018.

[20] B. Lazar, A. Sterian, S. Pusca, V. Paun, C. Toma, and C. Morarescu, "Simulating delayed pulses in organic materials," in *Proceedings of the Conference: International Conference on Computational Science and its Applications (ICCSA 2006), Computational Science and its Applications - ICCSA 2006*, vol. 3980, pp. 779–784PT 1 Book Series: Lecture Notes in Computer Science, Glasgow, UK, May 2006.

[21] X. Ran, Z. Yu, T. Xie, Y. Li, X. Wang, and P. Huang, "A novel dual-band binary branch fractal bionic antenna for mobile terminals," *International Journal of Antennas and Propagation*, vol. 2020, Article ID 6109093, 9 pages, 2020.

WILEY | Hindawi

Research Article

Nonfragile H_∞ Stabilizing Nonlinear Systems Described by Multivariable Hammerstein Models

Zeineb Rayouf, Chekib Ghorbel [ID], and Naceur Benhadj Braiek [ID]

Laboratory of Advanced Systems, Polytechnic High School of Tunisia, University of Carthage, BP 743, 2078, La Marsa, Tunisia

Correspondence should be addressed to Chekib Ghorbel; chekib.ghorbel@enit.rnu.tn

This paper presents the problem of robust and nonfragile stabilization of nonlinear systems described by multivariable Hammerstein models. The objective is focused on the design of a nonfragile feedback controller such that the resulting closed-loop system is globally asymptotically stable with robust H_∞ disturbance attenuation in spite of controller gain variations. First, the parameters of linear and nonlinear blocks characterizing the multivariable Hammerstein model structure are separately estimated by using a subspace identification algorithm. Second, approximate inverse nonlinear functions of polynomial form are proposed to deal with nonbijective invertible nonlinearities. Thereafter, the Takagi–Sugeno model representation is used to decompose the composition of the static nonlinearities and their approximate inverses in series with the linear subspace dynamic submodel into linear fuzzy parts. Besides, sufficient stability conditions for the robust and nonfragile controller synthesis based on quadratic Lyapunov function, H_∞ criterion, and linear matrix inequality approach are provided. Finally, a numerical example based on twin rotor multi-input multi-output system is considered to demonstrate the effectiveness.

1. Introduction

The nonlinear modeling of real-world processes, which are complex in nature, remains a challenging problem. However, much research works remain to be done for realization on nonlinear mathematical models that accurately represent these processes [1–4]. One way to cope with this difficulty is to use the block-oriented nonlinear models [5–7], which represent a combination of static nonlinear components and linear dynamic submodels. These models are popular in nonlinear modeling because of their advantages to be quite simple to understand and easy to use [8], for instance, the Hammerstein model (a static nonlinear component followed by a linear submodel), Wiener model (a linear submodel followed by a static nonlinear component), and Hammerstein–Wiener model (a linear submodel sandwiched by two static nonlinearities or vice versa). In particular, the simplest model structure of them is the Hammerstein model, which has been extensively used for modeling electrical generators [9], chemical processes [10], and biological processes [11] and is also used in signal processing applications [12].

Over the past decades, various parametric subspace identification methods have been very successful for the modeling of multivariable Hammerstein models. These methods include the iterative identification approach [13, 14], the overparameterization method [15], the blind approach [16], the instrumental variables method [17], the stochastic approach [18], and the least square support vector machines [19]. Most of them are based on the numerical subspace state-space system identification algorithm [20], the canonical variate analysis approach [21], and the multivariable output error state-space (MOESP) algorithm [10, 22].

From a control point of view, the conventional control scheme of a Hammerstein model has introduced the inverse of the nonlinear block into the appropriate place. This leads to reject the nonlinearity effect in the controller design [23]. Hence, the nonlinear control strategy problem is converted into a new linear one; also, any standard linear controller for a linear dynamic submodel can be applied. It should be a strong assumption that this nonlinearity is supposed to be exactly invertible [24–26]. In contrast, the performance of

this strategy becomes limited when the nonlinear component function is not bijective. In this view, many algorithms and approximations are used in the literature to determine the corresponding nonlinearity inverse. One may refer to latest research works based on polynomial form approximation [23, 27, 28], Bernstein–Bezier neural network [29], De Boor algorithm [30], and rational B-spline model approximation [31].

On the other hand, many studies have been devoted to the robust and nonfragile controller design problem for complex systems. Indeed, it is clear that relatively small perturbations in controller gain parameters can result in instability of the controlled system [32, 33]. Hence, it is necessary that any controller should be able to tolerate some bounded uncertainty in its parameters [3, 34, 35]. For instance, a nonfragile controller for uncertain nonlinear networked control systems was proposed in [36]. In [37], a nonfragile robust controller was investigated for uncertain large-scale systems. Lee et al. [38] proposed a nonfragile fuzzy H_∞ controller for nonlinear systems described in Takagi–Sugeno (T-S) fuzzy model, and so on. To our best knowledge, the nonfragile control problem for Hammerstein models has not been treated yet.

In this framework, we use the MOESP subspace identification algorithm, which mainly involves two aspects: (i) determining the order of the system and obtaining the structure of the estimated state-space model and (ii) identifying the mathematical model's unknown parameters from the available input-output data [10]. Afterwards, we propose a new control strategy for multivariable Hammerstein model including approximate inverse nonlinearities of polynomial form. Using then the T-S fuzzy model representation [1, 2, 34, 39], the composed nonlinear functions of the considered static nonlinearities and their approximate inverses in series with the linear dynamic submodel are decomposed into linear fuzzy parts. The resulting model is finally obtained by interpolating the constructed linear fuzzy parts through nonlinear fuzzy membership functions [2, 4, 35, 40]. In this regard, a nonfragile H_∞ feedback controller is designed subject to controller gain variations guaranteeing both the stability and disturbance attenuation of the controlled nonlinear system.

The main contributions of this paper are listed as follows:

(i) A modified subspace-based algorithm is used to identify nonlinear systems described by multivariable Hammerstein models.

(ii) Compared with the existing results using the normal nonlinearity inversion method, we derive a new control strategy based on approximate inverse nonlinear functions of polynomial form. Furthermore, we appeal the T-S fuzzy model representation to decompose the existing nonlinearities and facilitate the controller synthesis.

(iii) From a control point of view, we develop a robust and nonfragile H_∞ controller with variation in the control law that guarantees both the asymptotic stability and disturbance attenuation of the controlled nonlinear system and its identified multivariable Hammerstein model.

(iv) Besides, sufficient controller design conditions in terms of linear matrix inequalities (LMIs) are established, which can be efficiently solved by convex optimization techniques.

Following the introduction, this paper is organized as follows. The subspace identification method for multivariable Hammerstein model is presented in Section 2. Section 3 is reserved to the stability analysis and nonfragile H_∞ control synthesis. A numerical example based on twin rotor multi-input multi-output system (TRMS) is considered in Section 4 to demonstrate the effectiveness.

2. MOESP Algorithm-Based Subspace Identification

We consider the multi-input multi-output (MIMO) Hammerstein model configuration, as depicted in Figure 1. As mentioned obviously, the model's structure consists of m-static nonlinearities $f_i(\cdot)$ followed by a linear dynamic submodel.

More precisely, each nonlinear component $f_i(\cdot)$, for $i = 1, 2, \ldots, m$, is characterized by the following form:

$$v_{i,k} = f_i(u_{i,k}) = \lambda_{i1} u_{i,k} + \lambda_{i2} u_{i,k}^2 + \cdots + \lambda_{iv} u_{i,k}^v, \qquad (1)$$

and the linear dynamic submodel is described by the following state-space representation:

$$\begin{cases} x_{k+1} = Ax_k + B_1 V_k + B_2 w_k, \\ Y_k = Cx_k + DV_k + \varepsilon_k, \end{cases} \qquad (2)$$

where $x_k \in \mathbb{R}^n$ is the state vector, $V_k = \begin{pmatrix} v_{1,k} & v_{2,k} & \cdots & v_{m,k} \end{pmatrix}^\perp$ is the unmeasurable output, $w_k \in \mathbb{R}^n$ is the external disturbance vector, $\varepsilon_k \in \mathbb{R}^q$ is the measurement noise vector, $u_k = \begin{pmatrix} u_{1,k} & u_{2,k} & \cdots & u_{m,k} \end{pmatrix}^\perp$ is the input vector, $Y_k = \begin{pmatrix} y_{1,k} & y_{2,k} & \cdots & y_{q,k} \end{pmatrix}^\perp$ is the output vector, and the notation $(\perp)$ denotes the transposed element. $A \in \mathbb{R}^{n \times n}$, $B_1 = \begin{pmatrix} B_{11} & B_{12} & \cdots & B_{1m} \end{pmatrix} \in \mathbb{R}^{n \times m}$, $B_2 \in \mathbb{R}^{n \times n}$, $C \in \mathbb{R}^{q \times n}$, and $D = \begin{pmatrix} D_1 & D_2 & \cdots & D_m \end{pmatrix} \in \mathbb{R}^{q \times m}$ are unknown state-space matrices.

By substituting (1) into (2), we obtain the following open-loop model:

$$\begin{cases} x_{k+1} = Ax_k + B_1^\lambda U_k + B_2 w_k, \\ Y_k = Cx_k + D^\lambda U_k + \varepsilon_k, \end{cases} \qquad (3)$$

where $U_k = (U_{1,k} U_{2,k} \ldots U_{m,k})^\perp$, $U_{i,k} = (u_{i,k} u_{i,k}^2 \ldots u_{i,k}^v)^\perp$, $B_1^\lambda = (B_{11}^\lambda B_{12}^\lambda \ldots B_{1m}^\lambda)$, $D^\lambda = (D_1^\lambda D_2^\lambda \ldots D_m^\lambda)$, $B_{1i}^\lambda = B_{1i} \lambda_i^{\text{vec}}$, $D_i^\lambda = D_i \lambda_i^{\text{vec}}$, and $\lambda_i^{\text{vec}} = (\lambda_{i1} \lambda_{i2} \ldots \lambda_{iv})$, for $i = 1, 2, \ldots, m$.

In order to estimate the system order and determine the unknown elements, as are presented in system (3), we use the MOESP algorithm, which is basically defined by the following steps:
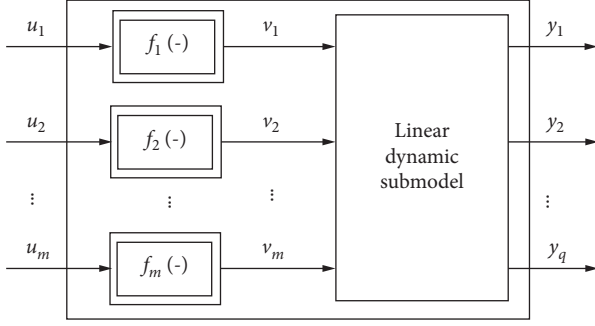
FIGURE 1: Multivariable Hammerstein model configuration.

(i) Step 1: for sake of simplicity and feasibility, we assume that $\|\lambda_i^{\text{vec}}\|_2 = 1$ and $\lambda_{i1} = 1$, for $i = 1, 2, \ldots, m$ [23, 28, 41].

(ii) Step 2: we determine the estimates $\widehat{A}$, $\widehat{B}_1^\lambda$, $\widehat{B}_2$, $\widehat{C}$, and $\widehat{D}^\lambda$ of matrices A, B_1^λ, B_2, C, and D^λ directly from the available input-output data.

(iii) Step 3: we compute a matrix estimate $\widehat{\Theta}_i$ of Θ_i, which is defined as

$$\Theta_i \triangleq \begin{pmatrix} B_{1i}^\lambda \\ D_i^\lambda \end{pmatrix} = \begin{pmatrix} B_{1i} \\ D_i \end{pmatrix} \lambda_i^{\text{vec}}, \tag{4}$$

by solving the following optimization problem:

$$\left(\widehat{B}_{1i}, \widehat{D}_i, \widehat{\lambda}_i^{\text{vec}} \right) = \arg \left(\min_{B_{1i}, D_i, \lambda_i^{\text{vec}}} \left(\left\| \widehat{\Theta}_i - \begin{pmatrix} B_{1i} \\ D_i \end{pmatrix} \lambda_i^{\text{vec}} \right\|_2^2 \right) \right). \tag{5}$$

(iv) Step 4: based on the singular value decomposition (SVD) theorem, as is detailed in [42], we calculate the partition of $\widehat{\Theta}_i$ as follows:

$$\widehat{\Theta}_i = \begin{bmatrix} U_1 & U_2 \end{bmatrix} \begin{bmatrix} \Sigma_1 & 0 \\ 0 & \Sigma_2 \end{bmatrix} \begin{bmatrix} V_1^\perp \\ V_2^\perp \end{bmatrix}, \tag{6}$$

where U_1, V_1, and Σ_1 are specific matrices of appropriate dimensions.

(v) Step 5: we compute finally the estimates $\widehat{B}_{1i}$, $\widehat{D}_i$, and $\widehat{\lambda}_i^{\text{vec}}$ so that the following system of equations is satisfied:

$$\begin{cases} \begin{bmatrix} \widehat{B}_{1i} \\ \widehat{D}_i \end{bmatrix} = U_1 \Sigma_1, \\ \widehat{\lambda}_i^{\text{vec}} = V_1, \quad \text{for } i = 1, 2, \ldots, m. \end{cases} \tag{7}$$

3. Nonfragile H_∞ Control Scheme Design

In this section, we discuss sufficient conditions that guarantee the global asymptotic stability in closed loop of the following system:

$$\begin{cases} x_{k+1} = A x_k + B_1 V_k + B_2 w_k, \\ z_k = C_z x_k + D_1 V_k + D_2 w_k, \end{cases} \tag{8}$$

where $C_z \in \mathbb{R}^{p \times n}$ is the output matrix of the controlled output vector $z_k \in \mathbb{R}^p$, $D_1 \in \mathbb{R}^{p \times m}$, and $D_2 \in \mathbb{R}^{p \times n}$.

In what follows, we assume that the m-nonlinearities:

$$v_{i,k} = f_i \left(u_{i,k} \right) = u_{i,k} + \lambda_{i2} u_{i,k}^2 + \cdots + \lambda_{iv} u_{i,k}^v, \tag{9}$$

are not bijective and approximated of the following form:

$$u_{i,k} = f_{i,\text{app}}^{-1} \left(\widehat{v}_{i,k} \right) = \beta_{i1} \widehat{v}_{i,k} + \beta_{i2} \widehat{v}_{i,k}^2 + \cdots + \beta_{iv} \widehat{v}_{i,k}^v + \text{hot}. \tag{10}$$

where (hot) denotes the higher order terms. As the nonlinearities (9) and (10) are in series, we may write

$$v_{i,k} = \psi_i \left(\widehat{v}_{i,k} \right) = f_i \left(f_{i,\text{app}}^{-1} \left(\widehat{v}_{i,k} \right) \right). \tag{11}$$

In addition, the parameters β_{ij} are determined by solving $\widehat{v}_i(+\infty) = v_i(+\infty)$, for $i = 1, 2, \ldots, m$. An example of calculation for the order $v = 3$ is detailed in Appendix A.

With the above approximation, system (8) is transformed as follows:

$$\begin{cases} x_{k+1} = A x_k + B_1^\rho \widehat{V}_k + B_2 w_k, \\ z_k = C_z x_k + D_1^\rho \widehat{V}_k + D_2 w_k, \end{cases} \tag{12}$$

where $B_1^\rho = \begin{pmatrix} B_{11}^{\rho_1} B_{12}^{\rho_2} \ldots B_{1m}^{\rho_m} \end{pmatrix}$, $D_1^\rho = \begin{pmatrix} D_{11}^{\rho_1} D_{12}^{\rho_2} \ldots D_{1m}^{\rho_m} \end{pmatrix}$, $B_{1i}^{\rho i} = B_{1i} \rho_{i,k} (\widehat{v}_{i,k})$, $D_{1i}^{\rho i} = D_{1i} \rho_{i,k} (\widehat{v}_{i,k})$, for $i = 1, 2, \ldots, m$, $\rho_{i,k}$ $(\widehat{v}_{i,k}) = \begin{cases} \psi_i (\widehat{v}_{i,k}) / \widehat{v}_{i,k} & \text{if } \widehat{v}_{i,k} \neq 0 \\ 1 & \text{else} \end{cases}$, and $\widehat{V}_k = \begin{pmatrix} \widehat{v}_{1,k} \widehat{v}_{2,k} \ldots \widehat{v}_{m,k} \end{pmatrix}^\perp$.

Using then the polytopic transformation method, the m-nonlinearities $\rho_i (\widehat{v}_{i,k})$ are decomposed as follows:

$$\rho_{i,k} \left(\widehat{v}_{i,k} \right) = H_i^1 \left(\widehat{v}_{i,k} \right) \overline{\sigma}_i + H_i^2 \left(\widehat{v}_{i,k} \right) \underline{\sigma}_i, \tag{13}$$

with

$$H_i^1 \left(\widehat{v}_{i,k} \right) = \frac{\rho_{i,k} \left(\widehat{v}_{i,k} \right) - \underline{\sigma}_i}{\overline{\sigma}_i - \underline{\sigma}_i}, \tag{14}$$

$$H_i^2 \left(\widehat{v}_{i,k} \right) = 1 - H_i^1 \left(\widehat{v}_{i,k} \right), \tag{15}$$

where $\overline{\sigma}_i$ and $\underline{\sigma}_i$ are the maximum and minimum of $\rho_i (\widehat{v}_{i,k})$, respectively.

For the convenience of notations, we define $H_i^j = H_i^j (\widehat{v}_{i,k})$, $w_i = w_i (\widehat{v}_{i,k})$, and $h_i = h_i (\widehat{v}_{j,k})$.

Thereafter, we construct the following fuzzy subsystems:

rule 1: if $\left(\widehat{v}_{1,k} \text{ is } H_1^1 \right)$ and $\left(\widehat{v}_{2,k} \text{ is } H_2^1 \right)$ and $\ldots \left(\widehat{v}_{m,k} \text{ is } H_m^1 \right)$,

then $x_{k+1} = A x_k + \widetilde{B}_{11} \widehat{V}_k + B_2 w_k, z_k$

$= C_z x_k + \widetilde{D}_{11} \widehat{V}_k + D_2 w_k,$ (16)

rule 2: if $\left(\widehat{v}_{1,k} \text{ is } H_1^1 \right)$ and $\left(\widehat{v}_{2,k} \text{ is } H_2^1 \right)$ and $\ldots \left(\widehat{v}_{m,k} \text{ is } H_m^2 \right)$,

then $x_{k+1} = A x_k + \widetilde{B}_{12} \widehat{V}_k + B_2 w_k, z_k = C_z x_k + \widetilde{D}_{12} \widehat{V}_k + D_2 w_k,$

$\vdots$

(17)

rule $\varsigma = 2^m$: if $\left(\widehat{v}_{1,k} \text{ is } H_1^2\right)$ and $\left(\widehat{v}_{2,k} \text{ is } H_2^2\right)$

and $\ldots \left(\widehat{v}_{m,k} \text{ is } H_m^2\right)$,

then $x_{k+1} = Ax_k + \widetilde{B}_{1\varsigma}\widehat{V}_k + B_2 w_k, z_k$ $\quad(18)$

$\qquad = C_z x_k + \widetilde{D}_{1\varsigma}\widehat{V}_k + D_2 w_k,$

where $\widetilde{B}_{11} = \begin{pmatrix} \overline{B}_{11}^{\rho_1} & \overline{B}_{12}^{\rho_2} & \ldots & \overline{B}_{1m}^{\rho_m} \end{pmatrix}$, $\widetilde{D}_{11} = \begin{pmatrix} \overline{D}_{11}^{\rho_1} & \overline{D}_{12}^{\rho_2} & \ldots \end{pmatrix}$
$\overline{D}_{1m}^{\rho_m}$), $\widetilde{B}_{12} = \begin{pmatrix} \overline{B}_{11}^{\rho_1} & \overline{B}_{12}^{\rho_2} & \ldots & \underline{B}_{1m}^{\rho_m} \end{pmatrix}$, $\widetilde{D}_{12} = \begin{pmatrix} \overline{D}_{11}^{\rho_1} & \overline{D}_{12}^{\rho_2} & \ldots \underline{D}_{1m}^{\rho_m} \end{pmatrix}$,
$\widetilde{B}_{1\varsigma} = \begin{pmatrix} \underline{B}_{11}^{\rho}\underline{B}_{12}^{\rho_2} \cdot \underline{B}_{1m}^{\rho_m} \end{pmatrix}$, $\widetilde{D}_{1\varsigma} = \begin{pmatrix} \underline{D}_{11}^{\rho}\underline{D}_{12}^{\rho_2} \cdot \underline{D}_{1m}^{\rho_m} \end{pmatrix}$, $\overline{B}_{1i}^{\rho_i} = \overline{\sigma}_i B_{1i}$,
$\underline{B}_{1i}^{\rho_i} = \underline{\sigma}_i B_{1i}$, $\overline{D}_{1i}^{\rho_i} = \overline{\sigma}_i D_{1i}$, and $\underline{D}_{1i}^{\rho_i} = \underline{\sigma}_i D_{1i}$, for $i = 1, 2, \ldots, m$.

As a consequence, the final system is inferred as follows:

$$\begin{cases} x_{k+1} = \sum_{i=1}^{\varsigma} h_i\left(Ax_k + \widetilde{B}_{1i}\widehat{V}_k + B_2 w_k\right), \\ z_k = \sum_{i=1}^{\varsigma} h_i\left(C_z x_k + \widetilde{D}_{1i}\widehat{V}_k + D_2 w_k\right), \end{cases} \quad(19)$$

where the nonlinear weighting functions are $h_i = w_i / \sum_{i=1}^{\varsigma} w_i$, such that $0 \le h_i \le 1$ and $\sum_{i=1}^{\varsigma} h_i = 1$, and

$$\begin{cases} w_1 = H_1^1 H_2^1 \ldots H_m^1, \\ w_2 = H_1^1 H_2^1 \ldots H_m^2, \\ \vdots \\ w_\varsigma = H_1^2 H_2^2 \ldots H_m^2. \end{cases} \quad(20)$$

For stabilizing system (19) in closed loop, we assume that each subsystem $(A, \widetilde{B}_{1i})$ is fully controllable and measurable. Then, we use the nonfragile control law:

$$\widehat{V}_k = -\overline{K}x_k, \quad(21)$$

with the uncertainty:

$$\overline{K} = K + \Delta K = (I + \mu\phi_k)K, \quad(22)$$

where $K \in \mathbb{R}^{m \times n}$ is the nominal controller, $\mu > 0$ is a scalar to be assigned, $I \in \mathbb{R}^{m \times m}$ denotes the identity matrix, and $\phi_k \in \mathbb{R}^{m \times m}$, such that $\phi_k^{\perp}\phi_k \le I$.

Substituting (21) into (19), we obtain the final controlled system:

$$\begin{cases} x_{k+1} = \sum_{i=1}^{\varsigma} h_i\left(\overline{G}_i x_k + B_2 w_k\right), \\ z_k = \sum_{i=1}^{\varsigma} h_i\left(\overline{F}_i x_k + D_2 w_k\right), \end{cases} \quad(23)$$

where $\overline{G}_i = G_i + \Delta G_i$, $\overline{F}_i = F_i + \Delta F_i$, $G_i = A - \widetilde{B}_{1i}K$, $\Delta G_i = -\mu\widetilde{B}_{1i}\phi_k K$, $F_i = C_z - \widetilde{D}_{1i}K$, and $\Delta F_i = -\mu\widetilde{D}_{1i}\phi_k K$.

The closed-loop system (23) is globally asymptotically stable with decay rate α and achieves a prescribed attenuation level γ if

$$\|T_{zw}\|_{\infty} = \sup_{\|w\|_2 \neq 0} \frac{\|z\|_2}{\|w\|_2} < \gamma. \quad(24)$$

As a consequence, we announce the following theorem.

Theorem 1. *The equilibrium* $(x = 0_{\mathbb{R}^n})$ *of the closed-loop system (23) is quadratically and globally asymptotically stable with decay rate α satisfying the control performance objective (24) if there exist positive scalars μ, τ_1, τ_2, $\delta_{12} = \tau_1^{-1} + \tau_2^{-1}$, and $\beta \in]0, 1[$, a common symmetric positive definite matrix $X \in \mathbb{R}^{n \times n}$, and $M \in \mathbb{R}^{m \times n}$ verifying the following LMI formulation:*

$$\underset{X,M,\gamma}{\text{minimize}}\, \beta$$

$$\text{subject to :} \begin{pmatrix} -\beta X & * & * & * & * \\ 0 & -\gamma^2 I & * & * & * \\ AX - \widetilde{B}_{1i}M & B_2 & -\ell_{33,i} & * & * \\ C_z X - \widetilde{D}_{1i}M & D_2 & 0 & -\ell_{44,i} & * \\ M & 0 & 0 & 0 & -\delta_{12}^{-1}I \end{pmatrix} < 0,$$

$$\quad(25)$$

for $i = 1, 2, \ldots, \varsigma$, *where* $\ell_{33,i} = X - \tau_1 \mu^2 \widetilde{B}_{1i}\widetilde{B}_{1i}^{\perp}$ *and* $\ell_{44,i} = I - \tau_2 \mu^2 \widetilde{D}_{1i}\widetilde{D}_{1i}^{\perp}$.

Then, the feedback gain K, as is shown in (22), is calculated by using the following relation:

$$K = MX^{-1}. \quad(26)$$

Proof. The controlled system (23) is globally asymptotically stable with decay rate α if there exist a discrete-time quadratic Lyapunov function $V_{\text{Lyap}}(x_k) = x_k^{\perp} P x_k > 0$ and a positive scalar $0 < \alpha < 1$ such that

$$\Delta V_{\text{Lyap}}(x_k) \le (\alpha^2 - 1)V_{\text{Lyap}}(x_k), \quad(27)$$

where $\Delta V_{\text{Lyap}}(x_k) = V_{\text{Lyap}}(x_{k+1}) - V_{\text{Lyap}}(x_k)$ and $P \in \mathbb{R}^{n \times n}$ is a symmetric positive definite matrix. By considering (27) in (24), we may write

$$\Delta V_{\text{Lyap}}(x_k) - (\alpha^2 - 1)V_{\text{Lyap}}(x_k) + z_k^{\perp}z_k - \gamma^2 w_k^{\perp}w_k < 0. \quad(28)$$

By, respectively, substituting the dynamics of x_{k+1} and z_k into (28), it becomes

$$\sum_{i=1}^{\varsigma} h_i \begin{pmatrix} x_k \\ w_k \end{pmatrix}^{\perp} \Gamma_i \begin{pmatrix} x_k \\ w_k \end{pmatrix} < 0, \quad(29)$$

where $\Gamma_i = \begin{pmatrix} \overline{G}_i^{\perp}P\overline{G}_i - \alpha^2 P + \overline{F}_i^{\perp}\overline{F}_i & * \\ B_2^{\perp}P\overline{G}_i + D_2^{\perp}D_2 & B_2^{\perp}PB_2 + D_2^{\perp}D_2 - \gamma^2 I \end{pmatrix}$ and the symbol $(*)$ represents the transposed element in the symmetric position.

As the nonlinear functions $h_i \in [0, 1]$, matrix inequality (29) is equivalent to $\Gamma_i < 0$, for $i = 1, 2, \ldots, \varsigma$. Using the Schur Complement, as is presented in Appendix B, we get

$$\begin{pmatrix} -\alpha^2 P & * & * & * \\ 0 & -\gamma^2 I & * & * \\ P\overline{G}_i & PB_2 & -P & * \\ \overline{F}_i & D_2 & 0 & -I \end{pmatrix} < 0. \quad(30)$$

Denoting $X = P^{-1}$, $M = KX$, and $\beta = \alpha^2$ and, respectively, premultiplying and postmultiplying (30) by positive definite matrix $\text{diag}(X, I, X, I)$ yields

$$
\begin{pmatrix}
-\beta X & * & * & * \\
0 & -\gamma^2 I & * & * \\
\overline{G}_i X & B_2 & -X & * \\
\overline{F}_i X & D_2 & 0 & -I
\end{pmatrix} < 0. \tag{31}
$$

As the above matrix inequality contains certain terms $\Psi_{i,k}$ and uncertain ones $\Delta\Psi_{i,k}$, (31) can be transformed as follows:

$$
\Psi_{i,k} + \Delta\Psi_{i,k} < 0, \tag{32}
$$

with

$$
\Psi_{i,k} = \begin{pmatrix}
-\beta X & * & * & * \\
0 & -\gamma^2 I & * & * \\
G_i X & B_2 & -X & * \\
F_i X & D_2 & 0 & -I
\end{pmatrix}, \tag{33}
$$

$$
\Delta\Psi_{i,k} = \begin{pmatrix}
0 & 0 & * & * \\
0 & 0 & 0 & 0 \\
-\mu\widetilde{B}_{1i}\phi_k M & 0 & 0 & 0 \\
-\mu\widetilde{D}_{1i}\phi_k M & 0 & 0 & 0
\end{pmatrix}. \tag{34}
$$

We notice that there are antidiagonal terms in $\Delta\Psi_{i,k}$. However, we use the Separation Lemma, as is defined in Appendix C, to transform them into diagonal terms as follows:

$$
\Delta\psi_{i,k} \leq \begin{pmatrix}
\delta_{12} M^\perp M & 0 & 0 & 0 \\
0 & 0 & 0 & 0 \\
0 & 0 & \tau_1\mu^2\widetilde{B}_{1i}\widetilde{B}_{1i}^\perp & 0 \\
0 & 0 & 0 & \tau_2\mu^2\widetilde{D}_{1i}\widetilde{D}_{1i}^\perp
\end{pmatrix}, \tag{35}
$$

where τ_1, τ_2, and $\delta_{12} = \tau_1^{-1} + \tau_2^{-1}$ are positive scalars to be assigned.

Referring to relations (33) and (35), we obtain

$$
\begin{pmatrix}
-\beta X + \delta_{12} M^\perp M & * & * & * \\
0 & -\gamma^2 I & * & * \\
G_i X & B_2 & -X + \tau_1\mu^2\widetilde{B}_{1i}\widetilde{B}_{1i}^\perp & * \\
F_i X & D_2 & 0 & -I + \tau_2\mu^2\widetilde{D}_{1i}\widetilde{D}_{1i}^\perp
\end{pmatrix} < 0. \tag{36}
$$

After some manipulations, we get the LMI formulation (25). □

$$
\begin{aligned}
&\underset{X,R,\gamma}{\text{minimize}}\, \beta \\
&\text{subject to:} \begin{pmatrix}
-\beta X & * & * & * \\
0 & -\gamma^2 I & * & * \\
AX - \widetilde{B}_{1i}M & B_2 & -X & * \\
C_z X - \widetilde{D}_{1i}M & D_2 & 0 & -I
\end{pmatrix} < 0, \quad \text{for } i = 1, 2, \ldots, \varsigma.
\end{aligned} \tag{37}
$$

In the following, a numerical example is provided to demonstrate the validity and the effectiveness of the proposed control scheme.

Remark 1. Consider system (19) with no uncertainty, *i.e.*, $\Delta K = 0$. Then, the origin of the closed-loop system (26) is globally asymptotically stable if [27]

4. Application to a TRMS

The objective of this simulation study is to stabilize the controlled TRMS and its identified multivariable
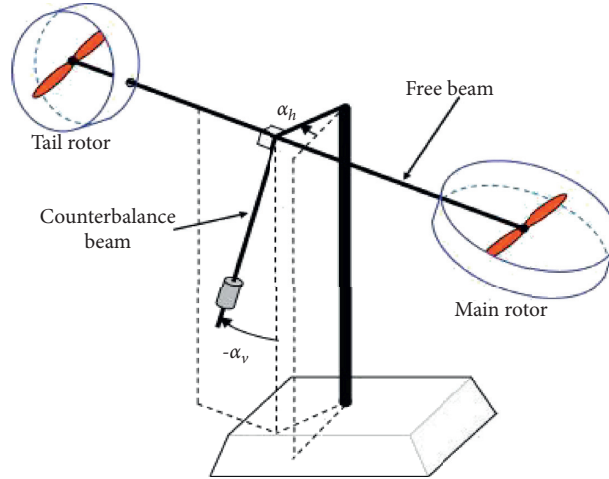
FIGURE 2: TRMS [43].

Hammerstein model at the origin, as an asymptotically stable equilibrium point. More precisely, its system behaviour resembles that of a helicopter, as is seen in Figure 2. It consists of two rotors (main and tail), which are situated on a beam together with a counterbalance. The inputs of the open-loop system are the voltages u_1 (V) and $u_2(V)$ applied, respectively, to the main and tail rotors. The first output is called pitch angle y_1 (rad) when the main rotor is free to rotate in the horizontal plane. The second output is called yaw angle y_2 (rad) when the tail rotor is free to rotate in the vertical plane.

The studied system is described by the following continuous-time nonlinear equations [43]:

$$\begin{cases} I_1\ddot{\psi} = M_1 - M_{FG} - M_{B\psi} - M_G, \\ I_2\ddot{\phi} = M_2 - M_{B\phi} - M_R, \end{cases} \tag{38}$$

where $M_1 = a_1\eta_1^2 + b_1\eta_1$, $M_{FG} = M_g\sin(\psi)$, $M_{B\psi} = B_{1\psi}\dot{\psi}$, $M_G = K_{gy}M_1\dot{\phi}\cos(\psi) - K_{gx}\dot{\phi}^2\sin(2\psi)$, $M_2 = a_2\eta_2^2 + b_2\eta_2$, $M_{B\phi} = B_{1\phi}\dot{\phi}$, $\dot{\eta}_1 = -T_{10}/T_{11}\eta_1 + k_1/T_{11}u_1$, $\dot{\eta}_2 = -T_{20}/T_{21}\eta_2 + k_2/T_{21}u_2$, $M_R = k_c\eta_1 1 + T_0 s/1 + T_p s$, and s is the Laplace variable. All parameters are defined in Appendix D.

4.1. Identification Result. From an identification point of view, we assume that the input-output data are available. Then, we consider that the sampling period is $T = 0.1$ s and the inputs are $u_{1,k} = 2.5\sin(0.6\pi kT)$ and $u_{2,k} = 2\sin(0.8\pi kT)$. Figures 3 and 4 depict the responses of the true (solid line) and estimated (dashed line) outputs of the open-loop system.

It is then clear that the nonlinear TRMS is accurately identified by 2-input 2-output Hammerstein state-space model, which is described by

$$\begin{cases} x_{k+1} = Ax_k + B_1V_k + B_2w_k, \\ Y_k = Cx_k + DV_k + \varepsilon_k, \\ v_{1,k} = u_{1,k} + 0.0381u_{1,k}^2 - 0.0457u_{1,k}^3, \\ v_{2,k} = u_{2,k} + 0.0237u_{2,k}^2 - 0.0118u_{2,k}^3, \end{cases} \tag{39}$$

where

$$x_k = \begin{pmatrix} x_{1,k} \\ x_{2,k} \\ x_{3,k} \\ x_{4,k} \end{pmatrix}, V_k = \begin{pmatrix} v_{1,k} \\ v_{2,k} \end{pmatrix}, Y_k = \begin{pmatrix} y_{1,k} \\ y_{2,k} \end{pmatrix}, w_k \in \mathbb{R}^4, \varepsilon_k \in \mathbb{R}^2,$$

$$A = \begin{pmatrix} 0.9709 & -0.3380 & 0.1232 & 0.0306 \\ 0.1179 & 0.9745 & 0.0093 & -0.0109 \\ -0.0375 & 0.0087 & 0.9974 & -0.0798 \\ 0.0109 & -0.0226 & 0.0270 & 0.8693 \end{pmatrix},$$

$$B_1 = \begin{pmatrix} 0.0111 & 0.0547 \\ -0.0131 & -0.0027 \\ 0.2172 & 0.3044 \\ 0.0865 & 0.0520 \end{pmatrix},$$

$$B_2 = \begin{pmatrix} -0.2292 & 0.5655 & 7.7293 & 0.2978 \\ 1.4445 & 0.2131 & -5.6435 & 0.0878 \\ -0.4621 & -0.0928 & -2.4361 & 0.1226 \\ -0.2324 & 0.0914 & 9.9696 & -0.7869 \end{pmatrix},$$

$$C = \begin{pmatrix} -0.0853 & 0.2915 & -0.1147 & 0.0093 \\ 0.0121 & -0.1440 & -0.3784 & -0.1127 \end{pmatrix},$$

$$D = \begin{pmatrix} -0.0326 & 0.0063 \\ 0.0284 & -0.0713 \end{pmatrix}.$$

$$\tag{40}$$
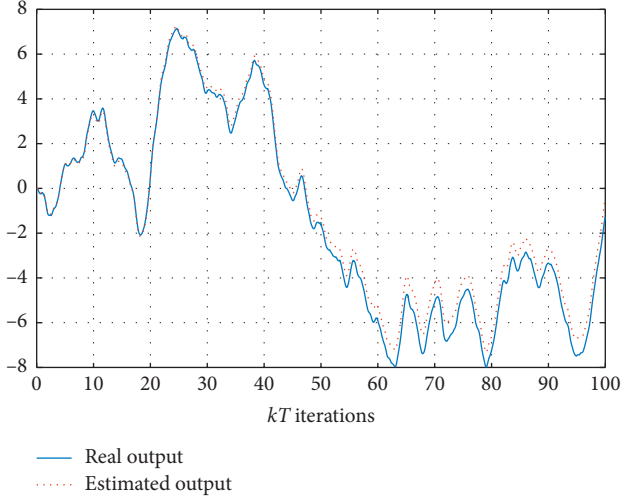
FIGURE 3: Response of the pitch angle of the open-loop system.
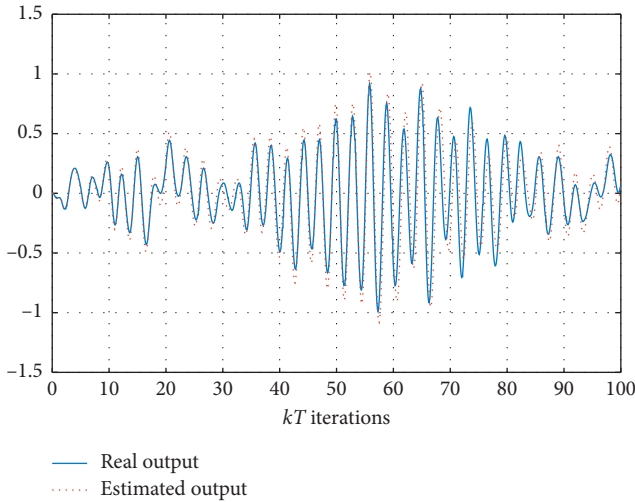
FIGURE 4: Response of the yaw angle of the open-loop system.

4.2. Control Results. From a control point of view, we assume that the inverse functions $u_{i,k} = f_{i,\text{app}}^{-1}(\widehat{v}_{i,k})$, for $i = \{1,2\}$, are approximated as follows:

$$\begin{cases} u_{1,k} = \widehat{v}_{1,k} - 0.0381\widehat{v}_{1,k}^2 + 0.1219\widehat{v}_{1,k}^3 + \text{hot}, \\ u_{2,k} = \widehat{v}_{2,k} - 0.0237\widehat{v}_{2,k}^2 + 0.0592\widehat{v}_{2,k}^3 + \text{hot}. \end{cases} \tag{41}$$

Choosing the scalars $\underline{\sigma}_1 = 0.4$, $\overline{\sigma}_1 = 1.7$, $\underline{\sigma}_2 = 0.3$, and $\overline{\sigma}_2 = 2$, Figure 5 depicts the evolution of nonlinearities $v_{i,k} = \psi_i(\widehat{v}_{i,k})$, for $i = \{1,2\}$. This leads to obtain, for the control scheme, the bounded control signals $\widehat{v}_{1,k} \in [-5.87, 5.73]$ and $\widehat{v}_{2,k} \in [-2.33, 2.24]$.

Afterwards, we assume that the controlled output z_k is expressed by

$$z_k = C_z x_k + D_1 V_k + D_2 w_k, \tag{42}$$

where $z_k = \begin{pmatrix} z_{1,k} \\ z_{2,k} \end{pmatrix}$, $C_z = C$, $D_1 = D$, and D_2

$$= \begin{pmatrix} 1 & 0 & 0 & 0 \\ 0 & 0 & 1 & 0 \end{pmatrix}.$$

By considering the pairs $(\overline{\sigma}_1, \overline{\sigma}_2)$, $(\overline{\sigma}_1, \underline{\sigma}_2)$, $(\underline{\sigma}_1, \overline{\sigma}_2)$, and $(\underline{\sigma}_1, \underline{\sigma}_2)$, we construct the following fuzzy subsystems:

$$\begin{aligned} &\text{rule 1: if} \left(\widehat{v}_{1,k} \text{ is } H_1^1\right) \text{ and } \left(\widehat{v}_{2,k} \text{ is } H_2^1\right), \\ &\text{then } x_{k+1} = Ax_k + \widetilde{B}_{11}\widehat{V}_k + B_2 w_k, z_k \\ &\qquad = C_z x_k + \widetilde{D}_{11}\widehat{V}_k + D_2 w_k, \end{aligned} \tag{43}$$

$$\begin{aligned} &\text{rule 2: if} \left(\widehat{v}_{1,k} \text{ is } H_1^1\right) \text{ and } \left(\widehat{v}_{2,k} \text{ is } H_2^2\right), \\ &\text{then } x_{k+1} = Ax_k + \widetilde{B}_{12}\widehat{V}_k + B_2 w_k, z_k \\ &\qquad = C_z x_k + \widetilde{D}_{12}\widehat{V}_k + D_2 w_k, \end{aligned} \tag{44}$$

$$\begin{aligned} &\text{rule 3: if} \left(\widehat{v}_{1,k} \text{ is } H_1^2\right) \text{ and } \left(\widehat{v}_{2,k} \text{ is } H_2^1\right), \\ &\text{then } x_{k+1} = Ax_k + \widetilde{B}_{13}\widehat{V}_k + B_2 w_k, z_k \\ &\qquad = C_z x_k + \widetilde{D}_{13}\widehat{V}_k + D_2 w_k, \end{aligned} \tag{45}$$

$$\begin{aligned} &\text{rule 4: if} \left(\widehat{v}_{1,k} \text{ is } H_1^2\right) \text{ and } \left(\widehat{v}_{2,k} \text{ is } H_2^2\right), \\ &\text{then } x_{k+1} = Ax_k + \widetilde{B}_{14}\widehat{V}_k + B_2 w_k, z_k \\ &\qquad = C_z x_k + \widetilde{D}_{14}\widehat{V}_k + D_2 w_k, \end{aligned} \tag{46}$$

where

$$\widetilde{B}_{11} = \begin{pmatrix} 0.0187 & 0.1094 \\ -0.0223 & -0.0054 \\ 0.3692 & 0.6088 \\ 0.1470 & 0.1040 \end{pmatrix}, \widetilde{B}_{12} = \begin{pmatrix} 0.0187 & 0.0164 \\ -0.0223 & -0.0008 \\ 0.3692 & 0.0913 \\ 0.1470 & 0.0156 \end{pmatrix},$$

$$\widetilde{B}_{13} = \begin{pmatrix} 0.0044 & 0.1094 \\ -0.0052 & -0.0054 \\ 0.0869 & 0.6088 \\ 0.0346 & 0.1040 \end{pmatrix}, \widetilde{B}_{14} = \begin{pmatrix} 0.0044 & 0.0164 \\ -0.0052 & -0.0008 \\ 0.0869 & 0.0913 \\ 0.0346 & 0.0156 \end{pmatrix},$$

$$\widetilde{D}_{11} = \begin{pmatrix} -0.0554 & 0.0126 \\ 0.0483 & -0.1426 \end{pmatrix}, \widetilde{D}_{12} = \begin{pmatrix} -0.0554 & 0.0019 \\ 0.0483 & -0.0214 \end{pmatrix},$$

$$\widetilde{D}_{13} = \begin{pmatrix} -0.0130 & 0.0126 \\ 0.0114 & -0.1426 \end{pmatrix}, \widetilde{D}_{14} = \begin{pmatrix} -0.0130 & 0.0019 \\ 0.0114 & -0.0214 \end{pmatrix}. \tag{47}$$

As the pairs $(A, \widetilde{B}_{1i})$, for $i = \{1,2,3,4\}$, are controllable, the resulting fuzzy system can be described as follows:

$$\begin{cases} x_{k+1} = \sum_{i=1}^{4} h_i \left(Ax_k + \widetilde{B}_{1i}\widehat{V}_k + B_2 w_k\right), \\ z_k = \sum_{i=1}^{4} h_i \left(C_z x_k + \widetilde{D}_{1i}\widehat{V}_k + D_2 w_k\right), \end{cases} \tag{48}$$

where the nonlinear weighting functions $h_i = w_i / \sum_{i=1}^{4} w_i$ are depicted in Figure 6.

Using the LMI formulation (25) with $\mu = 0.85$ and $\gamma = 0.7$, we obtain $\alpha = 0.794$, $\beta = 0.63$, and
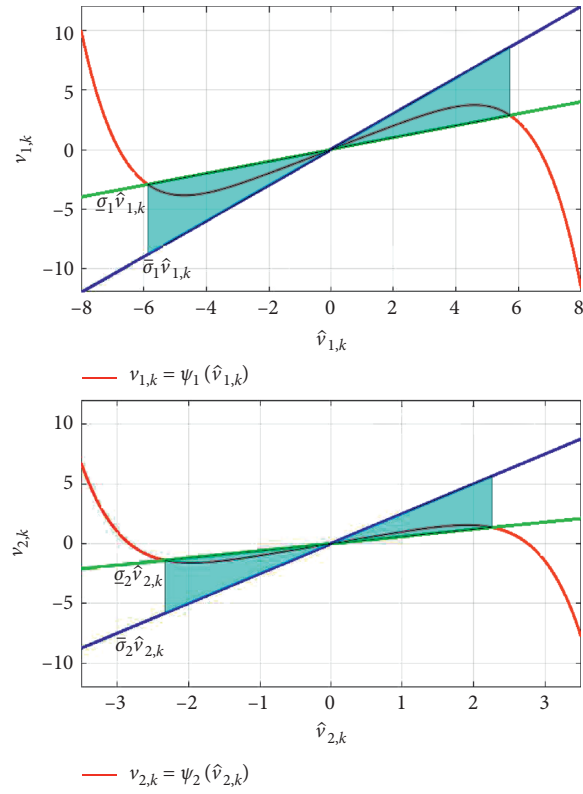
Figure 5: Evolution of nonlinear functions. Up Polt: $v_{1,k} = \psi_1(\hat{v}_{1,k})$. Down Polt: $v_{2,k} = \psi_2(\hat{v}_{2,k})$.
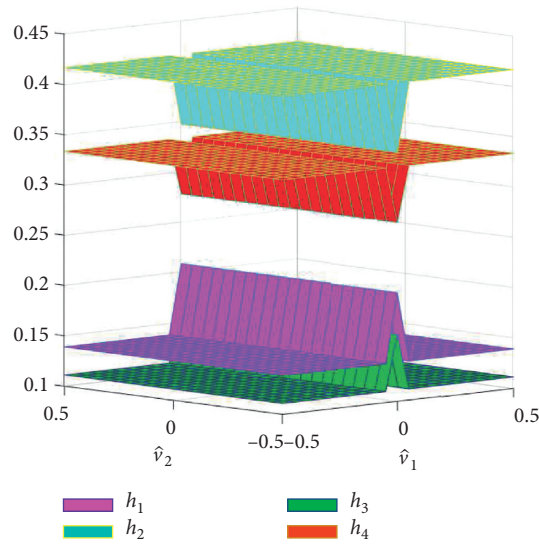
Figure 6: Weighting functions for the four fuzzy sets considered.

$$P = \begin{pmatrix} 6.4497 & 0.8651 & -0.2691 & 0.1327 \\ 0.8651 & 4.7781 & -0.3205 & 0.1191 \\ -0.2691 & -0.3205 & 5.0222 & 0.4860 \\ 0.1327 & 0.1191 & 0.4860 & 4.9015 \end{pmatrix},$$

$$K = \begin{pmatrix} -0.5072 & -0.2251 & 2.3094 & 1.4059 \\ 0.5327 & -0.0653 & 1.4641 & -0.4069 \end{pmatrix}. \tag{49}$$

Hence, by considering the nonfragile control law (21) subject to the uncertainty (22) with $\phi_k = \begin{pmatrix} 0.5\sin(\pi k) & 0 \\ 0 & 0.5\cos(\pi k) \end{pmatrix}$, the inferred controlled system can be described as follows:

$$\begin{cases} x_{k+1} = \sum_{i=1}^{4} h_i \left(\overline{G}_i x_k + B_2 w_k \right), \\ z_k = \sum_{i=1}^{4} h_i \left(\overline{F}_i x_k + D_2 w_k \right), \end{cases} \tag{50}$$

where $\overline{G}_i = G_i + \Delta G_i$, $\overline{F}_i = F_i + \Delta F_i$, $\Delta G_i = -\mu \widetilde{B}_{1i}\phi_k K$, $\Delta F_i = -\mu \widetilde{D}_{1i}\phi_k K$, for $i \in \{1, 2, 3, 4\}$, and

$$G_1 = \begin{pmatrix} 0.9221 & -0.3266 & -0.0802 & 0.0488 \\ 0.1095 & 0.9691 & 0.0686 & 0.0182 \\ -0.1745 & 0.1316 & -0.7467 & -0.3512 \\ 0.0301 & 0.0173 & -0.4649 & 0.7049 \end{pmatrix},$$

$$G_2 = \begin{pmatrix} 0.9716 & -0.3327 & 0.0560 & 0.0110 \\ 0.1070 & 0.9694 & 0.0619 & 0.0201 \\ 0.1011 & 0.0978 & 0.0110 & -0.5618 \\ 0.0772 & 0.0115 & -0.3354 & 0.6689 \end{pmatrix},$$

$$G_3 = \begin{pmatrix} 0.9149 & -0.3299 & -0.0471 & 0.0689 \\ 0.1181 & 0.9730 & 0.0293 & -0.0057 \\ -0.3177 & 0.0680 & -0.0946 & 0.0458 \\ -0.0269 & -0.0080 & -0.2052 & 0.8630 \end{pmatrix},$$

$$G_4 = \begin{pmatrix} 0.9644 & -0.3359 & 0.0890 & 0.0311 \\ 0.1157 & 0.9733 & 0.0226 & -0.0039 \\ -0.0421 & 0.0342 & 0.6631 & -0.1648 \\ 0.0201 & -0.0138 & -0.0757 & 0.8270 \end{pmatrix}, \tag{51}$$

$$F_1 = \begin{pmatrix} -0.1201 & 0.2798 & -0.0052 & 0.0923 \\ 0.1125 & -0.1425 & -0.2811 & -0.2386 \end{pmatrix},$$

$$F_2 = \begin{pmatrix} -0.1144 & 0.2791 & 0.0105 & 0.0880 \\ 0.0480 & -0.1345 & -0.4586 & -0.1893 \end{pmatrix},$$

$$F_3 = \begin{pmatrix} -0.0986 & 0.2894 & -0.1030 & 0.0328 \\ 0.0938 & -0.1508 & -0.1959 & -0.1867 \end{pmatrix}, \tag{52}$$

$$F_4 = \begin{pmatrix} -0.0929 & 0.2887 & -0.0874 & 0.0284 \\ 0.0293 & -0.1428 & -0.3733 & -0.1374 \end{pmatrix}.$$

Figures 7–10 show the simulation results of applying the designed nonfragile H_∞ controller to the TRMS (dashed line) and its identified Hammerstein model (solid line) with null

u₁ (model)
u₁ (system)
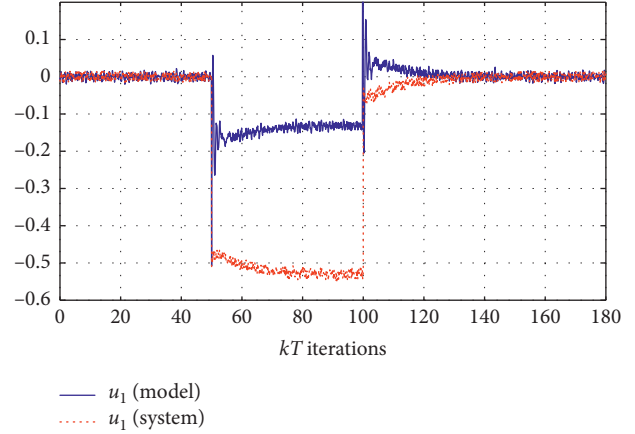
FIGURE 7: Control signal u_1 (V).

u₂ (model)
u₂ (system)
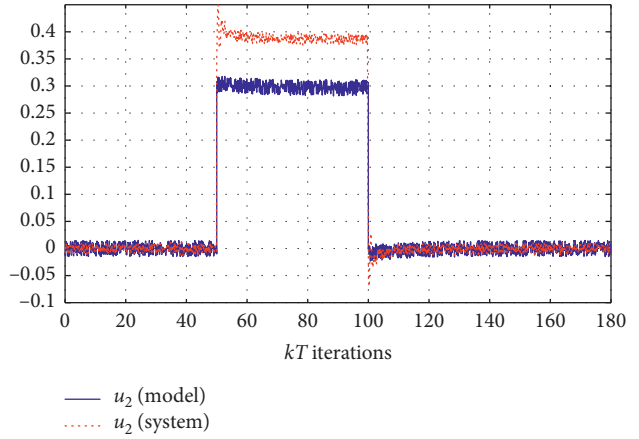
FIGURE 8: Control signal u_2 (V).

x₁ (model)
x₁ (system)
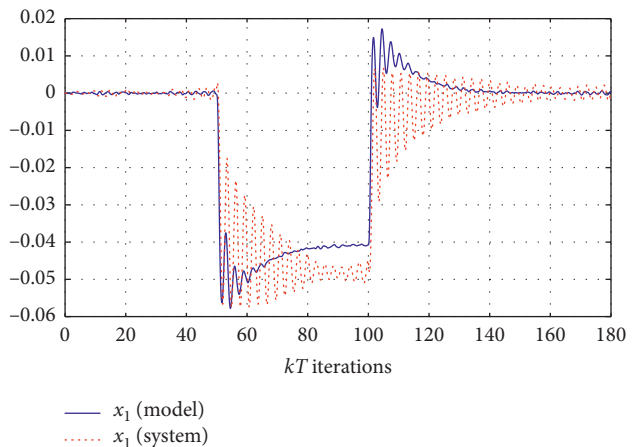
FIGURE 9: Response of the pitch angle of the closed-loop system.

initial conditions and the exogenous disturbance signal $w_k = \begin{pmatrix} \text{rand} & 0 & \text{rand} & 0 \end{pmatrix}^{\perp}$, where (rand) is a uniform number with a uniform distribution on the interval $[0, 0.01]$, which is added by $w_k^+ = -0.15$ if $50 \le kT \le 100$ and 0 otherwise.
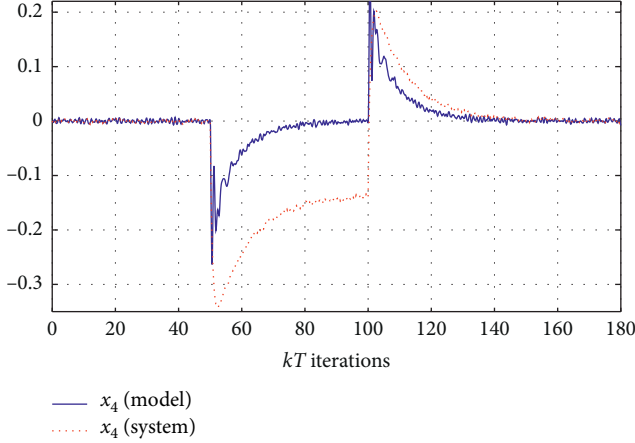
Figure 10: Response of the yaw angle of the closed-loop system.

The obtained results indicate that the designed robust and nonfragile H_∞ controller shows good results. However, the responses of the pitch and yaw angles of the controlled nonlinear system and its identified Hammerstein model can rapidly achieve the origin despite the presence of external disturbances and uncertainty in the control law.

5. Conclusion

In this paper, a nonfragile H_∞ feedback controller was designed for nonlinear systems described as multivariable Hammerstein model with separate nonlinearities. The parameters of the linear and nonlinear blocks characterizing the multivariable Hammerstein model structure were separately estimated using the MOESP identification algorithm. Unlike the normal control scheme, the inverses of the static nonlinearities were supposed not bijective and approximated by polynomial functions. The T-S fuzzy representation was used to simplify the nonlinear system description and reject the nonlinearity effect in the controller design. Based on the quadratic Lyapunov function and H_∞ criterion, robust H_∞ was then proposed to robustly stabilize the controlled nonlinear system and its identified Hammerstein model and guarantee the attenuation of disturbance effect in spite of controller gain variations. A TRMS was considered to illustrate the validity and the effectiveness of the designed stabilization scheme.

Appendix

A. Calculation of β_{ij} Scalars

The calculation of $\beta_{i,j}$ scalars are presented for $v = 3$. Then, we have

$$
\begin{cases}
v_{i,k} = f_i(u_{i,k}) = u_{i,k} + \lambda_{i2} u_{i,k}^2 + \lambda_{i3} u_{i,k}^3, \\
u_{i,k} = f_{i,\text{app}}^{-1}(\hat{v}_{i,k}) = \beta_{i1} \hat{v}_{i,k} + \beta_{i2} \hat{v}_{i,k}^2 + \beta_{i3} \hat{v}_{i,k}^3 + \text{hot.}
\end{cases}
\tag{A.1}
$$

Substituting the above quantities, we get

Table 1: TRMS parameters.

Symbol	Definition
u_1, u_2	Input signals
ψ	Pitch angle of the beam
ϕ	Yaw angle of the beam
I_1, I_2	Moment of inertia of vertical (horizontal) rotor
M_{FG}	Gravity momentum
$M_{B\psi}, M_{B\phi}$	Friction momentum forces
M_G	Gyroscopic momentum
a_i, b_i	Static parameters of motor i, $i = \{1, 2\}$
M_g	Gravity momentum
$B_{1\psi}, B_{1\phi}$	Friction momentums
K_{gy}, K_{gx}	Gyroscopic momentums
k_{ii}	Motor i gain
T_{i1}, T_{i0}	Motor i denominator
M_R	Cross reaction momentum approximation
k_c	Cross reaction momentum gain
T_p	Cross reaction momentum

$$
u_{i,k} = f_{i,\text{app}}^{-1}(\hat{v}_{i,k}) \approx \beta_{i1}\left(u_{i,k} + \lambda_{i2} u_{i,k}^2 + \lambda_{i3} u_{i,k}^3\right)
$$
$$
+ \beta_{i2}\left(u_{i,k} + \lambda_{i2} u_{i,k}^2 + \lambda_{i3} u_{i,k}^3\right)^2 + \beta_{i3}\left(u_{i,k} + \lambda_{i2} u_{i,k}^2 + \lambda_{i3} u_{i,k}^3\right)^3.
\tag{A.2}
$$

Then, we eliminate the powers higher than 3 of $u_{i,k}$. So, we get

$$
u_{i,k} = \beta_{i1} u_{i,k} + (\beta_{i1} + \beta_{i2}\lambda_{i2}) u_{i,k}^2
$$
$$
+ (\beta_{i1}\lambda_{i3} + 2\beta_{i2}\lambda_{i2} + \beta_{i3}) u_{i,k}^3 + \text{hot.}
\tag{A.3}
$$

We obtain finally $\beta_{i1} = 1$, $\beta_{i2} = -\lambda_{i2}$, and $\beta_{i3} = 2\lambda_{i2}^2 - \lambda_{i3}$.

B. Schur Complement

For matrices M, L, and Q with appropriate dimensions, the matrix inequality $\begin{pmatrix} M & * \\ L & Q \end{pmatrix} < 0$ is equal to (i) $Q < 0$, $M - L^\perp Q^{-1} L < 0$ and (ii) $M < 0$, $Q - LM^{-1}L^\perp < 0$ where M and Q are invertible and symmetric.

C. Separation Lemma

For matrices A and B with appropriate dimensions and positive scalars τ, one has $A^\perp B + B^\perp A \leq \tau A^\perp A + \tau^{-1} B^\perp B$.

D. TRMS Parameters

TRMS parameters are shown in Table 1.

Data Availability

No data were used to support this study.

Conflicts of Interest

The authors declare that there are no conflicts of interest regarding the publication of this paper.

References

[1] T. Takagi and M. Sugeno, "Fuzzy identification of systems and its applications to modeling and control," *IEEE Transactions on Systems, Man, and Cybernetics*, vol. 15, no. 1, pp. 116–132, 1985.

[2] K. Tanaka and M. Sugeno, "Stability analysis and design of fuzzy control systems," *Fuzzy Sets and Systems*, vol. 45, no. 2, pp. 135–156, 1992.

[3] N. Vafamand, S. Khorshidi, and A. Khayatian, "Secure communication for non-ideal channel via robust ts fuzzy observer-based hyperchaotic synchronization," *Chaos, Solitons & Fractals*, vol. 112, pp. 116–124, 2018.

[4] N. Vafamand, "Transient performance improvement of Takagi-Sugeno fuzzy systems by modified non-parallel distributed compensation controller," *Asian Journal of Control*, 2020.

[5] G. Mzyk, M. Bieganński, and B. Kozdraś, "Multistage identification of an NLN Hammerstein-Wiener system," in *Proceedings of the 22nd International Conference on Methods and Models in Automation and Robotics*, pp. 343–346, IEEE, Miedzyzdroje, Poland, August 2017.

[6] E. W. Bai, "Frequency domain identification of Hammerstein models," *IEEE Transactions on Automatic Control*, vol. 48, no. 4, pp. 530–542, 2003.

[7] M.-R. Rahmani and M. Farrokhi, "Fractional-order Hammerstein state-space modeling of nonlinear dynamic systems from input-output measurements," *ISA Transactions*, vol. 96, pp. 177–184, 2020.

[8] Y. Zhu, "Robust PID tuning using closed-loop identification," *IFAC Proceedings Volumes*, vol. 37, no. 1, pp. 161–166, 2004.

[9] M. Sadabadi, M. Karrari, and O. Malik, "Nonlinear identification of synchronous generator using Hammerstein model with piecewise linear static maps," *IEEE Lausanne Power Tech*, pp. 1067–1071, Article ID 2272601, 2007.

[10] R. K. Pearson and M. Pottmann, "Gray-box identification of block-oriented nonlinear models," *Journal of Process Control*, vol. 10, no. 4, pp. 301–315, 2000.

[11] I. W. Hunter and M. J. Korenberg, "The identification of nonlinear biological systems: Wiener and Hammerstein cascade models," *Biological Cybernetics*, vol. 55, no. 2-3, pp. 135–144, 1986.

[12] B. Satpati, C. Koley, P. Bhowmik, and S. Datta, "Nonlinear Hammerstein-Hammerstein identification of air preheating furnace of a pneumatic conveying and drying process," in *Proceedings of the 2014 IEEE Conference on Control Applications (CCA)*, pp. 397–402, IEEE, Juan Les Antibes, France, October 2014.

[13] Y. Liu and E.-W. Bai, "Iterative identification of Hammerstein systems," *Automatica*, vol. 43, no. 2, pp. 346–354, 2007.

[14] F. Ding and T. Chen, "Identification of Hammerstein nonlinear ARMAX systems," *Automatica*, vol. 41, no. 9, pp. 1479–1489, 2005.

[15] T. C. Hsia, "A multi-stage least squares method for identifying hammerstein model nonlinear systems," in *Proceedings of the 15th IEEE Conference on Decision and Control*, pp. 934–938, IEEE, Clearwater, FL, USA, December 1976.

[16] E. W. Bai and M. Fu, "A blind approach to Hammerstein model identification," *IEEE Transactions on Signal Processing*, vol. 50, no. 7, pp. 1610–1619, 2002.

[17] Z. Liao, Z. Zhu, S. Liang, C. Peng, and Y. Wang, "Subspace identification for fractional order Hammerstein systems based on instrumental variables," *International Journal of Control, Automation and Systems*, vol. 10, no. 5, pp. 947–953, 2012.

[18] W. Greblicki, "Nonlinearity estimation in Hammerstein systems based on ordered observations," *IEEE Transactions on Signal Processing*, vol. 44, no. 5, pp. 1224–1233, 1996.

[19] I. Goethals, K. Pelckmans, J. A. K. Suykens, and B. De Moor, "Identification of MIMO Hammerstein models using least squares support vector machines," *Automatica*, vol. 41, no. 7, pp. 1263–1272, 2005.

[20] P. Van Overschee and B. De Moor, "N4SID: subspace algorithms for the identification of combined deterministic-stochastic systems," *Automatica*, vol. 30, no. 1, pp. 75–93, 1994.

[21] W. E. Larimore, "Canonical variate analysis in identification, filtering, and adaptive control," in *Proceedings of the 29th IEEE Conference on Decision and Control*, pp. 596–604, IEEE, Honolulu, HI, USA, December 1990.

[22] J. C. Gómez and E. Baeyens, "Subspace-based identification algorithms for Hammerstein and Wiener models," *European Journal of Control*, vol. 11, no. 2, pp. 127–136, 2005.

[23] Z. Rayouf, C. Ghorbel, and N. B. Braiek, "A new Hammerstein model control strategy: feedback stabilization and stability analysis," *International Journal of Dynamics and Control*, vol. 7, no. 4, pp. 1453–1461, 2019.

[24] W. M. Haddad and V. Chellaboina, "Nonlinear control of Hammerstein systems with passive nonlinear dynamics," *IEEE Transactions on Automatic Control*, vol. 46, no. 10, pp. 1630–1634, 2001.

[25] T. Knohl, W. M. Xu, and H. Unbehauen, "Indirect adaptive dual control for Hammerstein systems using ann," *Control Engineering Practice*, vol. 11, no. 4, pp. 377–385, 2003.

[26] H. Wang, J. Zhao, Z. Xu, and Z. Shao, "Linear model predictive control for hammerstein system with unknown nonlinearities," *IFAC Proceedings Volumes*, vol. 46, no. 13, pp. 302–306, 2013.

[27] C. Ghorbel, Z. Rayouf, and N. Benhadj Braiek, "Robust stabilization and tracking control schemes for disturbed multi-input multi-output Hammerstein model in presence of approximate polynomial nonlinearities," *Proceedings of the Institution of Mechanical Engineers, Part I: Journal of Systems and Control Engineering*, vol. 101, 2020.

[28] Z. Rayouf, C. Ghorbel, and N. B. Braiek, "Identification and nonlinear PID control of Hammerstein model using polynomial structures," *Internatinal Journal of Advanced Computer Science and Applications*, vol. 8, no. 4, pp. 488–493, 2017.

[29] X. Hong and R. J. Mitchell, "Hammerstein model identification algorithm using Bezier-Bernstein approximation," *IET Control Theory & Applications*, vol. 1, no. 4, pp. 1149–1159, 2007.

[30] X. Hong, R. J. Mitchell, and S. Chen, "Modelling and control of Hammerstein system using B-spline approximation and the inverse of De Boor algorithm," *International Journal of Systems Science*, vol. 43, no. 10, pp. 1976–1984, 2012.

[31] S. Chen, X. Hong, J. Gao, and C. J. Harris, "Complex-valued B-spline neural networks for modeling and inverting Hammerstein systems," *IEEE Transactions on Neural Networks and Learning Systems*, vol. 25, no. 9, pp. 1673–1685, 2014.

[32] X. Chang, "Robust non-fragile H_∞ filtering of fuzzy systems with linear fractional parametric uncertainties," *IEEE Transactions on Fuzzy Systems*, vol. 20, no. 6, pp. 1001–1011, 2012.

[33] N. Vafamand, M. H. Asemani, and A. Khayatian, "TS fuzzy robust L 1 control for nonlinear systems with persistent bounded disturbances," *Journal of the Franklin Institute*, vol. 354, no. 14, pp. 5854–5876, 2017.

[34] H. Wang, S. Xie, B. Zhou, and W. Wang, "Non-fragile robust H_∞ filtering of Takagi-Sugeno fuzzy networked control

systems with sensor failures," *Sensors*, vol. 20, no. 1, pp. 1–16, 2020.

[35] A. Tiga, N. B. Braiek, and C. Ghorbel, "Proportional PDC design-based bobust stabilization and tracking control strategies for uncertain and disturbed T-S model," *Complexity*, vol. 1, pp. 1–9, 2020.

[36] Y. Zhang, G.-Y. Tang, and N.-P. Hu, "Non-fragile control for nonlinear networked control systems with long time-delay," *Computers & Mathematics with Applications*, vol. 57, no. 10, pp. 1630–1637, 2009.

[37] F. Xingjian, L. Xiaohe, H. Ming, and L. Yingchun, "Robust non-fragile control for non-linear singular discrete systems with time-delay," in *Proceedings of the 10th World Congress on Intelligent Control and Automation*, pp. 1139–1143, IEEE, Beijing, China, July 2012.

[38] J. W. Lee, H. H. Lee, J. K. Kim, and H. B. Park, "Robust and non-fragile fuzzy H_∞ controller design for discrete-time systems with parameter uncertainties and time delay," in *Proceedings of the 2009 International Conference on Information and Automation*, pp. 722–727, IEEE, Zhuhai, China, June 2009.

[39] N. Vafamand, M. M. Arefi, and A. Khayatian, "Nonlinear system identification based on Takagi-Sugeno fuzzy modeling and unscented Kalman filter," *ISA Transactions*, vol. 74, pp. 134–143, 2018.

[40] N. Vafamand, "Global non-quadratic Lyapunov-based stabilization of T–S fuzzy systems: a descriptor approach," *Journal of Vibration and Control*, vol. 26, no. 19-20, pp. 1765–1778, 2020.

[41] Y. Zhu, "Estimation of an N-L-N hammerstein-wiener model," *IFAC Proceedings Volumes*, vol. 35, no. 1, pp. 247–252, 2002.

[42] J. C. Gómez and E. Baeyens, "Subspace identification of multivariable Hammerstein and Wiener models," *IFAC Proceedings Volumes*, vol. 35, no. 1, pp. 55–60, 2002.

[43] D. Rotondo, F. Nejjari, and V. Puig, "Quasi-LPV modeling, identification and control of a twin rotor MIMO system," *Control Engineering Practice*, vol. 21, no. 6, pp. 829–846, 2013.

WILEY | Hindawi

Research Article

Dynamic Characteristic Analysis and Clutch Engagement Test of HMCVT in the High-Power Tractor

Yuan Chen [ID],[1] **Yu Qian,**[1] **Zhixiong Lu** [ID],[1] **Shuang Zhou,**[1] **Maohua Xiao** [ID],[1] **Petr Bartos,**[2] **Yeping Xiong** [ID],[3] **Guanghu Jin,**[4] **and Wei Zhang**[5]

[1]*College of Engineering, Nanjing Agricultural University, Nanjing 210031, China*
[2]*Faculty of Agriculture, University of South Bohemia, Studentska, České Budějovice 1668, Czech Republic*
[3]*Engineering and Physical Sciences, University of Southampton, Boldrewood Innovation Campus, Southampton SO16 7QF, UK*
[4]*National Key Laboratory of Science and Technology on Helicopter Transmission,*
 Nanjing University of Aeronautics and Astronautics, Nanjing 210016, China
[5]*Nanjing University of Aeronautics and Astronautics, Nanjing 210016, China*

Correspondence should be addressed to Zhixiong Lu; luzx@njau.edu.cn

Hydromechanical continuously variable transmission (HMCVT) is capable of bearing large torque and has wide transmission range, which is suitable for high-power tractors. Dynamic characteristics could influence the tractor life, especially in a high-power tractor. Wet clutch is the crucial component in the HMCVT, which could smooth and soft power transmission. Therefore, it is important to study the dynamic characteristics and implement the wet clutch test of HMCVT. In this paper, AMESim is used to establish virtual models of gearbox, pump-controlled hydraulic motor system, and shifting hydraulic system. Then, a simulation study of tractor operation under working condition is carried out. The internal and external meshing forces of the planetary row are analyzed. Finally, the wet clutch engagement process of HMCVT in the high-power tractor is tested to verify the oil pressure. The simulation results show that the values of internal and external meshing force become larger as the throttle opening increases. At the moment of shifting change, the meshing forces of the planetary gear have great impact. The clutch test shows that the trend of the oil filling curve obtained from the bench test is similar to that obtained from the theoretical curve, which verifies the simulation results.

1. Introduction

The main function of the tractor is to be used in conjunction with various traction and driving machines to complete agricultural field operations, earthwork engineering operations, transportation operations, and stationary operations [1]. The transmission performance of the gearbox will have an important impact on the tractor and its transmission system. The hydromechanical continuously variable transmission (HMCVT) has attracted extensive attention in recent years [2–5]. In order to meet the requirements of tractors working under multiple working conditions, at present, high-power tractor gearboxes are set with more gears. The increase of gears in gearboxes not only makes its

structure complex and error prone to operate, but also the dynamic characteristics of the tractor are difficult to guarantee [6].

Scholars have carried out a lot of research on HMCVT. The German company ZF [7] produced the S-Matic series of hydraulic mechanical transmissions, which used dual-row planetary row confluence to output power for the first time. The Japanese Company Komatsu [8] successfully developed a stepless speed change device suitable for construction machinery and applied it to the D155AX-3 bulldozer and WA380-3 loader. In recent years, various well-known gearbox manufacturers have launched HMCVT with independent intellectual property rights, such as John Deere, Caterpillar of the United States, and

Valtra of Finland [9]. The typical HMCVT model is shown in Figure 1.

Regarding mechanical characteristic analysis for HMCVT, Xia et al. [10] proposed an optimized design method for the selection of the structural parameters of the PCHMCVT to ensure competent overall performance. Zheng and Sun [11] used AMESim to establish a physical model of an HMCVT and simulated and analyzed the speed regulation characteristics, output torque characteristics, and acceleration characteristics of the pure hydraulic section of it. Zhang [12] and He et al. [13] have, respectively, optimized the design of the hydraulic mechanical stepless gearbox. Li et al. [14] analyzed the working principle of HMCVT and successfully developed a hydraulic mechanical stepless gearbox suitable for high-power tractors for both water and drought. Zhai et al. [15] introduced a two-stage planetary row device for the final transmission of a wheeled tractor, which is compact in structure, reliable in operation, and easy to install. Wang et al. [16] proposed a new type of compound planetary row transmission new hydraulic mechanical continuously variable transmission scheme based on the traditional single-row planetary and double planetary row. Guo et al. [17] established the conditions for synchronous shifting of multistage HMCVT and verified the high efficiency characteristics of it. Wang et al. [18] used the basic principles of dynamics to establish a tractor dynamic model and verified its good dynamic characteristics under ploughing condition. Xiao et al. [19, 20] studied the dynamic characteristics of the hydraulic circuit in HMCVT, and a fast system identification method was proposed. Cheng et al. [21–26] improved the genetic algorithm to implement the HMCVT parameter optimization, and the new proposed model can improve the HMCVT transmission efficiently and flexibly.

From the analysis above, we can see that scholars' research on HMCVT is focused on the structure characteristics or the shifting strategy, but there is little research on the dynamic characteristics and clutch engagement. In this paper, the HMCVT scheme and simulation model was proposed, the dynamic meshing forces were calculated, and the wet clutch engagement characteristics were tested for a high-power tractor.

2. Modeling

2.1. Gearbox Dynamic Model. This paper puts forward the HMCVT scheme, which is shown in Figure 2. This transmission scheme is a constant-ratio split-moment converging speed type. The engine power is divided into two power transmissions through the fixed-axis gear pair i_1 or $i_2 i_3$ ($i_2 i_3$ works in forward gear) and the hydraulic power distribution gear pair i_p. One power is transmitted to the common sun gear shafts of planetary rows K_1 and K_2 through the variable displacement pump-fix displacement motor, which is a hydraulic flow, and the other power is transmitted to the planet carrier K_1 and the ring gear K_2 through the fixed shaft gear pair (the planet carrier of K_1 and the gear ring of K_2 are firmly connected), which

is the mechanical flow. The hydraulic flow and mechanical flow converge in the planetary rows K_1 and K_2, and then the combined flow force is transmitted to the ring gear of K_1 or planet carrier K_2. Finally, by separately controlling the engagement of wet clutches C_1, C_2, and C_3, the power can be transmitted to the output shaft. In this process, stepless speed regulation can be realized in each section by controlling the displacement ratio of the variable pump.

AMESim has been widely used in aerospace, vehicles, construction machinery, ships, and other multidisciplinary fields and has become a platform for modeling and simulation of complex systems such as liquid, mechanical, electrical, electromagnetic, thermal analysis, and control. AMESim software is more and more widely used in modeling, simulation, and analysis of complex systems. AMESim is applied to the modeling process of HMCVT in this paper.

The planetary gear mechanism model is shown in Figure 3(a), and its mathematical model is shown as follows [27]:

$$
\begin{cases}
v_{1a} = -\dfrac{\text{Rad1} + \text{Rad2}}{\text{Rad1}} \cdot v_{ca} - \dfrac{\text{Rad2}}{\text{Rad1}} \cdot v_{2a}, \\[3mm]
v_0 = \dfrac{\text{Rad2} \cdot v_{2b} - \text{Rad1} \cdot v_{1a}}{\text{Rad2} - \text{Rad1}} + v_{ca}, \\[3mm]
T_{2b} = \text{fact}_{\text{eff}} \times \dfrac{\text{Rad2}}{\text{Rad1}} \times (T_{1b} - T_{1a}) + T_{2b}, \\[3mm]
T_{ca} = (T_{1b} - T_{1a}) + (T_{2b} - T_{2b}) + T_{cb},
\end{cases}
\tag{1}
$$

where v_{1a} is the rotational speed of Port 1A, v_{ca} is the rotational speed of Port 2A, v_{2b} is the rotational speed of Port 4B, v_0 is the rotational speed of the carrier, Rad_1 is the number of the sun gear, Rad_2 is the number of the ring gear, T_{2a} and T_{2b} are the input and output torque of the ring gear, and T_{ca} and T_{cb} are the input and output torque of the carrier.

The variable pump model (PU003 C) is selected from the Hydraulic library, as shown in Figure 3(b). The opening range of the variable pump model is $-1 \leq$ swash ≤ 1. When turning forward, port 3 is the oil outlet; when turning backward, port 3 is the oil inlet. The mathematical model of a variable pump is shown as follows:

$$
\begin{cases}
q_p = \dfrac{e \cdot v_p \cdot \text{swash}}{1000}, \\[3mm]
T_p = \dfrac{(p_{\text{AP}} - p_{\text{BP}}) \cdot e \cdot \text{swash}}{20 \cdot \pi},
\end{cases}
\tag{2}
$$

where q_p is the flow of the variable pump, e is the displacement of the pump, swash is the throttle opening of the pump, T_p is the shaft torque of the pump, and p_{AP} and p_{BP} are the inlet and outlet oil pressure.

The quantitative motor model (M0001 C) is selected from the Hydraulic library, and the mathematical model is shown as follows:
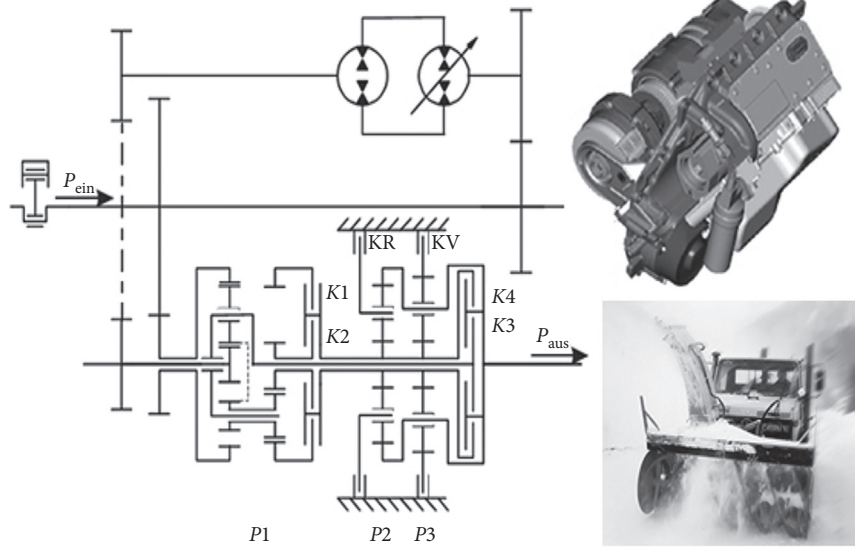
Figure 1: The HMCVT S-Matic.
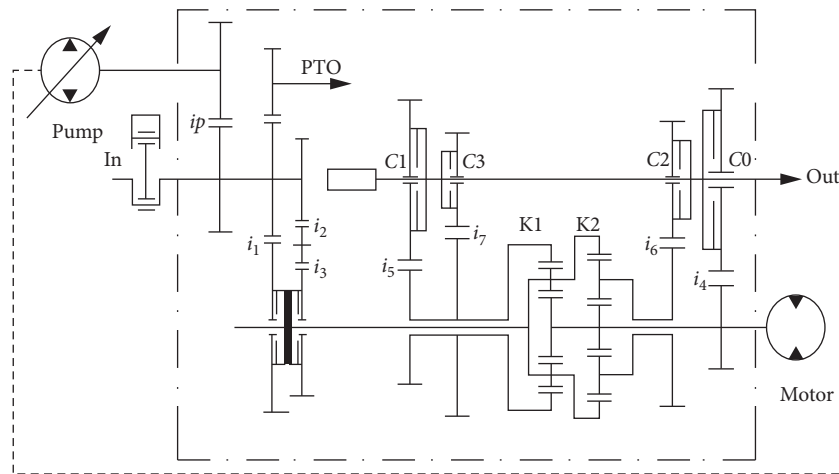
Figure 2: HMCVT scheme.

$$\begin{cases} q_m = \dfrac{e \cdot v_m}{1000}, \\[3mm] T_m = \dfrac{(p_{Am} - p_{Bm}) \cdot e \cdot \text{swash}}{20 \cdot \pi}, \end{cases} \quad (3)$$

where q_m is the flow of motor, v_m is the motor speed, T_m is the torque of the motor, and p_{Am} and p_{Bm} are the inlet and outlet oil pressure of the motor.

Based on the models of various parts, like the wet clutch, the oil circuit, the corresponding signal control elements, and the torque output elements, the simulation model of the shifting hydraulic system could be obtained, as shown in Figure 3(c).

According to the gearbox model, hydrostatic circuit, shifting system model, and tractor model, the simulation model of HMCVT is obtained, as shown in Figure 4.

3. Simulation Analysis of Tractor under Working Conditions

Figure 5 and Table 1 show the change of the internal and external meshing forces of the planetary row under working condition.

As can be seen from Figures 5(a) and 5(b), the internal and external meshing forces of the planetary row both have great impacts at the moment of the engine throttle opening change. The maximum and minimum values of internal meshing force are 3.33×10^6 N and 2.00×10^7 N, respectively. The maximum and minimum values of external meshing force are 2.20×10^7 N and 7.33×10^6 N, respectively.

They all become larger as the throttle opening increases. At the moment of shifting change, the internal and external meshing forces of the planetary gear have great impact at 2.5s–3.5 s. Then, the magnitudes of the meshing force change decrease, and the trend tends to be stable.

(a)   (b)

(c)
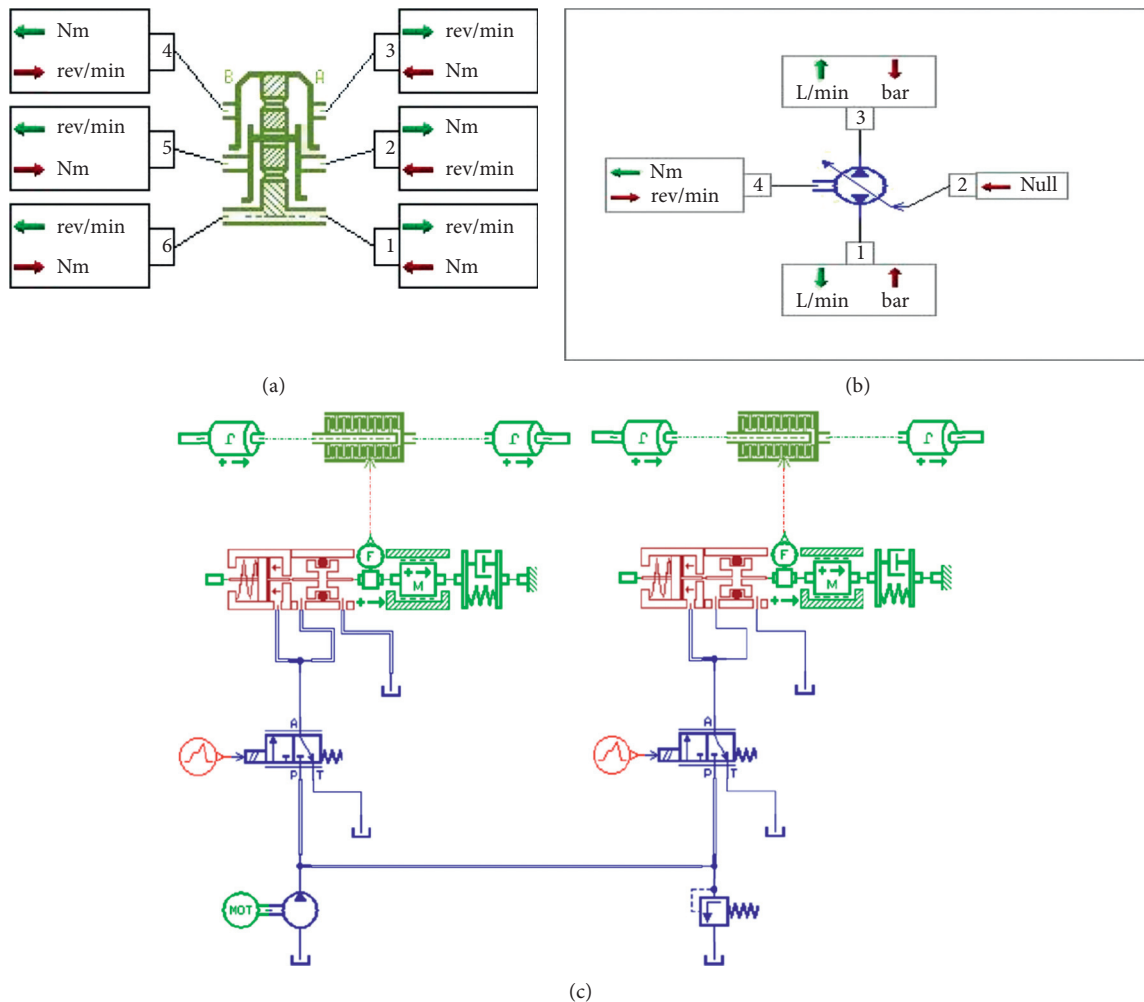
Figure 3: The model of the HMCVT component. (a) Planet gear. (b) Variable pump. (c) Shifting hydraulic system.

4. Clutch Engagement Characteristic Test of HMCVT

4.1. Power Drive Module. DEUTZ TCD2013L062 V engine was selected for the test. The accelerator control system of it is a dual-sensor control loop system, which is mainly composed of displacement sensor, current sensor, accelerator pedal, and stepping motor. The test sent an electric signal of speed adjustment to the engine by changing the pedal angle of the accelerator pedal. After the ECU got the control signal and then the stepper motor could be controlled by output current, the throttle opening can be changed.

The engine throttle opening was collected by displacement sensors, and ECU output current was collected by current sensors. The signals were compared with the original value in the input controller and realized the rapid adjustment of the engine speed controller according to the control algorithm.

This HMCVT test bench selected and designed the accelerator pedal according to the engine type and ECU, as is shown in Figure 6.

The bolt adjusting device was installed on the accelerator pedal, and the length of it was related to the change of the position of the accelerator pedal. The corresponding scale line was drawn on the bolt in direct proportion to the speed of the engine.

4.2. HMCVT Load Module. The dynamometer loaded the gearbox by outputting different quantities and can simulate the working state of the vehicle in different working conditions. The test bench selected the Lanlin DW250 (Figure 7) type eddy current dynamometer to match the rotation speed and power of the engine.

4.3. Oil Pressure Sensor. The JM-801 pressure sensor with a ceramic core was selected for the test bench. When the pressure was applied to the ceramic membrane, the surface of the membrane will undergo subtle deformation.

The resistance was printed on the back of the ceramic diaphragm, and the Wheatstone bridge can be formed. The Wheatstone bridge will generate a voltage signal due to voltage sensitive effect. The signal is proportional to the pressure and excitation current. The oil pressure value of C0,
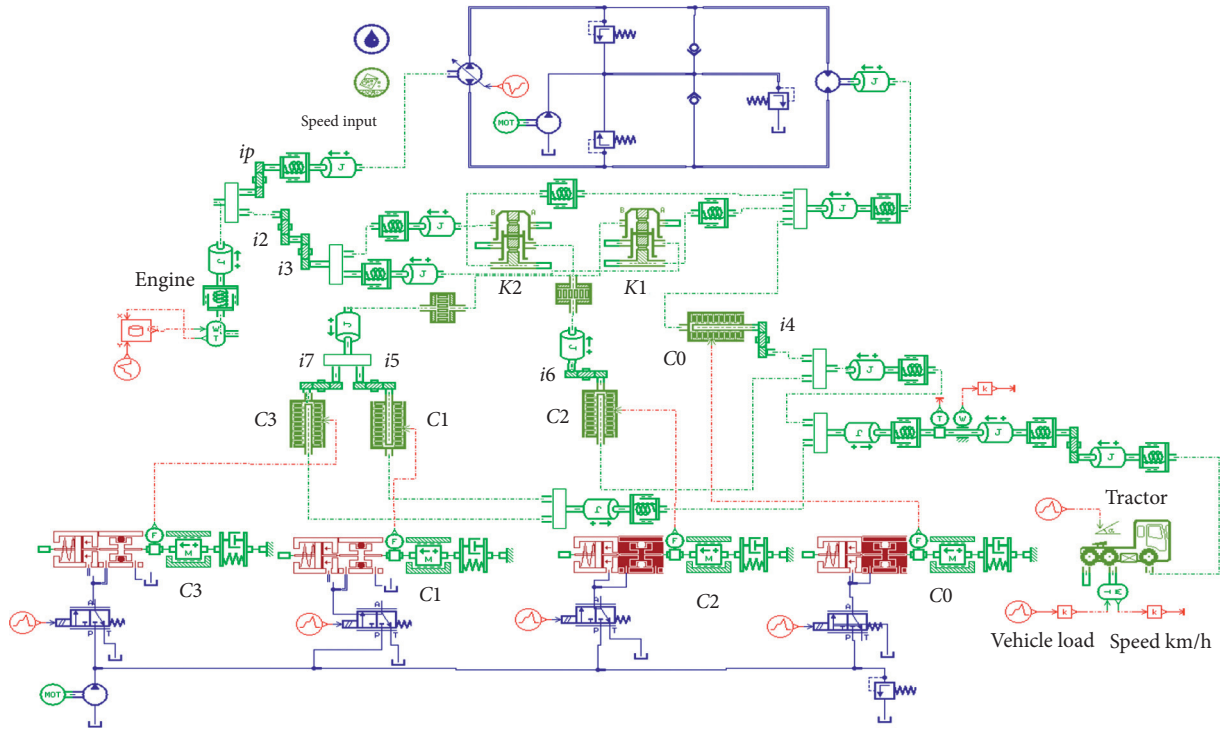
Figure 4: The simulation model of HMCVT.
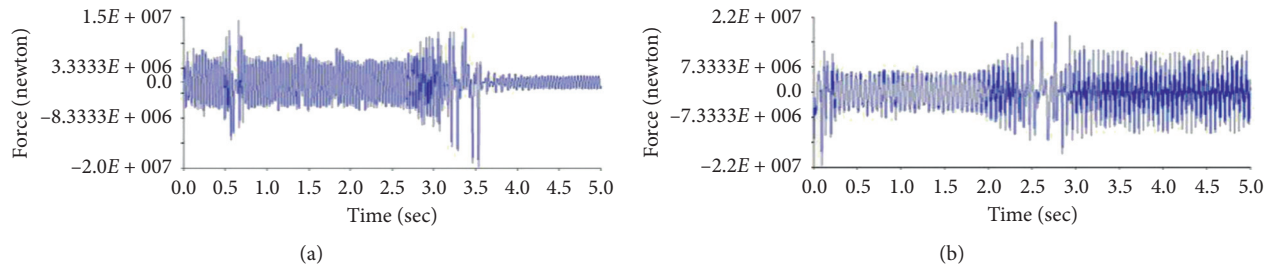
Figure 5: Meshing force of the planet gear. (a) Internal meshing force and (b) external meshing force.

Table 1: Internal and external meshing force in working condition.

Working condition	External meshing force (N)		Internal meshing force (N)	
	Maximum	Minimum	Maximum	Minimum
—	2.20×10^7	7.33×10^6	2.00×10^7	3.33×10^6

C1, C2, and lubrication main oil line in the platform can be read directly through the pressure indicator table (Figure 8).

4.4. Test Bench.
The overall structure diagram of the test bench is shown in Figure 9. The test bench was mainly composed of diesel engine, speed rising transmission, and support device. In the test bench, the diesel engine was used as the power source.

4.5. Clutch Oil Filling Test.
The structure of C0, C1, and C2 was basically the same, and this paper took C0 as an example

to carry out the bench test research on oil filling process. Test steps were as follows.

First, the engine was started to adjust the accelerator pedal and stabilize the output speed of the engine to 1295 r/min.

Secondly, the engagement button of C0 was pressed in the measurement platform. The oil pressure of the main oil relief valve was set at 2.8 MPa.

After receiving the electrical signal, the proportional directional valve of C0 pumped the filtered oil from the tank and sent to the clutch. The oil filling process of C0 is shown in Figure 10.

Figure 6: Accelerator pedal of the engine.
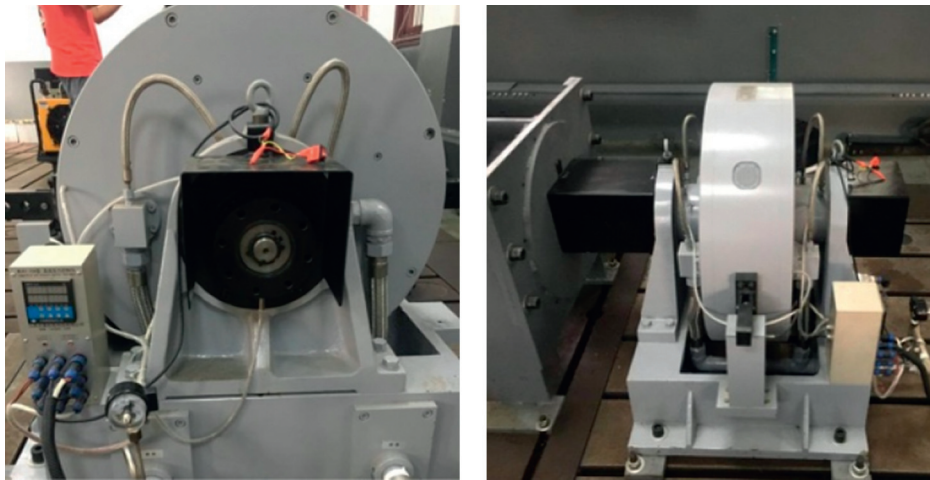
Figure 7: Eddy current dynamometer.

Figure 8: Oil pressure gauge.

4.5.1. 0-a Section. This section was mainly to eliminate the gap between the friction plates. The oil pressure raised from 0 MPa to 0.03 MPa rapidly. The slope of the variation of the curve in this section is 0.6.

4.5.2. a-b Section. The slope of the variation of the curve in this section is 0.52. At this stage, the piston compressed the spring under the action of the oil pressure, and the oil pressure increased with compression of the return spring. The oil pressure pf C0 rose slowly from 0.03 MPa to 0.42 MPa. The variation of oil pressure was related to the torque transferred by the clutch and piston stroke.

4.5.3. b-c Section. The slope of the variation of the curve in this section is 7.8. In this stage, the oil pressure of C0 rose rapidly from 0.42 MPa to 2.8 MPa, which was set by the relief valve in order to ensure the torque.

4.5.4. c-d Section. This section was the pressure holding stage. The oil pressure of C0 was maintained at 2.8 MPa.

Figure 9: The HMCVT test bench.
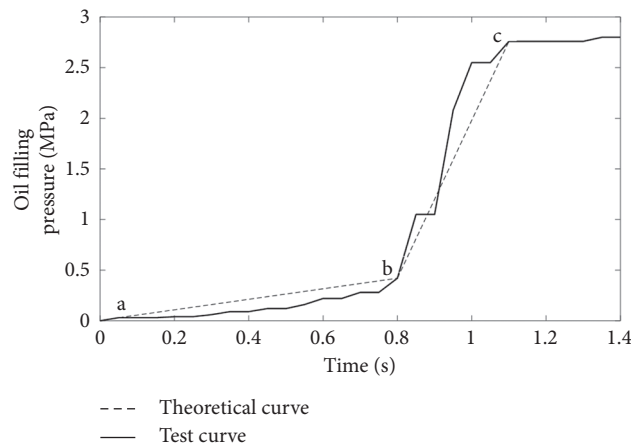
Figure 10: Oil filling characteristic curve of the wet clutch.

4.6. Test Discussion. The oil filling process can be divided according to the slope of the oil pressure change in each section. The oil filling time was short at 0–0.5 s, and the range of oil pressure change is 0.03 MPa. This section was the stage of rapid oil filling.

The oil filling duration of 0.05–0.8 s was 0.75 s, accounting for 68% of the total oil filling time. And, the variation range of oil pressure was 0.39 MPa, accounting for 14% of the set oil filling pressure. Therefore, this stage was the slow booster stage.

The oil filling duration of 0.8–1.1 s was 0.3 s, accounting for 27% of the total oil filling time. And, the variation range of oil pressure was 2.38 MPa, accounting for 85% of the set oil filling pressure. In a short time, the oil pressure showed a step rise. Therefore, the stage was the step booster stage.

During 1.1–1.4 s, the oil filling pressure reached the set value of 2.8 MPa and remained as such. Therefore, the stage was the pressure holding stage.

According to analysis, the oil filling curve obtained from the test bench had a similar trend to the theoretical curve. It verified the oil filling characteristics of the wet clutch and proved the accuracy of the HMCVT test bench.

5. Conclusions

In this paper, the dynamic characteristics of HMCVT were analyzed. The wet clutch engagement characteristics were tested. The analysis could be reference for the design of a high-power tractor. The conclusions can be made as follows:

(1) The values of internal and external meshing force become larger as the throttle opening increases.

(2) At the moment of shifting change, the meshing forces of the planetary gear have great impact.

(3) The magnitudes of the meshing force change decrease, and the trend tends to be stable after shifting change.

(4) The clutch test shows that the trend of oil filling is similar to the theoretical curve. The simulation model is reliable.

Data Availability

The data used to support the findings of this study are available from the corresponding author upon request.

Conflicts of Interest

The authors declare that there are no conflicts of interest regarding the publication of this paper.

Acknowledgments

References

[1] S. Y. Li, "Classification of tractor and performance analysis," *Agricultural Science & Technology and Equipment*, vol. 9, pp. 27–29, 2016.

[2] R. Antonio and M. Alarico, "Multi-objective optimization of hydro-mechanical power split transmissions," *Mechanism and Machine Theory*, vol. 62, pp. 112–128, 2013.

[3] M. Alarico and R. Antonio, "Fuel consumption reduction in urban buses by using power split transmissions," *Energy Conversion and Management*, vol. 71, pp. 159–171, 2013.

[4] R. Pfiffner, L. Guzzella, and C. H. Onder, "Fuel-optimal control of CVT powertrains," *Control Engineering Practice*, vol. 11, no. 3, pp. 329–336, 2003.

[5] Z. Farkas and G. Kerényi, "Power flows and efficiency analysis of out- and input coupled IVT," *Periodica Polytechnica Mechanical Engineering*, vol. 53, no. 2, pp. 61–68, 2009.

[6] G. M. Wang, H. Zhang, Y. X. Zhai et al., "Economic analysis of tractor steel belt power split continuously variable transmission," *Journal of Agricultural Mechanization Research*, vol. 42, no. 01, pp. 241–248, 2020.

[7] J. Fereydon, H. Tung-ming, and S. Keith, "Dynamic simulation modeling for heavy duty automatic transmission control development," *SAE International Journal of Engines*, vol. 101, pp. 704–715, 1992.

[8] N. L. Feng, *Research on Dynamic Characteristics Simulation and Fuzzy Control of Vehicle Comprehensive Transmission Shift*, Beijing Institute of Technology, Beijing, China, 2001.

[9] Q. F. Wu, "Brief introduction of the technology development of continuously variable tractors of major foreign companies," *Farm Machinery*, vol. 25, pp. 90–94, 2012.

[10] Y. Xia, D. Sun, D. Qin, and X. Zhou, "Optimisation of the power-cycle hydro-mechanical parameters in a continuously variable transmission designed for agricultural tractors," *Biosystems Engineering*, vol. 193, pp. 12–24, 2020.

[11] X. Z. Zheng and W. Sun, "Modeling and simulation of hydro-mechanical continuously variable transmission based on AMESim," *Modern Machinery*, vol. 5, pp. 31–34, 2017.

[12] H. J. Zhang, C. F. Wang, M. H. Xiao et al., "The design and transmission characteristic analysis of intermediate shaft type hydraulic-mechanical CVT," *Journal of Machine Design*, vol. 32, pp. 44–49, 2015.

[13] C. K. He, P. F. Lang, M. Kang et al., "Transmission design and force analysis of HMCVT for high power tractor," *Journal of Mechanical Transmission*, vol. 42, pp. 54–59, 2018.

[14] J. L. Li, L. T. Liu, M. H. Xiao et al., "Research on dynamic characteristics of hydro-mechanical continuously variable transmission," *Journal of Mechanical Strength*, vol. 39, pp. 14–19, 2017.

[15] Y. Zhai, J. W. Zhang, C. Ju et al., "A two-stage planet device for wheeled tractor final transmission," *Tractor & Farm Transporter*, vol. 43, pp. 65-66, 2016.

[16] T. T. Wang, M. Z. Zhang, and M. M. Cui, "Transmission characteristics of a new hydraulic mechanical continuously variable transmission," *Journal of Natural Science of Heilongjiang University*, vol. 34, pp. 724–731, 2017.

[17] R. Guo, M. Z. Zhang, C. Chen et al., "Characteristics analysis of the multi-range hydro-mechanical continuously variable transmission in tractors," *Journal of Chinese Agricultural Mechanization*, vol. 35, pp. 118–121, 2014.

[18] Q. S. Wang, M. Z. Zhang, D. Y. Bai et al., "Dynamic simulation of tractor equipped with multi-range hydro-mechanical CVT during ploughing," *Journal of Agricultural Mechanization Research*, vol. 39, pp. 232–236, 2017.

[19] M. Xiao, Y. J. Zhao, and J. F. KangYang, "Research on system identification based on hydraulic pump-motor of HMCVT," *Engineering in Agriculture, Environment and Food*, vol. 12, no. 4, pp. 420–426, 2019.

[20] M. Zhang, F. Zou, H. J. Zhang et al., "Vibration study of the gearbox of hydro-mechanical continuously variable transmission based on Mean Filter Method," *International Agricultural Engineering Journal*, vol. 26, pp. 82–87, 2017.

[21] Z Cheng, Z. X. Lu, and J. Qian, "A new non-geometric transmission parameter optimization design method for HMCVT based on improved GA and maximum transmission efficiency," *Computers and Electronics in Agriculture*, vol. 167, pp. 1–14, 2019.

[22] Z Cheng, Z. X. Lu, and F. Dai, "Research on HMCVT's efficiency model based on the improved SA algorithm," *Mathematical Problems in Engineering*, vol. 2019, Article ID 2856908, 10 pages, 2019.

[23] Z Cheng and Z. X. Lu, "A novel efficient feature dimensionality reduction method and its application in engineering," *Complexity*, vol. 2018, Article ID 2879640, 14 pages, 2018.

[24] Z. Cheng and Z. Lu, "Semi-empirical model for elastic tyre trafficability and methods for the rapid determination of its related parameters," *Biosystems Engineering*, vol. 174, pp. 204–218, 2018.

[25] Z. Cheng and Z. Lu, "Research on the PID control of the ESP system of tractor based on improved AFSA and improved SA," *Computers and Electronics in Agriculture*, vol. 148, pp. 142–147, 2018.

[26] Z. Cheng and Z. Lu, "Nonlinear research and efficient parameter identification of magic formula tire model," *Mathematical Problems in Engineering*, vol. 2017, Article ID 6924506, 9 pages, 2017.

[27] X. H. Li, *Design and Dynamic Characteristics Research on the Hydro-Mechanical Continuously Variable Transmission of Tractor*, Nanjing Agricultural University, Nanjing, China, 2017.

WILEY | Hindawi

Research Article

Composite One- to Six-Scroll Hidden Attractors in a Memristor-Based Chaotic System and Their Circuit Implementation

Ying Li,[1] **Xiaozhu Xia,**[1] **Yicheng Zeng** ⑩**,**[1] **and Qinghui Hong** ⑩[2]

[1]*School of Physics and Optoelectronic Engineering, Xiangtan University, Xiangtan, Hunan 411105, China*
[2]*College of Computer Science and Electronic Engineering, Hunan University, Changsha, Hunan 410000, China*

Correspondence should be addressed to Yicheng Zeng; yichengz@xtu.edu.cn and Qinghui Hong; 734798457@qq.com

Chaotic systems with hidden multiscroll attractors have received much attention in recent years. However, most parts of hidden multiscroll attractors previously reported were repeated by the same type of attractor, and the composite of different types of attractors appeared rarely. In this paper, a memristor-based chaotic system, which can generate composite attractors with one up to six scrolls, is proposed. These composite attractors have different forms, similar to the Chua's double scroll and jerk double scroll. Through theoretical analysis, we find that the new system has no fixed point; that is to say, all of the composite multiscroll attractors are hidden attractors. Additionally, some complicated dynamic behaviors including various hidden coexisting attractors, extreme multistability, and transient transition are explored. Moreover, hardware circuit using discrete components is implemented, and its experimental results supported the numerical simulations results.

1. Introduction

Recently, much effort has been devoted to the analysis of various chaotic systems owing to its potential applications [1–4]. To our knowledge, chaotic attractors are categorized as either self-excited attractors [5–7] or hidden attractors [8–11]. It should be particularly pointed out that hidden attractors have neither homoclinic nor heteroclinic orbits; thus, the Shil'nikov theorem [12] cannot be utilized to verify the existence of chaos, so that hidden chaotic systems attract great attention of scholars, and increasing number of researchers begin to study the rich dynamic behaviors of them.

As is known to all, multiscroll chaotic systems have aroused extensive interests for their much complicated dynamical properties than single-scroll ones. So, it is a more desirable task to explore the hidden multiscroll chaotic system, and there have been emerging related literatures on this topic. In 2016, Jafari et al. presented a novel no-equilibrium chaotic system with multiscroll hidden chaotic sea

by introducing a sine function into a 3D chaotic system [13]. In the same year, Hu et al. constructed two simple 3D chaotic systems without equilibrium based on an improved Sprott A system by adding a nonlinear function, from which hidden multiscroll attractors can be obtained [14]. Later, a new class of PWL dynamical system without equilibrium whose hidden chaotic attractors can display grid multiscroll has been introduced [15]. Deng and Wang proposed a multiscroll hidden chaotic system that has only two stable node-foci equilibrium points [16]. Hong et al. investigated a novel method for designing multidirection multibutterfly chaotic attractors (MDMBCA) without reconstructing nonlinear functions [17]. Furthermore, some memristive chaotic systems, which can generate hidden multiscroll or multiwing chaotic attractors, are reported [18, 19]. However, all of the hidden multiscroll attractors discussed above are of the same type attractor repeated in unidirectional or multidirection ones. Are there hidden multiscroll attractors, which are composed of different attractors? We are surprised that the answer is positive.

If an attractor is compounded from two or more different single-scroll attractors, which is called composite attractor, its dynamic characteristics are more complicated. The composite attractor has been already discovered in some self-excited chaotic systems. For example, Cang et al. proposed a Lorenz-like system with composite structure by controlling system parameters [20]. Zhang et al. reported an autonomous-system-based approach for creating composite chaotic attractors from a class of generalized Lorenz systems via switching control [21]. And then, Xiong et al. constructed a chaotic system, which can generate composite four-scroll attractor by adding a symbolic function into a 3D jerk system [22]. However, although the complexity of dynamic behavior of these chaotic systems, which can produce composite attractors, has increased, the operation methods and state equations have also been correspondingly complicated, and the circuit experiment is difficult to realize. Besides, these composite multiscroll chaotic attractors mentioned above are limited to self-excited attractors, and the hidden composite multiscroll attractors have not been reported up to now. It is obvious that designing a simple chaotic system, which can generate hidden composite multiscroll attractors, is a meaningful task.

Based on these considerations, we introduce a quadratic flux-controlled memristor into the 3D jerk chaotic system to construct a memristor-based hidden composite multiscroll chaotic system, which can produce composite one- to six-scroll hidden attractors through changing only one system parameter. It is pointed out that the composite six-scroll hidden attractor is composed of a Chua's double-scroll attractor and two jerk double-scroll attractors. Compared with [22], this new memristor-based hyperchaotic system has more complex dynamic behaviors including hyperchaotic composite multiscroll hidden attractors and extreme multistability phenomenon. These composite multiscroll attractors break the previous pattern of the same single-scroll attractor that appeared repeatedly and has not been reported in previous literature.

The rest of this paper is organized as follows. In Section 2, the mathematical model of the proposed memristive hyperchaotic system and its typical attractor are presented. In Section 3, complex hidden dynamic behaviors of this new system including controllable multiscroll hidden chaotic or hyperchaotic attractors, coexistence of hidden attractors, extreme multistability, and transient transition behavior are described. In Section 4, the corresponding circuit implementation and experiment results are presented. The conclusion is presented in the last section.

2. Memristive Hyperchaotic System and Its Typical Attractors

In 2016, Kengne et al. performed a simple 3D autonomous jerk system with cubic nonlinearity [23], which is described as

$$\begin{cases} \dot{x} = y, \\ \dot{y} = az, \\ \dot{z} = x - by - z - x^3, \end{cases} \tag{1}$$

where x, y, z are state variables, and a, b are positive tunable parameters. In order to construct a memristor-based hyperchaotic system, a quadratic flux-controlled memristor model [24] described in equation (2) is added into system (1):

$$\begin{cases} \dot{u} = v, \\ i = (m + nu)v, \end{cases} \tag{2}$$

where u, v and i denote the internal state of the memristor, the input of the memristor, and the output of the memristor model, respectively. The m, n are two real parameters of the memristor model. So, we constructed a 4D memristor-based chaotic system, which can generate composite multiscroll hidden attractors, and it is described as

$$\begin{cases} \dot{x} = y + z, \\ \dot{y} = az - \text{sgn}(z) + p, \\ \dot{z} = 2x - by - z - kW(u)y - x^3, \\ \dot{u} = cy, \end{cases} \tag{3}$$

in which x, y, z are state variables, a, b, c, k are real parameters, $W(u) = (m + nu)$ is the memductance function, and p is positive control parameter. From a dissipative perspective, the divergence of the new system (3) can easily be obtained as follows:

$$\nabla V = \frac{\partial \dot{x}}{\partial x} + \frac{\partial \dot{y}}{\partial y} + \frac{\partial \dot{z}}{\partial z} + \frac{\partial \dot{u}}{\partial u} = -1, \tag{4}$$

at any given point (x, y, z, u) of the state space. Consequently, the general condition of dissipativity related to the existence of attractive sets in our model is satisfied. The equilibrium points of system (3) can be obtained by solving the following equations: $\dot{x} = \dot{y} = \dot{z} = \dot{u} = 0$. It is obvious that the equations have no real solutions when parameter p is positive. That is to say, system (3) has no equilibrium, and it belongs to hidden chaotic system.

When fixing the control parameters $a = 3.5$, $b = 0.8$, $m = 0.1$, $n = 0.3$, $p = 0.01$, $k = 0.2$, $c = 0.01$ and selecting the initial conditions as $(0.1, 0.1, 0.1, 0.1)$, a composite six-scroll hidden chaotic attractor and its Poincaré map on $y = 0$ section as well as power spectrum are displayed in Figures 1(a)–1(c). As is depicted in Figure 1(a), the six-scroll attractor is composed of a Chua's double-scroll attractor and two jerk double-scroll attractors, and the two small jerk double-scroll attractors are inside the large Chua's double-scroll attractor, respectively. It is surprising that the composite six-scroll hidden chaotic attractors have never appeared before as far as we know.

3. Dynamic Analysis and Numerical Investigations

In this section, multifarious complicated dynamic behaviors including controllable multiscroll hidden attractors, coexisting of hidden chaotic or hyperchaotic attractors, extreme multistability, and transient transition behaviors of proposed system (3) are investigated in detail by means of

(a)

(b)

(c)
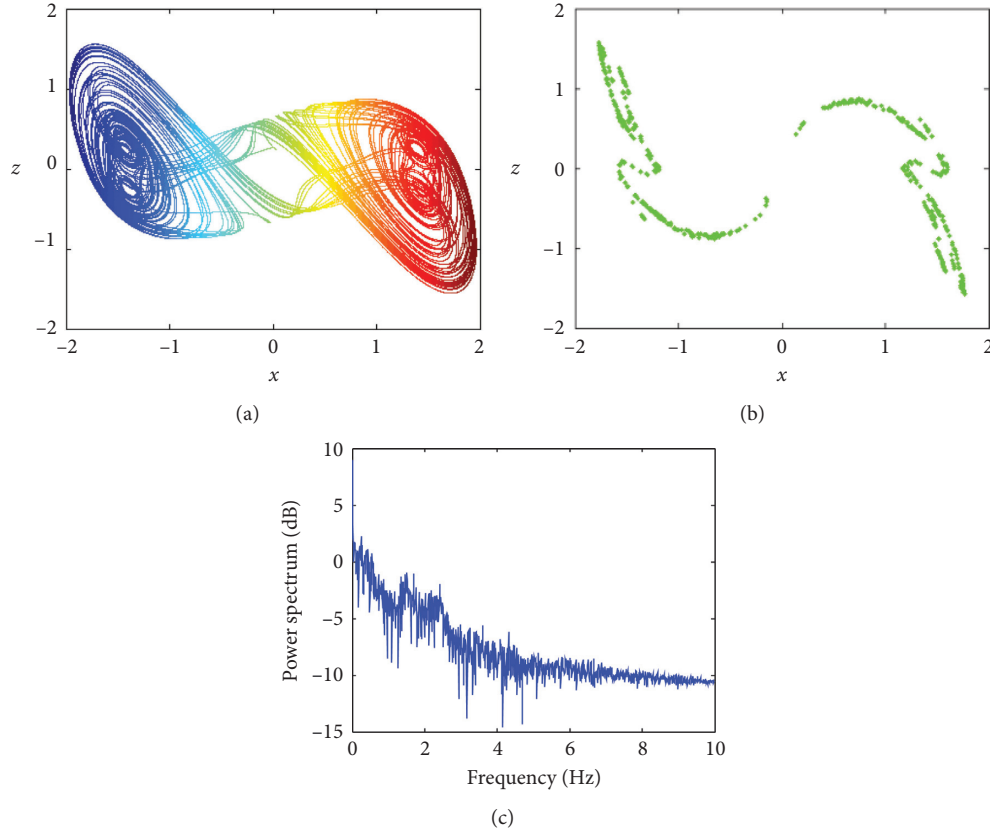
FIGURE 1: (a) The composite six-scroll hidden chaotic attractor. (b) The corresponding Poincaré mapping on $y = 0$ section. (c) The corresponding power spectrum.

Lyapunov exponent spectra, bifurcation diagrams, phase portraits, and time series. Note that all numerical simulations are carried out on MATLAB software, and the first 20000 points are discarded in the phase portraits.

3.1. Controllable Multiscroll Hidden Chaotic or Hyperchaotic Attractors.

One interesting phenomenon is that the newly proposed system (3) can generate composite one- to six-scroll hidden attractors by changing only one system parameter. Fixing the control parameters $b = 0.8$, $m = 0.1$, $n = 0.3$, $k = 0.2$, $c = 0.01$, $p = 0.01$ and changing the parameter a in the interval of [1.3, 5] with the initial conditions (0.1, 0.1, 0.1, 0.1), the corresponding bifurcation diagram is drawn in Figure 2(a). Additionally, using the famous Wolf method [25], the corresponding Lyapunov exponent spectrum proves the complexity of system (3) as depicted in Figure 2(b).

In reference to Figure 2(b), system (3) undergoes chaotic and hyperchaotic routes as follows: chaotic $(1.3 \leq a < 1.5) \longrightarrow$ hyperchaotic $(1.5 \leq a < 2.65) \longrightarrow$ chaotic $(2.56 \leq a < 3.06) \longrightarrow$ hyperchaotic $(3.06 \leq a < 3.42) \longrightarrow$ chaotic $(3.42 \leq a < 5)$. What surprised us is that system (3) generates composite one- to six-scrolls- hidden attractors when selecting appropriate parameters, and these attractors may exhibit either a symmetric or asymmetric structure. It is rare to see such attractors in an asymmetric system. Some typical hidden chaotic or hyperchaotic attractors with

different values of parameter a are shown in Figures 3(a)–3(l). Note that Figures 3(a) and 3(b) display a pair of asymmetric single-scroll hidden chaotic attractors at $a = 1.38$ and 2.92. Figures 3(c) and 3(d) show a pair of symmetric double-scroll hidden hyperchaotic attractors at $a = 2.3$ and 2.55, and the corresponding Lyapunov exponents are (0.213, 0.179, 0, −1.381) and (0.255, 0.209, 0, −1.444), respectively. Figures 3(e) and 3(f) exhibit two different double-scroll hidden chaotic attractors at $a = 2.946$ and 5. And a pair of asymmetric composite 3-scroll hidden chaotic and hyperchaotic attractors are drawn in Figures 3(g) and 3(h) with $a = 2.974$ and 3.117. Furthermore, a pair of symmetric composite 4-scroll hidden chaotic and hyperchaotic attractors, a composite 5-scroll hidden chaotic attractor, and a composite 6-scroll hidden hyperchaotic attractor are presented in Figures 3(i) and 3(l) with $a = 3.03$, 3.076, 3.055, and 3.125, respectively. To explain more intuitively and clearly, the different types of attractors with different values of parameter a are listed in Table 1. Consequently, the unusual controllable multiscroll hidden chaotic or hyperchaotic attractors of system (3) are innovative.

3.2. Coexistence of Hidden Attractors.

Nowadays, attractor coexisting is one of the common nonlinear dynamic phenomena, which is a chaotic system performing more than one concurrent attractor for a given set of system parameters under the different initial conditions [26–32]. In this section,

(a)

(b)
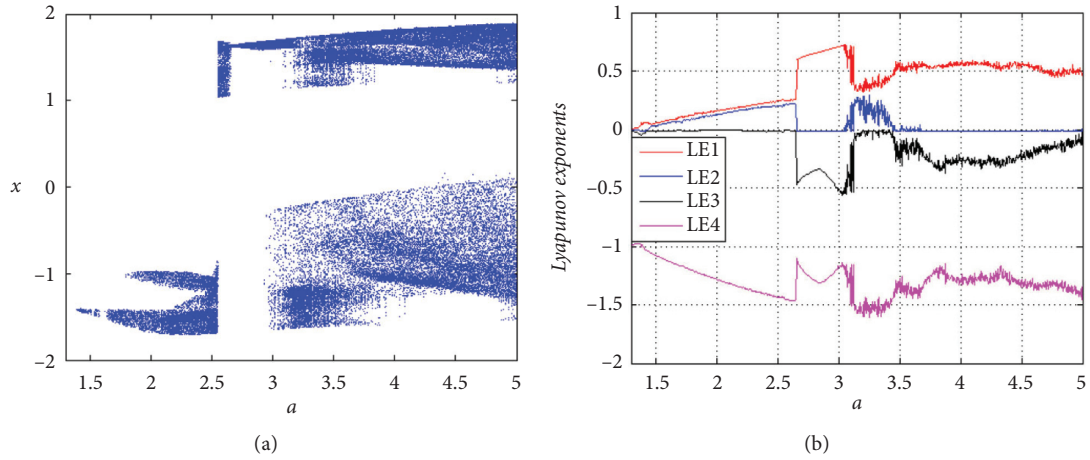
FIGURE 2: Dynamic behavior with increasing the parameter a in the interval of [1.3, 5]. (a) Bifurcation diagrams of *x*. (b) Lyapunov exponent spectrum.

(a)

(b)

(c)

(d)

(e)

(f)

(g)

(h)

(i)
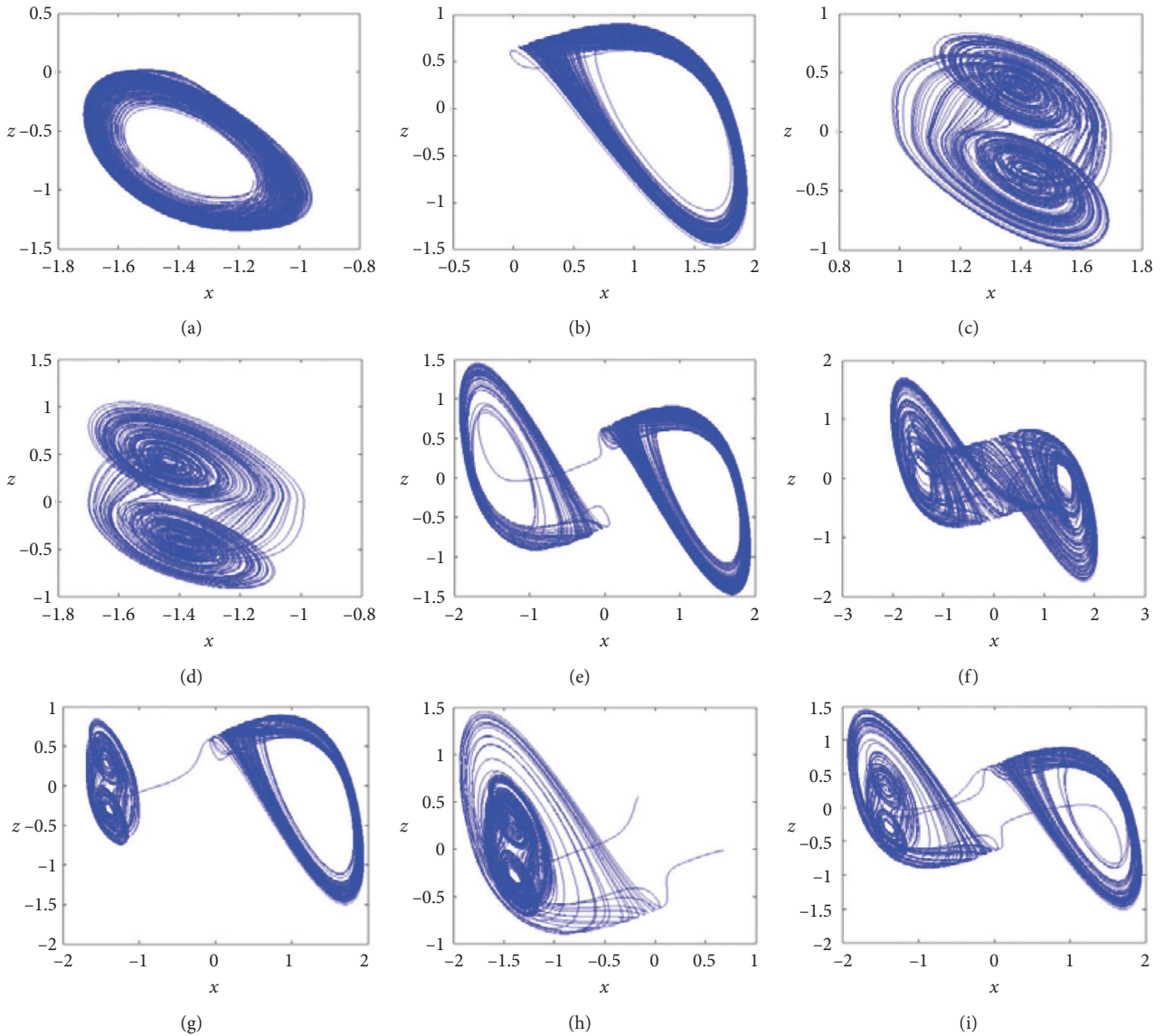
FIGURE 3: Continued.
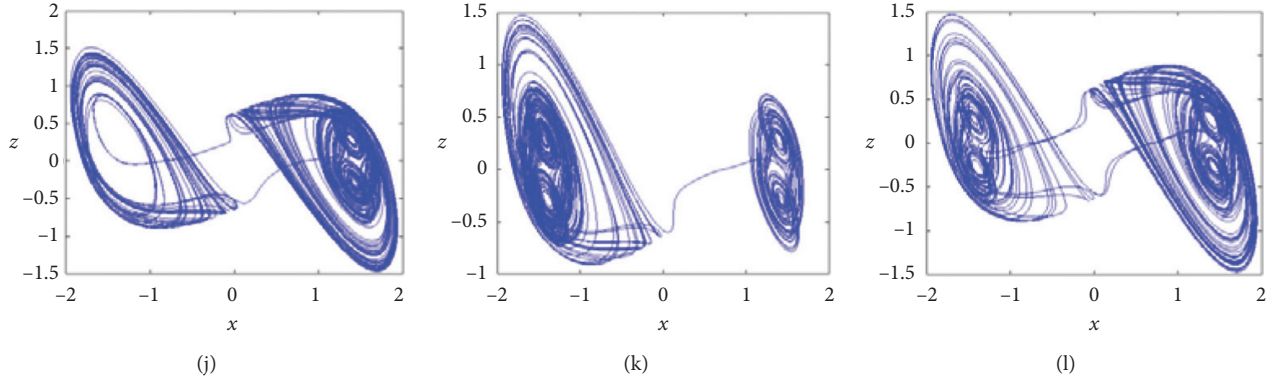
FIGURE 3: Some typical phase portraits with different parameter a. (a, b) A pair of asymmetric single-scroll chaotic attractors. (b) A pair of asymmetric single-scroll chaotic attractors. (c, d) A pair of symmetric double-scroll chaotic attractors. (e, f) Two different double-scroll chaotic attractors. (g, h) Two different composite 3-scroll chaotic attractors. (i, j) A pair of symmetric composite 4-scroll chaotic and hyperchaotic attractors. (k) A composite 5-scroll chaotic attractor. (l) A composite 6-scroll hyperchaotic attractor.

TABLE 1: Composite one- to six-scroll attractors of system (3) with variation of parameter a.

Parameter a	LE_S	Chaotic or hyperchaotic	The number of scrolls of hidden attractor	Diagrams
1.38	(+, 0, −, −)	Chaotic	Single-scroll	Figure 3(a)
2.92	(+, 0, −, −)	Chaotic	Single-scroll	Figure 3(b)
2.3	(+, +, 0, −)	Hyperchaotic	Double-scroll	Figure 3(c)
2.55	(+, +, 0, −)	Hyperchaotic	Double-scroll	Figure 3(d)
2.946	(+, 0, −, −)	Chaotic	Double-scroll	Figure 3(e)
5	(+, 0, −, −)	Chaotic	Double-scroll	Figure 3(f)
2.974	(+, 0, −, −)	Chaotic	3-scroll	Figure 3(g)
3.117	(+, +, 0, −)	Hyperchaotic	3-scroll	Figure 3(h)
3.03	(+, 0, −, −)	Chaotic	4-scroll	Figure 3(i)
3.076	(+, +, 0, −)	Hyperchaotic	4-scroll	Figure 3(j)
3.055	(+, 0, −, −)	Chaotic	5-scroll	Figure 3(k)
3.125	(+, +, 0, −)	Hyperchaotic	6-scroll	Figure 3(l)

the coexistence of hidden attractors with some specific parameters setting and initial conditions in system (3) is discussed. By selecting the control parameters as $b = 0.8$, $m = 0.1$, $n = 0.3$, $k = 0.2$, $c = 0.01$, $p = 0.01$, the coexisting bifurcation diagram of the state variable x with respect to the parameter a is described in Figure 4(a). Figure 4(b) displays the Lyapunov exponent spectrum under the initial conditions $(−0.1, −0.1, −0.1, −0.1)$, which is in accordance with the Lyapunov exponent spectrum under the initial conditions $(0.1, 0.1, 0.1, 0.1)$ in Figure 2(b). Various composite multiscroll chaotic or hyperchaotic hidden coexisting attractors are shown in Figure 5; they are including symmetric attractors and asymmetric attractors coexisting, odd number of attractors, and even number of attractors coexisting. The more detailed information is displayed in Table 2. All in all, it is informative and rare that so many composite multiscroll attractors coexist, which injects new blood into the field of chaos coexisting.

3.3. Extreme Multistability Relying on Memristor Initial Condition. In this subsection, we further studied the extreme multistability phenomenon [33–38] in system (3). To reveal extreme multistability phenomenon relying on

memristor initial condition, the typical parameters $a = 3.05$, $b = 0.8$, $c = 0.01$, $m = 0.1$, $n = 0.3$, $k = 0.2$, $p = 0.01$ and initial conditions $x(0) = 0.1$, $y(0) = 0.1$, $z(0) = 0.1$ are fixed. When the memristor initial condition $u(0)$ is increased gradually from −4.8 to 10, the bifurcation diagram of the state variable x and the Lyapunov exponent spectrum are plotted in Figures 6(a) and 6(b), respectively. As can be seen from Figure 6, the system has extremely rich dynamic characteristics.

To explain the coexistence of infinite number of attractors in system (2) more intuitively, several special values of u are selected as shown in Table 3 and the phase diagrams of the infinite coexisting attractors as shown in Figure 7.

Specially, when setting $a = 20$, $b = 0.8$, $m = 0.1$, $n = 0.3$, $k = 0.2$, $c = 0.01$, $p = 0.01$ and initial conditions $x(0) = 0.1$, $y(0) = 0.1$, $z(0) = 0.1$, and change the memristor initial condition $u(0)$ in the region of $[0, 8]$, the bifurcation diagram is plotted in Figure 8. In light of Figure 8, it is clear that the system goes through reverse period doubling bifurcation route from chaos to periodic. In order to illustrate this phenomenon of extreme multistability, there are seven types of hidden attractors, which are presented in Figure 9. In fact, more different types of hidden attractors can be obtained

(a)

(b)
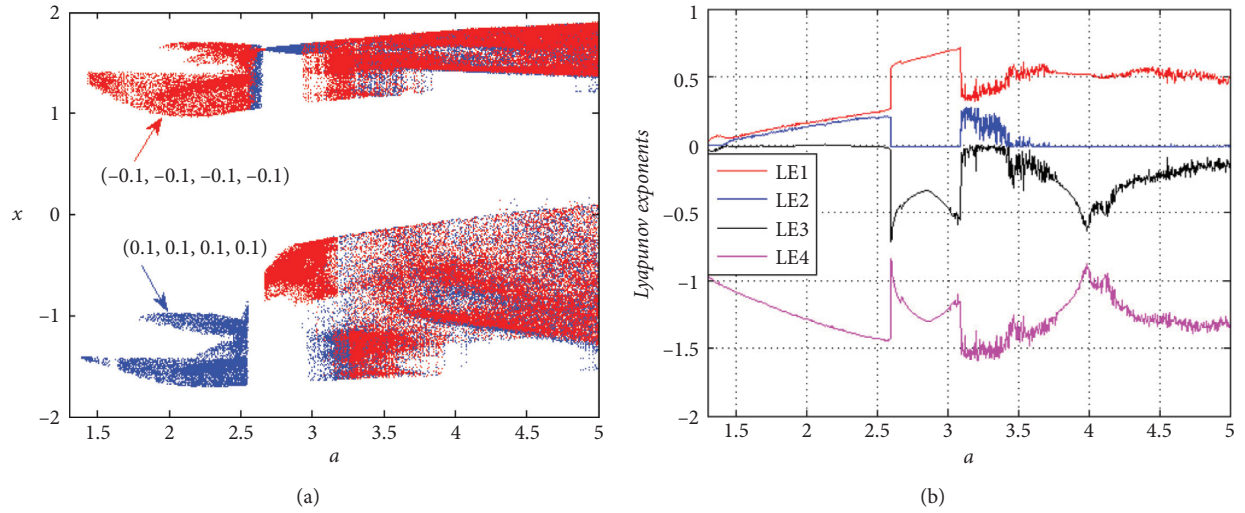
FIGURE 4: Coexisting bifurcation behaviors with increasing the parameter a in the interval of [1.3, 5]. (a) Coexisting bifurcation diagrams of the state variable (x). (b) Lyapunov exponent spectrum with initial conditions (−0.1, −0.1, −0.1, −0.1).

(a)

(b)

(c)

(d)

(e)

(f)

(g)

(h)

(i)
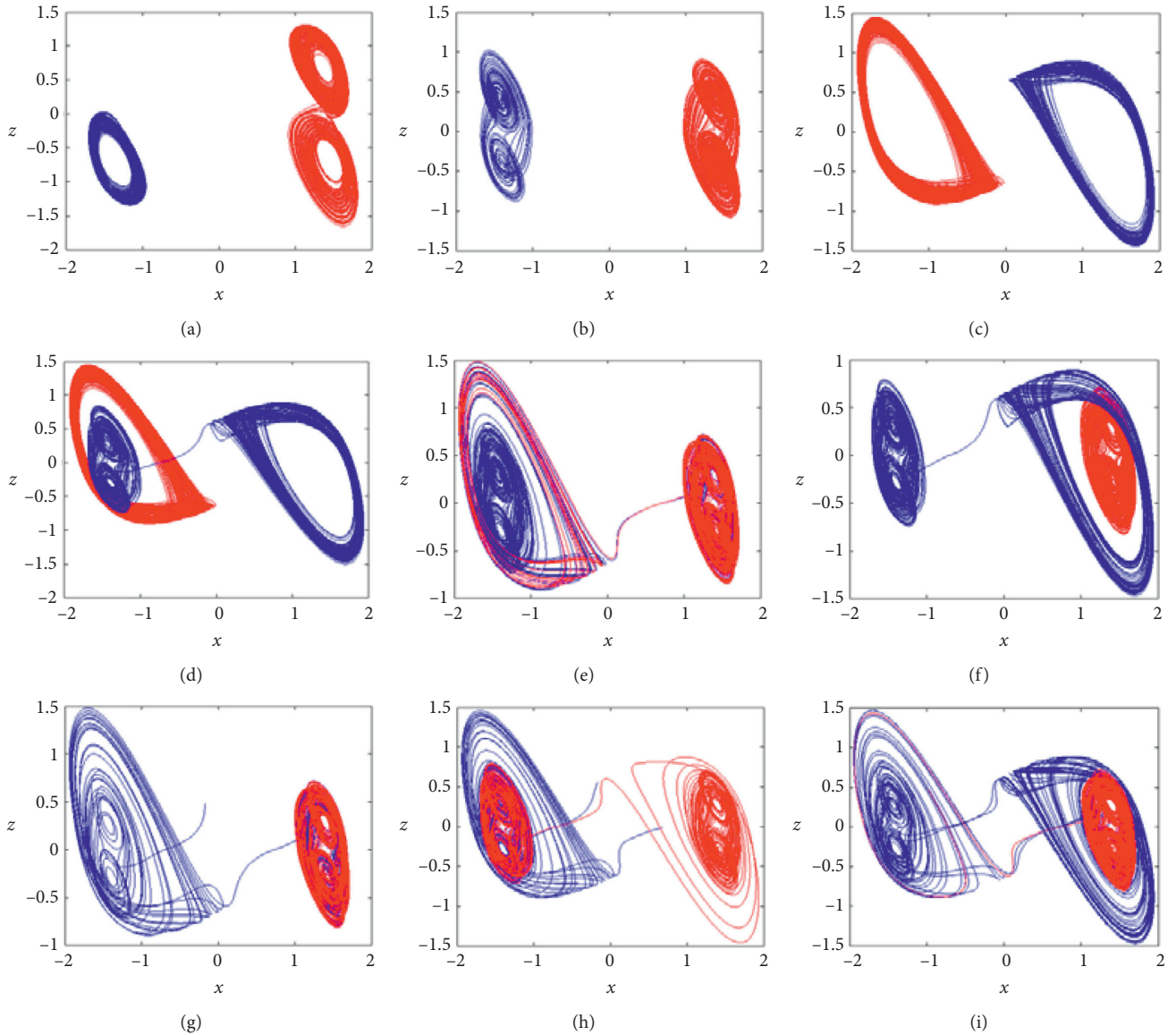
FIGURE 5: The coexisting chaotic or hyperchaotic hidden attractors with different values of parameter a.

TABLE 2: The coexisting multiscroll attractors of system (3) with different values of parameter a.

Parameter a	Chaotic or hyperchaotic	Coexisting attractors	Diagrams
1.38	Chaotic	A single scroll and a double-scroll	Figure 5(a)
2.3	Hyperchaotic	Two symmetric double-scroll	Figure 5(b)
2.92	Chaotic	Two symmetric single-scroll	Figure 5(c)
2.974	Chaotic	A 3-scroll and a single-scroll	Figure 5(d)
3.055	Chaotic	A 5-scroll and a 3-scroll	Figure 5(e)
3.095	Hyperchaotic	A 3-scroll and a double-scroll	Figure 5(f)
3.105	Hyperchaotic	A 5-scroll and a double-scroll	Figure 5(g)
3.117	Hyperchaotic	A 3-scroll and a 4-scroll	Figure 5(h)
3.125	Hyperchaotic	A 6-scroll and a double-scroll	Figure 5(i)

(a)

(b)
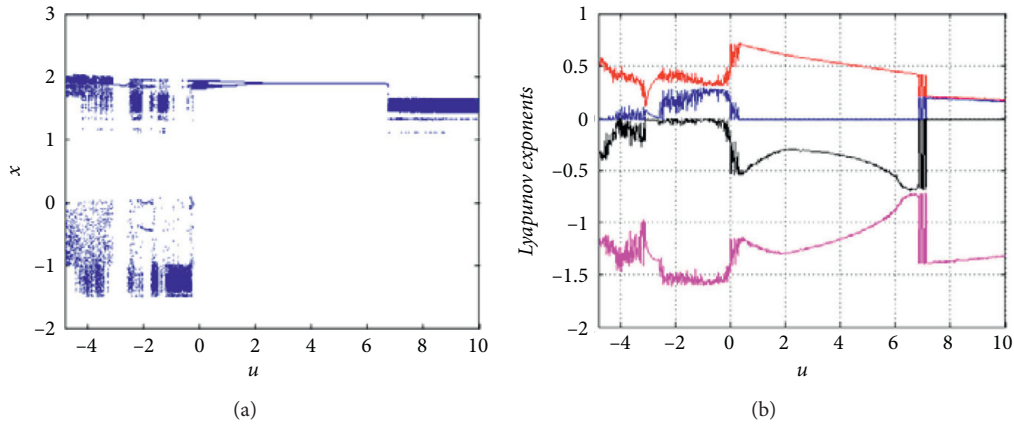
FIGURE 6: Bifurcation diagram and the Lyapunov exponent spectrum with respect to the initial conditions u (0) in region of [−4.8, 10].

TABLE 3: Extreme multistability behaviors of system (3).

Initial conditions	Types of coexisting multiple attractors	Diagrams
(0.1, 0.1, 0.1, −1.76); (0.1, 0.1, 0.1, 0.8); (0.1, 0.1, 0.1, 0.14); (0.1, 0.1, 0.1, 0.59)	Two single scroll and two double-scroll	Figure 7(a) red, green, cyan, magenta.
(0.1, 0.1, 0.1, −4.3); (0.1, 0.1, 0.1, 0.4); (0.1, 0.1, 0.1, 7.2)	Three double-scroll	Figure 7(b) magenta, green, cyan.
(0.1, 0.1, 0.1, 0.23); (0.1, 0.1, 0.1, 0.37)	Two 3-scroll	Figure 7(c) magenta, green.
(0.1, 0.1, 0.1, −0.18); (0.1, 0.1, 0.1,−0.1)	Two 4-scroll	Figure 7(d) magenta, green.
(0.1, 0.1, 0.1, −1.29); (0.1, 0.1, 0.1, − 0.42)	Two 5-scroll	Figure 7(e) magenta, green.
(0.1, 0.1, 0.1, −3.4); (0.1, 0.1, 0.1, −1.8)	Two 6-scroll	Figure 7(f) magenta, green.

under the different initial conditions. In general, Figures 7–9 intuitively reveal the coexisting infinitely many hidden hyperchaotic attractors, which indicates that system (3) possesses hidden extreme multistability indeed.

3.4. Transient Transition Behavior. In system exhibiting transient transition, the orbit is from one state (chaotic, periodic) to another state (chaotic, periodic) for a finite time interval before settling into a final state. Transient chaos with boundary crisis is often encountered in nonlinear dynamic systems [22, 39–43]. For the sake of verifying transient transition behavior in system (3), the system parameters are considered as $a = 3.115$, $b = 0.8$, $m = 0.1$, $n = 0.3$, $k = 0.2$, $c = 0.01$, $p = 0.01$, while the initial conditions are selected as (0.1, 0.1, 0.1, 0.1) and the time is $t = 1000$ s, and a phase diagram of six scrolls and the corresponding time-domain

waveform with state variables x and z are shown in Figures 10(a)–10(c). Figure 11 displays three different phase diagrams with different simulation time and the Lyapunov exponent spectrum with increased time. From the Lyapunov exponent spectrum in Figure 11(d), it is clearly seen that there are two Lyapunov exponents greater than zero at $t = 80$ s; that is to say, system (3) transitions from chaotic to hyperchaotic in the time of $t = 80$ s.

4. Circuit Implementation and Experiment Results

Circuit implementation provides an alternative approach to explore the novel no-equilibrium memristive hyperchaotic system (3), and it is the key to the chaos application. In this part, a suitable electrical circuit is designed and a hardware

(a)

(b)

(c)

(d)

(e)

(f)
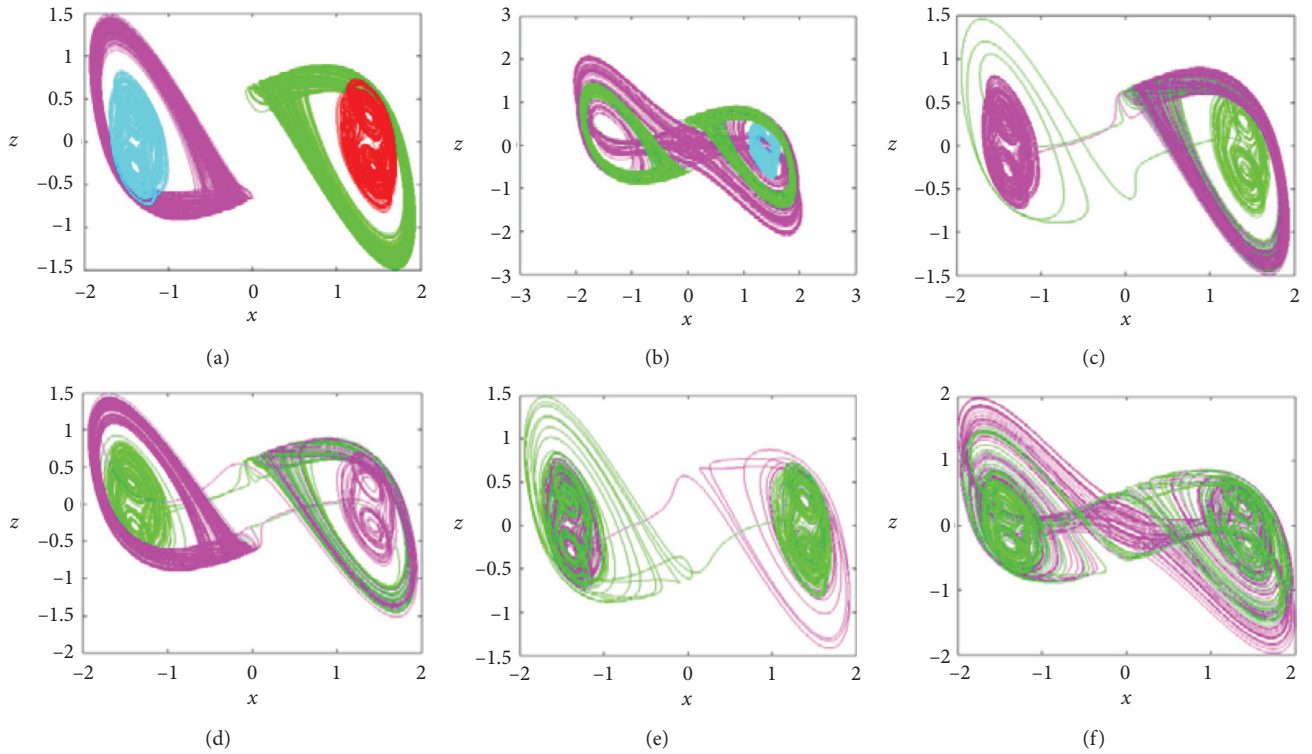
Figure 7: The coexistence of infinite number of attractors on x–z plane with different initial condition $u(0)$.
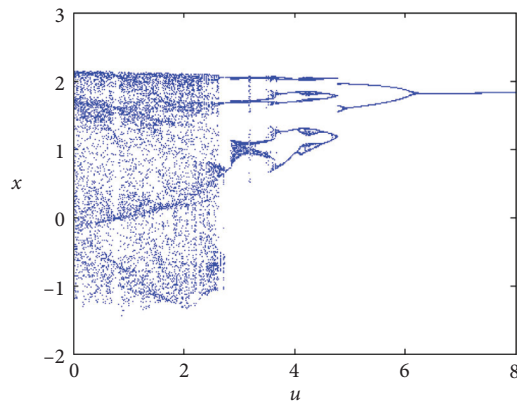
Figure 8: Bifurcation diagram with respect to the initial conditions $u(0)$ in region of $[0, 8]$.
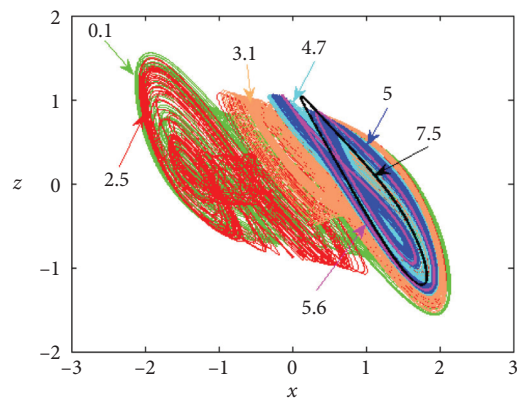
Figure 9: The coexistence of infinite number of attractors on x-z plane with different initial condition $u(0)$, the different attractors corresponding to the different values of $u(0)$ are marked with different colors.

(a)   (b)   (c)
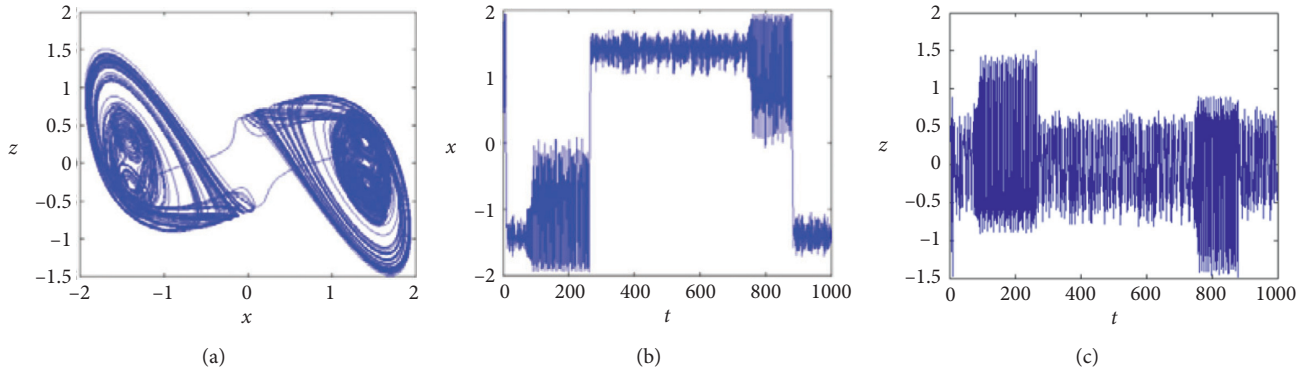
FIGURE 10: The transient transition behaviors of system (3). (a) A phase diagram of six-scroll hidden chaotic attractors. (b) Time-domain waveform of the variable (x). (c) Time-domain waveform of the variable z.

(a)   (b)

(c)   (d)
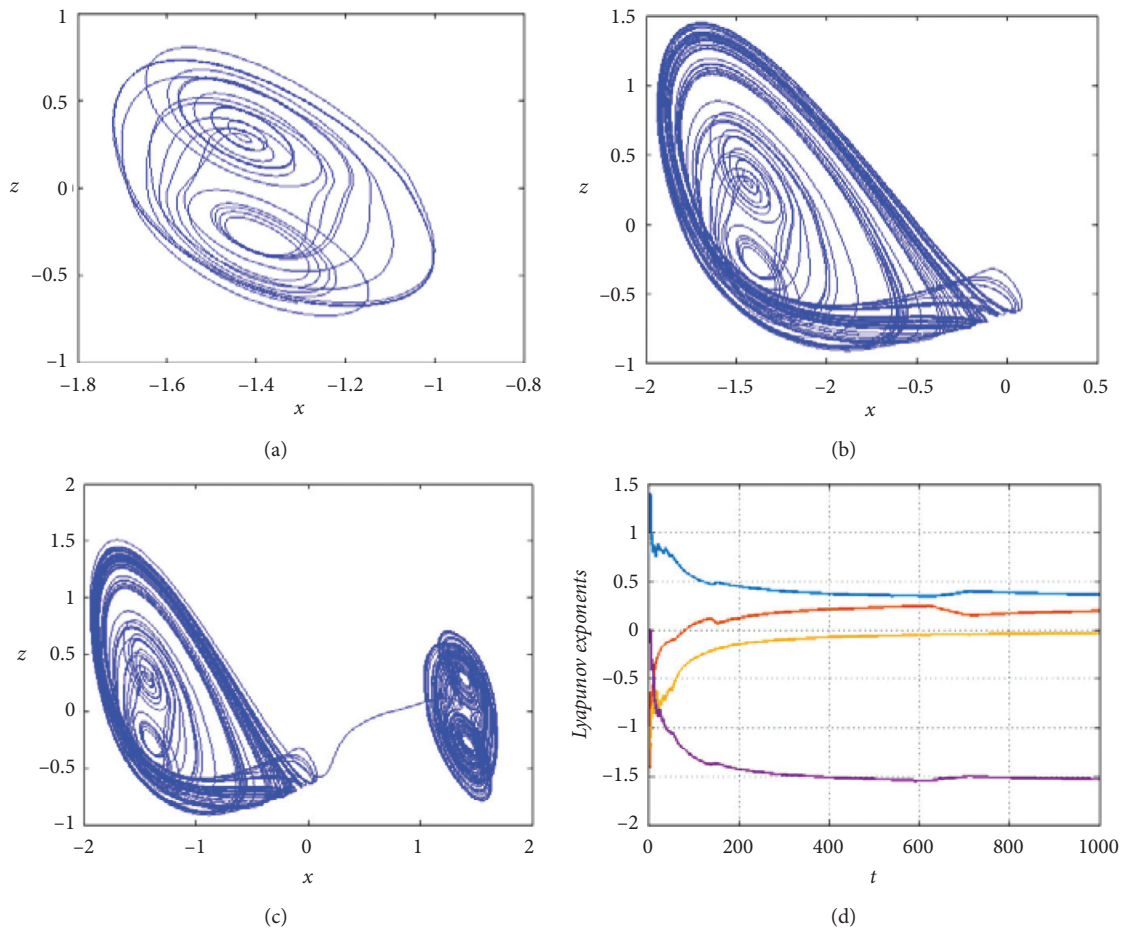
FIGURE 11: The transient transition behaviors with system (3). (a) A phase diagram of double-scroll hidden hyperchaotic attractors with $t = 80$ s. (b) A phase diagram of 3-scroll hidden chaotic attractors with $t = 250$ s. (c) A phase diagram of 5-scroll hidden hyperchaotic attractors with $t = 750$ s. (d) The Lyapunov exponent spectrum with increased time in the region of [0, 1000].

circuit is implemented to verify the theoretical results obtained previously. The circuit diagram of the proposed system (3) is provided in Figure 12, and the circuits in the dashed box are constructed for the symbolic function circuit and memristor equivalent circuit.

The operational amplifiers of Figure 12 are LF353, whose supply voltages are ±15 V. And multipliers A_1, A_2, A_3 are AD633 with output coefficient of 0.1. Based on system (3), select the system parameters as $a = 3.5$, $b = 0.8$, $m = 0.1$, $n = 0.3$, $k = 0.2$, $c = 0.01$, $p = 0.01$ and let $\gamma = \gamma_0 t$, where
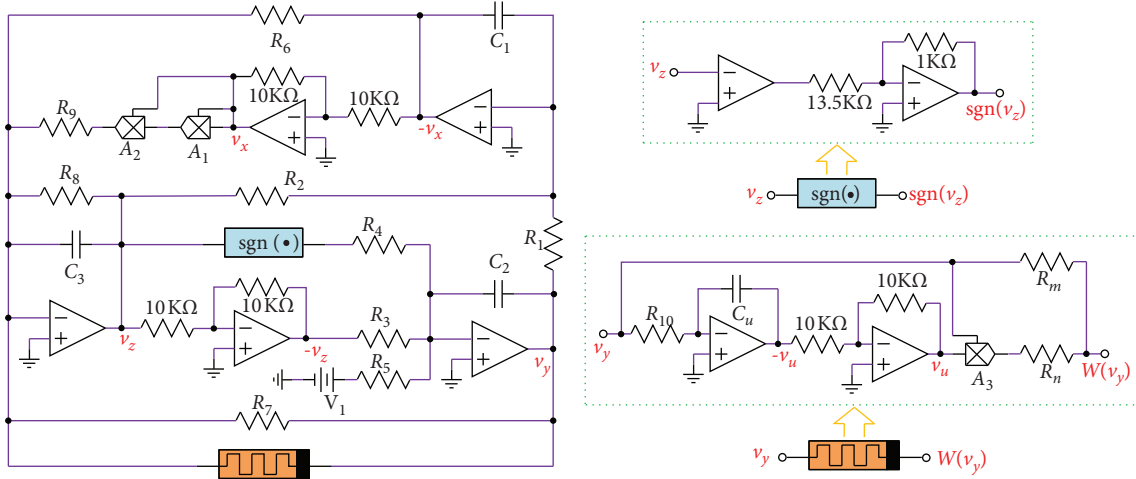
FIGURE 12: Circuit implementation of system (3).
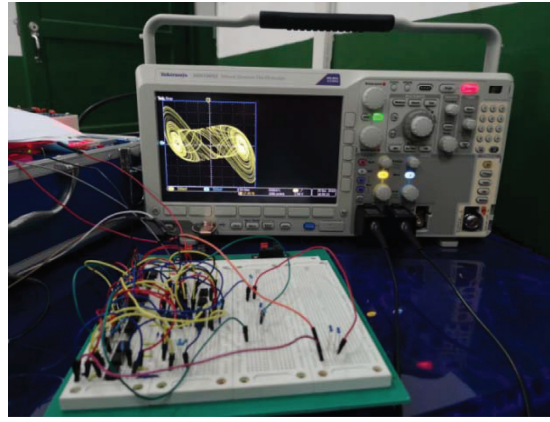
FIGURE 13: The hardware circuit test setup to realize system (3).

$\gamma_0 = 10000$ is the time-scale transformation factor and system (3) can be rewritten by

$$\begin{cases} \dot{x} = 10000y + 10000z, \\ \dot{y} = 35000z - 10000\text{sign}(z) + 100, \\ \dot{z} = 20000x - 8000y - 10000z - 2000W(u)y - 10000x^3, \\ \dot{v} = 100y, \end{cases}$$

(5)

where $W(u) = (m + nu)$. Considering Kirchhoff's law, the circuit equation of system (3) can be written as

$$\begin{cases} \dfrac{dv_x}{dt} = \left(\dfrac{1}{R_1 C_1}\right)v_y - \left(\dfrac{1}{R_2 C_1}\right)v_z, \\[2mm] \dfrac{dv_y}{dt} = \left(\dfrac{1}{R_3 C_2}\right)v_y - \left(\dfrac{1}{R_4 C_2}\right)\text{sign}(v_z) + \left(\dfrac{1}{R_5 C_2}\right)V_1, \\[2mm] \dfrac{dv_z}{dt} = \left(\dfrac{1}{R_6 C_3}\right)v_x - \left(\dfrac{1}{R_7 C_3}\right)v_y - \left(\dfrac{1}{R_8 C_3}\right)v_z - \left(\dfrac{1}{R_m C_3}\right)v_y - \left(\dfrac{1}{10R_n C_3}\right)v_u v_y - \left(\dfrac{1}{100R_9 C_3}\right)v_x^3, \\[2mm] \dfrac{dv_u}{dt} = \left(\dfrac{1}{R_{10} C_u}\right)v_y. \end{cases}$$

(6)
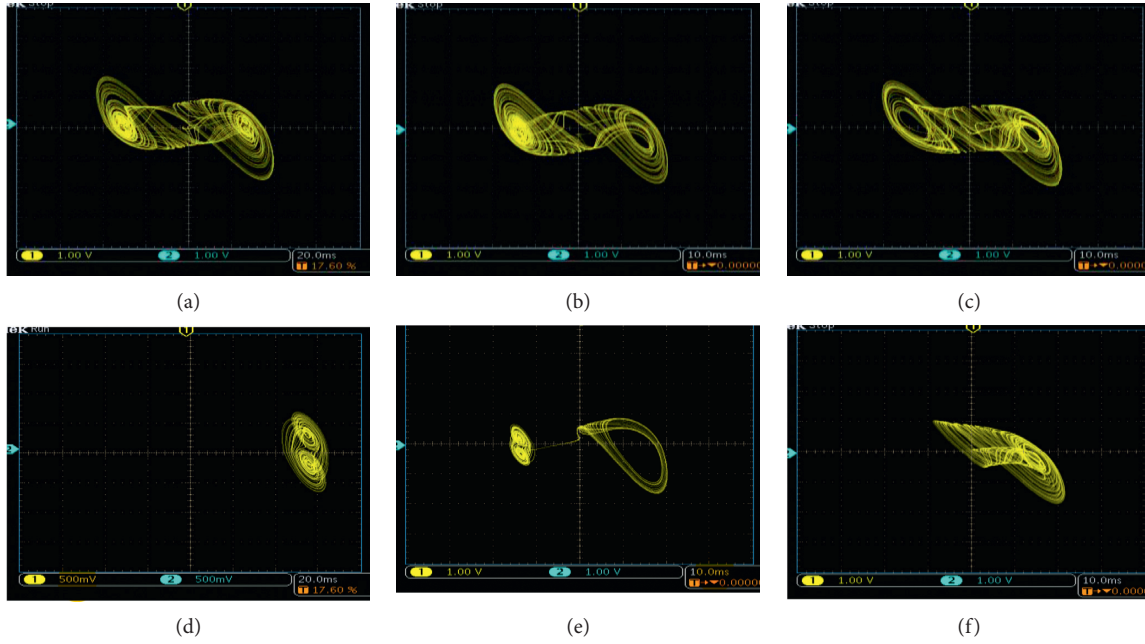
FIGURE 14: The screenshots of the digital oscilloscope of the different composite multiscroll attractors with different R_3. (a) Composite 6-scroll with $R_3 = 2.86 \, \text{k}\Omega$; (b) composite 4-scroll with $R_3 = 3.3 \, \text{k}\Omega$; (c) double-scroll with $R_3 = 0.5 \, \text{k}\Omega$; (d) double-scroll with $R_3 = 4.348 \, \text{k}\Omega$; (e) composite 3-scroll with $R_3 = 3.362 \, \text{k}\Omega$; (f) single-scroll with $R_3 = 0.263 \, \text{k}\Omega$.

Here, v_x, v_y, v_z and v_u are the voltages on capacitors C_1, C_2, C_3 and C_u, respectively, and the capacitors $C_1 = C_2 = C_3 = C_u = 10 \, \text{nF}$, $V_1 = -1 \, \text{V}$. Comparing equation (5) with equation (6) and keeping the corresponding coefficients equal, one gets $R_1 = R_2 = R_4 = R_8 = 10 \, \text{k}\Omega$, $R_3 = 2.86 \, \text{k}\Omega$, $R_5 = R_{10} = 10 \, \text{M}\Omega$, $R_6 = 5 \, \text{k}\Omega$, $R_7 = 12.5 \, \text{k}\Omega$, $R_9 = 100 \, \Omega$, $R_m = 500 \, \text{k}\Omega$, $R_n = 16.7 \, \text{k}\Omega$. Then, according to the circuit diagram in Figure 12, some off-the-shelf discrete components are used on the breadboard to build the hardware circuit as shown in Figure 13 and the parameters in the circuit are set as above. We can see a composite six-scroll chaotic attractor as shown in Figure 14(a) by using digital oscilloscope, which is well consistent with the phase diagram simulated with MATLAB in Figure 1(a). Lastly, keeping the values of R_1, R_2, R_4, R_5, R_6, R_7, R_8, R_9, R_m and R_n unchanged, and adjusting the values of R_3 to appropriate resistance, other composite multiscroll attractors can be obtained from this hardware circuit as shown in Figures 14(b)–14(f), which also agree with the results of MATLAB simulation aforementioned. All of what is discussed above demonstrates the effectiveness and feasibility of system (3).

5. Conclusion

In this paper, a memristor-based chaotic system with abundant dynamic behaviors is reported. Compared with other memristor-based chaotic systems, the new system can display composite one- to six-scroll hidden attractors by changing only one system parameter. And the composite multiscroll attractors are composed of different types of attractors. For example, a composite six-scroll attractor is composed of a Chua's double-scroll attractor and two jerk double-scroll attractors. The coexistence of symmetric and asymmetric attractors with different numbers of scrolls also reflects the particularity of the system. Furthermore, extreme multistability phenomenon and chaotic transient transition are investigated in the system. Finally, the feasibility of the proposed chaotic system is verified by hardware circuit, and the results match very well with the numerical simulations. Due to the fact that such a new chaotic system constructed in this paper has complex dynamic properties, it could be utilized advantageously in chaos-based engineering applications including image encryption, random bit generation, and chaos-based secure communication, and for future investigation.

Data Availability

The MATLAB simulation program data used to support the findings of this study are included within the supplementary information file. The simulation data of the study are reflected in the manuscript.

Conflicts of Interest

The authors declare that they have no conflicts of interest.

Acknowledgments

Supplementary Materials

The following is the supplementary description for the given supplementary material. Appendix A: MATLAB simulation code for phase portrait. Appendix B: MATLAB simulation code for bifurcation diagram. Appendix C: MATLAB simulation code for Lyapunov exponent spectrum. (*Supplementary Materials*)

References

[1] F. C. Moon and P. D. Stiefel, "Coexisting chaotic and periodic dynamics in clock escapements," *Philosophical Transactions of the Royal Society A: Mathematical, Physical and Engineering Sciences*, vol. 364, no. 1846, pp. 2539–2564, 2006.

[2] E. F. D. Goufo and I. T. Toudjeu, "Analysis of recent fractional evolution equations and applications," *Chaos, Solitons & Fractals*, vol. 126, pp. 337–350, 2019.

[3] C. Han, "An image encryption algorithm based on modified logistic chaotic map," *Optik*, vol. 181, pp. 779–785, 2019.

[4] C. Chen, L. Li, H. Peng, and Y. Yang, "Fixed-time synchronization of memristor-based BAM neural networks with time-varying discrete delay," *Neural Networks*, vol. 96, pp. 47–54, 2017.

[5] G. Litak, M. Borowiec, A. Syta, and K. Szabelski, "Transition to chaos in the self-excited system with a cubic double well potential and parametric forcing," *Chaos, Solitons & Fractals*, vol. 40, no. 5, pp. 2414–2429, 2009.

[6] J. C. Sprott, "Strange attractors with various equilibrium types," *The European Physical Journal Special Topics*, vol. 224, no. 8, pp. 1409–1419, 2015.

[7] E. F. Doungmo Goufo, "Mathematical analysis of peculiar behavior by chaotic, fractional and strange multiwing attractors," *International Journal of Bifurcation and Chaos*, vol. 28, no. 10, Article ID 1850125, 2018.

[8] Z. Wei, I. Moroz, J. C. Sprott et al., "Hidden hyperchaos and electronic circuit application in a 5D self-exciting homopolar disc dynamo," *Chaos: An Interdisciplinary Journal of Nonlinear Science*, vol. 27, no. 3, Article ID 33101, 2017.

[9] E. F. D. Goufo, "On chaotic models with hidden attractors in fractional calculus above power law," *Chaos, Solitons & Fractals*, vol. 127, pp. 24–30, 2019.

[10] M. A. Jafari, E. Mliki, A. Akgul et al., "Chameleon: the most hidden chaotic flow," *Nonlinear Dynamics*, vol. 88, no. 3, pp. 2303–2317, 2017.

[11] S. Jafari, J. C. Sprott, and S. M. R. Golpayegani, "Elementary quadratic chaotic flows with no equilibria," *Physics Letters A*, vol. 377, no. 9, pp. 699–702, 2013.

[12] L. P. Hashemi Golpayegani, "A case of the existence of a countable number of periodic motions," *Soviet Mathematics Docklady*, vol. 6, pp. 163–166, 1965.

[13] S. Jafari, V. T. Pham, and T. Kapitaniak, "Multiscroll chaotic sea obtained from a simple 3D system without equilibrium," *International Journal of Bifurcation and Chaos*, vol. 26, no. 2, Article ID 1650031, 2016.

[14] X. Hu, C. Liu, L. Liu, J. Ni, and S. Li, "Multi-scroll hidden attractors in improved Sprott A system," *Nonlinear Dynamics*, vol. 86, no. 3, pp. 1725–1734, 2016.

[15] R. J. Escalante-Gonzalez and E. Campos-Canton, "A class of Piecewise Linear Systems without equilibria with 3-D grid multiscroll chaotic attractors," *Institute of Electrical and Electronics Engineering Transactions on Circuits and Systems II: Express Briefs*, vol. 66, no. 8, pp. 1456–1460, 2018.

[16] Q. Deng and C. Wang, "Multi-scroll hidden attractors with two stable equilibrium points," *Chaos: An Interdisciplinary Journal of Nonlinear Science*, vol. 29, no. 9, Article ID 93112, 2019.

[17] Q. Hong, Y. Li, X. Wang et al., "A versatile pulse control method to generate arbitrary multi-direction multi-butterfly chaotic attractors," *Institute of Electrical and Electronics Engineering Transactions on Computer-Aided Design of Integrated Circuits and Systems*, vol. 38, no. 8, pp. 1480–1492, 2018.

[18] X. Hu, C. Liu, L. Liu et al., "Multi-scroll hidden attractors and multi-wing hidden attractors in a 5-dimensional memristive system," *Chinese Physics B*, vol. 26, no. 11, Article ID 110502, 2017.

[19] Z. Ling, C. Wang, and L. Zhou, "A novel no-equilibrium hyperchaotic multi-wing system via introducing memristor," *International Journal of Circuit Theory & Applications*, vol. 46, no. 2, 2017.

[20] S. Cang, Z. Wang, Z. Chen, and H. Jia, "Analytical and numerical investigation of a new lorenz-like chaotic attractor with compound structures," *Nonlinear Dynamics*, vol. 75, no. 4, pp. 745–760, 2014.

[21] C. Zhang, S. Yu, and G. Chen, "Design and implementation of compound chaotic attractors," *International Journal of Bifurcation and Chaos*, vol. 22, no. 5, Article ID 1250120, 2012.

[22] L. Xiong, S. Zhang, Y. Zeng, and B. Liu, "Dynamics of a new composite four-Scroll chaotic system," *Chinese Journal of Physics*, vol. 56, no. 5, pp. 2381–2394, 2018.

[23] J. Kengne, Z. T. Njitacke, and H. B. Fotsin, "Dynamical analysis of a simple autonomous jerk system with multiple attractors," *Nonlinear Dynamics*, vol. 83, no. 1-2, pp. 751–765, 2016.

[24] B. C. Bao, X. Zou, Z. Liu et al., "Generalized memory element and chaotic memory system," *International Journal of Bifurcation and Chaos*, vol. 23, no. 8, 2013.

[25] A. Wolf, J. B. Swift, H. L. Swinney, and J. A. Vastano, "Determining Lyapunov exponents from a time series," *Physica D: Nonlinear Phenomena*, vol. 16, no. 3, pp. 285–317, 1985.

[26] W. Zhou, G. Wang, Y. Shen et al., "Hidden coexisting attractors in a chaotic system without equilibrium point," *International Journal of Bifurcation and Chaos*, vol. 28, no. 10, 2018.

[27] V. Varshney, S. Sabarathinam, A. Prasad et al., "Infinite number of hidden attractors in memristor-based autonomous duffing oscillator," *International Journal of Bifurcation and Chaos*, vol. 28, no. 1, Article ID 1850013, 2018.

[28] D. Mathale, E. F. D. Goufo, and M. Khumalo, "Coexistence of multi-scroll chaotic attractors for fractional systems with exponential law and non-singular kernel," *Chaos, Solitons & Fractals*, vol. 139, Article ID 110021, 2020.

[29] H. Jahanshahi, A. Yousefpour, Z. Wei, R. Alcaraz, and S. Bekiros, "A financial hyperchaotic system with coexisting attractors: dynamic investigation, entropy analysis, control and synchronization," *Chaos, Solitons & Fractals*, vol. 126, pp. 66–77, 2019.

[30] L. Zhou, C. Wang, X. Zhang et al., "Various attractors, coexisting attractors and antimonotonicity in a simple fourth-order memristive twin-T oscillator," *International Journal of Bifurcation and Chaos*, vol. 28, no. 4, pp. 481–495, 2018.

[31] B. Bao, L. Xu, N. Wang, H. Bao, Q. Xu, and M. Chen, "Third-order RLCM-four-elements-based chaotic circuit and its coexisting bubbles," *AEU-International Journal of Electronics and Communications*, vol. 94, pp. 26–35, 2018.

[32] A. Bayani, K. Rajagopal, A. J. M. Khalaf et al., "Dynamical analysis of a new multistable chaotic system with hidden attractor: antimonotonicity, coexisting multiple attractors, and offset boosting," *Physics Letters A*, vol. 383, no. 13, pp. 1450–1456, 2019.

[33] M. S. Patel, U. Patel, A. Sen et al., "Experimental observation of extreme multistability in an electronic system of two coupled Rössler oscillators," *Physical Review E*, vol. 89, no. 2, Article ID 022918, 2014.

[34] C. B. Li and J. C. Sprott, "Multistability in the Lorenz system: a broken butterfly," *International Journal of Bifurcation & Chaos*, vol. 24, no. 10, p. 7, 2014.

[35] S. Jafari, A. Ahmadi, S. Panahi, and K. Rajagopal, "Extreme multi-stability: when imperfection changes quality," *Chaos, Solitons & Fractals*, vol. 108, pp. 182–186, 2018.

[36] B. C. Bao, H. Bao, N. Wang, M. Chen, and Q. Xu, "Hidden extreme multistability in memristive hyperchaotic system," *Chaos, Solitons & Fractals*, vol. 94, pp. 102–111, 2017.

[37] S. Zhang, Y. C. Zeng, Z. J. Li et al., "Generating one to four-wing hidden attractors in a novel 4D no-equilibrium chaotic system with extreme multistability," *Chaos*, vol. 28, no. 1, Article ID 013113, 2018.

[38] B. A. Mezatio, M. T. Motchongom, B. R. Wafo Tekam, R. Kengne, R. Tchitnga, and A. Fomethe, "A novel memristive 6D hyperchaotic autonomous system with hidden extreme multistability," *Chaos, Solitons & Fractals*, vol. 120, pp. 100–115, 2019.

[39] J. P. Singh and B. K. Roy, "Crisis and inverse crisis route to chaos in a new 3-D chaotic system with saddle, saddle foci and stable node foci nature of equilibria," *Optik*, vol. 127, no. 24, pp. 11982–12002, 2016.

[40] H. Bao, N. Wang, B. C. Bao et al., "Initial condition-dependent dynamics and transient period in memristor-based hypogenetic jerk system with four line equilibria," *Communications in Nonlinear Science and Numerical Simulation*, vol. 57, pp. 264–275, 2017.

[41] Y. Mukouyama, H. Kawasaki, D. Hara, and S. Nakanishi, "Transient chaotic behavior during simultaneous occurrence of two electrochemical oscillations," *Journal of Solid State Electrochemistry*, vol. 19, no. 11, pp. 3253–3263, 2015.

[42] S. Sabarathinam, C. K. Volos, and K. Thamilmaran, "Implementation and study of the nonlinear dynamics of a memristor-based duffing oscillator," *Nonlinear Dynamics*, vol. 87, no. 1, pp. 37–49, 2017.

[43] A. Yousefpour, H. Jahanshahi, J. M. Munoz-Pacheco et al., "A fractional-order hyper-chaotic economic system with transient chaos," *Chaos, Solitons & Fractals*, vol. 130, Article ID 109400, 2020.

WILEY | Hindawi

Research Article

On Behavioral Response of 3D Squeezing Flow of Nanofluids in a Rotating Channel

Mubashir Qayyum,[1] **Omar Khan,**[2] **Thabet Abdeljawad** ,[3,4,5] **Naveed Imran,**[6] **Muhammad Sohail** ,[6] **and Wael Al-Kouz**[7]

[1]*Department of Sciences and Humanities, National University of Computer and Emerging Sciences, Lahore, Pakistan*
[2]*Department of Computer Science, National University of Computer and Emerging Sciences, Peshawar, Pakistan*
[3]*Department of Mathematics and General Sciences, Prince Sultan University, Riyadh, Saudi Arabia*
[4]*Department of Medical Research, China Medical University, Taichung, Taiwan*
[5]*Department of Computer Science and Information Engineering, Asia University, Taichung, Taiwan*
[6]*Department of Applied Mathematics and Statistics, Institute of Space Technology, P.O. Box 2750, Islamabad 44000, Pakistan*
[7]*Mechanical and Maintenance Engineering Department, German Jordanian University, Amman, Jordan*

Correspondence should be addressed to Thabet Abdeljawad; tabdeljawad@psu.edu.sa

In this article, a behavioral study of three-dimensional (3D) squeezing flow of nanofluids with magnetic effect in a rotating channel has been performed. Using Navier–Stokes equations along with suitable similarity transformations, a nonlinear coupled ordinary differential system has been derived which models the 3D squeezing flow of nanofluids with lower permeable stretching porous wall where the channel is also rotating. The base fluid in the channel is considered to be water that contains different nanoparticles including silicon, copper, silver, gold, and platinum. The homotopy perturbation method (HPM) is employed for the solution of highly nonlinear coupled system. For validation purpose, system of equations is also solved through the Runge–Kutta–Fehlberg (RK45) scheme and results are compared with homotopy solutions, and excellent agreement has been found between analytical and numerical results. Also, validation has been performed by finding average residual error of the coupled system. Furthermore, the effects of various parameters such as nanoparticle volume fraction, suction parameter, characteristic parameter of the flow, magnetic parameter, rotation parameter, and different types of nanoparticles are studied graphically.

1. Introduction

Fluids exhibiting good thermal conductivity properties are a major requirement of many industrial applications involving heat transfer equipment. Typical examples are those of vehicular cooling systems, refrigerants, building services, and conventional industrial processing systems, such as petro-chemical, textile, paper, and food processing plants, to name a few [1–3]. To reduce costs and be energy efficient, the research and industrial community has continuously worked to develop and utilize fluids bearing high thermal conductivity. The concept of nanofluids was introduced in [4] which utilized suspended metallic nanoparticles (with a typical size of 100 Å) in conventional heat transfer fluids such as water or engine oil. Since metallic solids reflect heat conductivity of orders greater than conventional heat transfer fluids, this engineered form of fluids was received quite well by the industrial and research community. A comparison can be made on the basis of silver, 429 W/(m K); water, 0.613 W/(m K); and engine oil, 0.145 W/(m K) at 300 k; and liquid sodium, 89.44 W/(m K) at 371 k. Moreover, since the surface area to volume ratio is inversely proportional to the radius of a particle, suspended metals of nanometer scales would give better heat conductivity as compared to micrometer-sized particles.

Since the convective heat transfer coefficient is derived from continuity, momentum, and energy equations, its behaviour is significantly dependent on the velocity and temperature profile of the nanofluid's base fluid [1, 5]. Moreover, the heat and momentum transfer mechanisms are essentially the same and hence can be comparable on the basis of analogies. For instance, Reynold's analogy is applicable towards turbulent flows, Prandtl's analogy for laminar flows, von Korman's analogy for both laminar and turbulent flows with a buffer layer in between, and Chilton–Colburn analogy for transport independent flows [6]. The velocity is also dependent on the concentration of nanoparticles in a nanofluid such that a higher concentration may result in a flattening of the velocity profile [7]. Studies have also shown that the velocity profile is not uniform. For instance, near-wall velocity profile measurements have shown increased velocity gradient, with no slip, relative to the equivalent base fluid [8]. As such, the investigation of the velocity profile under different boundary conditions and flow models is of particular interest to the research community.

With this, a considerable volume of literature started to address the behaviour of nanofluids in context of different boundary conditions (convective [9], porous medium [10, 11]), characterization parameters of different fluids and suspended metals (Cu/Cu-TiO$_2$ [12, 13], Cu-H$_2$O/Cu-Kerosene [14]), and thermodynamic [15, 16] and magnetohydrodynamic [17–19] properties using analytical and/or numerical approaches. A comprehensive review of these aspects in general is presented in [1, 3, 20].

The study of squeezing flows that is normal to two parallel plates is an important problem in the area of fluid dynamics, having applications in hydraulic machinery, electric motors, food industry, bioengineering, and automobile engines, amongst others. The mechanics of these studies in context of turbulent, laminar, and transitional flows, and different non-Newtonian fluid models (e.g., power law [21], grade 2/3 [22], and Casson [23, 24]) have proved to be a significant challenge to the research community due to the involved nonlinearities. The squeezing flow response in context of parallel plates appears in [13, 25, 26], parallel moving plates are given in [27–29], orthogonal moving plates are discussed in [10], moving surface in [30], stretching surface in [31–33], and stretching cylinders are given in [34]. Likewise, the response to Casson flow is discussed in [16, 19, 32, 34], Hiemenz flow in [35], and bioconvection flows in [19, 36]. The studies have also been extended to nanofluids [1, 17, 25, 36, 37]. In [38], Naz et al. solved analytically the problem of variable thermophysical features of the three-dimensional flow of a non-Newtonian yield manifesting liquid with heat and mass transport in the presence of gyrotactic microorganisms over a nonlinear stretched surface. They utilized the boundary-layer theory to develop the governing partial differential equations. They concluded that the mounting values of the fluid parameter and magnetic parameter retard the fluid flow. Moreover [39], Ahmed et al. investigated analytically the problem of Jeffery–Hamel flow for second-grade fluid between two

nonparallel walls having a source or a sink at the cusp. Soret and Dufour effects are incorporated in the energy and concentration equations. For solution purposes, the authors used the homotopy analysis method (HAM). Variations in temperature and concentration profiles for varying in grained physical parameters in the flow model are discussed graphically. Also, Nusselt number and the skin friction coefficient along with Sherwood number are extracted numerically and analytically. In [40], Khan et al. investigated viscous incompressible fluid between two nonparallel plane walls, known as Jeffery–Hamel flow, under the influence of thermal radiation. They used the similarity technique to solve for the governing equations. Moreover, the same problem is solved numerically and a comparison between the two methods is conducted that yields a great result. They presented the rates of heat and mass transfer. Furthermore, the effects of the investigated parameters on the flow and heat transfer are discussed and analyzed. Additionally [41], Khan et al. studied analytically by employing similarity technique along with Runge–Kutta and homotopy analysis algorithms the unsteady magnetohydrodynamics flow with heat generation/absorption of H$_2$O saturated by tiny nanosized particles with various shapes over a thin slit. They found out that as the magnetic field increases, the nanofluid temperature increases and the motion decreases. In addition [42], Khan et al. investigated the flow of nanofluid over a curved Riga surface; they studied the impact of the freezing temperature and the diameter of the nanoparticles on the flow field and the heat transfer. They found out that the nanofluid velocity dropped by increasing the flow parameters γ and S, and an abrupt decrement occurred at the surface of the Riga sheet. Also [43], Naz et al. investigated the entropy analysis of 3D flow of Maxwell nanofluid containing gyrotactic microorganism in the presence of homogeneous-heterogeneous reactions with improved heat conduction and mass diffusion models over a stretched surface. They found out that entropy generation increases for higher values of radiation parameter and Brinkman number, whereas the Bejan number is reduced for the higher values of radiation and magnetic parameters.

From a numerical perspective, the various behaviours are explained on the basis of solutions over discrete points distributed throughout the problem domain. Solutions for remaining points are obtained by means of interpolation. For reasons of performance and accuracy, these points appear amidst regular geometries. In context of simpler domains, reduced number of dimensions is sufficient for such studies. However, by considering richer intricacies of involved physics, the simplified problem domain is compromised, giving failed predictions. In such situations, studies on the basis of 3D domain models, even for simpler geometry configurations, are imperative. The common approach in terms of nanofluids is the fourth-order Runge–Kutta family of integration methods [44, 45]. The same is also true from an analytical perspective that takes into account simplified assumptions. The usual approach for boundary value problems is the usage of perturbation

techniques. However, due to assumptions of small or large parameters, this is not sufficient. In this regard, a seminal work that combined these perturbation techniques with homotopy was proposed as the homotopy perturbation method (HPM) in [46–49]. Since its introduction, the method has been applied to different nonlinear equations [50–56]. Specifically, in the case of nanofluids, the method has been applied in [57–60]. Other approximation techniques that have been used for the case of fluid dynamics include the homotopy analysis method (HAM) [61] and optimal homotopy asymptotic method (OHAM) [62].

In this article, we provide a comprehensive description of the three-dimensional squeezing flow of nanofluids, considering a geometry involving a rotating channel. The flow is characterised on the basis of water as base fluid and different suspended nanoparticles. The study is performed on the basis of Navier–Stokes equations using similarity transforms. Both analytical and numerical solutions are obtained using the homotopy perturbation method and Runge–Kutta–Fehlberg scheme. Furthermore, validation of results has been performed by finding the average residual error of the coupled system. After validation, we present characterization of different configurations of nanofluids using parameters such as volume fraction, suction, flow, magnetism, and rotation.

In the remaining part of the paper, Section 2 includes mathematical formulation of the problem. Section 3 presents the basic theory of numerical approach. Section 4 comprises the results and discussion. Finally, conclusion is presented in Section 5.

2. Mathematical Formulation

We consider a 3D rotating incompressible and electrically conducting viscous nanofluid flow between two infinite horizontal plates. The lower plate is positioned at $y = 0$ and is stretched with a velocity $U_0(t) = ax/(1 - \gamma t)$ in x, where a is the stretching rate of the lower plate, and γ is a characteristic constant. The upper plate is at a variable distance $h(t) = \sqrt{\nu_f(1 - \gamma t)/a}$. The fluid is squeezed with a velocity $v_h = \mathrm{d}h/\mathrm{d}t$ in negative y-axis. The angular velocity Ω between the fluid and channel around y is $\Omega = \omega \widehat{J}/(1 - \gamma t)$, where J is the flux. The lower plate intakes the flow with a velocity $-V0/(1 - \gamma t)$. A magnetic field with density $B_0/\sqrt{1 - \gamma}$ is applied along the y-axis. The system is rotating along the y-axis (see Figure 1). These are then introduced to obtain similarity solutions by reducing the governing equations into a system of ordinary differential equations. The governing relation for continuity and momentum of nanofluid flow in the rotating frame of reference is given as follows:

$$\nabla \cdot V = 0, \tag{1}$$

$$\rho_{\mathrm{nf}}\left[\frac{\partial V}{\partial t} + (V \cdot \nabla)V + 2\Omega \times V\right] = \nabla \cdot T + J \times B, \tag{2}$$

where T is the Cauchy stress tensor, J is the magnetic flux, and B is the current density. The abovementioned governing equations can also be described by the following set of Navier–Stokes equations:
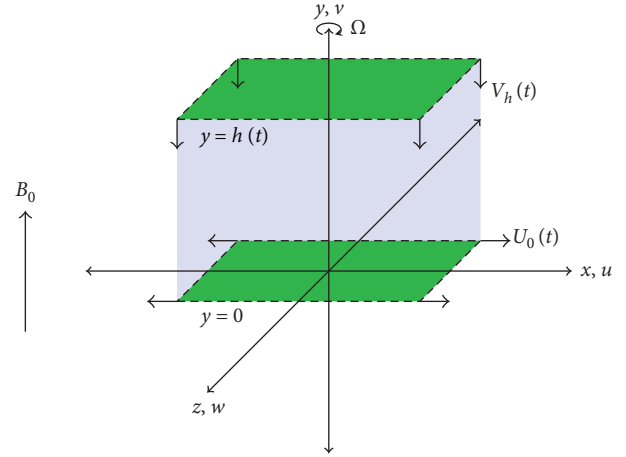
FIGURE 1: Geometry for the problem. A nanofluid is squeezed between two infinite horizontal parallel plates. The lower plate is at position $y = 0$ and stretched with a velocity $U_0(t)$, while the upper plate is at a variable height of $h(t)$. By movement of the upper plate in negative y-axis, the nanofluid is squeezed at a velocity of $v_h(t)$. Ω represents the angular velocity, while B_0 is the magnetic field density applied along y.

$$\frac{\partial u}{\partial x} + \frac{\partial v}{\partial y} = 0,$$

$$\frac{\partial u}{\partial t} + u\frac{\partial u}{\partial x} + v\frac{\partial u}{\partial y} + 2\frac{\omega^2}{1 - \gamma t} = -\frac{1}{\rho_{\mathrm{nf}}}\frac{\partial p}{\partial x} + \nu_{\mathrm{nf}}\left[\frac{\partial^2 u}{\partial x^2}\right.$$
$$\left. + \frac{\partial^2 u}{\partial y^2}\right] - \frac{\sigma B_0^2 u}{\rho_{\mathrm{nf}}(1 - \gamma t)},$$

$$\frac{\partial v}{\partial t} + u\frac{\partial v}{\partial x} + v\frac{\partial v}{\partial y} = -\frac{1}{\rho_{\mathrm{nf}}}\frac{\partial p}{\partial y} + \nu_{\mathrm{nf}}\left[\frac{\partial^2 v}{\partial x^2} + \frac{\partial^2 v}{\partial y^2}\right],$$

$$\frac{\partial w}{\partial t} + u\frac{\partial w}{\partial x} + v\frac{\partial w}{\partial y} - 2\frac{\omega u}{1 - \gamma t} = \nu_{\mathrm{nf}}\left[\frac{\partial^2 w}{\partial x^2} + \frac{\partial^2 w}{\partial y^2}\right]$$
$$- \frac{\sigma B_0^2 w}{\rho_{\mathrm{nf}}(1 - \gamma t)},$$

$$\tag{3}$$

where ρ_{nf} is the nanofluid density, $\nu_{\mathrm{nf}} = \mu_{\mathrm{nf}}/\rho_{\mathrm{nf}}$ is the nanofluid kinematic viscosity, σ is the electrical conductivity, B_0 is the magnetic field, and γ is a characteristic parameter representing inverse time, and $\gamma t < 1$. The constants for the model are given as

$$\mu_{\mathrm{nf}} = \frac{\mu_f}{(1 - \phi)^{2.5}},$$

$$\rho_{\mathrm{nf}} = (1 - \phi)\rho_f + \phi\rho_s, \tag{4}$$

where μ_f is the fluid fraction viscosity, ϕ is the nanoparticle volume fraction, and ρ_f and ρ_s are the densities of the fluid and of solid fractions. The thermophysical properties of different materials are given in Table 1 for reference. The boundary conditions at $y = 0$ are given as

TABLE 1: Thermophysical property for the base fluid, along with other nanoparticles.

Material	$\rho \, (\text{kg/m}^3)$
Water, H_2O	997.1
Silver, Ag	10500
Copper oxide, CuO	6320
Silicon, Si	2330
Gold, Au	19300
Aluminium oxide, Al_2O_3	3970
Copper, Cu	8933
Platinum, Pt	21450
Titanium dioxide, TiO_2	4250

$$u(x, y, t) = U_0 = \frac{ax}{1 - \gamma t},$$

$$v(x, y, t) = -\frac{V_0}{1 - \gamma t}, \tag{5}$$

$$w(x, y, t) = 0.$$

While for $y = h(t)$, are given as

$$u(x, y, t) = 0,$$

$$v(x, y, t) = V_h = \frac{dh}{dt} = \frac{-\gamma}{2} \sqrt{\frac{\nu_f}{a(1 - \gamma t)}}, \tag{6}$$

$$w(x, y, t) = 0,$$

where a is the stretching rate of the lower plate. The governing equations subject to similarity transformation in order to give ordinary differential equations in terms of a stream function ψ are given as

$$\psi = \sqrt{\frac{a\nu_f}{1 - \gamma t}} x f(\eta),$$

$$\eta = \frac{y}{h(t)},$$

$$u = \frac{\partial \psi}{\partial y} = U_0 f'(\eta), \tag{7}$$

$$v = -\frac{\partial \psi}{\partial x} = -\sqrt{\frac{a\nu_f}{1 - \gamma t}} f(\eta),$$

$$w = U_0 g(\eta).$$

Substitution of these similarity transforms to the governing Navier–Stokes equations, we have

$$\frac{\partial^3 f}{\partial \eta^3} + \frac{\nu_f}{\nu_{\text{nf}}} \left(f \frac{\partial^2 f}{\partial \eta^2} - \left(\frac{\partial f}{\partial \eta} \right)^2 - \beta \left(\frac{\partial f}{\partial \eta} + 0.5\eta \frac{\partial^2 f}{\partial \eta^2} \right) \right.$$

$$\left. - 2\Omega g - \frac{\rho_f}{\rho_{\text{nf}}} M^2 \frac{\partial f}{\partial \eta} \right) = \frac{(1 - \gamma t)^2 \nu_f}{\rho_{\text{nf}} a^2 x \nu_{\text{nf}}} \frac{\partial p}{\partial x},$$

$$-\frac{\partial^2 f}{\partial \eta^2} + \frac{\nu_f}{\nu_{\text{nf}}} \left(-f \frac{\partial f}{\partial \eta} + 0.5\beta \left(f + \eta \frac{\partial f}{\partial \eta} \right) \right) = \frac{1 - \gamma t}{\rho_{\text{nf}} a \nu_{\text{nf}}} \partial p \, \eta,$$

$$\frac{\partial^2 g}{\partial \eta^2} + \frac{\nu_f}{\nu_{\text{nf}}} \left(f \frac{\partial g}{\partial \eta} - \frac{\partial f}{\partial \eta} g - \beta \left(g + 0.5\eta \frac{\partial g}{\partial \eta} \right) + 2\Omega \frac{\partial f}{\partial \eta} \right)$$

$$- \frac{\mu_f}{\mu_{\text{nf}}} M^2 g = 0, \tag{8}$$

where $\beta = \gamma/a$ is the characteristic parameter of the flow, $\Omega = w/a$ is the rotation parameter, $M^2 = \sigma B_0^2 / \rho_f a$ is the magnetic parameter, and prime denotes differentiation with respect to η. To squeeze the flow, we take $\beta > 0$ for which the upper plates move downward with a velocity of $V_h < 0$, whereas for $\beta < 0$, the upper plate moves upwards with respect to the plane $y = 0$. $\beta = 0$ corresponds to a steady state. To reduce the number of independent variables as well as retain the similarity solution, the above are simplified by cross-differentiation, giving us

$$f^{iv} - \left(1 - \phi + \frac{\phi \rho_s}{\rho_f} \right)(1 - \phi)^{2.5} \times \left(f'f'' - ff''' + 2\Omega g' \right.$$

$$\left. + 0.5\beta \left(3f'' + \eta f''' \right) \right) - (1 - \phi)^{2.5} M^2 f'' = 0,$$

$$g'' + \left(1 - \phi + \frac{\phi \rho_s}{\rho_f} \right)(1 - \phi)^{2.5} \times \left(fg' - f'g - \beta (g + 0.5\eta g') \right.$$

$$\left. + 2\Omega f' \right) - (1 - \phi)^{2.5} M^2 g = 0. \tag{9}$$

Moreover, the transformed boundary conditions take the form:

$$\begin{aligned} f(0) &= w_0, \\ f'(0) &= 1, \\ g(0) &= 0, \\ f(1) &= 0.5\beta, \\ f'(1) &= 0, \\ g(1) &= 0, \end{aligned} \tag{10}$$

where $w_0 = V_0 / ah$ is the suction parameter. For this problem, the physical quantity of interest is the skin friction coefficient C_f along the wall at the lower and upper walls, defined as

$$C_{f,\text{lower}} = \frac{\mu_{\text{nf}} \left(\partial u/\partial y\right)_{y=0}}{\rho_{\text{nf}} U_0^2},$$

$$C_{f,\text{upper}} = \frac{\mu_{\text{nf}} \left(\partial u/\partial y\right)_{y=h(t)}}{\rho_{\text{nf}} U_0^2}. \qquad (11)$$

Substituting stream function to the abovementioned, we obtain

$$\overline{C}_{f,\text{lower}} = C_{f,\text{lower}} \text{Re}_x = \frac{f''(0)}{\left(1 - \phi + \phi \rho_s/\rho_f\right)\left(1 - \phi\right)^{2.5}},$$

$$\overline{C}_{f,\text{upper}} = C_{f,\text{upper}} \text{Re}_x = \frac{f''(1)}{\left(1 - \phi + \phi \rho_s/\rho_f\right)\left(1 - \phi\right)^{2.5}}, \qquad (12)$$

where $\text{Re}_x = \rho_f U_0 h/\mu_f$ is the local Reynolds number.

3. Basic Theory of Homotopy Perturbation Method

The basic theory of HPM can be exhibited using the following differential equation:

$$L(f) + N(f) - g(r) = 0, \quad r \in \Omega,$$

$$B\left(f, \frac{df}{dn}\right) = 0, \quad r \in \Upsilon, \qquad (13)$$

where Υ is the boundary of the domain Ω, and f is unknown and $g(r)$ is a known function. L, N, B are linear, nonlinear, and boundary operators, respectively. We construct a homotopy $\theta(r, p): \Omega \times [0, 1] \longrightarrow R$ which satisfies

$$\Psi(\theta, q) = (1 - q)[L(\theta) - L(f_0)] + q[L(\theta) + N(\theta) - g(r)] = 0,$$

$$r \in \Omega, \qquad (14)$$

where $q \in [0, 1]$ is an embedding parameter, and f_0 is the initial guess of (13) that satisfies the boundary conditions. From (14), we have

$$\Psi(\theta, 0) = L(\theta) - L(f_0) = 0,$$

$$\Psi(\theta, 1) = L(\theta) + N(\theta) - g(r) = 0. \qquad (15)$$

Thus, as q varies from 0 to 1, the solution $\theta(r, q)$ approaches from $f_0(r)$ to $\widetilde{f}(r)$. To obtain an approximate solution, we expand $\theta(r, q)$ in a Taylor series about q as follows:

$$\theta(r, q) = \theta_0 + \sum_{k=1}^{\infty} \theta_k q^k. \qquad (16)$$

Setting $q = 1$, the approximate solution of (13) would be

$$\widetilde{U} = \lim_{q \longrightarrow 1} \theta(r, q) = \sum_{k=1}^{\infty} \theta_k. \qquad (17)$$

Substituting equation (17) in equation (13) will give

$$R(x) = L[\widetilde{U}(x)] + N[\widetilde{U}(x)] - g(x). \qquad (18)$$

If R is approaching zero, $\widetilde{U}$ will then approach towards the exact solution.

4. Results and Discussion

In this article, an unsteady three-dimensional squeezing flow of electrically conducting nanofluid between two infinite horizontal planes in a rotating channel is considered. The composition of the nanofluid is made on the basis of different nanoparticles, including Silicon (Si), Copper (Cu), Silver (Ag), Gold (Au), and Platinum (Pt). These nanofluids with silicon composition are used for observing the effect of various parameters on the velocity profile. These parameters include the nanoparticle volume fraction ϕ, suction parameter w_0, characteristic parameter of the flow β, rotation parameter Ω, and magnetic parameter M. The formulated boundary value system described in Section 2 for these parameters is solved using HPM, which is then compared with numerical solutions obtained using the Runge–Kutta–Fehlberg method for validation purposes. A graphical representation for this validation is given in Figure 2, showing good agreement.

A detailed analysis of this validation is performed through residual errors, for $\phi = 0.9$, $w_0 = 0.5$, $\Omega = 1$, $\beta = 1$, and $M = 1$ in Tables 2 and 3 for both the HPM and RK45 methods individually. Validation with a variation of $\beta = 2$ is given in Tables 4 and 5. In both cases, the results from HPM-based solution are consistent and in good agreement with the numerical results. A comparative analysis on the basis of $\beta = (1, 2)$ using both HPM and RK45 is given in Table 6. The effect of the skin friction coefficient at both lower and upper walls is also given in Table 7.

After validation of the solutions, the behaviour response of nanofluids against various parameters is investigated. In all these investigations, $0 < \eta < 0.5$ corresponds to the lower half, while $0.5 < \eta < 1$ represents the upper half of the channel.

The effect of nanoparticle volume fraction ϕ on normal, axial, and transverse velocity components is given in Figure 3. Here, the static parameters are $w_0 = 0.5$, $\beta = 1$, $\Omega = 1$, and $M = 0.5$, while the variational parameter $\phi \varepsilon [0, 1]$. The general observation is that ϕ increases with respect to normal velocity. The axial velocity profile increases with an increase in the nanoparticle volume fraction in the lower half of the channel, while it decreases in the upper half. The transverse velocity decreases in the vicinity of lower surface, $(0 < \eta < 0.25)$, when the nanoparticle volume fraction increases. But other than that, an opposite trend has been observed in the rest of the channel $(0.25 < \eta < 1)$. These behaviours are justified because viscosity increases by increasing the nanomaterial volume fraction; as a result, the enhanced frictional force leads to the flow resistance.

The response of suction parameter (w_0) on the velocity profile is given in Figure 4, where it can be observed that the observable range of w_0 is at a maximum in the lower channel. The overall trend is similar to an exponential increase in this region. However, w_0 gets confined rapidly around the midpoint as η and w_0 approach 1. In the case of the axial velocity, it stands at maximum close to the lower wall at $\eta = 0$ and at the midpoint close to the upper wall at $\eta = 1$. In other cases, it decreases significantly as w_0

(a)

(b)
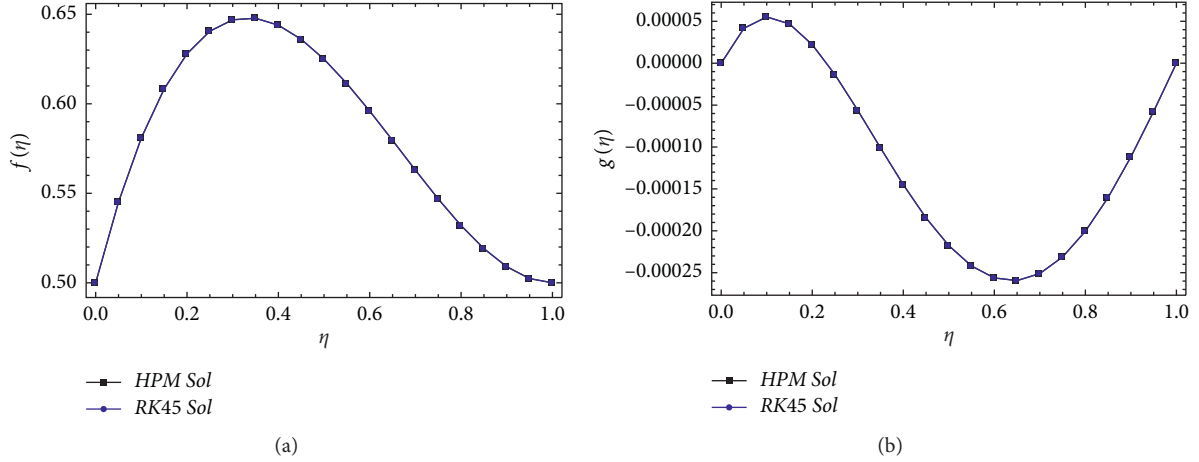
FIGURE 2: Comparison of analytical and numerical solutions. (a) Comparison of $f(\eta)$. (b) Comparison of $g(\eta)$.

TABLE 2: Homotopy-based solution along with residual errors when $\phi = 0.9$, $w_0 = 0.5$, $\Omega = 1$, $\beta = 1$, and $M = 1$.

η	f_{HPM}	g_{HPM}	Abs error equation (1)	Abs error equation (2)	Average Abs error
0.	0.5	0	8.306×10^{-8}	2.504×10^{-9}	4.278×10^{-8}
0.05	0.545121	0.0000417402	4.570×10^{-8}	2.524×10^{-9}	2.411×10^{-8}
0.10	0.580987	0.0000553098	1.937×10^{-8}	1.525×10^{-9}	1.045×10^{-8}
0.15	0.60835	0.0000468996	1.493×10^{-9}	4.431×10^{-11}	7.686×10^{-10}
0.20	0.627961	0.0000221747	9.986×10^{-9}	1.509×10^{-9}	5.748×10^{-9}
0.25	0.640574	−0.0000137254	1.662×10^{-8}	2.844×10^{-9}	9.735×10^{-9}
0.30	0.646938	−0.0000561855	1.962×10^{-8}	3.778×10^{-9}	1.170×10^{-8}
0.35	0.647805	−0.000101115	1.990×10^{-8}	4.223×10^{-9}	1.206×10^{-8}
0.40	0.643925	−0.000144946	1.817×10^{-8}	4.170×10^{-9}	1.117×10^{-8}
0.45	0.636048	−0.000184635	1.500×10^{-8}	3.672×10^{-9}	9.341×10^{-9}
0.50	0.624925	−0.000217661	1.088×10^{-8}	2.828×10^{-9}	6.859×10^{-9}
0.55	0.611304	−0.000242025	6.239×10^{-9}	1.763×10^{-9}	4.001×10^{-9}
0.60	0.595936	−0.00025625	1.448×10^{-9}	6.138×10^{-10}	1.031×10^{-9}
0.65	0.57957	−0.000259381	3.111×10^{-9}	4.837×10^{-10}	1.797×10^{-9}
0.70	0.562955	−0.000250985	7.086×10^{-9}	1.408×10^{-9}	4.247×10^{-9}
0.75	0.546841	−0.000231151	1.014×10^{-8}	2.061×10^{-9}	6.105×10^{-9}
0.80	0.531976	−0.000200489	1.199×10^{-8}	2.375×10^{-9}	7.187×10^{-9}
0.85	0.519111	−0.000160129	1.239×10^{-8}	2.313×10^{-9}	7.352×10^{-9}
0.90	0.508993	−0.000111724	1.114×10^{-8}	1.873×10^{-9}	6.508×10^{-9}
0.95	0.502373	−0.0000574492	8.143×10^{-9}	1.083×10^{-9}	4.613×10^{-9}
1.	0.5	2.7×10^{-21}	3.371×10^{-9}	1.180×10^{-19}	1.685×10^{-9}

increases. This results in a reverse flow due to discharge of a large amount of fluid particles in the vicinity of the lower wall, while on the upper wall, it becomes much more noticeable. In the case of the traverse component of velocity profile, there is almost no change as the maximum range of the velocity profile stands at 0.002. In this case, the velocity is nonexistent at both walls. In all these cases, the static parameters are $\phi = 0.9$, $\beta = 1$, $\Omega = 1$, and $M = 0.5$, while the variable parameter $w_0 \varepsilon [0, 1]$.

The effect of magnetic parameter M on the velocity profile is shown in Figure 5. Here, the static parameters are $\phi = 0.2$, $w_0 = 0.5$, $\beta = 1$, and $\Omega = 1$, while the variable parameters are $M \varepsilon [0, 0.6]$. In these cases, the normal velocity presents a tailed parabolic behaviour, as M is increased, where in the region in vicinity of lower plate shows an increased flow, but a decreased flow a little before the channel midpoint. The axial velocity component also has

dual behaviour, where it decreases with an increase in M in the lower channel, while showing an increasing behaviour in the upper channel. In the transverse component, the velocity component is zero at both the upper and lower walls, whereas at the center of the channel, the maximum range for different M stands at 0.04. But in general, a positive transverse velocity component is only observable if $M > 0.5$. The reason behind these behaviours is that application of magnetic field to an electrically conducting fluid gives rise to a resistive type force called the Lorentz force. This force has the tendency to slow down the motion of the fluid.

The effect of characteristic parameter β on the velocity profile, while the static parameters are $\phi = 0.9$, $w_0 = 0.5$, $\Omega = 1$, and $M = 0.5$ and while β varies in the interval $[-2.5, 2.5]$, is presented in Figures 6 and 7. Positive values of β representing movement of the upper plate towards the lower plate, all three velocity components, demonstrate an

TABLE 3: RK45 solution along with residual errors when $\phi = 0.9$, $w_0 = 0.5$, $\Omega = 1$, $\beta = 1$, and $M = 1$.

η	f_{RK45}	g_{RK45}	Error equation (1)	Error equation (2)	Average Abs error
0.	0.5	0	4.353×10^{-4}	1.868×10^{-8}	2.176×10^{-4}
0.05	0.545121	0.0000417403	2.140×10^{-4}	5.805×10^{-9}	1.070×10^{-4}
0.10	0.580987	0.0000553099	9.222×10^{-5}	8.619×10^{-10}	4.611×10^{-5}
0.15	0.60835	0.0000468997	3.185×10^{-5}	5.766×10^{-10}	1.592×10^{-5}
0.20	0.627961	0.0000221748	6.477×10^{-6}	7.509×10^{-10}	3.239×10^{-6}
0.25	0.640574	-0.0000137252	1.205×10^{-6}	6.336×10^{-10}	6.032×10^{-7}
0.30	0.646938	-0.0000561853	1.634×10^{-6}	5.402×10^{-10}	8.173×10^{-7}
0.35	0.647805	-0.000101115	3.276×10^{-7}	5.064×10^{-10}	1.640×10^{-7}
0.40	0.643925	-0.000144946	4.547×10^{-7}	4.915×10^{-10}	2.276×10^{-7}
0.45	0.636048	-0.000184635	3.610×10^{-7}	4.672×10^{-10}	1.807×10^{-7}
0.50	0.624925	-0.000217661	1.067×10^{-7}	4.345×10^{-10}	5.361×10^{-8}
0.55	0.611304	-0.000242025	3.463×10^{-7}	4.088×10^{-10}	1.733×10^{-7}
0.60	0.595936	-0.000256249	1.062×10^{-7}	3.986×10^{-10}	5.332×10^{-8}
0.65	0.57957	-0.000259381	3.624×10^{-7}	3.962×10^{-10}	1.814×10^{-7}
0.70	0.562955	-0.000250985	4.570×10^{-7}	3.857×10^{-10}	2.287×10^{-7}
0.75	0.546841	-0.000231151	3.247×10^{-7}	3.646×10^{-10}	1.625×10^{-7}
0.80	0.531976	-0.000200489	1.631×10^{-6}	3.611×10^{-10}	8.160×10^{-7}
0.85	0.519111	-0.000160129	1.203×10^{-6}	4.189×10^{-10}	6.019×10^{-7}
0.90	0.508993	-0.000111724	6.485×10^{-6}	5.075×10^{-10}	3.243×10^{-6}
0.95	0.502373	-0.0000574492	3.188×10^{-5}	3.023×10^{-10}	1.594×10^{-5}
1.	0.5	2.9×10^{-12}	9.233×10^{-5}	1.233×10^{-9}	4.616×10^{-5}

TABLE 4: Homotopy-based solution along with residual errors when $\phi = 0.9$, $w_0 = 0.5$, $\Omega = 1$, $\beta = 2$, and $M = 1$.

η	f_{HPM}	g_{HPM}	Error equation (1)	Error equation (2)	Average Abs error
0.	0.5	0	4.793×10^{-8}	1.700×10^{-8}	3.247×10^{-8}
0.05	0.548747	0.00021484	4.773×10^{-8}	1.224×10^{-8}	2.998×10^{-8}
0.10	0.594991	0.000396569	4.876×10^{-8}	5.672×10^{-9}	2.721×10^{-8}
0.15	0.638731	0.000546947	4.997×10^{-8}	1.859×10^{-9}	2.591×10^{-8}
0.20	0.67997	0.000667732	5.049×10^{-8}	9.659×10^{-9}	3.007×10^{-8}
0.25	0.718709	0.000760677	4.966×10^{-8}	1.716×10^{-8}	3.341×10^{-8}
0.30	0.754949	0.000827534	4.701×10^{-8}	2.394×10^{-8}	3.548×10^{-8}
0.35	0.78869	0.00087005	4.224×10^{-8}	2.967×10^{-8}	3.595×10^{-8}
0.40	0.819934	0.000889971	3.521×10^{-8}	3.413×10^{-8}	3.467×10^{-8}
0.45	0.84868	0.000889042	2.596×10^{-8}	3.719×10^{-8}	3.157×10^{-8}
0.50	0.874928	0.000869003	1.467×10^{-8}	3.882×10^{-8}	2.674×10^{-8}
0.55	0.89868	0.000831597	1.677×10^{-9}	3.905×10^{-8}	2.036×10^{-8}
0.60	0.919934	0.00077856	1.255×10^{-8}	3.795×10^{-8}	2.525×10^{-8}
0.65	0.938691	0.000711631	2.741×10^{-8}	3.565×10^{-8}	3.153×10^{-8}
0.70	0.95495	0.000632547	4.219×10^{-8}	3.233×10^{-8}	3.726×10^{-8}
0.75	0.96871	0.000543044	5.605×10^{-8}	2.815×10^{-8}	4.210×10^{-8}
0.80	0.979971	0.000444857	6.805×10^{-8}	2.329×10^{-8}	4.567×10^{-8}
0.85	0.988732	0.000339724	7.716×10^{-8}	1.793×10^{-8}	4.755×10^{-8}
0.90	0.994991	0.000229378	8.228×10^{-8}	1.221×10^{-8}	4.724×10^{-8}
0.95	0.998747	0.000115558	8.220×10^{-8}	6.221×10^{-9}	4.421×10^{-8}
1.	1.	1.1×10^{-18}	7.567×10^{-8}	3.715×10^{-20}	3.783×10^{-8}

increase (see Figure 6). On the contrary, the inverse movement is represented by the negative β values; all velocity components record a decrease as β is decreased (see Figure 7).

Effect of rotational parameter Ω on the velocity profile is depicted in Figure 8. For Ω, the normal velocity decreases as Ω is increased. The axial velocity shows a dual behaviour. In the lower part of the channel, there is a small decrease in the velocity as Ω is increased, whereas in the upper part of the channel, there is a small increase as Ω is increased. An inverse dual behaviour to the axial component is reflected in the transverse component. Here, there is small increase in velocity as Ω is increased in the lower quarter of the channel, whereas in the remaining three quarters, there is a major reversal of velocity as Ω is increased. Here, the static parameters are $\phi = 0.2$, $w_0 = 0.5$, $\beta = 1$, and $M = 0.5$, while the variational parameter is $\Omega = [3, 12]$. The transverse velocity component shows a similar behaviour in the case of increased nanoparticle volume fraction ϕ and the rotation parameter Ω. Magnitudes of these velocities are found to decease within the rotating channel with augmentation. One of the forces encountered in fluid flow with a rotating

TABLE 5: RK45 solution along with residual errors when $\phi = 0.9$, $w_0 = 0.5$, $\Omega = 1$, $\beta = 2$, and $M = 1$.

η	f_{RK45}	g_{RK45}	Error equation (1)	Error equation (2)	Average Abs error
0.	0.5	0	1.501×10^{-6}	5.984×10^{-10}	7.510×10^{-7}
0.05	0.548747	0.00021484	3.007×10^{-7}	2.663×10^{-10}	1.504×10^{-7}
0.10	0.594991	0.00039657	1.054×10^{-7}	7.585×10^{-11}	5.276×10^{-8}
0.15	0.638731	0.000546948	1.480×10^{-7}	4.817×10^{-12}	7.401×10^{-8}
0.20	0.67997	0.000667734	7.506×10^{-8}	2.357×10^{-11}	3.754×10^{-8}
0.25	0.718709	0.000760679	6.392×10^{-9}	1.921×10^{-11}	3.205×10^{-9}
0.30	0.754949	0.000827536	2.043×10^{-8}	1.337×10^{-11}	1.022×10^{-8}
0.35	0.78869	0.000870053	1.291×10^{-8}	1.253×10^{-11}	6.464×10^{-9}
0.40	0.819934	0.000889974	4.944×10^{-9}	1.454×10^{-11}	2.479×10^{-9}
0.45	0.84868	0.000889045	1.240×10^{-8}	1.537×10^{-11}	6.208×10^{-9}
0.50	0.874928	0.000869007	3.028×10^{-9}	1.366×10^{-11}	1.521×10^{-9}
0.55	0.89868	0.0008316	1.297×10^{-8}	1.152×10^{-11}	6.493×10^{-9}
0.60	0.919934	0.000778563	1.521×10^{-8}	1.208×10^{-11}	7.613×10^{-9}
0.65	0.938691	0.000711634	1.173×10^{-8}	1.533×10^{-11}	5.876×10^{-9}
0.70	0.95495	0.00063255	5.443×10^{-8}	1.557×10^{-11}	2.722×10^{-8}
0.75	0.96871	0.000543046	3.789×10^{-8}	5.230×10^{-12}	1.895×10^{-8}
0.80	0.979971	0.00044486	2.157×10^{-7}	8.678×10^{-12}	1.078×10^{-7}
0.85	0.988732	0.000339725	1.037×10^{-6}	3.236×10^{-11}	5.186×10^{-7}
0.90	0.994991	0.00022938	2.969×10^{-6}	3.052×10^{-10}	1.484×10^{-6}
0.95	0.998747	0.000115559	6.834×10^{-6}	1.212×10^{-9}	3.417×10^{-6}
1.	1.	1.2×10^{-14}	1.380×10^{-5}	3.545×10^{-9}	6.906×10^{-6}

TABLE 6: Similarity between HPM and RK45 solutions when $\phi = 0.9$, $w_0 = 0.5$, $\Omega = 1$, and $M = 1$.

η	$\beta = 1$			$\beta = 2$		
	$|f_{HPM} - f_{RK45}|$	$|g_{HPM} - g_{RK45}|$	System similarity	$|f_{HPM} - f_{RK45}|$	$|g_{HPM} - g_{RK45}|$	System similarity
0.	0	0	0	0	0	0
0.05	2.412×10^{-10}	1.637×10^{-11}	1.288×10^{-10}	3.539×10^{-11}	4.298×10^{-10}	7.606×10^{-21}
0.10	4.490×10^{-10}	5.474×10^{-11}	2.519×10^{-10}	5.962×10^{-11}	8.905×10^{-10}	2.654×10^{-20}
0.15	1.175×10^{-9}	9.915×10^{-11}	6.374×10^{-10}	7.397×10^{-11}	1.365×10^{-9}	5.050×10^{-20}
0.20	1.683×10^{-9}	1.420×10^{-10}	9.128×10^{-10}	7.972×10^{-11}	1.835×10^{-9}	7.316×10^{-20}
0.25	1.953×10^{-9}	1.790×10^{-10}	1.066×10^{-9}	7.861×10^{-11}	2.281×10^{-9}	8.968×10^{-20}
0.30	2.024×10^{-9}	2.074×10^{-10}	1.116×10^{-9}	7.257×10^{-11}	2.684×10^{-9}	9.741×10^{-20}
0.35	1.936×10^{-9}	2.250×10^{-10}	1.080×10^{-9}	6.328×10^{-11}	3.028×10^{-9}	9.583×10^{-20}
0.40	1.720×10^{-9}	2.310×10^{-10}	9.757×10^{-10}	5.206×10^{-11}	3.298×10^{-9}	8.587×10^{-20}
0.45	1.404×10^{-9}	2.257×10^{-10}	8.151×10^{-10}	3.989×10^{-11}	3.483×10^{-9}	6.948×10^{-20}
0.50	1.019×10^{-9}	2.103×10^{-10}	6.151×10^{-10}	2.755×10^{-11}	3.575×10^{-9}	4.926×10^{-20}
0.55	5.990×10^{-10}	1.871×10^{-10}	3.930×10^{-10}	1.572×10^{-11}	3.571×10^{-9}	2.807×10^{-20}
0.60	1.741×10^{-10}	1.588×10^{-10}	1.664×10^{-10}	4.997×10^{-12}	3.469×10^{-9}	8.670×10^{-21}
0.65	2.241×10^{-10}	1.282×10^{-10}	1.761×10^{-10}	4.088×10^{-12}	3.274×10^{-9}	6.693×10^{-21}
0.70	5.655×10^{-10}	9.813×10^{-11}	3.318×10^{-10}	1.099×10^{-11}	2.989×10^{-9}	1.643×10^{-20}
0.75	8.180×10^{-10}	7.073×10^{-11}	4.443×10^{-10}	1.492×10^{-11}	2.624×10^{-9}	1.958×10^{-20}
0.80	9.476×10^{-10}	4.764×10^{-11}	4.976×10^{-10}	1.452×10^{-11}	2.188×10^{-9}	1.589×10^{-20}
0.85	9.231×10^{-10}	2.953×10^{-11}	4.763×10^{-10}	8.116×10^{-12}	1.695×10^{-9}	6.881×10^{-21}
0.90	7.216×10^{-10}	1.600×10^{-11}	3.688×10^{-10}	4.466×10^{-12}	1.157×10^{-9}	2.585×10^{-21}
0.95	3.203×10^{-10}	5.652×10^{-12}	1.630×10^{-10}	1.623×10^{-11}	5.881×10^{-10}	4.773×10^{-21}
1.	3.622×10^{-10}	2.910×10^{-12}	1.825×10^{-10}	1.214×10^{-13}	1.263×10^{-14}	7.673×10^{-28}

channel is the Coriolis force which acts in a direction perpendicular to the rotational axis and the velocity of the body in the rotating frame. This is due to the fact that the rotation of the channel leads to resist the flow.

The behaviour of velocity profiles against different nanofluid composition is given in Figure 9. In general, the nanofluids having greater density of nanoparticles per unit area are affecting the velocity profiles significantly, where larger densities showed a decrease in normal velocity as compared to smaller densities. For a similar volume fraction of $\phi = 0.2$, Si-based nanoparticles with $\rho = 2330 \, \text{kg/m}^3$, i.e. the minimum most in the chosen group, reflected maximum normal velocity. In contrast, Pt having $\rho = 21450 \, \text{kg/m}^3$ as the highest density in the chosen group showed the minimum normal velocity. In the case of axial component, there is a dual behaviour, with high densities having a lower velocity in lower channel, and an increased velocity in the upper channel. However, the variation in velocity with

TABLE 7: Skin friction coefficient for various values of parameters at lower and upper walls.

ϕ	w_0	M	β	Ω	$C_{f,\text{lower}}$	$C_{f,\text{upper}}$
0.9	0.5	0.5	1.0	1.0	−0.00574602	0.00286874
0.6					−22.3924	10.7677
0.3					−7.4334	3.28618
0.0					−4.48572	1.80803
0.9	0.0				−143.722	−143.706
	0.1				−229.876	−57.5714
	0.2				−316.041	28.5537
	0.3				−402.217	114.67
	0.6				−660.81	372.963
	0.9				−919.501	631.173
0.2	0.5	0.0			−5.96224	2.56784
		1.0			−6.06434	2.54659
		2.0			−6.36118	2.48844
		4.0			−7.40657	2.33973
		6.0			−8.64416	2.39013
0.9		0.5			−574.602	286.874
			1.5		−359.247	71.5441
			2.0		−143.847	−143.831
			2.5		71.5972	−359.25
			−1.0		−1435.58	1147.75
			−1.5		−1650.71	1362.85
			−2.0		−1865.79	1577.92
			−2.5		−2080.84	1792.93
0.2			1.0	0.5	−5.9823	2.56287
				1.0	−5.98791	2.56244
				3.0	−6.04779	2.55783
				5.0	−6.16755	2.54862
				7.0	−6.3472	2.5348
				9.0	−6.58672	2.51637
				12.0	−7.05828	2.4801

(a)

(b)

FIGURE 3: Continued.

(c)
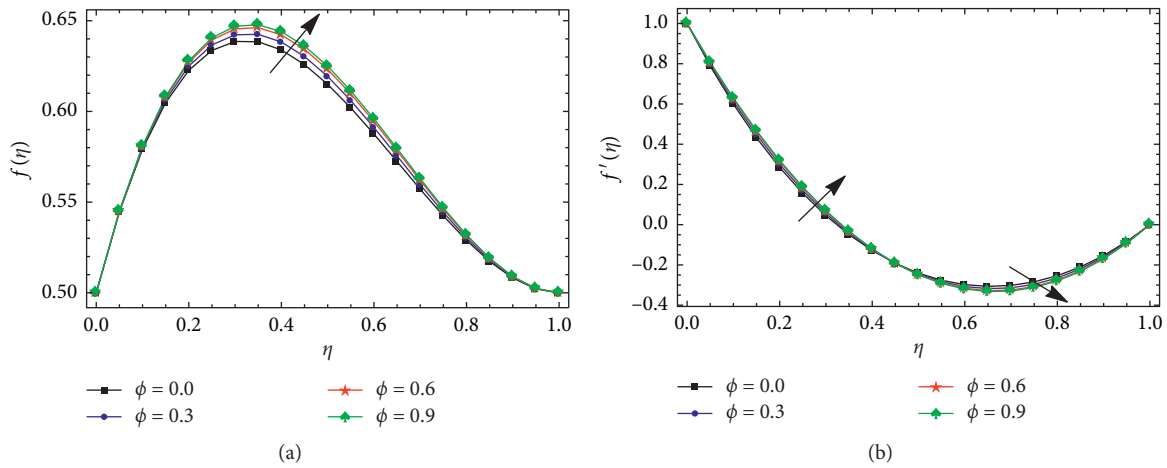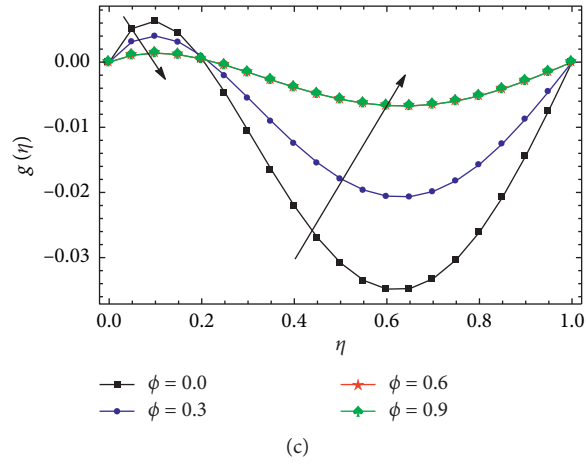
Figure 3: Effect of nanoparticle volume fraction ϕ on the velocity profile when $w_0 = 0.5$, $\beta = 1$, $\Omega = 1$, and $M = 0.5$. (a) Normal component of velocity. (b) Axial component of velocity. (c) Transverse component of velocity.

(a)

(b)

(c)

Figure 4: Effect of suction parameter w_0 on the velocity profile when $\phi = 0.9$, $\beta = 1$, $\Omega = 1$, and $M = 0.5$. (a) Normal component of velocity. (b) Axial component of velocity. (c) Transverse component of velocity.

(a)

(b)

(c)
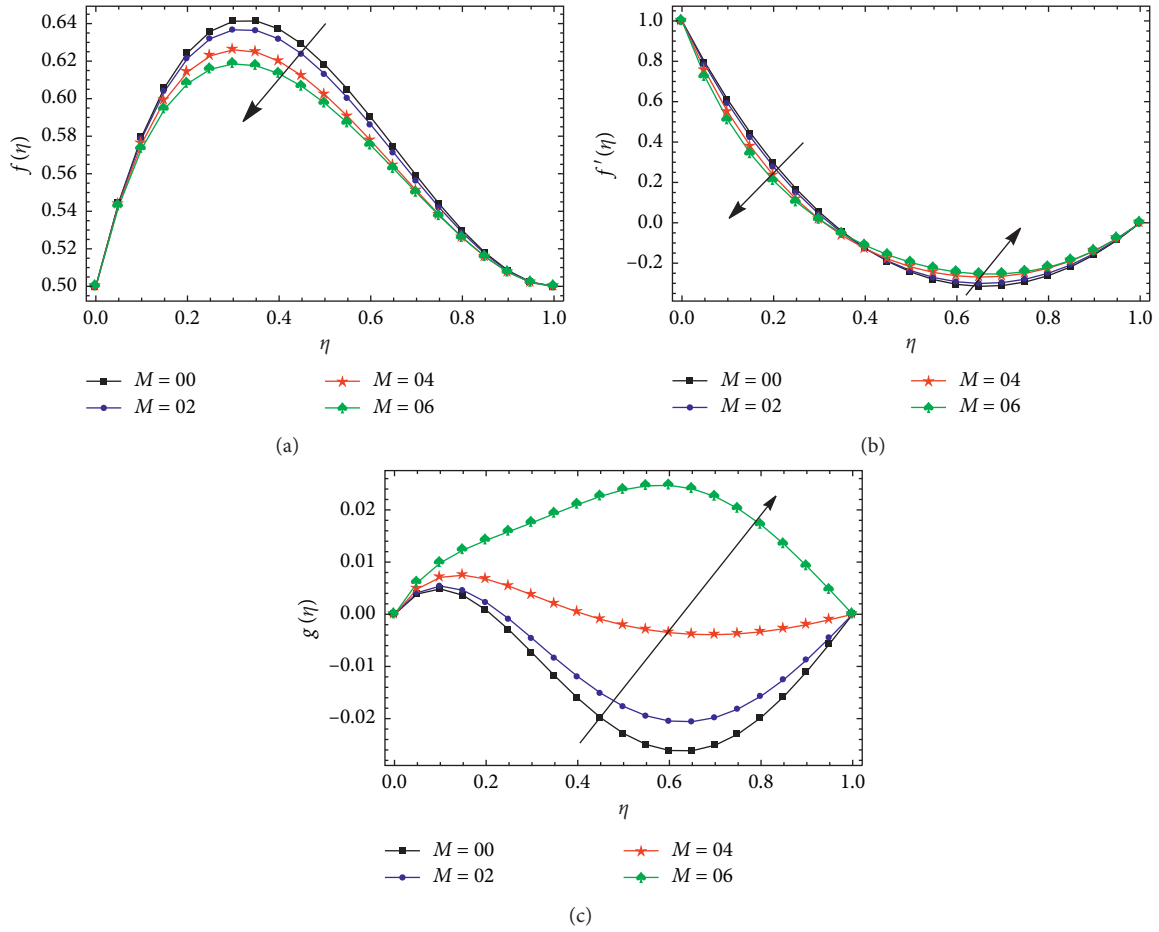
FIGURE 5: Effect of magnetic parameter M on the velocity profile when $\phi = 0.2$, $w_0 = 0.5$, $\beta = 1$, and $\Omega = 1$. (a) Normal component of velocity. (b) Axial component of velocity. (c) Transverse component of velocity.

(a)

(b)
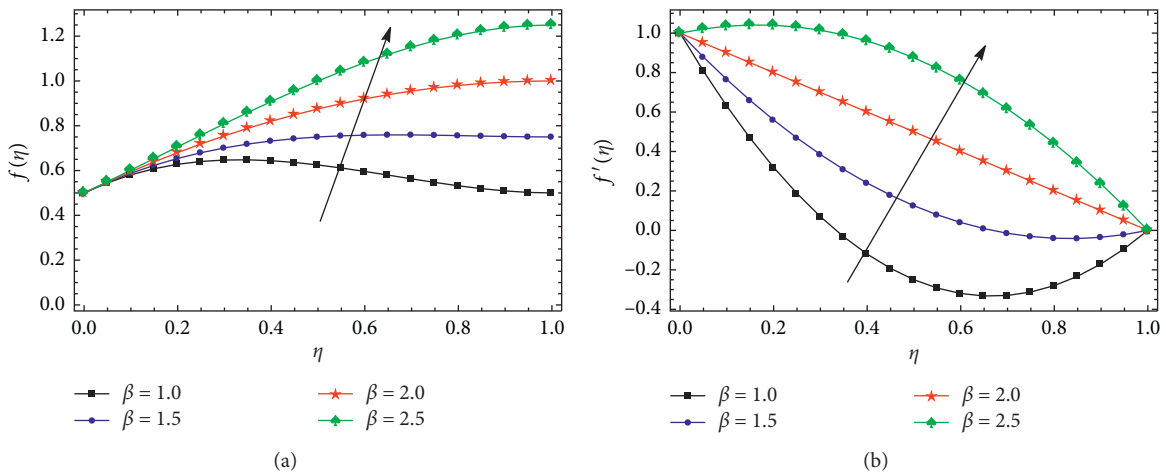
FIGURE 6: Continued.

(c)
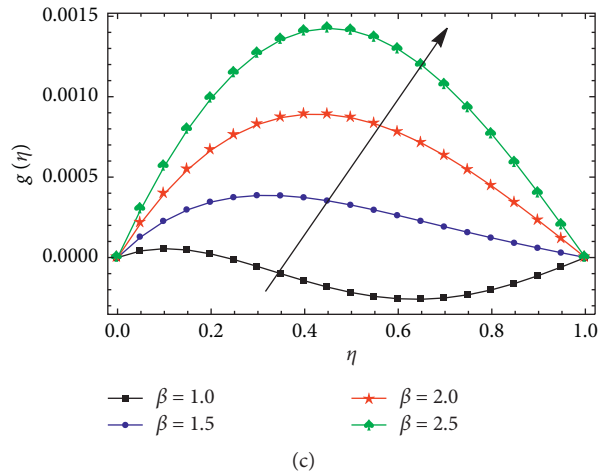
FIGURE 6: Effect of positive values of characteristic parameter β on the velocity profile when $\phi = 0.9$, $w_0 = 0.5$, $\Omega = 1$, and $M = 0.5$. (a) Normal component of velocity. (b) Axial component of velocity. (c) Transverse component of velocity.

(a)

(b)

(c)
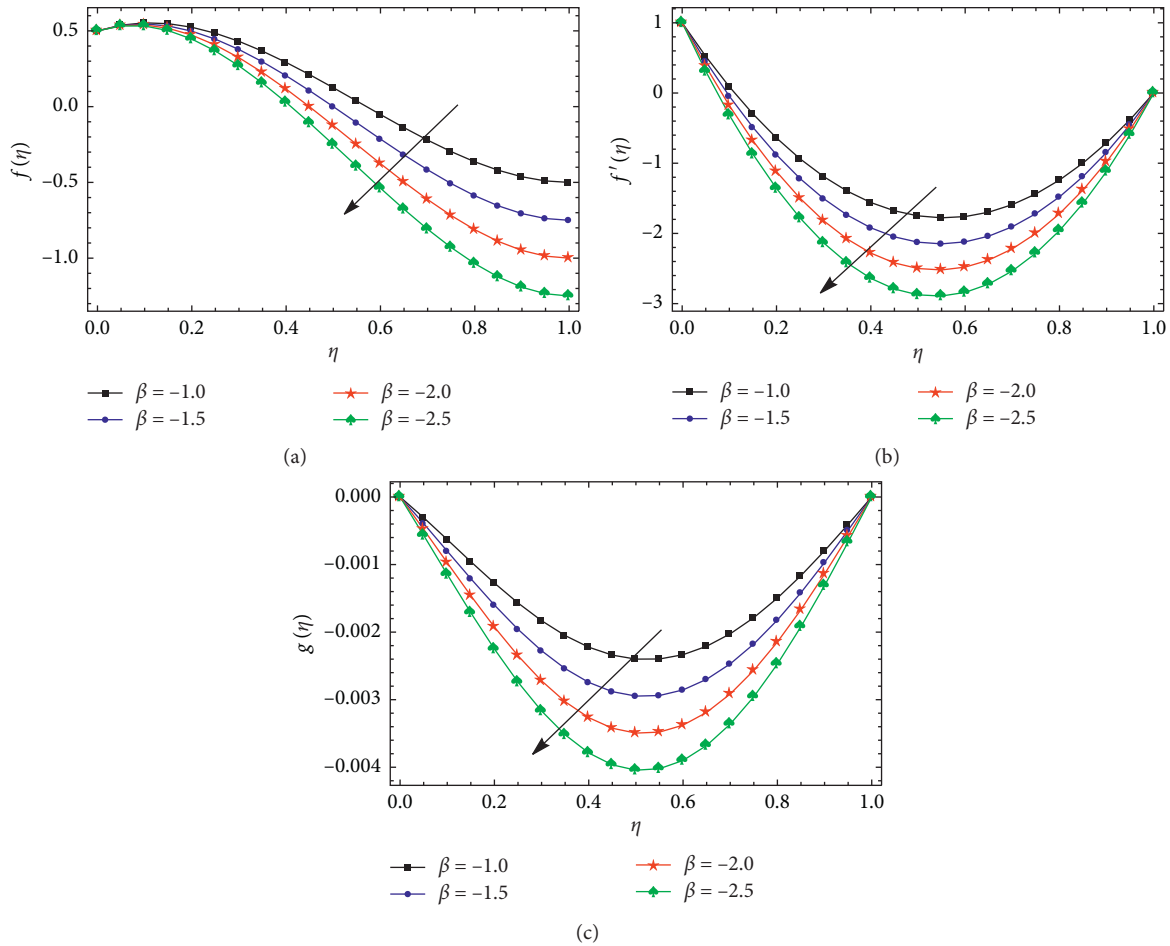
FIGURE 7: Effect of negative values of characteristic parameter β on the velocity profile when $\phi = 0.9$, $w_0 = 0.5$, $\Omega = 1$, and $M = 0.5$. (a) Normal component of velocity. (b) Axial component of velocity. (c) Transverse component of velocity.
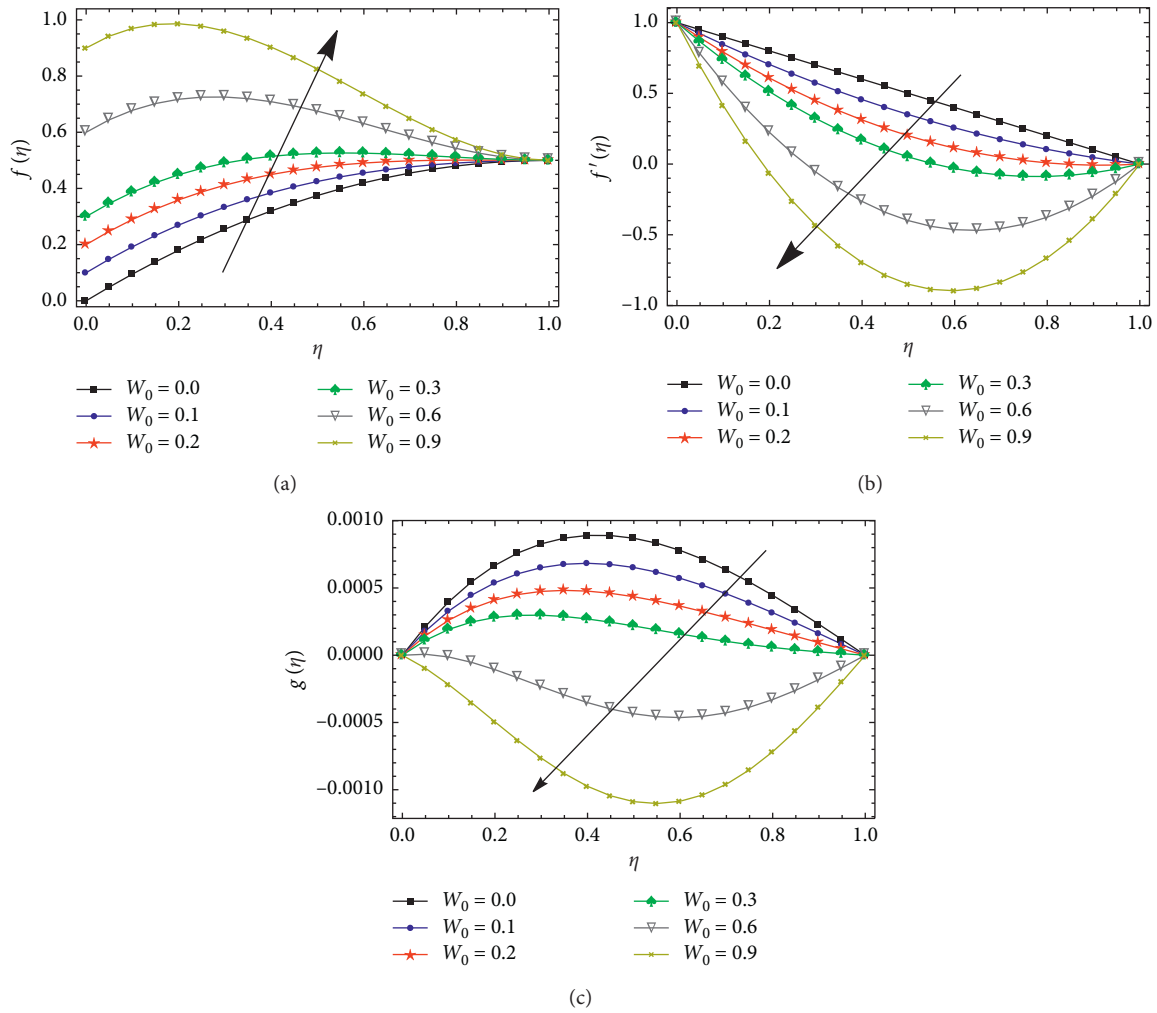
(a)

(b)

(c)

FIGURE 8: Effect of rotational parameter Ω on the velocity profile when $\phi = 0.2$, $w_0 = 0.5$, $\beta = 1$, and $M = 0.5$. (a) Normal component of velocity. (b) Axial component of velocity. (c) Transverse component of velocity.

(a)

(b)

FIGURE 9: Continued.

(c)

FIGURE 9: Effect of various types of nanoparticles on the velocity profile when $\phi = 0.2$, $w_0 = 0.5$, $\Omega = 1$, $\beta = 1$, and $M = 0.5$. (a) Normal component of velocity. (b) Axial component of velocity. (c) Transverse component of velocity.
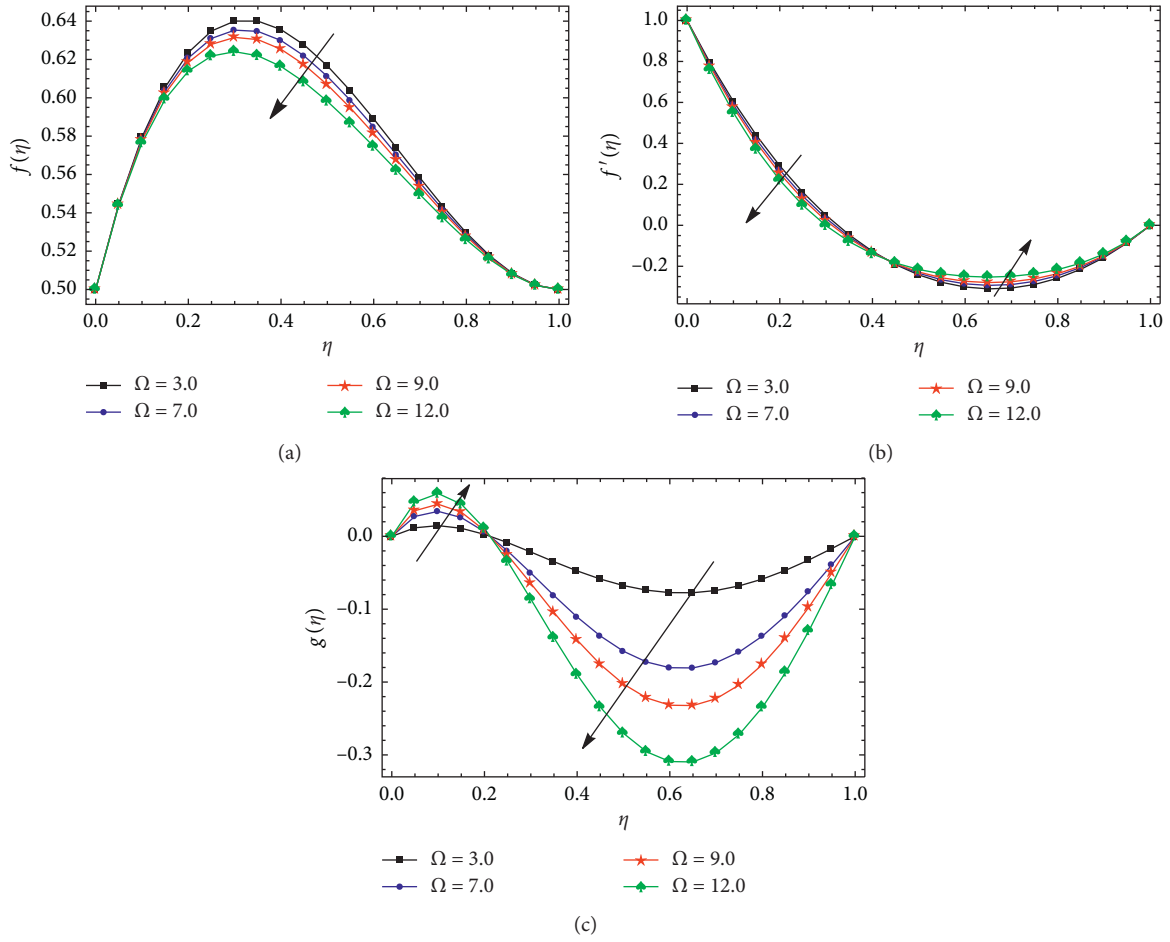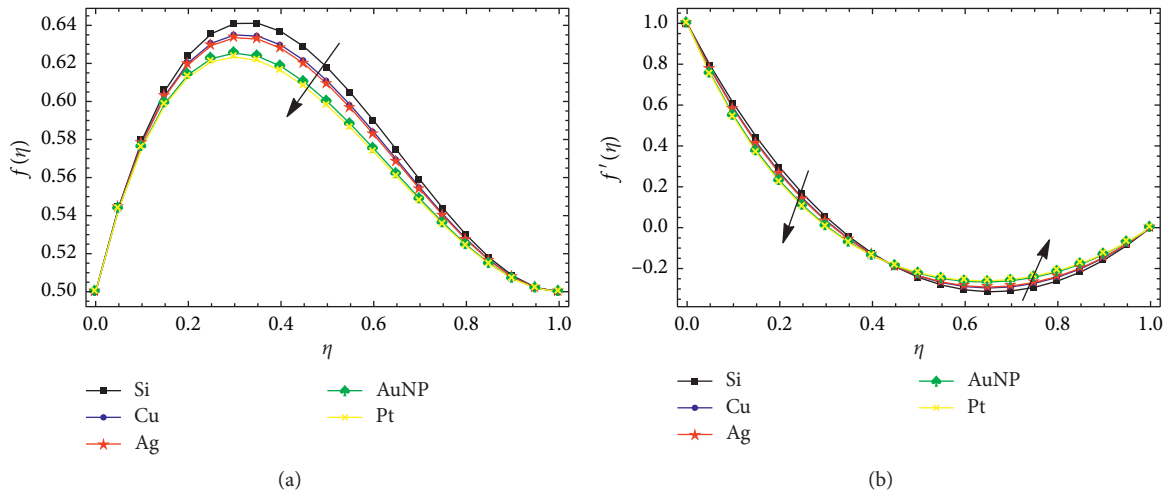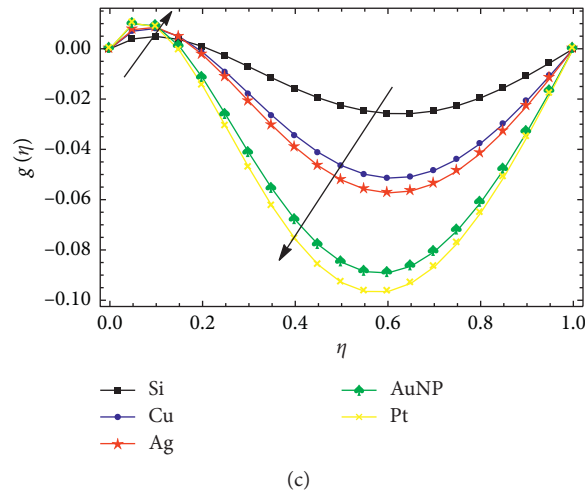
respect to different densities is quite small. In the transverse case, nanofluids with high densities show larger velocity profile in the lower quarter of the channel, whereas a weak reverse and decreasing flow in the remaining of the channel.

5. Conclusion

In this article, an unsteady electrically conducting 3D squeezing flow of nanofluid in a rotating channel on a lower permeable stretching wall is considered. In this study, water is taken as base fluid along with five different types of nanoparticles, including silicon (Si), copper (Cu), silver (Ag), gold (Au), and platinum (Pt), being analyzed in the simulations. Important physical parameters are considered here; the nanoparticle volume fraction (ϕ), the suction parameter (w_0), the characteristic parameter of the flow (β), the rotation parameter (Ω), and the magnetic parameter (M). Resulting boundary value system is solved through the HPM and Runge–Kutta–Fehlberg method (RK45). Analysis reveals that the motion of the upper plate significantly effects the velocity profile in the channel. Also, large values of nanoparticle volume fraction reduce the effects of rotation parameter Ω and magnetic parameter M.

Nomenclature

β: Characteristic parameter of the flow
Ω: Rotation parameter
M^2:   Magnetic parameter
w_0:   Suction parameter
Re_x: Local Reynolds number
σ: Electrical conductivity
ρ: Density
μ: Dynamic viscosity
η: A scaled boundary-layer coordinate
ν: Kinematic viscosity
γ: Characteristic constant parameter
ω: Constant angular velocity
ϕ: Nanoparticle volume fraction

a: Lower plate stretching rate
B: External uniform magnetic field
B_0:   Constant magnetic flux density
C_f: Skin friction coefficient
f, g: Self-similar velocities
$h(t)$:   Upper plane distance
J: Magnetic flux
f: Fluid phase
s: Solid phase
nf: Nanofluid.

Data Availability

The authors confirm that the data supporting the findings of this study are available within the article.

Conflicts of Interest

The authors have no conflicts of interest regarding the publication of this paper.

Acknowledgments

References

[1] N. Freidoonimehr, B. Rostami, M. M. Rashidi, and E. Momoniat, "Analytical modelling of three dimensional squeezing nanofluid flow in a rotating channel on a lower stretching porous wall," *Mathematical Problems in Engineering*, vol. 2014, Article ID 692728, 14 pages, 2014.

[2] K. V. Wong and O. De Leon, "Applications of nanofluids: current and future," *Advances in Mechanical Engineering*, vol. 2, p. 519659, 2010.

[3] W. Yu and H. Xie, "A review on nanofluids: preparation, stability mechanisms, and applications," *Journal of Nanomaterials*, vol. 2012, Article ID 435873, 17 pages, 2012.

[4] S. U. S. Choi and J. A. Eastman, "Enhancing thermal conductivity of fluids with nanoparticles," Technical report, Argonne National Laboratory, Lemont, IL, USA, 1995.

[5] M. E. Meibodi, M. Vafaie-Sefti, A. Rashidi, and M. Tabasi, "An estimation for velocity and temperature profiles of nanofluids in fully developed turbulent flow conditions," *International Communications in Heat and Mass Transfer*, vol. 37, no. 7, pp. 895–900, 2010.

[6] D. Kalal, "Analogies between the heat and the momentum transfer," in *Numerical Modelling and Experimental Testing of Heat Exchangers*, pp. 157–171, Springer, Berlin, Germany, 2019.

[7] K. S. Hwang, S. P. Jang, and S. U. S. Choi, "Flow and convective heat transfer characteristics of water-based al2o3 nanofluids in fully developed laminar flow regime," *International Journal of Heat and Mass Transfer*, vol. 52, no. 1-2, pp. 193–199, 2009.

[8] A. Kanjirakat and R. Sadr, "Near-wall velocity profile measurement for nanofluids," *AIP Advances*, vol. 6, no. 1, p. 015308, 2016.

[9] A. Alsaedi, M. Awais, and T. Hayat, "Effects of heat generation/absorption on stagnation point flow of nanofluid over a surface with convective boundary conditions," *Communications in Nonlinear Science and Numerical Simulation*, vol. 17, no. 11, pp. 4210–4223, 2012.

[10] K. Ali, M. Z. Akbar, M. F. Iqbal, and M. Ashraf, "Numerical simulation of heat and mass transfer in unsteady nanofluid between two orthogonally moving porous coaxial disks," *AIP Advances*, vol. 4, no. 10, p. 107113, 2014.

[11] M. A. Mansour and S. E. Ahmed, "A numerical study on natural convection in porous media-filled an inclined triangular enclosure with heat sources using nanofluid in the presence of heat generation effect," *Engineering Science and Technology, an International Journal*, vol. 18, no. 3, pp. 485–495, 2015.

[12] A. G. Madaki, R. Roslan, M. S. Rusiman, and C. S. K. Raju, "Analytical and numerical solutions of squeezing unsteady cu and tio2-nanofluid flow in the presence of thermal radiation and heat generation/absorption," *Alexandria Engineering Journal*, vol. 57, no. 2, pp. 1033–1040, 2018.

[13] M. Sheikholeslami and D. D. Ganji, "Heat transfer of cu-water nanofluid flow between parallel plates," *Powder Technology*, vol. 235, pp. 873–879, 2013.

[14] U. Khan, N. Ahmed, M. Asadullah, and S. Tauseef Mohyuddin, "Effects of viscous dissipation and slip velocity on two-dimensional and axisymmetric squeezing flow of Cu-water and Cu-kerosene nanofluids," *Propulsion and Power Research*, vol. 4, no. 1, pp. 40–49, 2015.

[15] M. Sheikholeslami and D. D. Ganji, "Nanofluid hydrothermal behavior in existence of lorentz forces considering joule heating effect," *Journal of Molecular Liquids*, vol. 224, pp. 526–537, 2016.

[16] M. Zubair, Z. Shah, A. Dawar, S. Islam, P. Kumam, and A. Khan, "Entropy generation optimization in squeezing magnetohydrodynamics flow of casson nanofluid with viscous dissipation and joule heating effect," *Entropy*, vol. 21, no. 8, p. 747, 2019.

[17] T. Hayat, T. Muhammad, A. Qayyum, A. Alsaedi, and M. Mustafa, "On squeezing flow of nanofluid in the presence of magnetic field effects," *Journal of Molecular Liquids*, vol. 213, pp. 179–185, 2016.

[18] A. S. Dogonchi and D. D. Ganji, "Investigation of mhd nanofluid flow and heat transfer in a stretching/shrinking convergent/divergent channel considering thermal radiation," *Journal of Molecular Liquids*, vol. 220, pp. 592–603, 2016.

[19] O. O. Sharifuddin Ansari, M. Trivedi, and S. P. Goqo, "Magnetohydrodynamic bioconvective casson nanofluid flow: a numerical simulation by paired quasilinearisation," *Journal Archive*, vol. 6, 2020.

[20] X.-Q. Wang and A. S. Mujumdar, "A review on nanofluids-part I: theoretical and numerical investigations," *Brazilian Journal of Chemical Engineering*, vol. 25, no. 4, pp. 613–630, 2008.

[21] H. I. Andersson and B. S. Dandapat, "Flow of a powerlaw fluid over a stretching sheet," *Appl Anal Continuous Media*, vol. 1, no. 339, 1992.

[22] M. Sajid, I. Ahmad, T. Hayat, and M. Ayub, "Unsteady flow and heat transfer of a second grade fluid over a stretching sheet," *Communications in Nonlinear Science and Numerical Simulation*, vol. 14, no. 1, pp. 96–108, 2009.

[23] E. W. Mrill, A. M. Benis, E. R. Gilliland, T. K. Sherwood, and E. W. Salzman, "Pressure flow relations of human blood hollow fibers at low flow rates," *Journal of Applied Physiology*, vol. 20, pp. 954–967, 1965.

[24] D. A. McDonald, *Blood Flows in Arteries*, Arnold, London, UK, 2nd edition, 1974.

[25] M. Sheikholeslami, D. D. Ganji, and H. R. Ashorynejad, "Investigation of squeezing unsteady nanofluid flow using adm," *Powder Technology*, vol. 239, pp. 259–265, 2013.

[26] A. K. Gupta and S. Saha Ray, "Numerical treatment for investigation of squeezing unsteady nanofluid flow between two parallel plates," *Powder Technology*, vol. 279, pp. 282–289, 2015.

[27] M. Azimi and R. Riazi, "Analytical solution of unsteady go-water nanofluid flow and heat transfer between two parallel moving plates," *Indian Journal of Chemical Technology (IJCT)*, vol. 23, no. 1, pp. 47–52, 2016.

[28] N. Hedayati and A. Ramiar, "Investigation of two phase unsteady nanofluid flow and heat transfer between moving parallel plates in the presence of the magnetic field using GM," *Transport Phenomena in Nano and Micro Scales*, vol. 4, no. 2, pp. 47–53, 2016.

[29] M. Sheikholeslami and D. D. Ganji, "Nanofluid flow and heat transfer between parallel plates considering brownian motion using DTM," *Computer Methods in Applied Mechanics and Engineering*, vol. 283, pp. 651–663, 2015.

[30] M. S. Abdel-Wahed, E. M. A. Elbashbeshy, and T. G. Emam, "Flow and heat transfer over a moving surface with non-linear velocity and variable thickness in a nanofluids in the presence of brownian motion," *Applied Mathematics and Computation*, vol. 254, pp. 49–62, 2015.

[31] A. S. Dogonchi and D. D. Ganji, "Thermal radiation effect on the nano-fluid buoyancy flow and heat transfer over a stretching sheet considering Brownian motion," *Journal of Molecular Liquids*, vol. 223, pp. 521–527, 2016.

[32] M. Mustafa and J. A. Khan, "Model for flow of casson nanofluid past a non-linearly stretching sheet considering magnetic field effects," *AIP Advances*, vol. 5, no. 7, p. 077148, 2015.

[33] N. G. Rudraswamy, B. J. Gireesha, and M. R. Krishnamurthy, "Effect of internal heat generation/absorption and viscous dissipation on MHD flow and heat transfer of nanofluid with particle suspension over a stretching surface," *Journal of Nanofluids*, vol. 5, no. 6, pp. 1000–1010, 2016.

[34] S. M. R. Shah Naqvi, T. Muhammad, and M. Asma, "Hydromagnetic flow of casson nanofluid over a porous stretching cylinder with Newtonian heat and mass conditions," *Physica A: Statistical Mechanics and its Applications*, vol. 550, p. 123988, 2020.

[35] R. Kandasamy, I. Muhaimin, A. B. Khamis, and R. b. Roslan, "Unsteady hiemenz flow of cu-nanofluid over a porous wedge in the presence of thermal stratification due to solar energy radiation: lie group transformation," *International Journal of Thermal Sciences*, vol. 65, pp. 196–205, 2013.

[36] B. Bin-Mohsin, N. Ahmed, U. Khan et al., "A bioconvection model for a squeezing flow of nanofluid between parallel plates in the presence of gyrotactic microorganisms," *The European Physical Journal Plus*, vol. 132, no. 4, p. 187, 2017.

[37] A. Dib, A. Haiahem, and B. Bou-Said, "Approximate analytical solution of squeezing unsteady nanofluid flow," *Powder Technology*, vol. 269, pp. 193–199, 2015.

[38] R. Naz, Z. Shah, P. Kumam, P. Thounthong, and M. Sohail, "Exploration of temperature dependent thermophysical characteristics of yield exhibiting non-Newtonian fluid flow under gyrotactic microorganisms," *AIP Advances*, vol. 9, no. 12, 2019.

[39] N. Ahmed, S. T. Mohyud-Din, Adnan, and U. Khan, "Thermo-diffusion and diffusion-thermo effects on flow of second grade fluid between two inclined plane walls," *Journal of Molecular Liquids*, vol. 224, pp. 1074–1082, 2016.

[40] U. Khan, S. T. Mohyud-Din, Adnan, and M. Asadullah, "Analytical and numerical investigation of thermal radiation effects on flow of viscous incompressible fluid with stretchable convergent/divergent channels," *Journal of Molecular Liquids*, vol. 224, pp. 768–775, 2016.

[41] U. Khan, S. T. Mohyud-Din, K. S. Nisar, Adnan, and S. Z. Zaidi, "Investigation of thermal transport in multi-shaped cu nanomaterial-based nanofluids," *Materials*, vol. 13, no. 12, p. 2737, 2020.

[42] U. Khan, N. Ahmed, S. T. Mohyud-Din et al., "Impacts of freezing temperature based thermal conductivity on the heat transfer gradient in nanofluids: applications for a curved riga surface," *Molecules*, vol. 25, no. 9, p. 2152, 2020.

[43] R. Naz, S. I. Abdelsalam, and M. Sohail, "On the onset of entropy generation for a nanofluid with thermal radiation and gyrotactic microorganisms through 3d flows," *Physica Scripta*, vol. 95, no. 4, p. 045206, 2020.

[44] M. Sheikholeslami and D. D. Ganji, "Numerical investigation for two phase modeling of nanofluid in a rotating system with permeable sheet," *Journal of Molecular Liquids*, vol. 194, pp. 13–19, 2014.

[45] M. Sheikholeslami and H. B. Rokni, "Nanofluid two phase model analysis in existence of induced magnetic field," *International Journal of Heat and Mass Transfer*, vol. 107, pp. 288–299, 2017.

[46] J. H. He, "Homotopy perturbation technique," *Computer Methods in Applied Mechanics and Engineering*, vol. 178, no. 3-4, pp. 257–262, 1999.

[47] J.-H. He, "A coupling method of a homotopy technique and a perturbation technique for non-linear problems," *International Journal of Non-linear Mechanics*, vol. 35, no. 1, pp. 37–43, 2000.

[48] J.-H. He, "Homotopy perturbation method: a new nonlinear analytical technique," *Applied Mathematics and Computation*, vol. 135, no. 1, pp. 73–79, 2003.

[49] J.-H. He, "Homotopy perturbation method for solving boundary value problems," *Physics Letters A*, vol. 350, no. 1-2, pp. 87-88, 2006.

[50] A. M. Siddiqui, M. Ahmed, and Q. K. Ghori, "Couette and Poiseuille flows for non-Newtonian fluids," *International Journal of Nonlinear Sciences and Numerical Simulation*, vol. 7, no. 1, pp. 15–26, 2006.

[51] A. M. Siddiqui, R. Mahmood, and Q. K. Ghori, "Thin film flow of a third grade fluid on a moving belt by he's homotopy perturbation method," *International Journal of Nonlinear Sciences and Numerical Simulation*, vol. 7, no. 1, pp. 7–14, 2006.

[52] N. Herisanu and V. Marinca, "Optimal homotopy perturbation method for non conservative dynamical system of a rotating electrical machine," *Zeitschrift für Naturforschung A*, vol. 67, 2012.

[53] F. Wang and W. L. Zhang, "A new extended homotopy perturbation method for nonlinear differential equations," *Mathematical and Computer Modelling*, vol. 55, 2012.

[54] A. N. Golshan, S. S. Nourazar, H. G. Fard, A. Yaldirim, and A. Campo, "A modified homotopy perturbation method coupled with the fourier transform for nonlinear and singular lane-emden equations," *Applied Mathematics Letters*, vol. 26, 2013.

[55] M. Qayyum, H. Khan, M. T. Rahim, and I. Ullah, "Modeling and analysis of unsteady axisymmetric squeezing fluid flow through porous medium channel with slip boundary," *PLoS One*, vol. 10, no. 3, 2015.

[56] M. Qayyum and H. Khan, "Behavioral study of unsteady squeezing flow through porous medium," *Journal of Porous Media*, vol. 19, no. 1, pp. 83–94, 2016.

[57] S. S. Nourazar, M. Habibi Matin, and M. Simiari, "The HPM applied to MHD nanofluid flow over a horizontal stretching plate," *Journal of Applied Mathematics*, vol. 2011, Article ID 876437, 17 pages, 2011.

[58] M. Hatami, D. Jing, D. Song, M. Sheikholeslami, and D. D. Ganji, "Heat transfer and flow analysis of nanofluid flow between parallel plates in presence of variable magnetic field using hpm," *Journal of Magnetism and Magnetic Materials*, vol. 396, pp. 275–282, 2015.

[59] A. Malvandi, D. D. Ganji, F. Hedayati, and E. Yousefi Rad, "An analytical study on entropy generation of nanofluids over a flat plate," *Alexandria Engineering Journal*, vol. 52, no. 4, pp. 595–604, 2013.

[60] N. Dalir and S. S. Nourazar, "Solution of the boundary layer flow of various nanofluids over a moving semi-infinite plate using HPM," *Mechanics*, vol. 20, no. 1, pp. 57–63, 2014.

[61] M. Mustafa, T. Hayat, and S. Obaidat, "On heat and mass transfer in the unsteady squeezing flow between parallel plates," *Meccanica*, vol. 47, no. 7, pp. 1581–1589, 2012.

[62] M. Qayyum, H. Khan, M. T. Rahim, and I. Ullah, "Analysis of unsteady axisymmetric squeezing fluid flow with slip and no-slip boundaries using OHAM," *Mathematical Problems in Engineering*, vol. 2015, Article ID 860857, 11 pages, 2015.

WILEY | Hindawi

Research Article

Nonlinear Dynamics in a Chemical Reaction under an Amplitude-Modulated Excitation: Hysteresis, Vibrational Resonance, Multistability, and Chaos

A. V. Monwanou,[1] A. A. Koukpémèdji,[1,2] C. Ainamon,[1] P. R. Nwagoum Tuwa,[1,3,4] C. H. Miwadinou [1,5] and J. B. Chabi Orou[1]

[1]*Laboratoire de Mécanique des Fluides, de la Dynamique Nonlinéaire et de la Modélisation des Systèmes Biologiques (LMFDNMSB), Institut de Mathématiques et de Sciences Physiques, Porto-Novo, Benin*

[2]*Département de Physique, FAST-Natitingou, Université Nationale des Sciences, Technologies, Ingénierie et Mathématiques, Abomey, Benin*

[3]*Laboratory of Modelling and Simulation in Engineering, Biomimetics and Prototypes and TWAS Research Unit, Faculty of Science, University of Yaoundé I, P. O. 812, Yaoundé, Cameroon*

[4]*Research Unit of Industrial Systems Engineering and Environment (RU-ISEE), Fosto-Victor University Institute of Technology, University of Dschang, P. O. Box 134, Bandjoun, Cameroon*

[5]*Département de Physique, ENS-Natitingou, Université Nationale des Sciences, Technologies, Ingénierie et Mathématiques, Abomey, Benin*

Correspondence should be addressed to C. H. Miwadinou; clement.miwadinou@imsp-uac.org

This paper deals with the effects of an amplitude-modulated (AM) excitation on the nonlinear dynamics of reactions between four molecules. The computation of the fixed points of the autonomous nonlinear chemical system has been made in detail using the Cardan's method. Hopf bifurcation has been also successfully checked. Routes to chaos have been investigated through bifurcations structures, Lyapunov exponent, phase portraits, and Poincaré section. The effects of the control force on chaotic motions have been strongly analyzed, and the control efficiency is found in the cases $g = 0$ (unmodulated case) and $g \neq 0$ with $\Omega = \omega$ and $\Omega/w \neq p/q$; p and q are simple positive integers. Vibrational resonance (VR), hysteresis, and coexistence of several attractors have been studied in detail based on the relationship between the frequencies of the AM force. Results of analytical investigations are validated and complemented by numerical simulations.

1. Introduction

Nonlinear dynamics is a multidisciplinary field that covers not only mathematics but also engineering, physics, chemistry, and biology. A monograph, authored by Strogatz [1], would be the first place to start if one is interested in learning about this topic. In the past decade, the study of complex dynamics and chemistry of oscillating reaction under the influence of external perturbation received much attention and various results such as period-doubling bifurcation leading to chaotic motion, quasiperiodic route to chaos, coexistence of multiple attractors, hysteresis, and vibrational resonance have been obtained [2–12]. The chemical oscillating reactions in a continuously stirred tank reactor (CSTR) is one of the first biochemical oscillations discovered. For considerable theoretical progress on the nature of chemical oscillation, the only known chemical oscillators were either biological in origin, like the glycolytic and oxidase-peroxidase systems; either discovered accidentally, like the Bray and BZ reactions; or variants of those reactions [2–12]. In these chemical oscillations, various dynamics behaviors are studied by many researchers. For

instance, nonequilibrium phenomena such as oscillations, bistability, complex oscillations, and quasichaotic behavior of the reaction are revealed by these studies. One of the main challenges has been to predict and to control these phenomena in nonlinear chemical oscillations for potential applications (see [2–15]). The study of these oscillations has been made with a periodically external excitation or a parametric excitation [11, 12]. Moreover, the study of these oscillations is more advantageous for systems with the AM (amplitude modulation) [14]. However, some new dynamical phenomena including controllable frequency can be also presented. Binous and Bellagi [2] present the solution of four problems drawn from the chemical and biochemical engineering field of study. These problems illustrate various important aspects of nonlinear dynamics such as limit cycles, quasiperiodic and chaotic behaviors, time series and phase portraits, power spectra, the time-delay reconstruction diagrams, Hopf bifurcation, bifurcation diagrams, and steady state multiplicity. Among a large number of examples, they have selected the following case studies because it illustrates the basic nonlinear dynamics concepts: the glycolytic oscillator model first suggested by Selkov in 1968 in order to elucidate the mechanism that living cells use to obtain energy from sugar breakdown; the oregonator model derived by Field, Koros, and Noyes in the early 1970s, which elucidates the famous oscillatory behavior observed in the Belousov-Zhabotinsky (BZ) reaction; the steady state multiplicity in a biochemical reactor for both the Monod and substrate inhibition kinetics; and the three-variable autocatalator, first proposed by Peng, Scott, and Showalter in 1990. Guruparan et al. [3] considered Brusselator chemical system driven by an amplitude-modulated (AM) force and studied numerically the dynamics of Brusselator chemical system driven by an amplitude-modulated force with widely different frequencies. They showed the occurrence of hysteresis and vibrational resonance and the coexistence of several period-T orbits, bifurcations of them, routes to chaos, and quasiperiodic and chaotic orbits. They have characterized periodic orbits, quasiperiodic orbits, chaotic orbits, hysteresis, and vibrational resonance using bifurcation diagram, maximal Lyapunov exponent, phase portrait, Poincaré map, and resonance plots. Shabunin et al. [5] introduced the lattice limit cycle (LLC) model as a minimal mean-field scheme which can model reactive dynamics on lattices (low-dimensional supports) producing nonlinear limit cycle oscillations. They have found that, under the influence of an external periodic force, the dynamics of the LLC may be drastically modified. Synchronization phenomena, bifurcations, and transitions to chaos are also observed as a function of the excitation force. Taking advantage of the drastic change in the dynamics due to the periodic forcing, they found that it is possible to modify the output/product or the production rate of a chemical reaction at will, simply by applying a periodic force to it, without the need to change the support properties or the experimental conditions. Blekhman and Landa [6] considered resonances caused by a biharmonical external force with two different frequencies (the so-called vibrational resonances) using a bistable oscillator described by a Duffing equation as an

example. It is shown that, in the case of a weakly damped oscillator, these resonances are conjugate; they occur as either the low and high frequency is varied. In addition, the resonances occur as the amplitude of the high-frequency excitation is varied. It is also shown that the high-frequency action induces the change in the number of stable steady states; these bifurcations are also conjugate and are the cause of the seeming resonance in an overdamped oscillator. Roy-Layinde et al. [7] examined the phenomenon of vibrational resonance (VR) and analyzed in a biharmonically driven two-fluid plasma model with nonlinear dissipation. They derived analytically an equation for the slow oscillations of the system in themes of the parameters of the fast signal using the method of direct separation of motion. The presence of a high-frequency externally applied electric field is found to significantly modify the systems dynamics and, consequently, induce VR. They have identified the origin of the VR in the plasma model, not only from the effective plasma potential but also from the contributions of the effective nonlinear dissipation. Besides several dynamical changes, including multiple symmetry-breaking bifurcations, attractor escapes, and reversed period-doubling bifurcations, numerical simulations also revealed the occurrence of single and double resonances induced by symmetry-breaking bifurcations. Landa and McClintock [8] considered the effect of a high-frequency force on the response of a bistable system to a low-frequency signal for both the overdamped and weakly damped cases. They have shown that the response can be optimized by an appropriate choice of vibration amplitude. This vibrational resonance displays many analogies to the well-known phenomenon of stochastic resonance, but with the vibrational force filling the role usually played by noise. Jeevarathinam et al. [9] analyzed the vibrational resonance in the Duffing oscillator system in the presence of a gamma-distributed time-delayed feedback and an integrative time-delayed (uniformly distributed time delays over a finite interval) feedback. Particularly, applying a theoretical procedure, they obtain an expression for the response amplitude at the low frequency of the driving biharmonic force. For both double-well potential and single-well potential cases, they are able to identify the regions in parameter space where either two resonances, a single resonance, or no resonance occur. Theoretically predicted values of the response amplitude and the values of a control parameter at which resonance occurs are in good agreement with their numerical simulation. The analysis shows a strong influence of both types of time-delayed feedback on vibrational resonance. In the present paper, we seek hysteresis, vibrational resonance, and chaos in the system of reactions between four molecules when it is subjected to an external amplitude modulation excitation. More precisely, after an in-depth analysis of the fixed points and of the Hopf bifurcation for the autonomous system, the effects of the modulated amplitude force on the dynamics of the chemical reaction considered have been studied in detail and the efficiency of the control force was analyzed. The paper is structured as follows: Section 2 gives the mathematical modeling of chemical model, while Section 3 analyses the fixed points and their stability and the possibility to

obtain the Hopf bifurcation. In Section 4, in-depth details of the bifurcation and the route to chaos when the system is under the periodically external excitation are presented. Section 5 deals with vibrational resonance, bifurcation, route to chaos, bistability, coexistence of attractors, and hysteresis for $\Omega \gg \omega$. Section 6 analyses the effect of AM excitation when $\Omega = \omega$ and $\Omega/w \neq p/q$, where p and q are simple positive integers. Finally, the conclusion of the research is given in Section 7.

2. Chemical Model and Its Mathematical Equations

In this work, we consider the autonomous system of reactions between four molecules as in [5, 16]:

$$2X + 2Y \xrightarrow{k_1} 3Y + S, \; X + S \xrightarrow{k_2} 2Y, Y + S \xrightarrow{k_3} 2S. \quad (1)$$
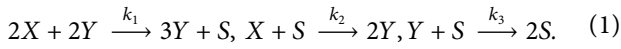
X, Y, and S are molecules of the types X and Y and empty lattice sites, respectively, while k_1, k_2, and k_3 are kinetic constants of the corresponding reactions. The complex oscillatory dynamics and the formation of spatial patterns observed experimentally have been predicted with great success by reactive multimolecular patterns [5, 12, 16–21]. Indeed, at the beginning of the 80 years, experimentally, "vacation models" were written by reactive quadrimolecular stages. In these models, increasing the number of vacant sites results in an increase in autocatalytic behavior, which results in oscillatory behavior. The reactions between nitrogen monoxide and carbon monoxide (NO + CO), nitrogen monoxide and ammonia (NO + NH$_3$), and nitrogen monoxide and dihydrogen (NO + H$_2$), which all use the platinum surface Pt as catalyst, are well-known models of vacancies [18]. In each of these reactions, an autocatalytic behavior linked to vacant sites is observed, and this explains, amongst other nonlinear phenomena, the "surface explosion" phenomena observed frequently in heterogeneous catalysis representing narrow peaks of the product concentrations at regular temporal intervals [5, 12, 16–21].

In the mean-field approach, the kinetic equations for the evolution of the relative concentrations of the molecules (x, y) and of empty sites (S) can be written as follows [5, 16]:

$$\frac{\mathrm{d}x}{\mathrm{d}t} = -2k_1 x^2 y^2 + k_2 xs, \quad (2)$$

$$\frac{\mathrm{d}y}{\mathrm{d}t} = k_1 x^2 y^2 - k_3 ys, \quad (3)$$

$$\frac{\mathrm{d}s}{\mathrm{d}t} = 2k_1 x^2 y^2 - k_2 xs + k_3 ys. \quad (4)$$

It is easily shown that a condition of conservation is fulfilled:

$$\frac{\mathrm{d}x}{\mathrm{d}t} + \frac{\mathrm{d}y}{\mathrm{d}t} + \frac{\mathrm{d}s}{\mathrm{d}t} = 0, \quad (5)$$

and hence, $x + y + s = $ cste. By choosing this constant equal to 1, we have $x + y + s = 1$, and putting it in equation (3), the system is reduced to the following system:

$$\frac{\mathrm{d}x}{\mathrm{d}t} = -2k_1 x^2 y^2 + k_2 x (1 - x - y), \quad (6)$$

$$\frac{\mathrm{d}y}{\mathrm{d}t} = k_1 x^2 y^2 - k_3 y (1 - x - y). \quad (7)$$

The complex dynamic behaviors of this system under the action of a sinusoidal force have been studied in-depth [5, 16]. Recently, the importance of the amplitude modulated force has been proven for the control of complex dynamics of certain systems such as mechanical and electrical systems [14, 15] and biochemical and chemical systems [3, 11–13]. In this work, we consider the dynamics of molecules in the chemical reaction under the external amplitude-modulated excitation, which can be described by a system of two differential equations of order 1. So we modify the original model (7) of the LLC oscillator by adding an amplitude modulation force to the right themes of the first equation. So, we have

$$\frac{\mathrm{d}x}{\mathrm{d}t} = -2k_1 x^2 y^2 + k_2 x (1 - x - y) \\ + (F + 2G \cos \Omega_0 t) \sin w_0 t, \quad (8)$$

$$\frac{\mathrm{d}y}{\mathrm{d}t} = k_1 x^2 y^2 - k_3 y (1 - x - y), \quad (9)$$

where F is the amplitude of unmodulated force, G is the degree of modulation, and w_0 and Ω_0 are the frequencies of the AMF.

Using the time rescaling $\tau = k_1 t$ and notation $\dot{x} = \mathrm{d}x/\mathrm{d}\tau$, we reduce the system (8) as follows:

$$\dot{x} = -2x^2 y^2 + \alpha x (1 - x - y) \\ + (f + 2g \cos \Omega \tau) \sin \omega \tau \quad (10)$$

$$\dot{y} = x^2 y^2 - \beta y (1 - x - y), \quad (11)$$

with $\alpha = k_2/k_1 > 0; \beta = k_3/k_1 > 0$, $f = F/k_1$, $g = G/k_1$, $\Omega = \Omega_0/k_1$, and $w = w_0/k_1$.

3. Equilibrium Points and Its Stability Analysis

We consider the system (10) in the absence of the excitation AM and we seek the fixed points. Indeed, we have

$$-2x^2 y^2 + \alpha x (1 - x - y) = 0, \quad (12)$$

$$x^2 y^2 - \beta y (1 - x - y) = 0. \quad (13)$$

The resolution of the system formed by these two equations comes down to that of the following equation:

$$\frac{4\beta^2}{\alpha^2} y^4 - \beta y \left(1 - \frac{2\beta}{\alpha} y - y\right) = 0. \quad (14)$$

The fixed points of the autonomous system are $E_0(0, 0)$ and $E_*(x^*, y^*)$ whose coordinates (x^*, y^*) are obtained after solving the following equation:

$$\frac{4\beta^2}{\alpha^2}y^3 - \beta\left(1 - \frac{2\beta}{\alpha}y - y\right) = 0. \tag{15}$$

To solve equation (15), we set $p = ((\alpha/2) + (\alpha^2/4\beta))$ and $q = -\alpha^2/4\beta$.

So, we have

$$y^3 + py + q = 0. \tag{16}$$

By taking the Cardan technique [11], the resolution of equation (16) amounts to looking for the roots of a trinome. If Δ is the discriminant of this trinomial, we have

$$D = 27\Delta = 4p^3 + 27q^2. \tag{17}$$

Here, $\alpha > 0$ and $\beta > 0$ so $p^3 > 0$ and $q^2 > 0$ and then $D > 0$.

Equation (16) has only one real solution, which is $T = ((-q \pm \sqrt{\Delta})/2)$. So, we have $E_3 = (x_3, y_3)$, where

$$
\begin{aligned}
x_3 &= \sqrt[3]{\frac{\beta^2}{\alpha}(1-\delta)} + \sqrt[3]{\frac{\beta^2}{\alpha}(1+\delta)}, \\
y_3 &= \sqrt[3]{\frac{\alpha^2}{8\beta}(1-\delta)} + \sqrt[3]{\frac{\alpha^2}{8\beta}(1-\delta)},
\end{aligned}
\tag{18}
$$

with

$$\delta = \sqrt{\frac{(\alpha+2\beta)^3}{27\alpha\beta} + 1} \tag{19}$$

On the contrary, by combining the equations of the system (12), we have $x + y = 1$.

Thus, we have $E_1(0, 1)$ and $E_2 = (1, 0)$.

In total, the autonomous system admits exactly four fixed points $E_0(0, 0)$ (trivial), $E_1(0, 1)$ (semitrivial), $E_2(1, 0)$ (semitrivial), and $E_3(x_3, y_3)$ (nontrivial).

The study of the stability of each fixed point is made by searching the Jacobian of the autonomous system associated. The Jacobian of the autonomous system associated with each fixed point $E_0(0, 0)$ or $E_*(x^*, y^*)$ is as follows:

$$J = \begin{pmatrix} -4x^*y^{*2} + \alpha(1 - x^* - y^*) - \alpha x^* & -4x^{*2}y^* - \alpha x^* \\ 2x^*y^{*2} + \beta y^* & 2x^{*2}y^* - \beta(1 - x^* - y^*) + \beta y^* \end{pmatrix}. \tag{20}$$

For $E_0(0, 0)$, the eigenvalues of the Jacobian J are $\lambda_1 = \alpha$ and $\lambda_2 = -\beta$, which are reals and have opposite signs because $\alpha > 0$ and $\beta > 0$. Hence, E_0 is a saddle point. Then, the two eigenvalues of the Jacobian J associated with $E_1(0, 1)$ are $\lambda_1 = 0$ and $\lambda_2 = \beta > 0$, and therefore, E_1 is the unrobust point. On the contrary, for $E_2(1, 0)$, the eigenvalues are $\lambda_1 = 0$ and $\lambda_2 = -\alpha < 0$, and therefore, E_2 is a robust point. Finally, for $E_3(x_3, y_3)$, the characteristic equation giving the eigenvalues of J is

$$\lambda^2 + \sigma_1\lambda + \sigma_2 = 0, \tag{21}$$

with $\sigma_1 = -(a_1 + a_2)$ and $\sigma_2 = a_1a_4 - a_2a_3$, where

$$
\begin{aligned}
a_1 &= -4x_3y_3^2 + \alpha(1 - 2x_3 - y_3), \\
a_2 &= -4x_3^2y_3 - \alpha x_3, \\
a_3 &= 2x_3y_3^2 + \beta y_3, \\
a_4 &= 2x_3^2y_3 - \beta(1 - x_3 - 2y_3).
\end{aligned}
\tag{22}
$$

If $\sigma_1^2 = 4\sigma_2$, then equation (21) has only one solution, and the fixed point E_3 is a center. For $\sigma_1^2 > 4\sigma_2$, the eigenvalues are

$$
\begin{aligned}
\lambda_1 &= \frac{-\sigma_1 - \sqrt{\sigma_1^2 - 4\sigma_2}}{2}, \\
\lambda_2 &= \frac{-\sigma_1 + \sqrt{\sigma_1^2 - 4\sigma_2}}{2}.
\end{aligned}
\tag{23}
$$

In this case, the equilibrium point E_3 is a node. If $\sigma_1^2 < 4\sigma_2$, then

$$
\begin{aligned}
\lambda_1 &= \frac{-\sigma_1 - i\sqrt{\sigma_1^2 + 4\sigma_2}}{2}, \\
\lambda_2 &= \frac{-\sigma_1 + i\sqrt{-\sigma_1^2 + 4\sigma_2}}{2},
\end{aligned}
\tag{24}
$$

and E_3 is either a focus or a center. By virtue of the Routh–Hurwitz criterion [22, 23], the fixed point E_3 is stable if and only if $\sigma_1 > 0$ and $\sigma_2 > 0$ if not the fixed point is unstable. We now look for the Hopf bifurcation assuming that $\lambda = iw$ ($w > 0$). Let us insert λ in equation (21), and we have

$$-w^2 + i\sigma_1 w + \sigma_2 = 0, \tag{25}$$

with $w = \sqrt{\sigma_2}$ and $\sigma_1 = a_1 + a_4 = 0$.

Assuming β fixed and taking α as a bifurcation parameter, differentiating both sides of the characteristic equation (21) associated to E_3 with respect to α_H, we obtain

$$\frac{d\lambda}{d\alpha} = -\frac{1}{2}\frac{d\sigma_1}{d\alpha} - \frac{1}{2\lambda}\frac{d\sigma_2}{d\alpha}, \tag{26}$$

$$R_e\left(\frac{d\lambda}{d\alpha}\right) = -\frac{1}{2}\frac{d\sigma_1}{d\alpha}, \tag{27}$$

where $\alpha = \alpha_H$ and $\lambda = iw$. Thus, if for $\alpha = \alpha_H$, $\sigma_1 = 0$, and $R_e(d\lambda/d\alpha) \neq 0$, then $\alpha = \alpha_H$ is a Hopf bifurcation value for the equilibrium point system E_3. In short, we have the following Theorem 1.

Theorem 1. *If β is fixed, system (8) in absence of the AM force has a Hopf bifurcation at equilibrium point $E_3(x_3, y_3)$ when α passes through the critical value α_H, which verifies simultaneously the following relations (16 and 17):*

$$\alpha - \beta - \frac{1}{2}\alpha\left[\frac{\alpha^2(1-\delta)}{\beta}\right]^{1/3} + \beta\left[\frac{\alpha^2(1-\delta)}{\beta}\right]^{1/3} - 2\alpha\left[\frac{\beta^2(1-\delta)}{\alpha}\right]^{1/3} + \beta\left[\frac{\beta^2(1-\delta)}{\alpha}\right]^{1/3}$$

$$- \left[\frac{\alpha^2(1-\delta)}{\beta}\right]^{2/3}\left[\frac{\beta^2(1-\delta)}{\alpha}\right]^{1/3} + \left[\frac{\alpha^2(1-\delta)}{\beta}\right]^{1/3}\left[\frac{\beta^2(1-\delta)}{\alpha}\right]^{2/3}$$

$$- \frac{1}{2}\alpha\left[\frac{\alpha^2(1+\delta)}{\beta}\right]^{1/3} + \beta\left[\frac{\alpha^2(1+\delta)}{\beta}\right]^{1/3} - 2\left[\frac{\alpha^2(1-\delta)}{\beta}\right]^{1/3}\left[\frac{\beta^2(1-\delta)}{\alpha}\right]^{1/3}\left[\frac{\alpha^2(1+\delta)}{\beta}\right]^{1/3}$$

$$+ \left[\frac{\beta^2(1-\delta)}{\alpha}\right]^{2/3}\left[\frac{\alpha^2(1+\delta)}{\beta}\right]^{1/3} - \left[\frac{\beta^2(1-\delta)}{\alpha}\right]^{1/3}\left[\frac{\alpha^2(1+\delta)}{\beta}\right]^{2/3} - 2\alpha\left[\frac{\beta^2(1+\delta)}{\alpha}\right]^{1/3} \tag{28}$$

$$+ \beta\left[\frac{\beta^2(1+\delta)}{\alpha}\right]^{1/3} - \left[\frac{\alpha^2(1-\delta)}{\beta}\right]^{2/3}\left[\frac{\beta^2(1+\delta)}{\alpha}\right]^{1/3} + 2\left[\frac{\alpha^2(1-\delta)}{\beta}\right]^{1/3}\left[\frac{\beta^2(1-\delta)}{\alpha}\right]^{1/3}\left[\frac{\beta^2(1+\delta)}{\alpha}\right]^{1/3}$$

$$- 2\left[\frac{\alpha^2(1-\delta)}{\beta}\right]^{1/3}\left[\frac{\alpha^2(1-\delta)}{\beta}\right]^{1/3}\left[\frac{\beta^2(1+\delta)}{\alpha}\right]^{1/3} + 2\left[\frac{\alpha^2(1+\delta)}{\beta}\right]^{1/3}\left[\frac{\beta^2(1-\delta)}{\alpha}\right]^{1/3}\left[\frac{\beta^2(1+\delta)}{\alpha}\right]^{1/3}$$

$$- \left[\frac{\alpha^2(1+\delta)}{\beta}\right]^{2/3}\left[\frac{\beta^2(1+\delta)}{\alpha}\right]^{1/3} + \left[\frac{\beta^2(1+\delta)}{\alpha}\right]^{2/3}\left[\frac{\alpha^2(1-\delta)}{\beta}\right]^{1/3} + \left[\frac{\beta^2(1+\delta)}{\alpha}\right]^{2/3}\left[\frac{\alpha^2(1+\delta)}{\beta}\right]^{1/3} = 0,$$

$$\left(-4y_3^2 + 4x_3y_3 - 2\alpha + \beta\right)\frac{dx_3}{d\alpha} + \left(2x_3^2 - 8x_3y_3 - \alpha + 2\beta\right)\frac{dy_3}{d\alpha} - 2x_3 - y_3 + 1 \neq 0. \tag{29}$$

To support this theorem, we represent the real part of the eigenvalues associated with the equilibrium point $E_3(x_3, y_3)$ in the case where the eigenvalues are complex as a function of α for fixed values of β. Figure 1 shows the critical values $\alpha_H \approx 0.00845, \alpha_H \approx 0.0237, \alpha_H \approx 0.059, \alpha_H \approx 0.0875$ of α corresponding to the Hopf bifurcation points H_1, H_2, H_3 and H_4 respectively. By a simple calculation, we show that each of these values verifies simultaneously (28) and (29). It should also be noted that the critical value αH for the Hopf bifurcation increases with β. At the moment of its birth, through Hopf bifurcation of the point $E_3(x_3, y_3)$, the oscillations have infinitesimally small amplitude and near-harmonic shape (see Figure 2).

4. Bifurcation and Route to Chaos for $g = 0$

Before studying the influence of the AM excitation on the dynamics of the system, let us analyze the effect of each

parameter α, β, and f on the dynamics of the unmodulated system. Indeed, we represent the bifurcation diagram, the Lyapunov exponent, the phase space, and the Poincaré section taking as control parameters f and β. In the remains of this work, we take $\omega = 0.0481$, $\alpha > 0$, $O > 0$, $x(0) = 0.5$, and $y(0) = 0.5$. From all results of the simulations carried out in the case of the unmodulated system ($g = 0$), we note that the chemical reaction studied can present a very rich dynamic such as periodic, multiperiodic, quasiperiodic, and chaotic oscillations. In addition, we observe phenomena such as hysteresis, multistability, coexistence of periodic, multi-periodic, quasiperiodic, and chaotic attractors (see Figures 3–6). All these phenomena prove that very complex dynamics can be observed in the nonlinear chemical reaction studied. Thus, Figure 3 represents the bifurcation diagram and corresponding Lyapunov exponents for the system when f varies in the domain $0 \leq f \leq 0.003$, the other parameters being fixed. From this figure, it emerges that the
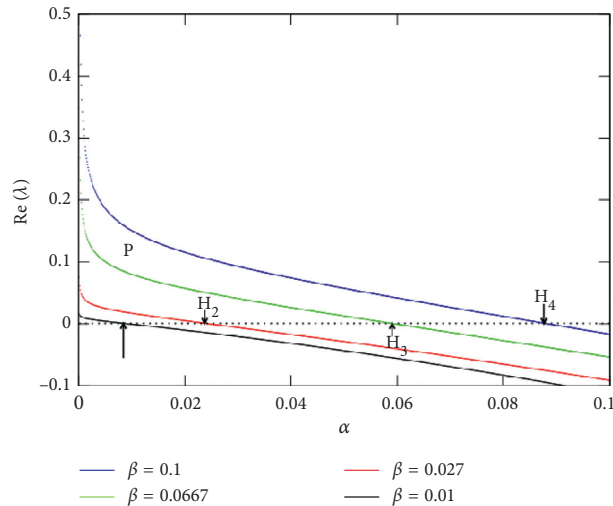
FIGURE 1: Real part of the eigenvalues versus α for different values of β. H_1, H_2, H_3 and H_4 are the points where Re $(\lambda) = 0$.
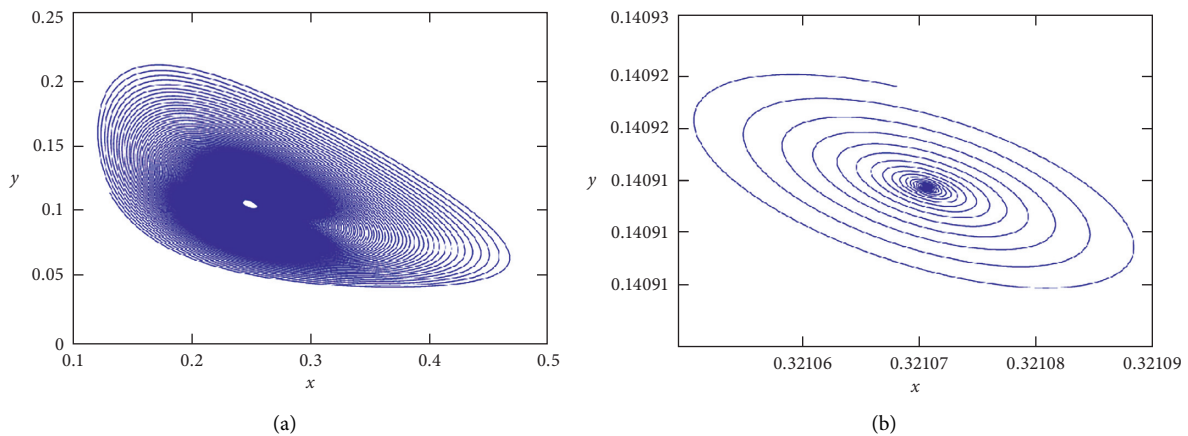

(a)

(b)

FIGURE 2: Phase portraits of the autonomous system for parameter values corresponding to Hopf bifurcation at fixed point $E_3 = (x_3, y_3)$ (a): $\alpha'_H = 0.00845$; $\beta = 0.01$ and (b): $\alpha'_H = 0.0237$; $\beta = 0.027$.

chemical oscillations are quasiperiodic, multiperiodic, and chaotic. When we compare the dynamics of the system when f increases from 0 to 0.003 (blue color) to that is obtained when f decreases from 0.003 to 0 (red color), we note apart from chemical oscillations of the same nature which are observed on a large domain that the system presents the coexistence of the attractors of period $6T$ with quasiperiodic attractors for $0.0011162 < f < 0.001131$, attractors of period $5T$ with quasiperiodic attractors for $0.001521 < f < 0.00156103$ and $0.001598 \leq f < 0.0017485$, attractors of period $5T$ with attractors of period $10T$ for $0.00156103 < f < 0.001598$, and attractors of period $5T$ with chaotic attractors for $0.00298 < f \leq 0.003$. The chaotic behavior of chemical oscillations predicted by the bifurcation diagram and its corresponding Lyapunov exponent (Figure 3) is confirmed by the phase space (Figure 4(a)) and the corresponding Poincaré section (Figure 4(b)) obtained for $f = 0.0025$. For $f = 0.00165$ and with two different initial conditions, we have plotted the phase space and the corresponding Poincaré section in Figure 5. We clearly note through this figure the coexistence of the quasiperiodic attractors (Figures 5(a) and 5(b)) with the attractors of period $5T$ (Figures 5(c) and 5(d)) thus justifying this phenomenon. To understand the influence of the nonlinear parameters α and β on the nature of the oscillations of the chemical reaction considered, we consider now β as the bifurcation parameter. Thus, Figure 6 shows the effect of the parameter α on the bifurcation diagram when β varies between 0.03 and 0.1. As it can be seen in this figure, the chaotic, periodic, multiperiodic, and quasiperiodic behaviors also depend on β. We take note that chaotic oscillations can only exist when $0.02 \leq \alpha < 0.05$, and outside this domain, the chemical oscillations are periodic. It should be noted that the numerical simulations have shown that α and β have almost the same effects on the chemical dynamics of the studied reaction.

(a)

(b)
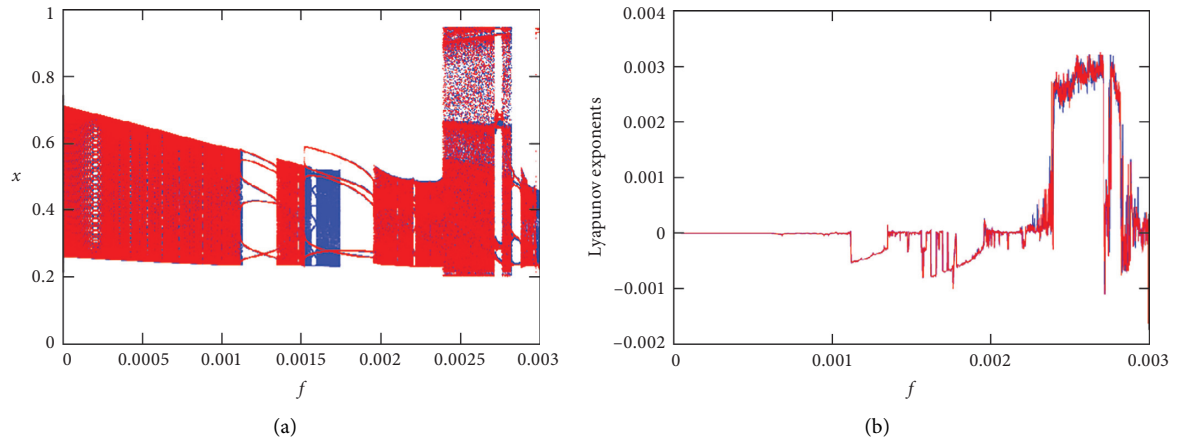
Figure 3: Bifurcation diagram and its corresponding Lyapunov exponent of nonlinear chemical reaction with $\omega = 0.0481$, $\alpha = 0.0413$, $\beta = 0.0667$, and $g = 0$. Bifurcation diagrams and its corresponding Lyapunov exponent are obtained by scanning the parameter f upwards (blue) and downwards (red).

(a)

(b)
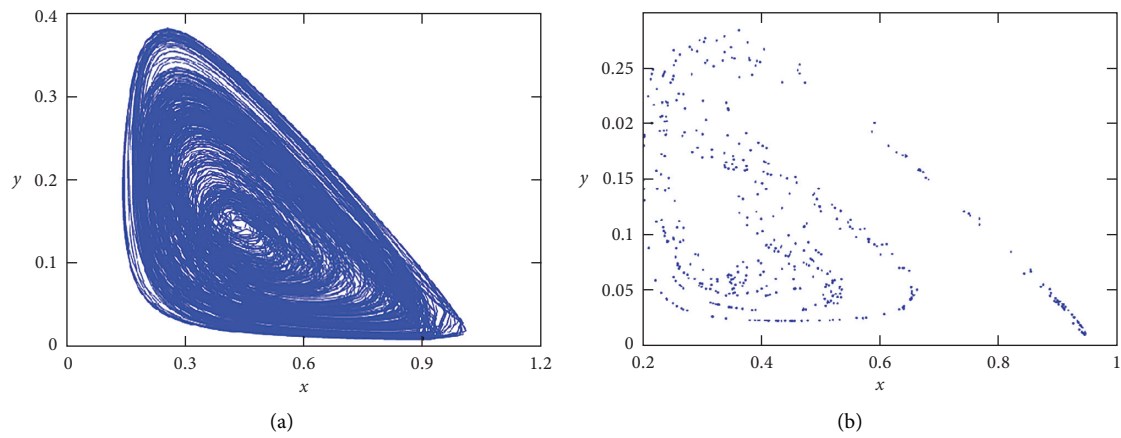
Figure 4: Chaotic phase portrait and its Poincaré section of nonlinear chemical reaction with parameters of Figure 3 and $f = 0.0025$.

(a)

(b)
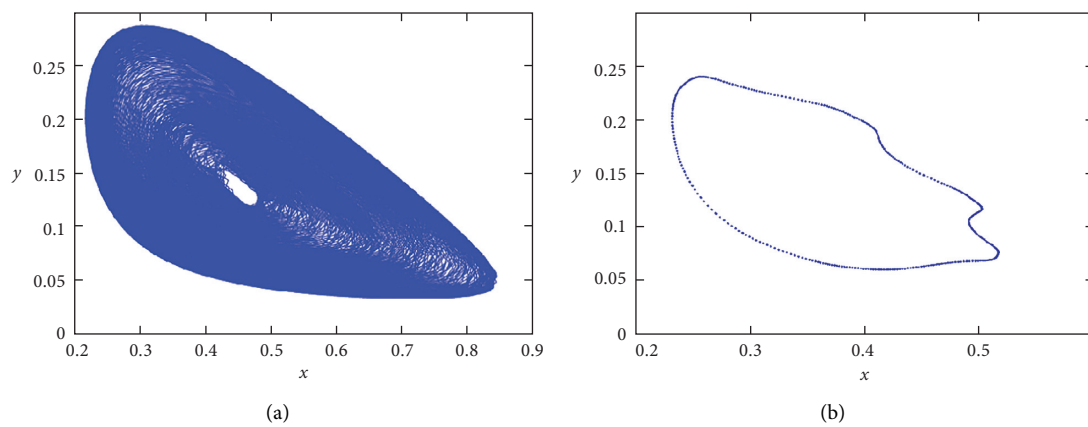
Figure 5: Continued.

(c)

(d)
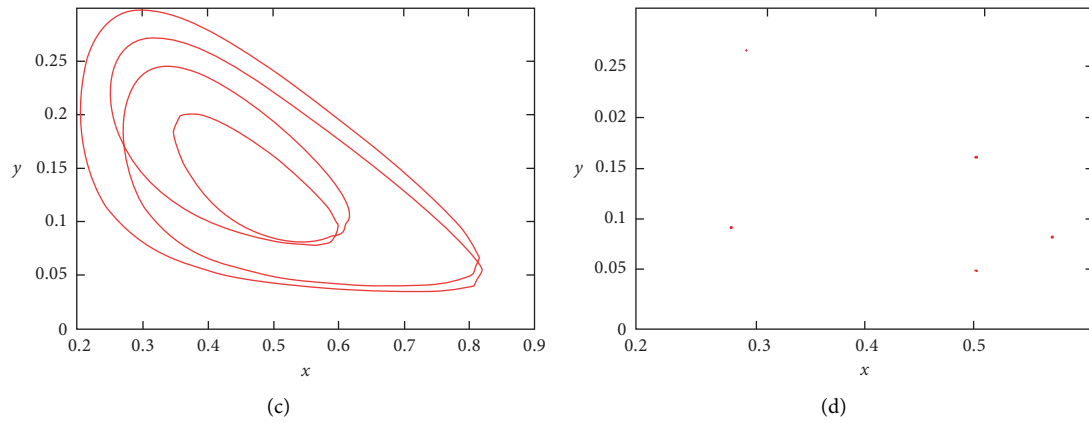
FIGURE 5: Phase space and its corresponding Poincaré section of nonlinear chemical reaction with $f = 0.00165$ and other parameters of Figure 3. (a, b) Quasiperiodic attractor for initial conditions (0.5, 0.5) and (c, d) attractor of period $5T$ for initial conditions (0.1, 0.1).

(a)

(b)

(c)
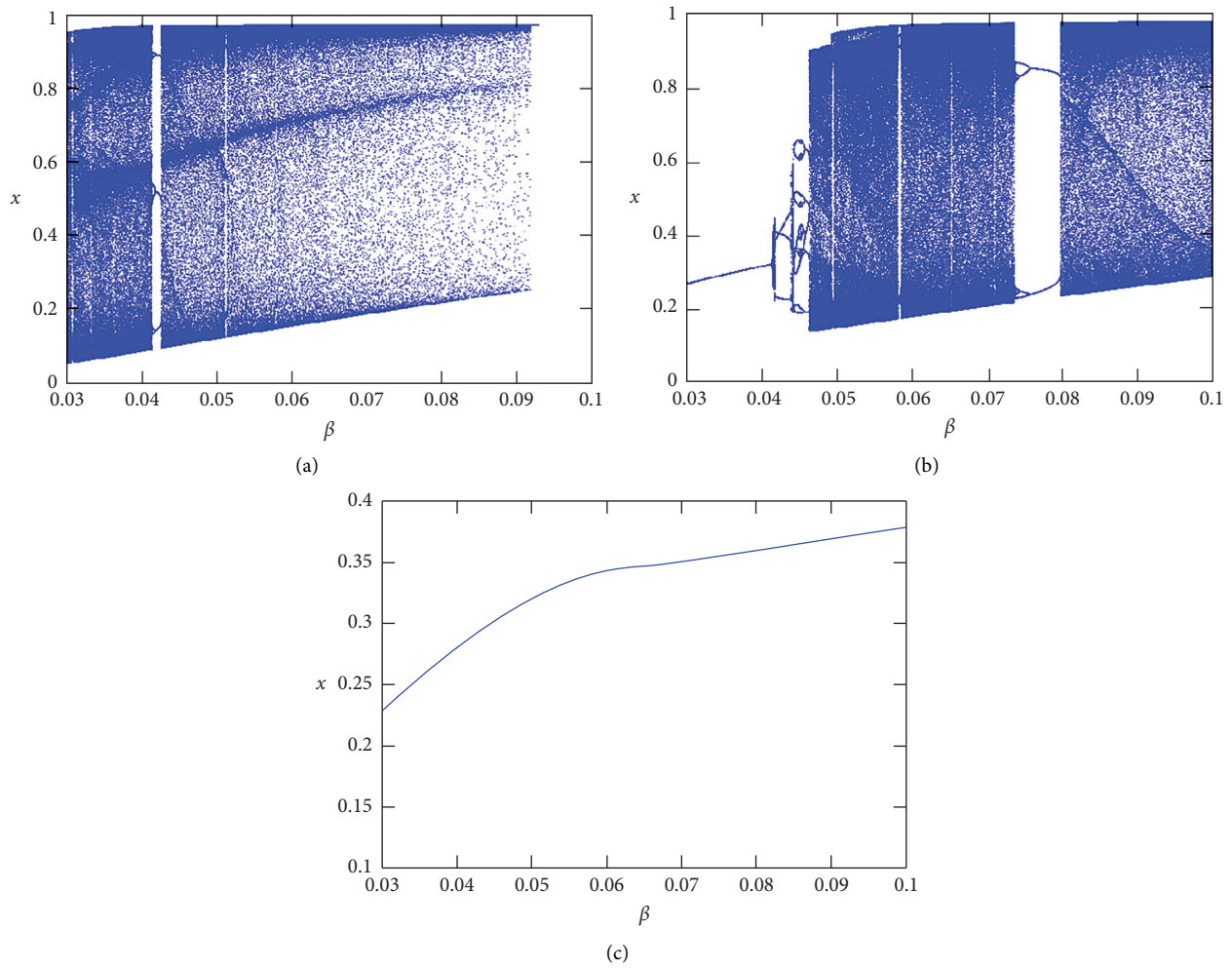
FIGURE 6: Effect of α on bifurcation diagram of nonlinear chemical reaction with $\omega = 0.0481$, $f = 0.00165$, and $g = 0$: (a) $\alpha = 0.02$; (b) $\alpha = 0.03$; (c) $\alpha = 0.05$.

5. Effect of AM Force on the System with $\Omega \gg \omega$

5.1. Vibrational Resonance and Amplitude Response. In a nonlinear dynamical system driven by a biharmonic force consisting of a low-frequency ω and a high-frequency Ω with $\Omega \omega$, when the amplitude g of the high-frequency force is varied, the amplitude response at the low-frequency ω exhibits a resonance. This high-frequency force-induced resonance is called vibrational resonance [3, 6–9]. To determine the VR, we use the amplitude of the response at the frequency ω of the signal. Indeed, using the fourth-order Runge–Kutta algorithm, with time step size, we numerically integrate the system (10) of the chemical reaction under consideration. Thus, the numerical solution $x(\tau)$ allows to calculate the amplitude response Q through the following formula:

$$Q = \frac{\sqrt{Q_s^2 + Q_c^2}}{f}, \qquad (30)$$

where

$$Q_s = \frac{2}{n\pi} \int_0^{nT} x(\tau)\sin \omega\tau d\tau,$$
$$Q_c = \frac{2}{n\pi} \int_0^{nT} x(\tau)\cos \omega\tau d\tau, \qquad (31)$$

with $T = 2\pi/\omega$ the response period and $n = 500$.

We compute Q with a low-frequency force only, a high-frequency only, and with both forces.

For $f = 0$, Q is determined as $\sqrt{Q_s^2 + Q_c^2}$, Q_s and Q_c and representing the Fourier coefficients of the output signal at the frequency $2\pi T$ and Q the amplitude of the response to this same frequency. Indeed, for $\Omega = 80\omega$ with ω being small, the different results are shown in Figures 7–9. Figures 7(a) and 7(b) represent the variation in Q depending, respectively, on f for $g = 0$ and g for $f = 0$ when $\omega = 0.0481$. From Figure 7(a), we note the presence of several peaks, and while $f = 0$, we have a single maximum for which $g = 0.003301$ and $Q = 0.00092802$. When g varies from 0 to 0.05 with $f 6 = 0$ and $\Omega = 80\omega$, the VR appears and we observe that its persistence, its form, its maximum amplitude, and the value of g at the resonance depends not only on f and ω but also on nonlinear parameters α and β of the nonlinear chemical action considered. Indeed, a multiresonance appears for $\omega < 0.06$ (see Figure 8(a)) and disappears when $0.06 \leq \omega < 0.09$. For $0.09 \leq \omega \leq 0.1$, the VR becomes a double resonance with two different Q_{max} (see Figure 8(b)) and disappears again when $0.1 < \omega \leq 0.14$ and then reappears in the form of a monoresonance when $\omega > 0.14$ (see Figure 8(c)). Finally, we note that when g varies from 0 to 0.05, the maximum amplitude Q_{max} decreases when the frequency ω increases.

Figure 9 shows when g varies from 0 to 0.05, $\Omega = 80\omega$ with $\omega = 0.16$, and the influence of the parameters f, α, are β (Figures 9(a)–9(c), respectively) is shown on the VR. From Figure 9(a), we note that the maximum value of the amplitude of the response decreases when f increases and we obtain a double resonance when $f = 0.0011$. Figure 9(b) shows that the parameter α also influences the vibrational resonance. Finally, we notice through Figure 9(c) that VR exists when $0.06 < \beta < 0.08$ and that the parameter β also has the same effects on VR as in the case of α. In conclusion, the birth and the disappearance of the vibrational resonance in the chemical reaction studied can be strongly controlled not only by the AM force but also by the parameters α and β of the chemical reaction.

5.2. Hysteresis, Coexistence of Attractors, and Multistability. In this section, we analyze the effect of g on chemical dynamics when $\Omega \gg \omega$ by looking the hysteresis and coexistence of attractors phenomena. For this, we represent the bifurcation diagram by varying g with $\Omega = 80\omega$ (Figure 10).

When we compare the dynamics of the system when g increases from 0 to 0.1 (blue color, Figure 10(a)) to that obtained when g decreases from 0.1 to 0 (red color, Figure 10(b)), we note that the chemical oscillations of the same kind are observed but with amplitudes that outside x different especially for multiperiodical oscillations. This difference in amplitude noted shows that the chemical oscillations do not follow the same path as going back and forth when we increase g from 0 to 0.1 and when we decrease it from 0.1 to 0: this phenomenon is called hysteresis. There also needs to be a domain where multiperiodic attractors coexist with attractors of period $2T$ and attractors of period $4T$ on the one hand and also the coexistence on the other hand of the chaotic attractors with the attractors of period $4T$ and multiperiodic attractors. The phenomena of hysteresis and coexistence of attractors are very visible in Figure 10 (confirmed by Figure 11) and show multistable behaviors and hysteresis in the system. Thus, for $\Omega = 80\omega$, the chemical oscillations become more complex for the reaction considered. Figure 12 shows the effect of β on the chemical oscillations and the two phenomena obtained. We deduce that when the parameter $\beta \in [0, 0.06]$, the chemical oscillations are not chaotic and there is coexistence of periodic attractors and the presence of hysteresis.

The chemical oscillations become very varied, and we note periodic, multiperiodic, quasiperiodic, and chaotic behaviors with the presence and persistence of hysteresis and the coexistence of multiple attractors when $\beta \in [0.06, 0.7]$. Finally, for $\beta > 0.7$, we observe a total dominance of chaotic oscillations and the disappearance of the hysteresis phenomenon. The parameters α and f have similar effects to that of β reason for which we decided not to represent the figures

(a)

(b)
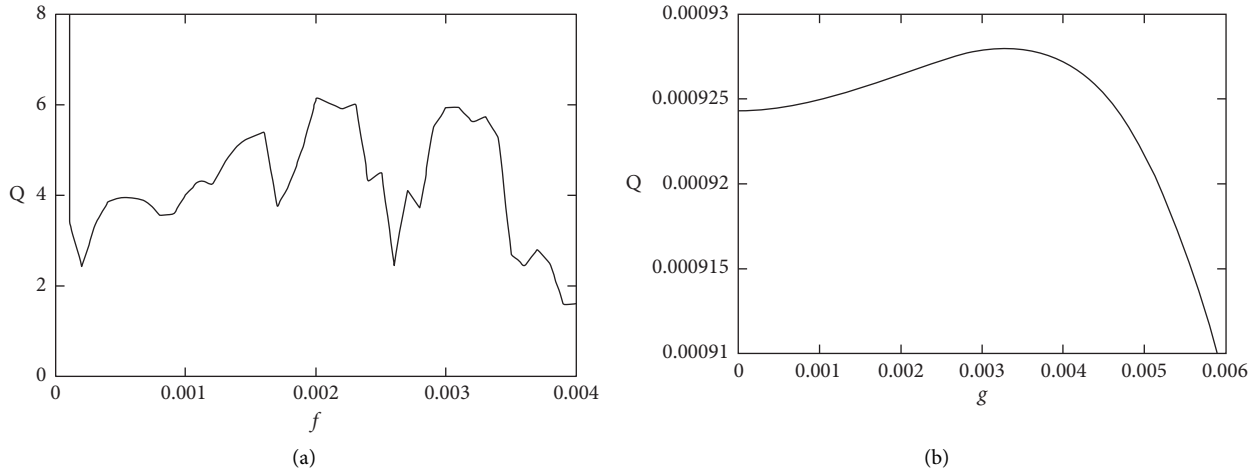
FIGURE 7: (a) Variation in numerically computed Q against the control parameter f with $\omega = 0.0481$, $\alpha = 0.0413$, $\beta = 0.0667$, and $g = 0$; (b) variation in numerically computed Q against the control parameter g with $\omega = 0.0481$, $\Omega = 80\,\omega$, $\alpha = 0.0413$, $\beta = 0.0667$, and $f = 0$.

(a)

(b)

(c)

FIGURE 8: Effect of frequency ω on response amplitude Q versus g with $\omega = 0.0481$, $\Omega = 80\omega$, $\alpha = 0.0413$, $\beta = 0.0667$, and $f = 0.001$.

translating these effects. We notice that the parameter g and the frequencies of the AM force have a very important effect on the dynamics of the system as well as on the phenomena of hysteresis and coexistence of attractors.

More precisely, g can be used to reduce the domains where the oscillations are quasiperiodic, the domains of coexistence of attractors, and to make disappear completely hysteresis.

6. Effect of AM Force in the System with $\omega = \Omega$

Here, the effect of the AM force is analyzed in the case $\omega = \Omega$. For this reason, we chose g as the bifurcation parameter, and the results obtained are shown in Figure 13. From the analysis of Figure 13, it appears that the variation in α can make disappear chaotic and quasiperiodic oscillations but preserves the phenomena of hysteresis and coexistence of

(a)

(b)

(c)
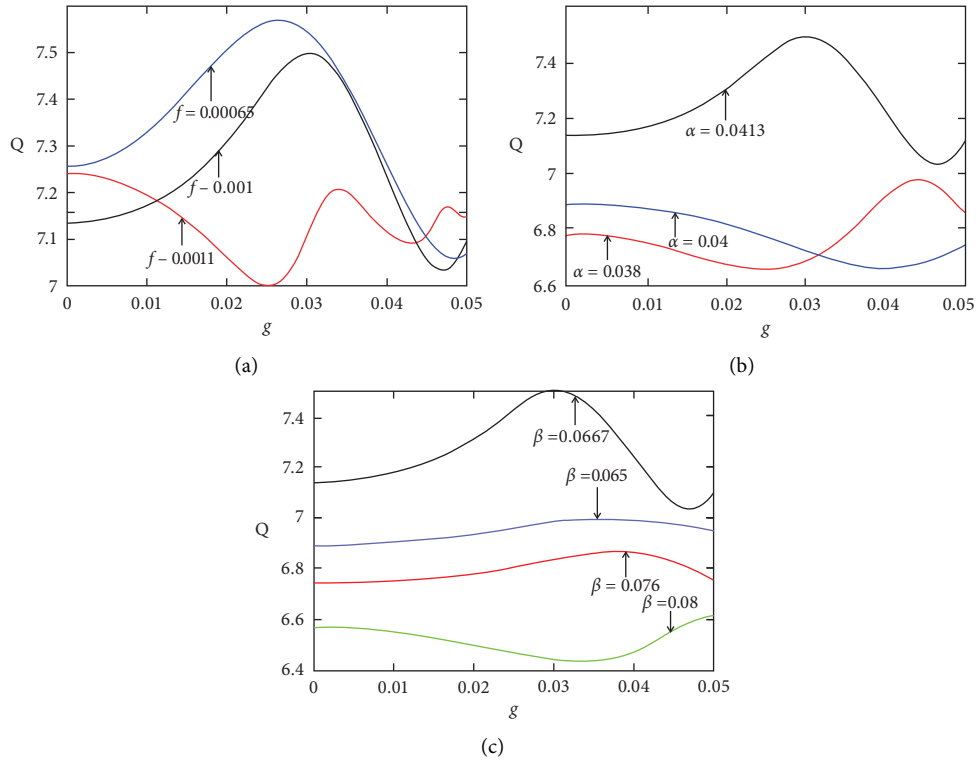
FIGURE 9: (a) Effect of amplitude f on response amplitude Q versus g with $\omega = 0.016$, $\Omega = 80\omega$, $\alpha = 0.0413$, and $\beta = 0.0667$; (b) effect of nonlinear parameter α on response amplitude Q versus g with $\omega = 0.016$, $\Omega = 80\,\omega$, $\beta = 0.0667$, and $f = 0.001$; (c) effect of nonlinear parameter $\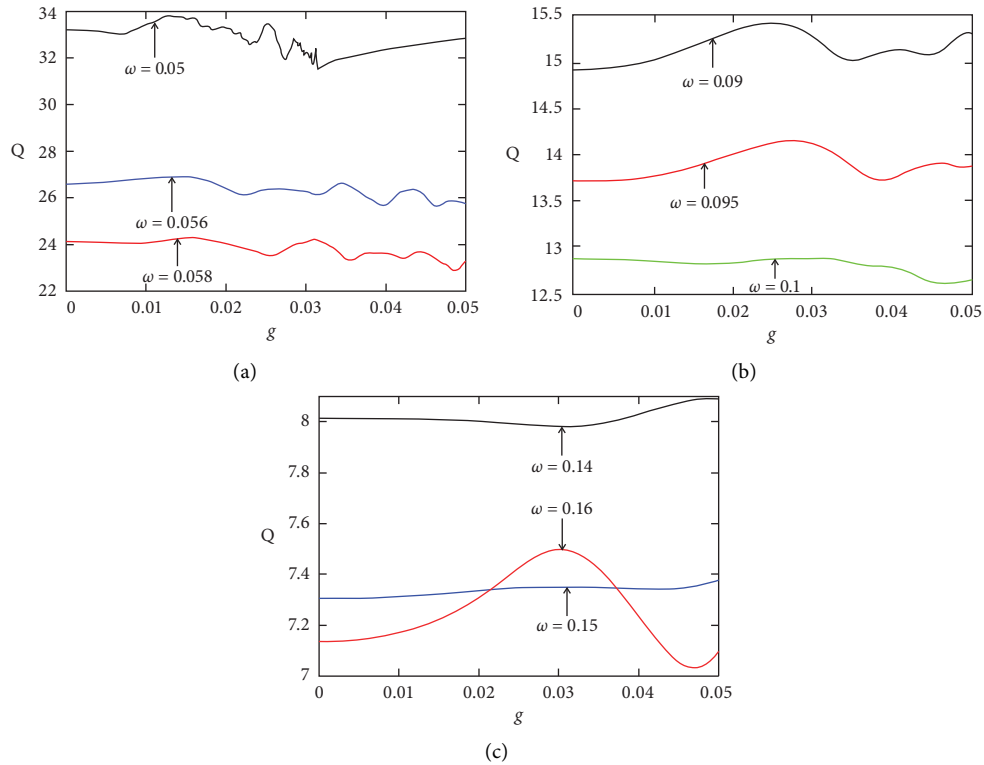beta$ on response amplitude Q versus g with $\omega = 0.016$, $\Omega = 80\,\omega$, $\alpha = 0.0413$, and $f = 0.001$.

(a)

(b)
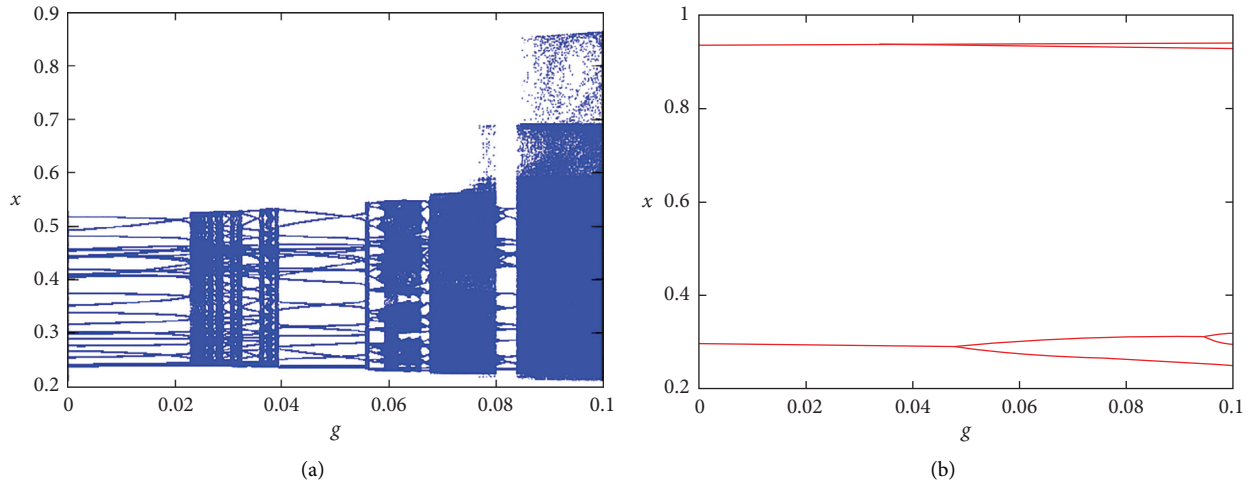
FIGURE 10: Bifurcation diagram and its corresponding Lyapunov exponent of nonlinear chemical reaction with $\omega = 0.0481$, $\Omega = 80\omega$, $\alpha = 0.0413$, $f = 0.002$, and $\beta = 0.0667$. Bifurcation diagrams and its corresponding Lyapunov exponent are obtained by scanning the parameter g upwards (a) and downwards (b).

attractors. In addition, the simulations (the figures of which are not shown here) have shown that the parameters β and f reduce the two phenomena and also act on the chemical oscillations of the model studied. Figure 14 represents the Poincaré section of nonlinear chemical reaction and shows

the 3T-periodic, 4T-periodic, and chaotic oscillations as also obtained in Figure 13. Finally, we look for the effect of the AM force when the frequencies of the amplitude modulation force are not resonant and such that their relationship to each other is irrational.

(a)

(b)
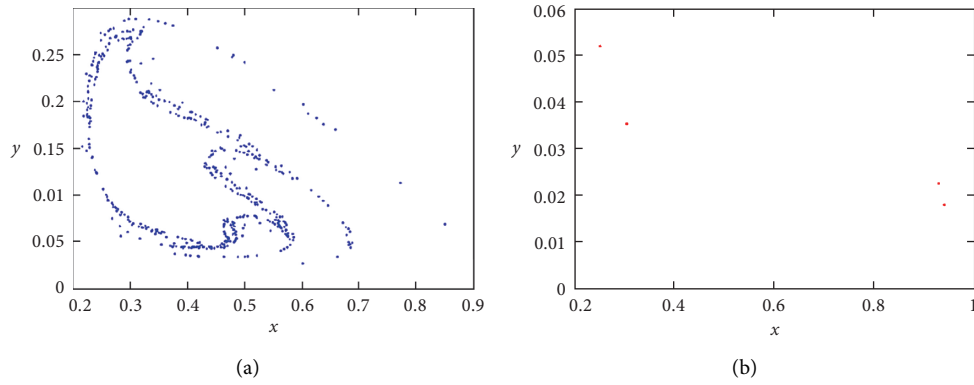
FIGURE 11: Poincaré section of nonlinear chemical reaction with $g = 0.09$ and other parameters of Figure 10: (a) chaotic attractor for initial conditions (0.1, 0.1); (b) attractor of period $4T$ for initial conditions (0.5, 0.5).

(a)

(b)
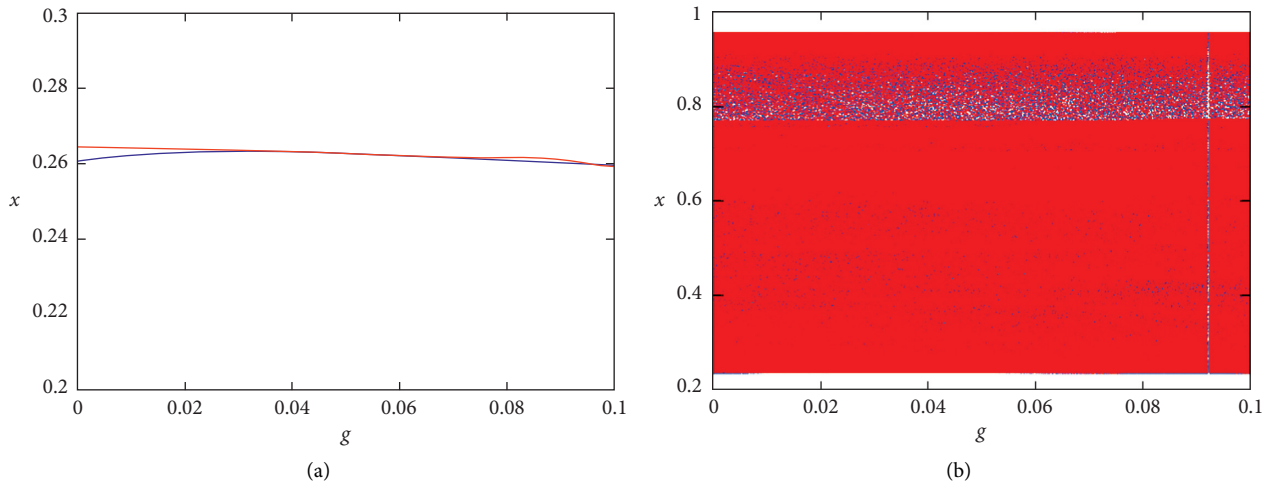
FIGURE 12: Effect of β on bifurcation diagram and its corresponding Lyapunov exponent of nonlinear chemical reaction with $\omega = 0.0481$, $\Omega = 80\,\omega$, $\alpha = 0.0413$, and $f = 0.002$: (a) $\beta = 0.04$; (b) $\beta = 0.08$. Bifurcation diagrams and its corresponding Lyapunov exponent are obtained by scanning the parameter g upwards (blue) and downwards (red).


(a)

(b)
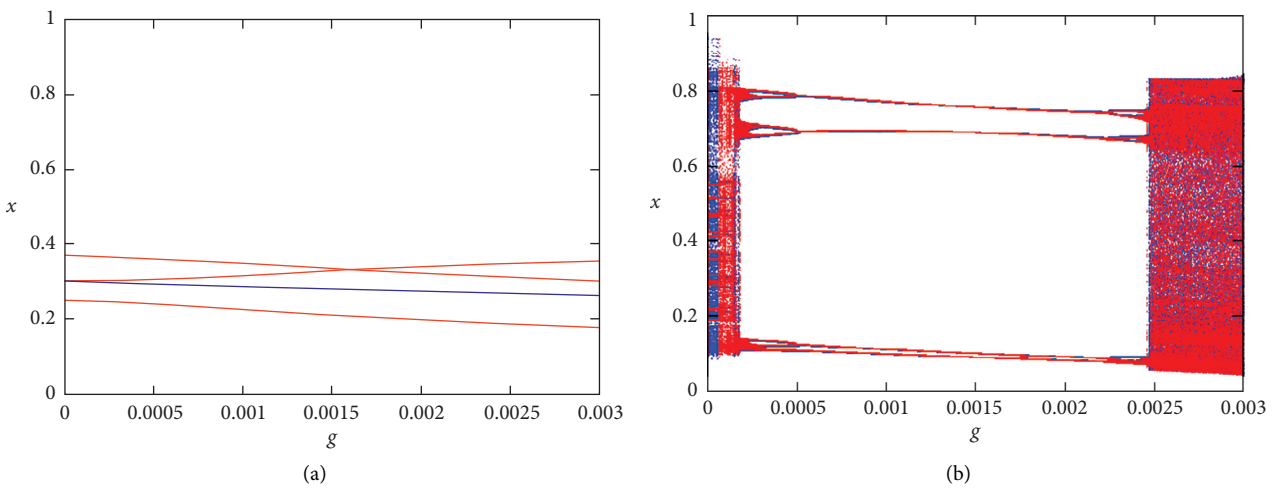
FIGURE 13: Continued.

(c)
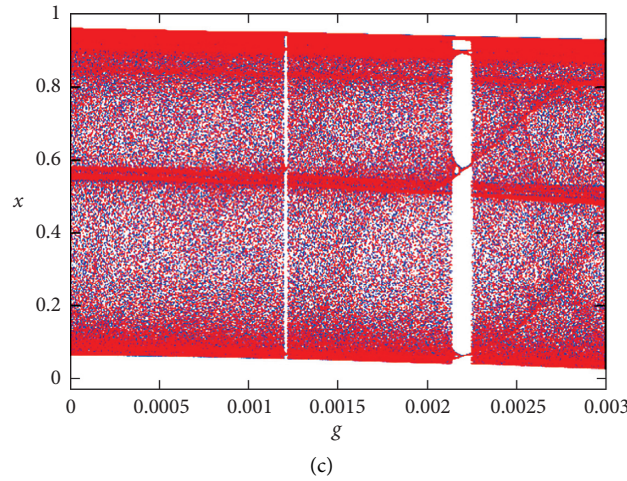
FIGURE 13: Effect of parameter α on bifurcation diagram of nonlinear chemical reaction with $\Omega = \omega = 0.0481$, $f = 0.002$, and $\beta = 0.04$: (a) $\alpha = 0.03$; (b) $\alpha = 0.028$; (c) $\alpha = 0.02$. Bifurcation diagrams and its corresponding Lyapunov exponent are obtained by scanning the parameter g upwards (blue) and downwards (red).

(a)

(b)

(c)
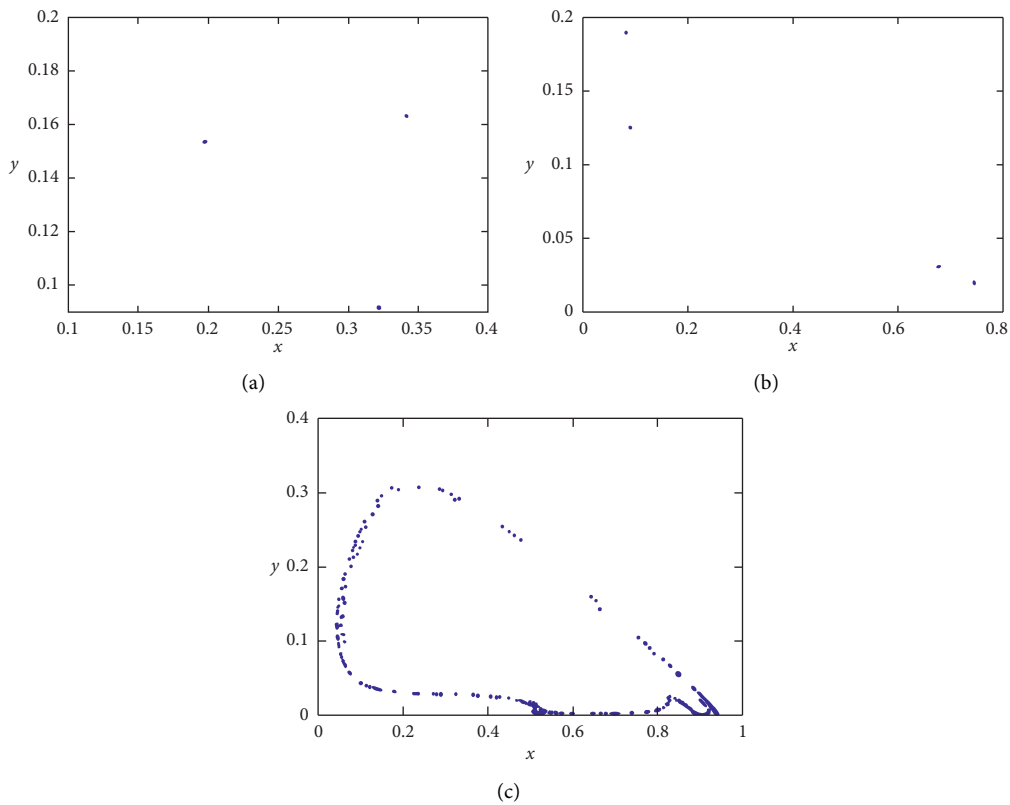
FIGURE 14: Effect of α on Poincaré section of nonlinear chemical reaction with $g = 0.002$ and other parameters of Figure 13: (a) $\alpha = 0.03$: attractor of period $3T$; (b) $\alpha = 0.028$: attractor of period $4T$; (c) $\alpha = 0.02$: chaotic attractor.

For this, we take $\omega = 0.0481$ and $\Omega = (\sqrt{5} - 1)/2$; we also seek the dynamics of the system by constructing the bifurcation diagram considering g as control parameter. Figures 15 and 16, respectively, represent the effects of β and

f on the bifurcation diagram. When we analyze these figures, we note the same remarks as the case where $\omega = \Omega$ except that here each of the parameters β and f can be used to reduce or even eliminate the chaotic chemical oscillations.

(a)

(b)

(c)
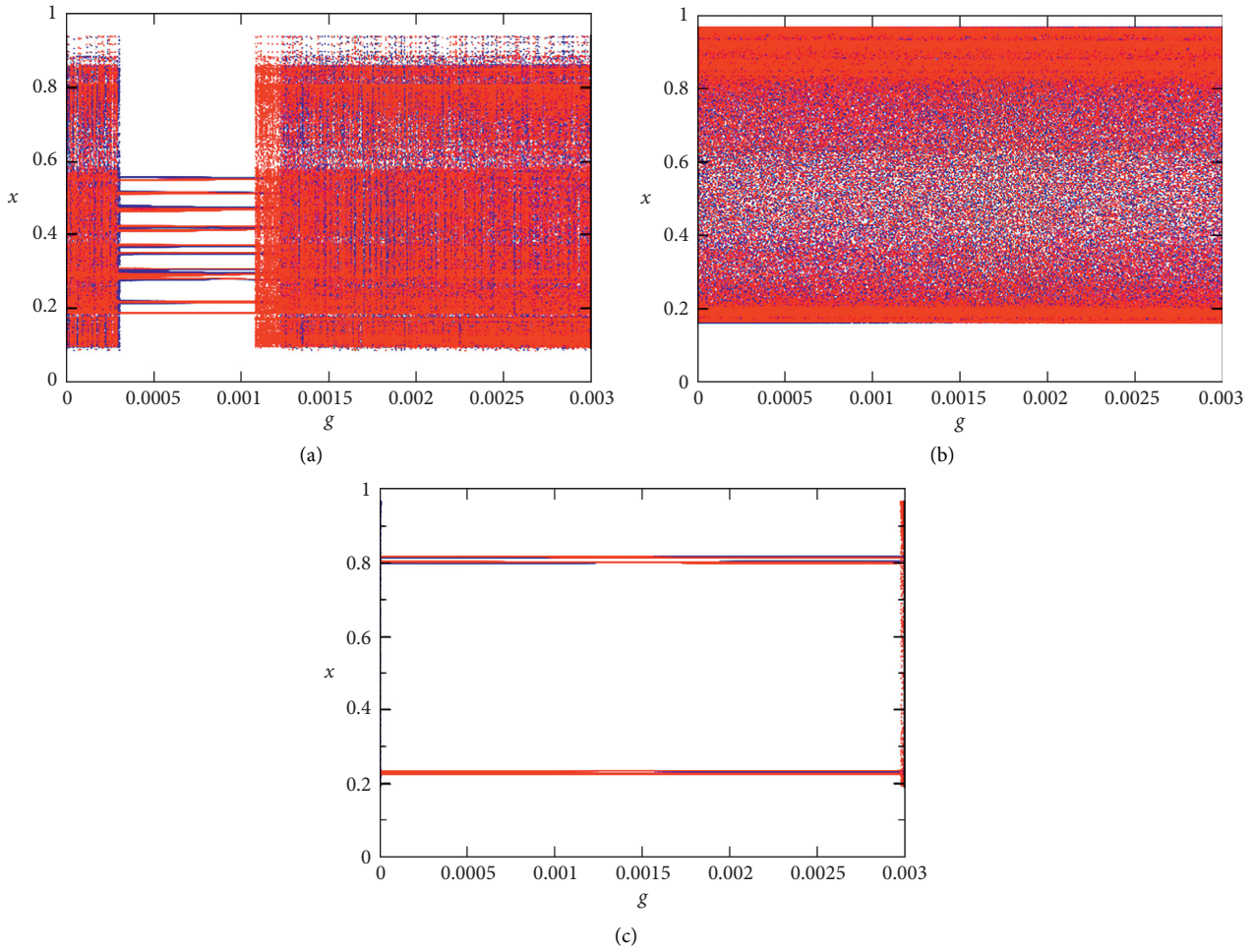
Figure 15: Effect of parameter β on bifurcation diagram of nonlinear chemical reaction with $\omega = 0.0481$, $\Omega = (\sqrt{5}-1)/2$, $f = 0.002$, and $\alpha = 0.28$: (a) $\beta = 0.04$; (b) $\beta = 0.06$; (c) $\beta = 0.07$. Bifurcation diagrams and its corresponding Lyapunov exponent are obtained by scanning the parameter g upwards (blue) and downwards (red).

(a)

(b)

Figure 16: Continued.

FIGURE 16: Effect of parameter f on bifurcation diagram of nonlinear chemical reaction with $\omega = 0.0481$, $\Omega = (\sqrt{5}-1)/2$, $\alpha = 0.28$, and $\beta = 0.04$: (a) $f = 0$; (b) $f = 0.002$; (c) $f = 0.0025$. Bifurcation diagrams and its corresponding Lyapunov exponent are obtained by scanning the parameter g upwards (blue) and downwards (red).
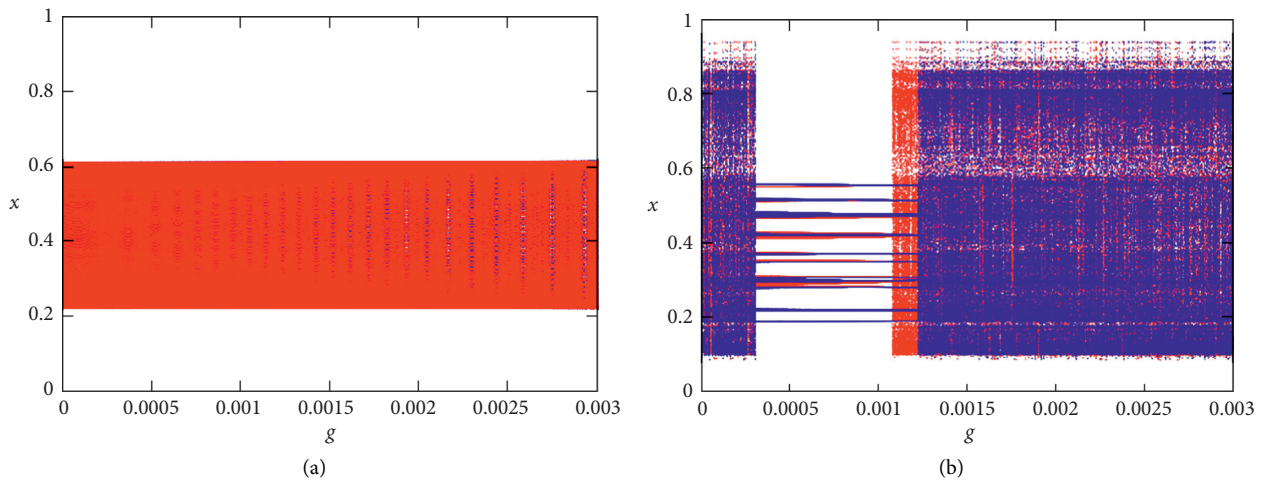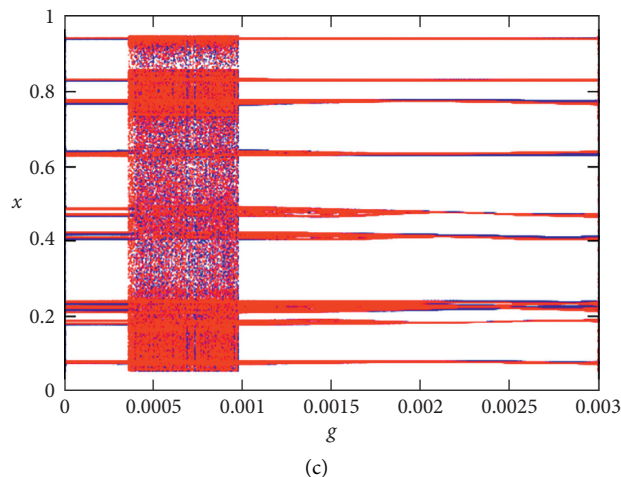
7. Conclusions

In this work, we have studied the influence of an amplitude-modulated force on the chemical oscillations of reactions between four molecules. We have looked for fixed points and their natures when the system is autonomous. It appears that the autonomous system admits exactly four fixed points. The nature of the nontrivial fixed point depends of parameters α and β, and Hopf bifurcation is obtained for these two parameters for the nontrivial equilibrium point. The dynamics of the chemical system considered has been widely analyzed in the unmodulated case, and periodic, multiperiodic, quasiperiodic, and chaotic chemical oscillations have been obtained. Domains of existence of hysteresis, of coexistence of quasiperiodic attractors with attractors of period $5T$ and attractors of period $6T$, and of coexistence of multiperiodic attractors with chaotic attractors have been obtained. From the simulations made, it should be noted that, for certain values of the nonlinear parameters α and β, the complex dynamics can be controlled and even reduced to a periodic oscillation. For $g \neq 0$ and for $\Omega \neq \omega$, complex phenomena such as vibrational resonance (VR), hysteresis, and coexistence of attractors appear and are very remarkable and can be well controlled either by the AM force or by the parameters α and β. The domains of existence of these different phenomena are less important when $\Omega = \omega$. When the frequencies of the amplitude modulation force are not resonant and are such that their relationship to each other is irrational, the multiperiodic attractors when they exist are of period $\geq 4T$ and their domains of existence are more important. Finally, our work confirmed the chaotic oscillation and the Hopf bifurcation obtained in [5] and proved that the appearance of VR, hysteresis, multistability, and coexistence of various attractors in the chemical reaction is considered. The presence of VR shows that the amplitude of oscillations of concentrations can be explored, while the hysteresis phenomenon indicates that the amplitude of oscillations of concentrations will not be able to follow the same path of evolution when the control parameter increases or decreases following the same path. The multistability and the coexistence of attractors obtained reveal that the stable or unstable nature of the chemical oscillations and of the chemical attractors in the same domain of the parameters is considered. The use of the amplitude modulated force has shown that the various complex phenomena obtained can be controlled.

Data Availability

No data were used in this study.

Conflicts of Interest

The authors declare that there are no conflicts of interest regarding the publication of this paper.

References

[1] S. Strogatz, *Nonlinear Dynamics and Chaos: With Applications to Physics, Biology, Chemistry, and Engineering*, Ingram Publisher Services US, New York, NY, USA, 2nd edition, 2014.

[2] H. Binous and A. Bellagi, "Introducing nonlinear dynamics to chemical and biochemical engineering graduate students using Mathematica," *Computer Applications in Engineering Education*, vol. 27, no. 1, pp. 1–19, 2018.

[3] S. Guruparan, B. Ravindran Durai Nayagam, V. Ravichandran, V. Chinnathambi, and S. Rajasekar, "Hysteresis, vibrational resonance and chaos in brusselator chemical system under the excitation of amplitude modulated force," *Chemical Science Review and Letters*, vol. 4, no. 15, pp. 870–879, 2015.

[4] M. Gruebelle and P. G. Wolynes, "Vibrational energy flow and chemical reactions," *Accounts of Chemical Research*, vol. 37, pp. 261–267, 2004.

[5] A. Shabunin, V. Astakhov, V. Demidov et al., "Modeling chemical reactions by forced limit-cycle oscillator:

synchronization phenomena and transition to chaos," *Chaos, Solitons & Fractals*, vol. 15, no. 2, pp. 395–405, 2003.

[6] I. I. Blekhman and P. S. Landa, "Conjugate resonances and bifurcations in nonlinear systems under biharmonical excitation," *International Journal of Non-linear Mechanics*, vol. 39, no. 3, pp. 421–426, 2004.

[7] T. O. Roy-Layinde, J. A. Laoye, O. O. Popoola, and U. E. Vincent, "Analysis of vibrational resonance in biharmonically driven plasma," *Chaos*, vol. 26, pp. 1–9, 2016.

[8] P. S. Landa and P. V. E. McClintock, "Vibrational resonance," *Journal of Physics A: Mathematical General*, vol. 33, no. 45, pp. 433–438, 2000.

[9] C. Jeevarathinam, S. Rajasekar, and M. A. F. Sanju´an, "Vibrational resonance in the Duffing oscillator with distributed time-delayed feedback," *Journal of Applied Nonlinear Dynamics*, vol. 4, pp. 1–15, 2015.

[10] P. Sarkar and D. S. Ray, "Vibrational antiresonance in nonlinear coupled systems," *Physical Review E*, vol. 99, no. 52221, pp. 1–7, 2019.

[11] D. L. Olabodé, C. H. Miwadinou, V. A. Monwanou, and J. B. Chabi Orou, "Effects of passive hydrodynamics force on harmonic and chaotic oscillations in nonlinear chemical dynamics," *Physica D*, vol. 386387, pp. 49–59, 2019.

[12] C. H. Miwadinou, A. V. Monwanou, J. Yovogan, L. A. Hinvi, P. R. Nwagoum Tuwa, and J. B. Chabi Orou, "Modeling nonlinear dissipative chemical dynamics by a forced modified Van der Pol-Duffing oscillator with asymmetric potential: chaotic behaviors predictions," *Chinese Journal of Physics*, vol. 56, no. 3, pp. 1089–1104, 2018.

[13] H. G. Enjieu Kadji and B. R. Nana Nbendjo, "Passive aerodynamics control of plasma instabilities," *Communications in Nonlinear Science and Numerical Simulation*, vol. 17, no. 4, pp. 1779–1794, 2012.

[14] C. H. Miwadinou, A. V. Monwanou, L. A. Hinvi, and J. B. Chabi Orou, "Effect of amplitude modulated signal on chaotic motions in a mixed Rayleigh-Liénard oscillator," *Chaos, Solitons & Fractals*, vol. 113, pp. 89–101, 2018.

[15] C. H. Miwadinou, A. V. Monwanou, A. A. Koukpemedji, Y. J. F. Kpomahou, and J. B. Chabi Orou, "Chaotic motions in forced mixed Rayleigh-Li´enard oscillator with external and parametric periodic excitations," *International Journal of Bifurcation and Chaos*, vol. 28, no. 3, pp. 1–16, 2018.

[16] A. Shabunin, F. Baras, and A. Provata, "Oscillatory reactive dynamics on surfaces: a lattice limit cycle model," *Physical Review E*, vol. 66, pp. 1–11, 2002.

[17] G. Nicolis and I. Prigogine, *Self-organization in Nonequilibrium Systems*, Wiley, New York, NY, USA, 1977.

[18] R. Imbihl and G. Ertl, "Oscillatory kinetics in heterogeneous catalysis," *Chemical Reviews*, vol. 95, no. 3, pp. 697–733, 1995.

[19] C. G. Takoudis, L. D. Schmidt, and R. Aris, "Isothermal sustained oscillations in a very simple surface reaction," *Surface Science*, vol. 105, no. 1, pp. 325–333, 1981.

[20] I. G. Kevrekidis, L. D. Schmidt, and R. Aris, "Some common features of periodically forced reacting systems," *Chemical Engineering Science*, vol. 41, no. 5, pp. 1263–1276, 1986.

[21] M. A. Taylor and I. G. Kevrekidis, "Some common dynamic features of coupled reacting systems," *Physica D: Nonlinear Phenomena*, vol. 51, no. 1–3, pp. 274–292, 1991.

[22] C. Hayashi, *Nonlinear Oscillations in Physical Systems*, McGraw-Hill, New York, NY, USA, 1964.

[23] A. H. Nayfeh, *Introduction to Perturbation Techniques*, John Wiley & Sons, New York, NY, USA, 1981.

WILEY | Hindawi

Research Article

Dynamics Analysis of a Betel Nut Addiction Spreading Model on Scale-Free Networks

He Wang,[1] Tao Li [ID],[1,2] Xinming Cheng,[3] Yu Kong,[1] and Yangmei Lei[1]

[1]*School of Electronics and Information, Yangtze University, Jingzhou 434023, China*
[2]*National Demonstration Center for Experimental Electrical and Electronic Education, Yangtze University, Jingzhou 434023, China*
[3]*School of Automation, Central South University, Changsha 410083, China*

Correspondence should be addressed to Tao Li; taohust2008@163.com

Medical research has shown that overeating betel nut can be addictive and can damage health. More serious cases may cause mouth cancer and other diseases. Even worse, people's behavior habit of chewing betel nut may influence each other through social interaction with direct or indirect ways, such as face-to-face communication, Facebook, Twitter, microblog, and WeChat, which leads to the spreading phenomenon of betel nut addiction. In order to investigate the dynamic spreading characteristics of betel nut addiction, a PMSR (Potential-Mild-Severe-Recovered) betel nut addiction spreading model is presented on scale-free networks. The basic reproductive number R_0 and equilibria are derived. Theoretical results indicate that the basic reproductive number R_0 is significantly dependent on the topology of the underlying networks, and some influence parameters. The existence of equilibria is determined by the basic reproductive number R_0. Furthermore, we prove that if $R_0 < 1$ the addiction-elimination equilibrium is globally asymptotically stable. If $R_0 > 1$, the betel nut addiction spreading is permanent, and the addiction-prevailing equilibrium is globally attractive. Finally, numerical simulations confirm the theoretical analysis results.

1. Introduction

The habit of chewing betel nut is common in many places around the world [1–8]. It is worth noting that overeating betel nut can be addictive and is harmful to health [8, 9]. It is found that betel nut affects the health of the nervous, gastrointestinal, metabolic, respiratory, and reproductive systems. More serious cases may cause mouth cancer and other diseases. Betel nut is classified in the first category of carcinogens by the International Agency for Research on Cancer [9–11]. Even worse, people's behavior habit of chewing betel nut may influence each other through social contact, which leads to the spreading phenomenon of betel nut addiction. The widespread spread of betel nut addiction, in turn, exacerbates the damage to people's health and even the whole society.

It is very important to control the spreading phenomenon of betel nut addiction. In recent years, the research on

betel nut addiction has attracted the attention of many scholars and researchers. Murphy et al. confirmed that the formation of the "chewing betel nut" habit could be due to exposure to and influence by betel nut chewers through statistical analysis [12]. As indicated in [13], the cultural differences can affect the spreading of betel nut addiction in society. Ghani et al. identified the factors which influence the development of betel nut addiction. They also proposed the health policies to prevent addiction [14]. Moss et al. [15] showed that the critical factors of addiction were contact with addicts and the self-prevention consciousness. Many researchers studied the addictiveness and harmfulness of the "chewing betel nut" habit [16–19], but few focused on the spreading dynamics of betel nut addiction. There are some studies in social information and disease spreading dynamics [20–25]. Liu et al. studied the spreading dynamics of cyber violence [26]. Barabási and Albert studied the impact of neighboring infection on the computer virus spread [27].

These studies can give some help for the analysis of the spreading dynamics of betel nut addiction. Through the study of addiction spreading dynamics, we can comprehensively and systematically learn about the addiction spreading mechanism and influence factors, which is helpful to control the spread of betel nut addiction. Meanwhile, some researchers found that the scale-free property is an important property of social networks [28–32]. Obviously, the spread of betel nut addiction is based on social networks. So, based on scale-free networks, we study the spreading dynamics of betel nut addiction in the paper. Apparently, the marketing strategy of betel nut has a great influence on sales, and at the same time, it affects the spreading of betel nut addiction. Taking into account the influence of betel nut advertising campaigns and the heterogeneity of underlying spreading networks, we present a new comprehensively PMSR (Potential-Mild-Severe-Recovered) betel nut addiction spreading model.

The rest of the paper is as follows. In Section 2, the PMSR betel nut addiction spreading model is proposed and described. In Section 3, the basic reproductive number and equilibriums are derived at first. Then, we analyze the globally asymptotic stability of addiction-elimination equilibrium, the permanence of the addiction spreading, and the global attractivity of addiction-prevailing equilibrium. Section 4 presents the results of our numerical simulation. Finally, we conclude the paper in Section 5.

2. Model Formulation

We present a new comprehensively PMSR (Potential-Mild-Severe-Recovered) betel nut addiction spreading model. The model has the spread sketch in Figure 1. In the model, nodes are used to stand for individuals, and edges are used to stand for the relationships between individuals. The whole population is divided into four distinct classes, namely, potential individuals (P), mild addicts (M), severe addicts (S), and recovered individuals (R). P nodes refer to the people who do not have addictive behavior of chewing betel nut; M nodes refer to the people who have mild addiction of the "chewing betel nut" habit; S nodes refer to the people who have severe addiction of the "chewing betel nut" habit; and R nodes refer to the people who get rid of the addiction.

In the spreading process of betel nut addiction, these states are subjected to the following rules:

(1) If a potential individual is influenced by a mild addict with direct or indirect ways, such as face-to-face communication, Facebook, Twitter, microblog, and WeChat, then he or she will convert into a mild addict with probability ρ_1. Similarly, if a potential individual is influenced by a severe addict with direct or indirect ways, then he or she will convert into a mild addict with probability ρ_2.

(2) The parameter α is defined as an influence parameter of betel nut advertisements. In real life, the marketing strategy of betel nut will influence people to try to purchase betel nut.
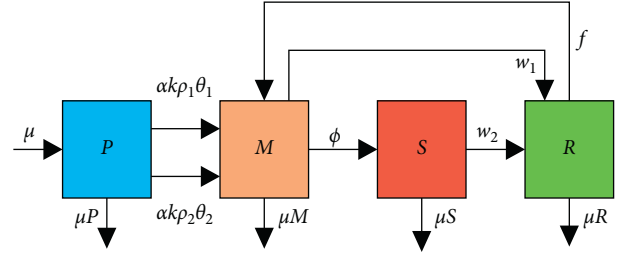
FIGURE 1: The flow diagram of the PMSR model.

(3) A mild addict may convert into a severe addict with probability φ or get rid of the addiction with probability w_1.

(4) The severe addict may get rid of the addiction with probability w_2.

(5) Considering the relapse of addiction, a recovered individual may convert into a mild addict with probability f.

(6) Here, we assume that the immigration rate equals the emigration rate, and the rate constant is μ.

We define $P_k(t)$, $M_k(t)$, $S_k(t)$, and $R_k(t)$ as the relative densities of potential individuals, mild addicts, severe addicts, and recovered individuals nodes of degree k at time t, respectively. According to the above description and assumption, we can get the PMSR model as follows:

$$
\begin{cases}
\dfrac{dP_k(t)}{dt} = \mu - k\alpha(\rho_1\theta_1 + \rho_2\theta_2)P_k(t) - \mu P_k(t), \\[2mm]
\dfrac{dM_k(t)}{dt} = k\alpha(\rho_1\theta_1 + \rho_2\theta_2)P_k(t) + fR_k(t) \\[2mm]
\qquad\qquad - (\varphi + \mu + w_1)M_k(t), \\[2mm]
\dfrac{dS_k(t)}{dt} = \varphi M_k(t) - (w_2 + \mu)S_k(t), \\[2mm]
\dfrac{dR_k(t)}{dt} = \omega_2 S_k(t) + w_1 M_k(t) - (f + \mu)R_k(t),
\end{cases}
\tag{1}
$$

where $\theta_1(t)$ and $\theta_2(t)$ denote the probability of a contact pointing to a mild addict and a severe addict, respectively, and

$$
\theta_1(t) = \frac{1}{\langle k \rangle} \sum_{k=1}^{\infty} kH(k)M_k(t),
\tag{2}
$$

$$
\theta_2(t) = \frac{1}{\langle k \rangle} \sum_{k=1}^{\infty} kH(k)S_k(t).
\tag{3}
$$

Here, $\langle k \rangle = \sum_k kH(k)$ represents the average degree values of the network and $H(k)$ represents the degree distribution. $M(t) = \sum_k H(k)M_k(t)$ is the density of all the mild addicts and $S(t) = \sum_k H(k)S_k(t)$ is the density of all the severe addicts.

According to the normalization conditions, we have

$$P_k(t) + M_k(t) + S_k(t) + R_k(t) = 1. \qquad (4)$$

Obviously, the initial values for system (1) are as follows:

$$\begin{aligned} P_k(0) &> 0, \\ M_k(0) &\geq 0, \\ S_k(0) &\geq 0, \\ C_k(0) &\geq 0, \quad k = 1, 2, ..., n. \end{aligned} \qquad (5)$$

Then, we obtain that

$$\begin{aligned} P_k(t) &> 0, \\ M_k(t) &\geq 0, \\ S_k(t) &\geq 0, \\ C_k(t) &\geq 0, \quad k = 1, 2, ..., n \text{ and } t \geq 0. \end{aligned} \qquad (6)$$

3. Stability Analysis of the Model

In this section, we analyze the dynamic properties of the PMSR betel nut addiction spreading model.

Theorem 1. *According to system (1), the basic reproductive number is defined as follows:*

$$R_0 = \frac{\alpha(f + \mu)[\rho_1(\mu + w_2) + \rho_2\varphi]}{[(w_2 + \mu)(w_1 + f + \mu) + \varphi(w_2 + f + \mu)]\mu}. \qquad (7)$$

There always exists an addiction-elimination equilibrium $E_0(1, 0, 0, 0)$, and if $R_0 > 1$, system (1) has a unique addiction-prevailing equilibrium $E_+(P_k^*, M_k^*, S_k^*, R_k^*)$.

Proof. It can be easy to find that system (1) satisfies $R_k(t) = 1 - P_k(t) - M_k(t) - S_k(t)$. According to system (1), we can get

$$\begin{cases} \dfrac{dP_k(t)}{dt} = \mu - k\alpha(\rho_1\theta_1 + \rho_2\theta_2)P_k(t) - \mu P_k(t), \\[2mm] \dfrac{dM_k(t)}{dt} = k\alpha(\rho_1\theta_1 + \rho_2\theta_2)P_k(t) \\[2mm] \qquad + f(1 - P_k(t) - M_k(t) - S_k(t)) - (\varphi + \mu + w_1)M_k(t), \\[2mm] \dfrac{dS_k(t)}{dt} = \varphi M_k(t) - (d + \mu)S_k(t). \end{cases} \qquad (8)$$

Obviously, there is an addiction-elimination equilibrium $E_0(1, 0, 0, 0)$ in system (1). It is easy to verify that system (8) satisfies the conditions $(A_1) - (A_5)$ in [33]. By using the next generation matrix method [33], system (8) can get

$$\frac{dx}{dt} = Z(x) - V(x), \qquad (9)$$

where

$$x = (P_k, M_k, S_k)^T,$$

$$Z(x) = \begin{pmatrix} -k\alpha(\rho_1\theta_1(t) + \rho_2\theta_2(t))P_k(t) \\ k\alpha(\rho_1\theta_1(t) + \rho_2\theta_2(t))P_k(t) \\ 0 \end{pmatrix}, \qquad (10)$$

$$V(x) = \begin{pmatrix} \mu P_k(t) \\ (w_1 + \mu + \varphi)M_k(t) - fC_k(t) \\ (w_2 + \mu)S_k(t) - \varphi M_k(t) \end{pmatrix}.$$

At the addiction-elimination equilibrium E_0, the Jacobian matrices of $Z(x)$ and $V(x)$ can get

$$\begin{aligned} Z &= JZ(E_0) \\ &= \begin{pmatrix} 0 & Z_{12} & Z_{13} \\ 0 & Z_{22} & Z_{23} \\ 0 & 0 & 0 \end{pmatrix}, \\ V &= JV(E_0) \\ &= \begin{pmatrix} V_{11} & 0 & 0 \\ V_{21} & V_{22} & V_{23} \\ 0 & V_{32} & V_{33} \end{pmatrix}, \end{aligned} \qquad (11)$$

where

$$Z_{12} = \frac{-\alpha\rho_1}{\langle k\rangle}\begin{bmatrix} 1 \\ 2 \\ \vdots \\ n \end{bmatrix}\begin{bmatrix} 1P(1) & 2P(2) & \cdots & nP(n) \end{bmatrix},$$

$$Z_{13} = \frac{-\alpha\rho_2}{\langle k\rangle}\begin{bmatrix} 1 \\ 2 \\ \vdots \\ n \end{bmatrix}\begin{bmatrix} 1P(1) & 2P(2) & \cdots & nP(n) \end{bmatrix},$$

$$Z_{22} = \frac{\alpha\rho_1}{\langle k\rangle}\begin{bmatrix} 1 \\ 2 \\ \vdots \\ n \end{bmatrix}\begin{bmatrix} 1P(1) & 2P(2) & \cdots & nP(n) \end{bmatrix},$$

$$Z_{23} = \frac{\alpha\rho_2}{\langle k\rangle}\begin{bmatrix} 1 \\ 2 \\ \vdots \\ n \end{bmatrix}\begin{bmatrix} 1P(1) & 2P(2) & \cdots & nP(n) \end{bmatrix}.$$

$$(12)$$

Here,

$$
\begin{aligned}
V_{11} &= \mu I, \\
V_{21} &= f I, \\
V_{22} &= (w_1 + \mu + \varphi + f) I, \\
V_{23} &= f I, \\
V_{32} &= -\varphi I, \\
V_{33} &= (w_2 + \mu) I,
\end{aligned}
\tag{13}
$$

where I is the identity matrix. So, we can get the basic reproductive number:

$$
\begin{aligned}
R_0 &= \rho(ZV^{-1}) \\
&= \frac{\langle k^2 \rangle}{\langle k \rangle} \frac{\alpha(f + \mu)[\rho_1(\mu + w_2) + \rho_2\varphi]}{[(w_2 + \mu)(w_1 + f + \mu) + \varphi(w_2 + f + \mu)]\mu},
\end{aligned}
\tag{14}
$$

where $\langle k^2 \rangle = \sum_k k^2 P(k)$.

Next, it is clear that system (1) has an equilibrium $E_0 = \{(1, 0, 0, 0)\}_k$. To get the addiction-prevailing equilibrium $E^*(P_k^*, M_k^*, S_k^*, R_k^*)$, system (1) satisfies

$$
\begin{aligned}
\frac{\mathrm{d}P_k(t)}{\mathrm{d}t} &= 0, \\
\frac{\mathrm{d}M_k(t)}{\mathrm{d}t} &= 0, \\
\frac{\mathrm{d}S_k(t)}{\mathrm{d}t} &= 0, \\
\frac{\mathrm{d}R_k(t)}{\mathrm{d}t} &= 0.
\end{aligned}
\tag{15}
$$

So, we can know

$$
\begin{cases}
\mu - k\alpha(\rho_1\theta_1 + \rho_2\theta_2)P_k(t) - \mu P_k(t) = 0, \\
k\alpha(\rho_1\theta_1 + \rho_2\theta_2)P_k(t) + fR_k(t) - (\varphi + \mu + w_1)M_k(t) = 0, \\
\varphi M_k(t) - (w_2 + \mu)S_k(t) = 0, \\
w_2 S_k(t) + w_1 M_k(t) - (f + \mu)R_k(t) = 0.
\end{cases}
\tag{16}
$$

According to the above equations, we get

$$
\begin{cases}
P_k = \dfrac{\mu[w_1(w_2 + \mu) + (f + \mu)(w_2 + \mu) + \varphi(w_2 + f + \mu)]}{k\alpha(\rho_1\theta_1 + \rho_2\theta_2)(w_2 + \mu)(f + \mu)}M_k, \\[4mm]
S_k = \dfrac{\varphi}{w_2 + \mu}M_k, \\[4mm]
R_k = \dfrac{(w_2 + \mu)w_1 + \varphi w_2}{(w_2 + \mu)(f + \mu)}M_k.
\end{cases}
\tag{17}
$$

By using the normalization condition $P_k^*(t) + M_k^*(t) + S_k^*(t) + R_k^*(t) = 1$, we get

$$
\begin{cases}
P_k^* = \dfrac{\mu[w_1(w_2 + \mu) + (f + \mu)(w_2 + \mu) + \varphi(w_2 + f + \mu)]}{k\alpha(\rho_1\theta_1^* + \rho_2\theta_2^*)(w_2 + \mu)(f + \mu)}M_k^*, \\[4mm]
M_k^* = \dfrac{(f + \mu)w_1(w_2 + \mu) + \mu[(f + \mu)(w_2 + \mu) + \varphi(w_2 + f + \mu)]}{(w_2 + \mu)(f + \mu)(w_1 + \mu + \varphi)}, \\[4mm]
S_k^* = \dfrac{\varphi}{w_2 + \mu}M_k^*, \\[4mm]
R_k^* = \dfrac{(w_2 + \mu)w_1 + \varphi w_2}{(w_2 + \mu)(f + \mu)}M_k^*.
\end{cases}
\tag{18}
$$

And, for $\theta_1^* = 1/\langle k \rangle \sum_{k=1}^{\infty} kP(k)M_k^*(t)$, $\theta_2^* = 1/\langle k \rangle \sum_{k=1}^{\infty} kP(k)S_k^*(t)$, we get

$$
\begin{aligned}
\theta_1^* &= \frac{w_2 + \mu}{\varphi}\theta_2^*, \\
\theta_2^* &= \frac{\varphi}{w_2 + \mu}\theta_1^*.
\end{aligned}
\tag{19}
$$

By substituting the second equation of system (16) into equation (2), we get

$$
\begin{aligned}
\theta_1^* &= \frac{1}{\langle k \rangle} \sum_{k=1}^{\infty} kP(k)M_k^*(t) \\
&= \frac{1}{\langle k \rangle} \sum_{k=1}^{\infty} kP(k) \frac{k\alpha(\rho_1\theta_1^* + \rho_2\theta_2^*)(w_2 + \mu)(f + \mu)}{[k\alpha(\rho_1\theta_1^* + \rho_2\theta_2^* + \mu)][(w_2 + \mu)(f + \mu) + \varphi(f + \mu)]} \\
&= \frac{1}{\langle k \rangle} \sum_{k=1}^{\infty} k^2 P(k) \frac{k\alpha(f + \mu)(w_2 + \mu)[\rho_1(w_2 + \mu) + \rho_2\varphi]\theta_1^*}{k\alpha(w_2 + \mu)(f + \mu)[\rho_1(w_2 + \mu) + \rho_2\varphi]\theta_1^* + A_k} \\
&= f(\theta_1^*),
\end{aligned}
\tag{20}
$$

where

$$A_k = \mu(w_2 + \mu)(f + \mu)[(w_2 + \mu) + \varphi + k\alpha\varphi]$$
$$+ k\alpha\varphi(f + \mu)[(w_2 + \mu)\rho_1 + \varphi\rho_2]\theta_1^*. \quad (21)$$

Obviously, $\theta_1^* = 0$ satisfies system (20). System (20) has a unique nontrivial solution provided that

$$\left.\frac{df(\theta_1^*)}{d\theta_1^*}\right|_{\Theta_1^* = 0} > 1, \quad f(1) \le 1. \quad (22)$$

So, we get

$$R_0 = \frac{\langle k^2 \rangle}{\langle k \rangle} \frac{\alpha(f + \mu)[\rho_1(\mu + w_2) + \rho_2\varphi]}{[(w_2 + \mu)(w_1 + f + \mu) + \varphi(w_2 + f + \mu)]\mu} > 1. \quad (23)$$

Thus, a unique nontrivial solution exists if and only if $R_0 > 1$ According to equation (17), we know

$$0 < P_k^\infty < 1,$$
$$0 < M_k^\infty < 1,$$
$$0 < S_k^\infty < 1, \quad (24)$$
$$0 < R_k^\infty < 1.$$

Therefore, the addiction-prevailing equilibrium $E^*(P_k^*, M_k^*, S_k^*, R_k^*)$ is well defined. Then, when $R_0 > 1$, there is a unique positive equilibrium $E^*(P_k^*, M_k^*, S_k^*, R_k^*)$. The proof is completed.

Remark 1. The basic reproductive number R_0 is obtained by equation (23), which depends on the fluctuations of the degree distribution $\langle k^2 \rangle / \langle k \rangle$ and some model parameters. When the heterogeneity of the degree distribution $\langle k^2 \rangle / \langle k \rangle$ is larger, the basic reproductive number R_0 is greater, i.e., the larger heterogeneity of the degree distribution can promote the spreading of betel nut addiction. Obviously, as the influence parameter α of betel nut advertisements increases, the basic reproductive number R_0 increases.

Theorem 2. *If $R_0 < 1$, the addiction-elimination equilibrium E_0 is globally asymptotically stable. If $R_0 > 1$, the addiction spreading phenomenon is persistent, i.e., there exists a constant $\eta > 0$, such that*

$$\lim_{t \longrightarrow \infty} \inf(M(t) + S(t)) = \lim_{t \longrightarrow \infty} \inf \sum_k H(k)(M_k(t) + S_k(t)) \ge \eta. \quad (25)$$

Proof. For the addiction-elimination equilibrium, system (8) has the Jacobian matrix as follows:

$$J = \begin{pmatrix} A_{11} & \cdots & A_{1n} \\ \vdots & \ddots & \vdots \\ A_{n1} & \cdots & A_{nn} \end{pmatrix}, \quad (26)$$

where

$$A_{11} = \begin{pmatrix} \alpha\rho_1 P_1 - (w_1 + \mu + \varphi) & \alpha\rho_2 P_1 & f \\ \varphi & -(w_2 + \mu) & 0 \\ w_1 & w_2 & -(f + \mu) \end{pmatrix},$$

$$A_{1n} = \begin{pmatrix} \alpha\rho_1 P_n & \alpha\rho_2 P_n & 0 \\ 0 & 0 & 0 \\ 0 & 0 & 0 \end{pmatrix},$$

$$A_{n1} = \begin{pmatrix} n\alpha\rho_1 P_n & n\alpha\rho_2 P_n & 0 \\ 0 & 0 & 0 \\ 0 & 0 & 0 \end{pmatrix},$$

$$A_{nn} = \begin{pmatrix} n\alpha\rho_1 P_n - (w_1 + \mu + \varphi) & n\alpha\rho_2 P_n & f \\ \varphi & -(w_2 + \mu) & 0 \\ w_1 & w_2 & -(f + \mu) \end{pmatrix}. \quad (27)$$

So, the characteristic polynomial of the addiction-elimination equilibrium is

$$(\lambda + w_1 + \mu + \varphi)^{n-1}(\lambda + w_2 + \mu)^{n-1}(\lambda^2 + p\lambda + q)$$
$$\cdot (\lambda + f + \mu)^{n-1} = 0, \quad (28)$$

where

$$p = (w_2 + \mu)(w_1 + f + \mu) + \varphi(w_2 + f + \mu)$$
$$+ (f + \mu)(w_1 + \mu) + \mu(w_2 + \mu + \varphi)$$
$$- [\rho_1(f + \mu + w_2 + \mu) + \rho_2\varphi\alpha]\sum_{i=1}^n iP_i - fw_1,$$

$$q = (w_1 + \mu + \varphi)(w_2 + \mu)(f + \mu) + f\varphi w_2$$
$$- \alpha(f + \mu)[\rho_1(w_2 + \mu) + \rho_2\varphi]\sum_{i=1}^n iP_i - fw_1(w_2 + \mu). \quad (29)$$

When $R_0 < 1$, we can get

$$R_0 = \frac{\langle k^2 \rangle}{\langle k \rangle} \frac{\alpha(f + \mu)[\rho_1(\mu + w_2) + \rho_2\varphi]}{[(w_2 + \mu)(w_1 + f + \mu) + \varphi(w_2 + f + \mu)]\mu} < 1. \quad (30)$$

It also means

$$[(w_2 + \mu)(w_1 + f + \mu) + \varphi(w_2 + f + \mu)]\mu$$
$$> \alpha(f + \mu)[\rho_1(\mu + w_2) + \rho_2\varphi]\sum_{i=1}^n iP_i. \quad (31)$$

In other words, we get $p > 0$ and $q > 0$. According to the above proof, the real eigenvalues λ of matrix J are all negative when $R_0 < 1$. Furthermore, if and only if $R_0 > 1$, there is a unique positive eigen value λ of matrix J. By using the Perron–Frobenius theorem, the maximal real part of all eigenvalues of λ is positive only if $R_0 > 1$. Through the theorem of Lajmanovich and York [34], we can get the results. The proof is completed.

Lemma 1 (see [35]). *If $a > 0, b > 0$ and $dx(t)/dt \geq b - ax$, when $t \geq 0$ and $x(0) \geq 0$, we have $\lim_{t \to \infty} \inf x(t) \geq b/a$; if $a > 0, b > 0$ and $dx(t)/dt \leq b - ax$, when $t \geq 0$ and $x(0) \geq 0$, we have $\lim_{t \to \infty} \sup x(t) \leq b/a$.*

Next, the global attractivity of the addiction-prevailing equilibrium is discussed. The main result is given in the following theorem.

Theorem 3. *Suppose that $(P_k(t), M_k(t), S_k(t))$ is a solution of system (8) satisfying initial conditions $M_k(t) > 0$ or $S_k(t) > 0$. If $R_0 > 1$, then*

$$\lim_{t \to \infty} (P_k(t), M_k(t), S_k(t)) = (P_k^*(t), M_k^*(t), S_k^*(t)), \tag{32}$$

where $(P_k^*(t), M_k^*(t), S_k^*(t))$ is the addiction-prevailing equilibrium of system (8) for $k = 1, 2, \ldots, n$.

Proof. In the course of the proving, we followed the methods of reference [35]. In the following, we suppose that k is an integer between 1 and n. According to Theorem 2, there exists a positive constant $0 < \tau < 1/3$ and a large enough constant $T > 0$ such that $M_k(t) \geq \tau$ and $S_k(t) \geq \tau$ for $t > T$. Therefore, $\theta_1(t) > \tau, \theta_2(t) > \tau$ for $t > T$. Substituting this into the first equation of system (8), it is easy to get

$$\frac{dP_k(t)}{dt} = \mu - k\alpha(\rho_1\theta_1 + \rho_2\theta_2)P_k(t) - \mu P_k(t)$$
$$\leq \mu - [k\alpha(\rho_1 + \rho_2)\tau + \mu]P_k(t), \quad t > T. \tag{33}$$

From Lemma 1, according to the standard comparison theorem of differential equation theory, for any given positive constant $0 < \tau_1 < k(\rho_1 + \rho_2)\tau/(\mu + ka(\rho_1 + \rho_2)\tau)$, there exists $t_1 > T$, such that $P_k(t) \leq X_k^{(1)} - \tau_1$ for $t > t_1$, where

$$X_k^{(1)} = \frac{\mu}{\mu + k\alpha(\rho_1 + \rho_2)\tau} + 2\tau_1 < 1. \tag{34}$$

From system (8), it is easy to obtain

$$\frac{dM_k}{dt} = [k\alpha(\rho_1\theta_1 + \rho_2\theta_2) + f](1 - M_k(t))$$
$$- (w_1 + \mu + \varphi)M_k(t), \quad t > t_1. \tag{35}$$

So, the constant $0 < \tau_2 < \min\{1/2, w_1 + \mu + \varphi/2[k\alpha(\rho_1 + \rho_2)\tau + w_1 + \mu + \varphi + f]\}$, there exists $t_2 > t_1$, so $M_k(t) \leq Y_k^{(1)} - \tau_2$ for $t > t_2$, where

$$Y_k^{(1)} = \frac{2k(\rho_1 + \rho_2)\tau + f}{2k(\rho_1 + \rho_2)\tau + f + w_1 + \mu + \varphi} + 2\tau_2 < 1. \tag{36}$$

From system (8), it is easy to obtain

$$\frac{dS_k(t)}{dt} \leq \varphi(1 - S_k(t)) - (w_2 + \mu)S_k(t), \quad t > t_2. \tag{37}$$

Thus, for constant $0 < \tau_3 < \min\{1/3, \tau_2, w_2 + \mu/2(\varphi + w_2 + \mu)\}$, there exists $t_3 > t_2$, so $S_k(t) \leq Z_k^{(1)} - \tau_3$ for $t > t_3$, where

$$Z_k^{(1)} = \frac{\varphi}{\varphi + w_2 + \mu} + 2\tau_3 < 1. \tag{38}$$

Then, replacing $M_k(t) \leq Y_k^{(1)} - \tau_2$ and $S_k(t) \leq Z_k^{(1)} - \tau_3$ into the first equation of system (8), we get

$$\frac{dP_k(t)}{dt} = \mu - k\alpha(\rho_1\theta_1(t) + \rho_2\theta_2(t))P_k(t) - \mu P_k(t)$$
$$\geq \mu - [k\alpha(\rho_1 + \rho_2)\tau + \mu]P_k(t), \quad t > T. \tag{39}$$

Thus, for constant $0 < \tau_4 < \min\{1/4, \mu/2[k\alpha(\rho_1 + \rho_2)\tau + \mu]\}$, there exists $t_4 > t_3$, such that $P_k(t) \geq x_k^{(1)} + \tau_4$ for $t > t_4$, where

$$x_k^{(1)} = \frac{\mu}{\alpha k(\rho_1 + \rho_2)\tau + \mu} - 2\tau_4 > 0. \tag{40}$$

Then, substituting $\theta_1(t) > \tau, \theta_2(t) > \tau$ into system (8), it follows that

$$\frac{dM_k(t)}{dt} \geq k\alpha(\rho_1 + \rho_2)\tau x_k^{(1)} - (w_1 + \mu + \varphi)M_k(t) + f\tau, \quad t > t_4. \tag{41}$$

Hence, for constant $0 < \tau_5 < \min\{1/5, k\alpha(\rho_1 + \rho_2)\tau x_k^{(1)} + f\tau/2(w_1 + \mu + \varphi)\}$, there exists $t_5 > t_4$, such that $M_k(t) \geq y_k^{(1)} + \tau_5$ for $t > t_5$, where

$$y_k^{(1)} = \frac{k\alpha(\rho_1 + \rho_2)\tau x_k^{(1)} + f\tau}{w_1 + \mu + \varphi} - 2\tau_5 > 0. \tag{42}$$

Therefore,

$$\frac{dS_k(t)}{dt} \geq \varphi y_k^{(1)} - (w_2 + \mu)S_k(t), \quad t > t_5. \tag{43}$$

Hence, for constant $0 < \tau_6 < \min\{1/6, \tau_5, \varphi y_k^{(1)}/2(w_2 + \mu)\}$, there exists $t_6 > t_5$, such that $S_k(t) \geq z_k^{(1)} + \tau_6$ for $t > t_6$, where

$$z_k^{(1)} = \frac{\varphi y_k^{(1)}}{w_2 + \mu} - 2\tau_6 > 0. \tag{44}$$

Because τ is a small positive constant, we can get

$$0 < x_k^{(1)} < P_k < X_k^{(1)} < 1,$$
$$0 < y_k^{(1)} < M_k < Y_k^{(1)} < 1, \tag{45}$$
$$0 < z_k^{(1)} < S_k < Z_k^{(1)} < 1.$$

Let

$$q^{(j)} = \sum_{i=1}^{n} P_i(y_i^{(j)} + z_i^{(j)}),$$
$$Q^{(j)} = \sum_{i=1}^{n} P_i(Y_i^{(j)} + Z_i^{(j)}), \tag{46}$$
$$j = 1, 2, \ldots, n.$$

From the above discussion, we have

$$0 < q^{(1)} \le (\rho_1 \theta_1 + \rho_2 \theta_2) \le Q^{(1)} < \rho_1 + \rho_2, \quad t > t_6. \quad (47)$$

And, we substitute $M_k(t) \ge y_k^{(1)} + \tau_5$, $S_k(t) \ge z_k^{(1)} + \tau_6$ into system (8), we can get

$$\frac{dP_k(t)}{dt} \le \mu - (k\alpha q^{(1)} + \mu)P_k(t), \quad t > t_6. \quad (48)$$

Consequently, for constant $0 < \tau_7 < \min\{1/7, \tau_6\}$, there exists $t_7 > t_6$, such that

$$P_k(t) \le X_k^{(2)} \triangleq \min\left\{ X_k^{(1)} - \tau_1, \frac{\mu}{\mu + k\alpha q^{(1)}} + \tau_7 \right\}, \quad t > t_7. \quad (49)$$

Thus,

$$\frac{dM_k(t)}{dt} \le k\alpha Q^{(1)} X_k^{(2)} - (w_1 + \varphi + \mu)M_k(t)$$
$$+ f\left(1 - M_k(t) - x_k^{(1)} - z_k^{(1)}\right) \quad (50)$$
$$\le k\alpha Q^{(1)} X_k^{(2)} - (w_1 + \varphi + \mu)M_k(t)$$
$$+ f\left(1 - x_k^{(1)} - z_k^{(1)}\right), \quad t > t_7.$$

Consequently, for constant $0 < \tau_8 < \min\{1/8, \tau_7\}$, there exists $t_8 > t_7$, such that

$$M_k(t) \le Y_k^{(2)} \triangleq \min\left\{ Y_k^{(1)} - \tau_2, \frac{kQ^{(1)} X_k^{(2)} + f\left(1 - x_k^{(1)} - z_k^{(1)}\right)}{w_1 + \varphi + \mu + f} + \tau_8 \right\}, \quad t > t_8. \quad (51)$$

As a result, it follows that

$$\frac{dS_k(t)}{dt} \le \varphi M_k^{(2)} - (w_2 + \mu)S_k(t), \quad t > t_9. \quad (52)$$

Therefore, for constant $0 < \tau_9 < \min\{1/9, t\tau_8\}$, we can get

$$S_k(t) \le Z_k^{(2)} \triangleq \min\left\{ Z_k^{(1)} - \tau_3, \frac{\varphi Y_k^{(2)}}{w_2 + \mu} + \tau_9 \right\}, \quad t > t_9. \quad (53)$$

Substituting $M_k(t) \le Y_k^{(2)}, S_k(t) \le Z_k^{(2)}$ and $\rho_1 \theta_1 + \rho_2 \theta_2 \le Q^{(2)}$ into system (8), where

$$\frac{dP_k(t)}{dt} \ge \mu - (k\alpha Q^{(2)} + \mu)P_k(t), \quad t > t_9. \quad (54)$$

Hence, for constant $0 < \tau_{10} < \min\{1/10, t\tau_9 n, q\mu/2(k\alpha Q^{(2)} + \mu)\}$, there exists $t_{10} > t_9$, such that $P_k(t) \ge x_k^{(2)} + \tau_{10}$ for $t > t_{10}$, where

$$x_k^{(2)} = \max\left\{ x_k^{(1)} + \tau_4, \frac{\mu}{\mu + k\alpha Q^{(2)}} - 2\tau_{10} \right\}. \quad (55)$$

Thus,

$$\frac{dM_k(t)}{dt} \ge k\alpha q^{(1)} x_k^{(2)} - (\varphi + w_1 + \mu)M_k(t)$$
$$+ f\left(1 - M_k(t) - x_k^{(1)} - z_k^{(1)}\right), \quad t > t_{10}. \quad (56)$$

So, for constant $0 < \tau_{11} < \min\{1/11, t\tau_{10}n, qk\alpha q^{(1)} x_k^{(2)} + f(1 - x_k^{(1)} - z_k^{(1)})/2(w_1 + \varphi + \mu + f)\}$, there exists $t_{11} > t_{10}$, and $M_k(t) \ge y_k^{(2)} + \tau_{11}$ for $t > t_{11}$, where

$$y_k^{(2)} = \max\left\{ y_k^{(1)} + \tau_5, \frac{k\alpha q^{(1)} x_k^{(2)} + f\left(1 - x_k^{(1)} - z_k^{(1)}\right)}{w + f + \varphi + \mu} - 2\tau_{11} \right\}. \quad (57)$$

Similarly,

$$\frac{dS_k(t)}{dt} \ge \varphi y_k^{(2)} - (w_2 + \mu)S_k(t), \quad t > t_{11}. \quad (58)$$

Therefore, for constant $0 < \tau_{12} < \min\{1/12, t\tau_{11}n, q\varphi y_k^{(2)}/2(w_2 + \mu)\}$, there exists $t_{12} > t_{11}$, and $S_k(t) \ge z_k^{(2)} + \tau_{12}$ for $t > t_{12}$, where

$$z_k^{(2)} = \max\left\{ z_k^{(1)} + \tau_6, \frac{\varphi y_k^{(2)}}{w_2 + \mu} - 2\tau_{12} \right\}. \quad (59)$$

According to the above discussion and analyses, we can obtain six sequences: $\{X_k^{(l)}\}$, $\{Y_k^{(l)}\}$, $\{Z_k^{(l)}\}$, $\{x_k^{(l)}\}$, $\{y_k^{(l)}\}$, and $\{z_k^{(l)}\}$. We can find that the first three sequences are monotonically increasing, and the last three sequences are strictly monotonically decreasing, and there is a sufficiently large positive integer H such that, for $l \ge H$,

$$\begin{cases} X_k^{(l)} = \dfrac{\mu}{\mu + k\alpha q^{(l-1)}} + \tau_{6l-5}, \\[4mm] Y_k^{(l)} = \dfrac{k\alpha Q^{(l-1)} X_k^{(l)} + f\left(1 - x_k^{(l-1)} - z_k^{(l-1)}\right)}{w_1 + \varphi + f + \mu} + \tau_{6l-4}, \\[4mm] Z_k^{(l)} = \dfrac{\varphi Y_k^{(l)}}{w_2 + \mu} + \tau_{6l-3}, \\[4mm] x_k^{(l)} = \dfrac{\mu}{\mu + k\alpha Q^{(l)}} - 2\tau_{6l-2}, \\[4mm] y_k^{(l)} = \dfrac{k\alpha q^{(l-1)} x_k^{(l)} + f\left(1 - X_k^{(h)} - Z_k^{(h)}\right)}{w_1 + \varphi + f + \mu} - 2\tau_{6l-1}, \\[4mm] z_k^{(l)} = \dfrac{\varphi y_k^{(l)}}{w_2 + \mu} - 2\tau_{6l-1}. \end{cases} \quad (60)$$

It is easy to find that

$$x_k^{(l)} \le P_k(t) \le X_k^{(l)},$$
$$y_k^{(l)} \le M_k(t) \le Y_k^{(l)},$$
$$z_k^{(l)} \le S_k(t) \le Z_k^{(l)}, \tag{61}$$
$$t > t_{6l}.$$

Since the sequential limits of system (60) exist, let $\lim_{l\to\infty}\Omega_k^{(l)} = \Omega_k$, where $\Omega_k^{(l)} \in \{X_k^{(l)}, Y_k^{(l)}, Z_k^{(l)}, x_k^{(l)}, y_k^{(l)}, z_k^{(l)}, Q_k^{(l)}, q_k^{(l)}\}$ and $\Omega_k \in \{X_k, Y_k, Z_k, x_k, y_k, z_k, Q_k, q_k\}$.

Since $0 < \tau_l < 1/l$, it has $\tau_l \to 0$ as $l \to \infty$. Supposing $l \to \infty$, it follows from (61) that

$$X_k = \frac{\mu}{k\alpha q + \mu},$$

$$Y_k = \frac{k\alpha Q X_k + f(1 - x_k - z_k)}{w_1 + f + \mu + \varphi},$$

$$Z_k = \frac{\varphi}{w_2 + \mu} Y_k,$$

$$x_k = \frac{\mu}{k\alpha Q + \mu}, \tag{62}$$

$$y_k = \frac{k\alpha q x_k + f(1 - X_k - Z_k)}{w_1 + f + \mu + \varphi},$$

$$z_k = \frac{\varphi}{w_2 + \mu} y_k,$$

where

$$q = \sum_{i=1}^{n} P_i(y_i + z_i),$$
$$Q = \sum_{i=1}^{n} P_i(Y_i + Z_i). \tag{63}$$

Furthermore,

$$Y_k = \frac{\{kQ\alpha[(w_2 + \mu)(w_2 + \mu)(k\alpha Q\mu + f(k\alpha q + \mu)) + \varphi f(k\alpha q + \mu) - (k\alpha q + \mu)(f(w_2 + \mu)(w_2 + \mu) + \varphi k\alpha q) + f\varphi]\}}{\{(k\alpha q + \mu)(k\alpha Q + \mu)(w_1 + f + \mu + \varphi)(w_2 + \mu)(w_2 + \mu)\}},$$

$$y_k = \frac{kq\alpha[\{(w_2 + \mu)(w_2 + \mu)(k\alpha q\mu + f(k\alpha Q + \mu)) + \varphi f(k\alpha Q + \mu)\} - (k\alpha Q + \mu)(f(w_2 + \mu)(w_2 + \mu) + \varphi k\alpha Q) + f\varphi]}{(k\alpha q + \mu)(k\alpha Q + \mu)(w_1 + f + \mu + \varphi)(w_2 + \mu)(w_2 + \mu)}. \tag{64}$$

Substituting (62) and (64) into Q and q, respectively, we obtain

$$1 = \frac{\varphi + w_2 + \mu}{w_2 + \mu} \sum_{i=1}^{n} iP_i \left\{ \frac{\{k\alpha[(w_2 + \mu)(w_2 + \mu)(k\alpha Q\mu + f(k\alpha q + \mu)) + \varphi f(k\alpha q + \mu)] - (k\alpha q + \mu)[(f(w_2 + \mu)(w_2 + \mu) + \varphi k\alpha q) + f\varphi]\}}{(k\alpha q + \mu)(k\alpha Q + \mu)(w_1 + f + \mu + \varphi)(w_2 + \mu)(w_2 + \mu)} \right\},$$

$$1 = \frac{\varphi + w_2 + \mu}{w_2 + \mu} \sum_{i=1}^{n} iP_i \left\{ \frac{\{k\alpha[(w_2 + \mu)(w_2 + \mu)(k\alpha q\mu + f(k\alpha Q + \mu)) + \varphi f(k\alpha Q + \mu)] - (k\alpha Q + \mu)[(f(w_2 + \mu)(w_2 + \mu) + \varphi k\alpha Q) + f\varphi]\}}{(k\alpha q + \mu)(k\alpha Q + \mu)(w_1 + f + \mu + \varphi)(w_2 + \mu)(w_2 + \mu)} \right\} \tag{65}$$
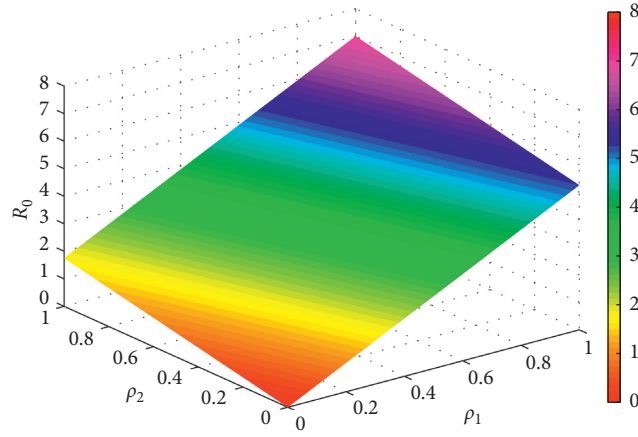
FIGURE 2: The influence of parameters ρ_1 and ρ_2 on R_0.
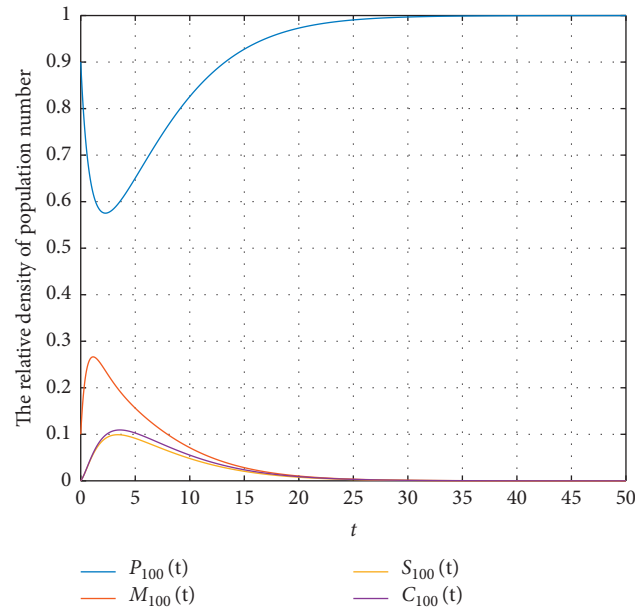
FIGURE 3: The time series and orbits of four states with $R_0 < 1$.

From the above two equations, we can get

$$(Q - q)\frac{\varphi + w_2 + \mu}{w_2 + \mu}\sum_{i=1}^{n} iP_i\left\{\frac{[(kaq + \mu) - (kaQ + \mu)][(f(w_2 + \mu)(w_2 + \mu) + \varphi kaQ) + f\varphi]}{(kaq + \mu)(kaQ + \mu)(w_1 + f + \mu + \varphi)(w_2 + \mu)(w_2 + \mu)}\right\} \equiv 0. \tag{66}$$

It is clear that $Q = q$. So, $\sum_{i=1}^{n} P_i[(Y_i - y_i) + (Z_i - z_i)] = 0$, which is equivalent to $Y_i = y_i$ and $Z_i = z_i$ for $1 \leq i \leq n$. Then, from systems (61) and (62), it can be concluded that

$$\lim_{t \to \infty} P_k(t) = X_k = x_k,$$
$$\lim_{t \to \infty} M_k(t) = Y_k = y_k, \tag{67}$$
$$\lim_{t \to \infty} R_k(t) = Z_k = z_k.$$
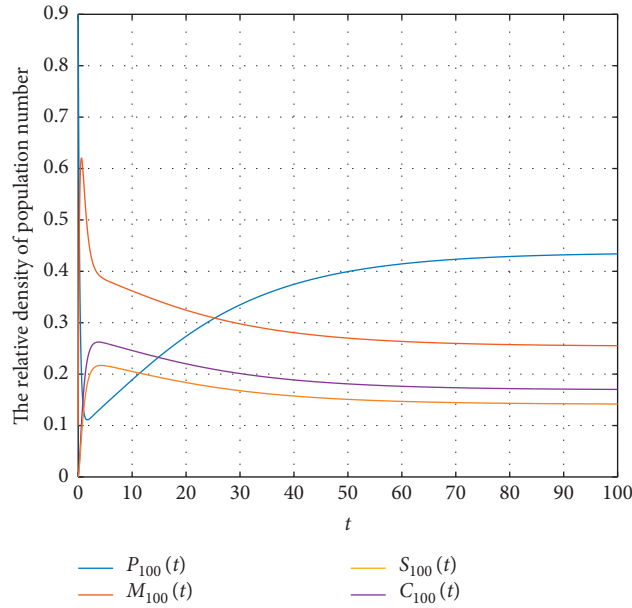
FIGURE 4: The time series and orbits of four states with $R_0 > 1$.

(a)

(b)
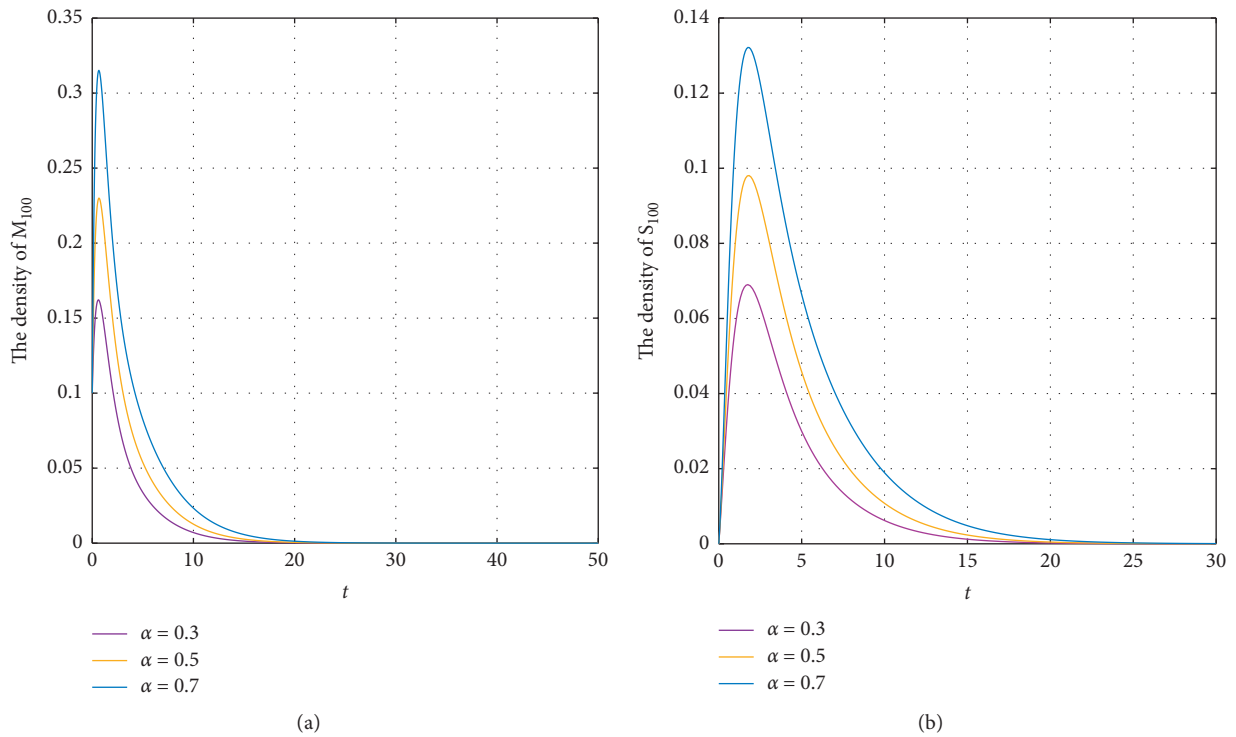
FIGURE 5: The prevalence of M_{100} and S_{100} versus t to different α with $R_0 < 1$.

4. Numerical Simulations

This section illustrates the analytical results through numerical simulations. Based on scale-free network, we have

Finally, $Q = q$ is substituted into system (64). For system (62), we can get $X_k = P_k^*$, $Y_k = M_k^*$, and $Z_k = R_k^*$. This proof is completed.

$H(k) = ck^{-3}$ in system (1), and the parameter c satisfies $\sum_{k=1}^{n} ck^{-3} = 1$, $n = 1000$.

In Figure 2, the parameters are chosen as $\mu = 0.3$, $\alpha = 0.2$, $\varphi = 0.3$, $w_2 = 0.5$, $w_1 = 0.3$, and $f = 0.6$. We can see that the larger the ρ_1 and ρ_2, the larger the R_0, i.e., long time contact with mild addicts and severe addicts both can increase the spreading speed of betel nut addiction. This also means that if people's health knowledge is improved, the
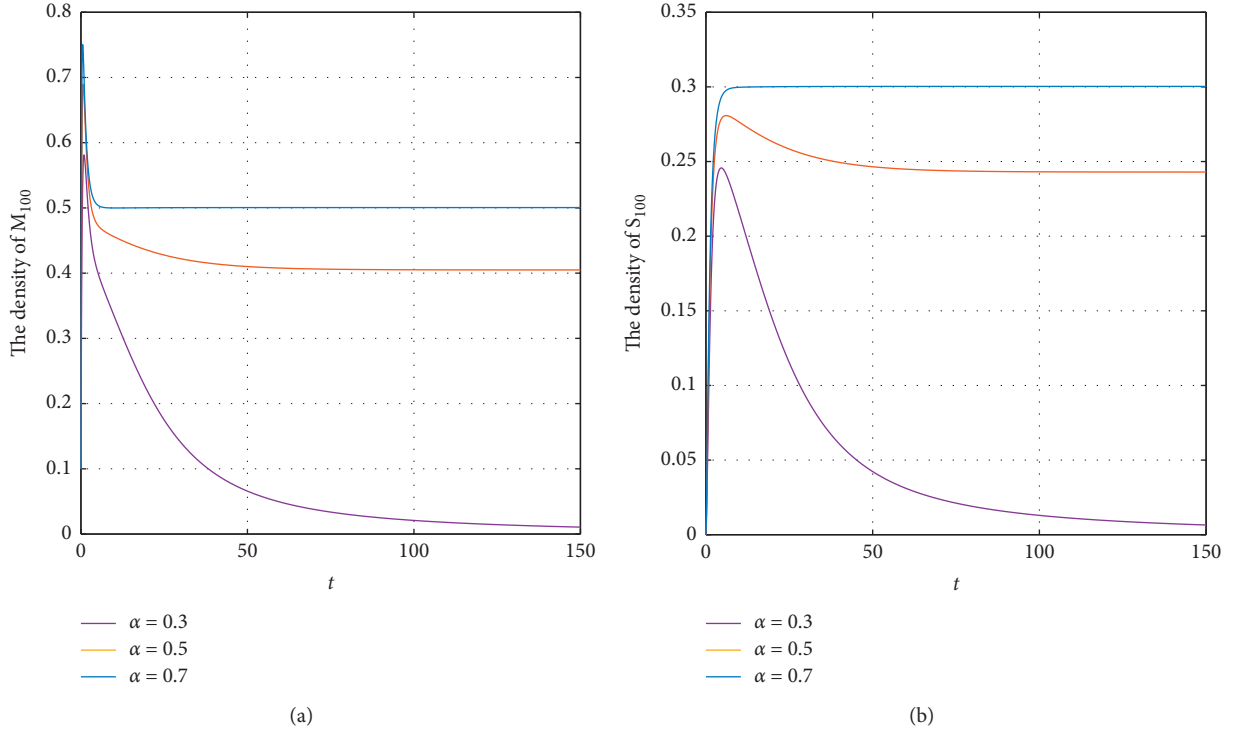
FIGURE 6: The prevalence of M_{100} and S_{100} versus t to different α with $R_0 > 1$.

probability of people chewing betel nut is reduced. The spreading of betel nut addiction will be weakened.

In Figure 3, we choose $\mu = 0.3$, $\alpha = 0.2$, $\varphi = 0.4$, $w_2 = 0.4$, $w_1 = 0.3$, $f = 0.6$, $\rho_1 = 0.4$, and $\rho_2 = 0.4$, thus the basic reproductive number $R_0 = 0.8090 < 1$. We can see that there is almost no spreading of betel nut addiction when $R_0 < 1$, which means that betel nut addiction will eventually disappear. It also suggests that the addiction-elimination equilibrium E_0 is globally asymptotically stable when $R_0 < 1$. This also means that restricting the marketing strategy of betel nut and controlling the recurrence rate of betel nut addiction will weaken the spreading of betel nut addiction.

In Figure 4, we choose $\mu = 0.3$, $\alpha = 0.5$, $\varphi = 0.4$, $w_2 = 0.3$, $w_1 = 0.3$, $f = 0.6$, $\rho_1 = 0.7$, and $\rho_2 = 0.7$, thus the basic reproductive number $R_0 = 3.7163 > 1$. We can see that the number of mild addicts and severe addicts will maintain at a positive constant, i.e., the spreading phenomenon of betel nut addiction is permanent on the scale-free networks when $R_0 > 1$.

In Figure 5, we choose $\mu = 0.4$, $\varphi = 0.6$, $w_2 = 0.6$, $w_1 = 0.4$, $f = 0.2$, $\rho_1 = 0.2$, and $\rho_2 = 0.2$, thus the basic reproductive number $R_0 < 1$. We can see that the corresponding M_{100} and S_{100} decrease significantly as the parameter α decreases, i.e., a smaller parameter α can weaken the spreading phenomenon of betel nut addiction. This also means that the marketing strategies of betel nut merchants have a great influence on the spreading of betel nut addiction.

In Figure 6, we choose $\mu = 0.3$, $\varphi = 0.4$, $w_2 = 0.3$, $w_1 = 0.3$, $f = 0.6$, $\rho_1 = 0.7$, and $\rho_2 = 0.7$, thus the basic reproductive number $R_0 > 1$. Figure 6 describes the change of

the mild addicts M_{100} and severe addicts S_{100} with different rate α. We can see that when $R_0 > 1$, M_{100} and S_{100} both grow to positive constants with the increasing of parameter α. This figure shows that a larger α can lead to the larger value of betel nut addiction spreading level. It means that restricting the marketing strategies of betel nut plays a vital role in controlling the spread of betel nut addiction.

5. Conclusions

In this paper, a new comprehensively PMSR betel nut addiction spreading model has been proposed. By the mean-field theory, we have obtained the basic reproduction number R_0 addiction-elimination equilibrium E_0, and addiction-prevailing equilibrium E_+. If $R_0 < 1$, the addiction-elimination equilibrium E_0 is globally asymptotically stable, i.e., betel nut addiction spreading behavior will eventually disappear. If $R_0 > 1$, the spreading dynamical behavior of betel nut addiction is persistent and globally asymptotically stable. Moreover, we found that the larger the parameters ρ_1 and ρ_2, the larger the basic reproductive number R_0, i.e., long-term and frequent contact with mild addicts and severe addicts can increase the spreading phenomenon of betel nut addiction. Furthermore, a larger α can increase the spread speed and range of betel nut addiction. Therefore, controlling the spread of betel nut addiction requires restricting the marketing strategies adopted by betel nut merchants and widely publicizing the harmfulness of chewing betel nut. The research results have important guiding significance in controlling the spreading of betel nut addiction.

Data Availability

Conflicts of Interest

Acknowledgments

References

[1] Y.-C. Ko, Y.-L. Huang, C.-H. Lee, M.-J. Chen, L.-M. Lin, and C.-C. Tsai, "Betel quid chewing, cigarette smoking and alcohol consumption related to oral cancer in Taiwan," *Journal of Oral Pathology and Medicine*, vol. 24, no. 10, pp. 450–453, 1995.

[2] C.-H. Lee, Y.-C. Ko, H.-L. Huang et al., "The precancer risk of betel quid chewing, tobacco use and alcohol consumption in oral leukoplakia and oral submucous fibrosis in southern Taiwan," *British Journal of Cancer*, vol. 88, no. 3, p. 366, 2003.

[3] A. Znaor, P. Brennan, V. Gajalakshmi et al., "Independent and combined effects of tobacco smoking, chewing and alcohol drinking on the risk of oral, pharyngeal and esophageal cancers in Indian men," *International Journal of Cancer*, vol. 105, no. 5, pp. 681–686, 2003.

[4] P. C. Gupta and S. Warnakulasuriya, "Global epidemiology of areca nut usage," *Addiction Biology*, vol. 7, no. 1, pp. 77–83, 2002.

[5] B. J. Boucher and N. Mannan, "Metabolic effects of the consumption of areca catechu," *Addiction Biology*, vol. 7, no. 1, pp. 103–110, 2002.

[6] S. Warnakulasuriya, C. Trivedy, and T. J. Peters, "Areca nut use: an independent risk factor for oral cancer," *The Health Problem is Under-Recognised*, vol. 324, no. 799, 2002.

[7] H. Mehrtash, K. Duncan, M. Parascandola et al., "Defining a global research and policy agenda for betel quid and areca nut," *Lancet Oncology*, vol. 18, no. 12, 2017.

[8] C. Trivedy, S. Warnakulasuriya, and T. J. Peters, "Areca nuts can have deleterious effects," *BMJ*, vol. 318, no. 7193, p. 1287, 1999.

[9] M. A. Lopezvilchez, V. Seidel, M. Farre et al., "Areca-nut abuse and neonatal withdrawal syndrome," *Pediatrics*, vol. 117, no. 1, 2006.

[10] J.-C. Weng, T.-W. Kao, G.-J. Huang, Y.-S. Tyan, H.-C. Tseng, and M.-C. Ho, "Evaluation of structural connectivity changes in betel-quid chewers using generalized q-sampling MRI," *Psychopharmacology*, vol. 234, no. 13, pp. 1945–1955, 2017.

[11] Science Daily, "Researcher finds key clues about "betel nut" addiction that plagues millions worldwide," October 2015, https://www.sciencedaily.com/releases/2015/10/151021161034.htm.

[12] K. L. Murphy and T. A. Herzog, "Sociocultural factors that affect chewing behaviors among betel nut chewers and ex-chewers on guam," *Hawai'i Journal of Medicine & Public Health*, vol. 74, no. 12, pp. 406–411, 2015.

[13] C.-H. Lee, A. M.-S. Ko, S. Warnakulasuriya et al., "Inter-country prevalences and practices of betel-quid use in south, southeast and eastern asia regions and associated oral preneoplastic disorders: an international collaborative study by asian betel-quid consortium of south and east Asia," *International Journal of Cancer*, vol. 129, no. 7, pp. 1741–1751, 2011.

[14] W. M. Ghani, I. A. Razak, Y. Yang et al., "Factors affecting commencement and cessation of betel quid chewing behaviour in Malaysian adults," *BMC Public Health*, vol. 11, no. 1, p. 82, 2011.

[15] J. Moss, C. Kawamoto, P. Pokhrel et al., "Developing a betel quid cessation program on the island of guam," *Pacific Asia inquiry*, vol. 6, no. 1, pp. 144–150, 2015.

[16] A. Ariyawardana, A. Athukorala, and A. Arulanandam, "Effect of betel chewing, tobacco smoking and alcohol consumption on oral submucous fibrosis: a case-control study in Sri Lanka," *Journal of Oral Pathology and Medicine*, vol. 35, no. 4, pp. 197–201, 2006.

[17] C.-C. Lin, I. Tamí-Maury, W.-F. Ma et al., "Social and cultural context of betel quid consumption in taiwan and implications for prevention and cessation interventions," *Substance Use & Misuse*, vol. 52, no. 5, pp. 646–655, 2017.

[18] H. A. Seedat and C. W. van Wyk, "Betel chewing and dietary habits of chewers without and with submucous fibrosis and with concomitant oral cancer," *South African Medical Journal = Suid-Afrikaanse Tydskrif Vir Geneeskunde*, vol. 74, no. 11, p. 572, 1988.

[19] S. Williams, A. Malik, S. Chowdhury, and S. Chauhan, "Sociocultural aspects of areca nut use," *Addiction Biology*, vol. 7, no. 1, pp. 147–154, 2002.

[20] X. Liu, T. Li, H. Xu, and W. Liu, "Spreading dynamics of an online social information model on scale-free networks," *Physica A: Statistical Mechanics and Its Applications*, vol. 514, pp. 497–510, 2019.

[21] Y. Lei, T. Li, Y. Wang, G. Ye, S. Sun, and Z. Xia, "Spreading dynamics of a CPFB group booking preferential information model on scale-free networks," *IEEE Access*, vol. 7, pp. 156287–156300, 2019.

[22] X. Liu, T. Li, M. Tian et al., "Rumor spreading of a SEIR model in complex social networks with hesitating mechanism," *Advances in Difference Equations*, vol. 2018, no. 1, pp. 1–24, Article ID 391, 2018.

[23] T. Li, Y. Wang, Z.-H. Guan et al., "Spreading dynamics of a SIQRS epidemic model on scale-free networks," *Communications in Nonlinear Science and Numerical Simulation*, vol. 19, no. 3, pp. 686–692, 2014.

[24] Y. Wang, Z. Jin, Z. Yang, Z.-K. Zhang, T. Zhou, and G.-Q. Sun, "Global analysis of an SIS model with an infective vector on complex networks," *Nonlinear Analysis: Real World Applications*, vol. 13, no. 2, pp. 543–557, 2012.

[25] Y. Wang and J. Cao, "Global dynamics of a network epidemic model for waterborne diseases spread," *Applied Mathematics and Computation*, vol. 237, pp. 474–488, 2014.

[26] W. Liu, T. Li, X. Cheng et al., "Spreading dynamics of a cyber violence model on scale-free networks," *Physica A: statistical mechanics and its applications*, vol. 531, Article ID 121752, 2019.

[27] A.-L. Barabási and R. Albert, "Emergence of scaling in random networks," *Science*, vol. 286, no. 5439, pp. 509–512, 1999.

[28] R. Albert and A. Barabasi, "Statistical mechanics of complex networks," *Reviews of Modern Physics*, vol. 74, no. 1, pp. 47–97, 2001.

[29] M. Liu, G. Sun, Z. Jin, and T. Zhou, "An analysis of transmission dynamics of drug-resistant disease on scale-free networks," *Applied Mathematics and Computation*, vol. 222, pp. 177–189, 2013.

[30] R. Pastor-Satorras and A. Vespignani, "Epidemic spreading in scale-free networks," *Physical Review Letters*, vol. 86, no. 14, p. 3200, 2001.

[31] J. C. Nacher, M. Hayashida, and T. Akutsu, "Emergence of scale-free distribution in protein-protein interaction networks based on random selection of interacting domain pairs," *BioSystems*, vol. 95, no. 2, pp. 155–159, 2009.

[32] P. Van den Driessche and J. Watmough, "Reproduction numbers and sub-threshold endemic equilibria for compartmental models of disease transmission," *Mathematical Biosciences*, vol. 180, no. 1-2, pp. 29–48, 2002.

[33] A. Lajmanovich and J. A. Yorke, "A deterministic model for gonorrhea in a nonhomogeneous population," *Mathematical Biosciences*, vol. 28, no. 3-4, pp. 221–236, 1976.

[34] F. Chen, "On a nonlinear nonautonomous predator-prey model with diffusion and distributed delay," *Journal of Computational and Applied Mathematics*, vol. 180, no. 1, pp. 33–49, 2005.

[35] G. Zhu, X. Fu, and G. Chen, "Spreading dynamics and global stability of a generalized epidemic model on complex heterogeneous networks," *Applied Mathematical Modelling*, vol. 36, no. 12, pp. 5808–5817, 2012.

WILEY | Hindawi

Research Article

Dynamics of a Virological Model for Cancer Therapy with Innate Immune Response

Ayoub Nouni,[1] Khalid Hattaf ⬤,[1,2] and Noura Yousfi[1]

[1]*Laboratory of Analysis, Modeling and Simulation (LAMS), Faculty of Sciences Ben M'sik, Hassan II University of Casablanca,*
 P.O. Box 7955 Sidi Othman, Casablanca, Morocco
[2]*Centre Régional des Métiers de l'Education et de la Formation (CRMEF), 20340 Derb Ghalef, Casablanca, Morocco*

Correspondence should be addressed to Khalid Hattaf; k.hattaf@yahoo.fr

The aim of this work is to present a virological model for cancer therapy that includes the innate immune response and saturation effect. The presented model combines both the evolution of a logistic growing tumor and time delay which stands for the period of the viral lytic cycle. We use the delay differential equation in order to model this time which also means the time needed for the infected tumor cells to produce new virions after viral entry. We show that the delayed model has four equilibria which are the desired outcome therapy equilibrium, the complete failure therapy equilibrium, the partial success therapy free-immune equilibrium when the innate immune response has not been established, and the partial success therapy equilibrium with immune response. Furthermore, the stability analysis of equilibria and the Hopf bifurcation are properly exhibited.

1. Introduction

Combination therapy approaches have shown a serious promise to deal with cancers that are resistant to traditional therapeutic procedures. Oncolytic virotherapy, also called the selective therapy, is a developable technique that adopts replication competent viruses as a new treatment to destroy cancer cells without causing damage to normal cells [1–4]. Different researches have investigated combination strategies with oncolytic virotherapy and chemotherapeutic drugs in order to optimize both the effect of the added therapy and the viral oncolysis [5, 6]. Many mathematical models of viral infection and immune response have been established in order to study the behavior as well as the dynamics of the cancer cells. According to Phan and Tian [7], the dynamics of the system, when they considered a composed ODE's dimensional model, is ruled by the viral burst size and some parameters in relation to the innate immune response. They have shown that getting the immune response involved in the system makes the oncolytic virotherapy more difficult by establishing more equilibria when the viral burst size is lower than a critical value,

whereas the model has the same behavior like in the case when the immune response is excluded when the viral burst size is big. In 2018, Kim et al. [8] proposed a delayed mathematical model with two controls to describe cancer viral therapy dynamics and to reduce total tumor cell numbers as well as the costs of two therapies. They performed the stability analysis and the existence of Hopf bifurcation. They also inspected the optimal oncolytic immunotherapy treatment with respect to the time delay. However, it is important to notice that either these works did not incorporate the nonlinear relationship between viral dose and infection rate or they did not consider the survival probability of the infected cells during the latent period not to mention the absorbtion rate of the virus. Recently, Hattaf [9] proposed a virological model that incorporates the general infection rate for the two types of transmission, humoral immunity, and three time delays. He found that the entire behavior of the presented model is determined and ruled by the basic reproduction number and the reproduction number for humoral immunity. The study investigated the dynamical behaviors of the model including Hopf bifurcation and stability switches.

Based on the above and the model for oncolytic virotherapy [10], we propose the following model:

$$
\begin{cases}
\dfrac{\mathrm{d}x(t)}{\mathrm{d}t} = rx(t)\left(1 - \dfrac{x(t)+y(t)}{K}\right) - \left(\dfrac{\beta x(t)v(t)}{1+\alpha v(t)}\right), \\[2mm]
\dfrac{\mathrm{d}y(t)}{\mathrm{d}t} = \dfrac{\beta x(t-\tau)v(t-\tau)e^{-m\tau}}{1+\alpha v(t-\tau)} - \delta y(t) - py(t)z(t), \\[2mm]
\dfrac{\mathrm{d}v(t)}{\mathrm{d}t} = N\delta y(t) - \dfrac{n\beta x(t)v(t)}{1+\alpha v(t)} - \mu v(t) - qv(t)z(t), \\[2mm]
\dfrac{\mathrm{d}z(t)}{\mathrm{d}t} = cy(t)z(z) - bz(t),
\end{cases}
\tag{1}
$$

where $x(t)$, $y(t)$, and $v(t)$ have the same meaning as in [10] which are, respectively, the quantities of uninfected tumor cells, damaged tumor cells, and oncolytic virus. On the other hand, $z(t)$ denotes the concentration of the innate immune cells at time t. The tumor grows logistically at a rate r and K is the maximal carrying capacity of tumor cells. The infection rate in the oncoviral therapy model [7] has been modeled by a bilinear incidence which is not reasonable in case of a high concentration of oncolytic virus. Therefore, it is very reasonable to model the infection rate by a saturated incidence of the form $(\beta xv)/(1+\alpha v)$, where β and α are positive constants which, respectively, describe the infection process and the saturation effect. The parameters δ and μ represent, respectively, the death rate of the damaged tumor cells and the virus clearance rate while n describes the absorbtion rate of the virus in the extracellular tissue, whereas N is the number of new viruses which appear after a disruption-lysis of a damaged tumor cell. The constants p and q stand for the immune killing rate of damaged cells and viruses, respectively, while b represents the immune clearance rate and c is the incitement rate of the innate immune system. Ultimately, the delay τ expresses the time of latent period while the quantity $e^{-m\tau}$ exemplifies the probability of getting through from time $t-\tau$ to time t, where m is the death rate for unproductive-damaged cells.

Our purpose in this work is to extend our model in [10] by introducing the role of the innate immune response in oncolytic virotherapy. Additionally, the model studied in [7] is a special case of system (1) when the time period of the lytic cycle and saturation effect are not considered, that is, $\tau = 0$ and $\alpha = 0$. Otherwise, this paper is organized as follows. In Section 2, we give some preliminary results and we discuss the conditions of the existence of equilibria. Section 3 deals with stability analysis and provides conditions under which the system undergoes the Hopf bifurcation. Finally, Section 4 is devoted to discussion and conclusion.

2. Positiveness, Boundedness, and Equilibria

In this section, we prove the positivity and the boundedness of solutions of model (1).

Let $\mathscr{C} = C([-\tau,0],\mathrm{IR}^4)$ be the Banach space of continuous functions mapping the interval $[-\tau,0]$ into IR^4 with the topology of the uniform convergence. According to the fundamental theory of functional differential equations [11], model (1) has a unique solution $(x(t),y(t),v(t),z(t))$ with respect to initial values $(x_0,y_0,v_0,z_0) \in \mathscr{C}$. Additionally, we also assume that the initial values satisfy the following biological conditions:

$$
\begin{aligned}
x_0(\theta) &\geq 0, \\
y_0(\theta) &\geq 0, \\
v_0(\theta) &\geq 0, \\
z_0(\theta) &\geq 0, \\
\theta &\in [-\tau,0].
\end{aligned}
\tag{2}
$$

Theorem 1. *Each solution of model (1) starting from initial condition (2) remains positive and bounded for all $t \geq 0$.*

Proof. From the first and the fourth equations of (1), we get

$$
\begin{aligned}
x(t) &= x(0)e^{\int_0^t r(1-x(s)+y(s)/K)-\beta v(s)/1+\alpha v(s)\mathrm{d}s}, \\
z(t) &= z(0)e^{-bt+\int_0^t cy(s)\mathrm{d}s},
\end{aligned}
\tag{3}
$$

which leads to $x(t) \geq 0$ and $z(t) \geq 0$ for all $t \geq 0$. From the second and third equations of (1), we have

$$
y(t) = y(0)e^{-\delta t - \int_0^t pz(s)\mathrm{d}s} + e^{-m\tau-\delta t-\int_0^t pz(s)\mathrm{d}s}\int_0^t \frac{\beta x(s-\tau)v(s-\tau)}{1+\alpha v(s-\tau)}e^{\delta s + \int_0^s pz(u)\mathrm{d}u}\mathrm{d}s,
$$

$$
v(t) = \left(v(0)e^{-\int_0^t n\beta x(s)/1+\alpha v(s)+qz(s)\mathrm{d}s} + N\delta\int_0^t y(u)e^{\mu u - \int_u^t n\beta x(s)/1+\alpha v(s)+qz(s)\mathrm{d}s}\mathrm{d}u\right)e^{-\mu t}.
$$

$$
\tag{4}
$$

Clearly, $y(t) \geq 0$ and $v(t) \geq 0$ for $t \in [0, \tau]$. This procedure can be repeated on the interval $[\eta\tau, (\eta+1)\tau]$ for all $\eta \in \mathbb{IN}$. Then, $y(t) \geq 0$ and $v(t) \geq 0$ for all $t \geq 0$.

Through the first equation of (1), we have

$$\frac{dx(t)}{dt} \leq rx(t)\left(1 - \frac{x(t)}{K}\right). \tag{5}$$

Applying the comparison principle, we get

$$\limsup_{t \longrightarrow +\infty} x(t) \leq K. \tag{6}$$

Therefore, $x(t)$ is bounded. Let

$$T(t) = x(t-\tau)e^{-m\tau} + y(t) + \frac{p}{c}z(t). \tag{7}$$

For $t > \tau$, we have

$$\frac{dT(t)}{dt} = rx(t-\tau)\left(1 - \frac{x(t-\tau) + y(t-\tau)}{K}\right)e^{-m\tau}$$

$$- \delta y(t) - \frac{pb}{c}z(t)$$

$$\leq rK\left(1 - \frac{x(t-\tau)}{K}\right)e^{-m\tau} - \delta y(t) - \frac{pb}{c}z(t)$$

$$\leq rKe^{-m\tau} - \rho T(t), \tag{8}$$

where $\rho = \min\{r, \delta, b\}$. Consequently,

$$T(t) \leq \gamma, \tag{9}$$

where $\gamma = \max\{T(0), rKe^{-m\tau}/\rho\}$. This implies that $T(t)$ is bounded on $(\tau, +\infty)$. According to the continuity of $T(t)$ on $[0, \tau]$, we concluded that $T(t)$ is also bounded on $[0, \tau]$. Therefore, $y(t)$ and $z(t)$ are bounded for all $t \geq 0$.

By the third equation of (1) and the boundedness of $y(t)$, we find

$$\limsup_{t \longrightarrow +\infty} v(t) \leq \frac{rKN\delta e^{-m\tau}}{\mu\rho}. \tag{10}$$

Then, $v(t)$ is bounded. This completes the proof.

Next, we discuss the existence of equilibria of model (1). Denote

$$\mathcal{R}_0 = \frac{NK\beta}{n\beta K + \mu}e^{-m\tau} = \frac{1}{\delta} \times \frac{N\delta}{n\beta K + \mu} \times K\beta \times e^{-m\tau}, \tag{11}$$

where $1/\delta$ is the average life expectancy of the infected tumor cells, $(N\delta)/(n\beta K + \mu)$ is the viral quantity generated from one infected cell during its survival period, K the number of uninfected tumor cells at the beginning of the infection, and $e^{-m\tau}$ is the probability of surviving from time $t - \tau$ to time t. Therefore, $\mathcal{R}_0$ is the basic reproduction number of model (1) which biologically describes the average number of the newly infected tumor cells generated from one infected cell at the beginning of the infection.

In absence of the innate immune response, system (1) reduced to the model in [10]. Then, (1) always has two equilibria $E_0(0,0,0,0)$ and $E_1(K,0,0,0)$ if $\mathcal{R}_0 \leq 1$. However,

model (1) has another equilibrium $E_2(x_2, y_2, v_2, 0)$ if $\mathcal{R}_0 > 1$, where

$$x_2 = \frac{\mu r + K\delta(N - ne^{m\tau})(r\alpha - \beta) + \sqrt{\Delta}}{2r(N - ne^{m\tau})(\beta e^{-m\tau} + \alpha\delta)},$$

$$y_2 = \frac{rx_2(K - x_2)}{rx_2 + K\delta e^{m\tau}}, \tag{12}$$

$$v_2 = \frac{\delta(N - ne^{m\tau})}{\mu}y_2,$$

with $\Delta = [K\delta(N - ne^{m\tau})(\beta - r\alpha) - \mu r]^2 + 4\mu\delta Kre^{m\tau}(N - ne^{m\tau})(\beta e^{-m\tau} + \delta\alpha)$.

In presence of the innate immune response, we have

$$x = \frac{(crK\alpha - br\alpha - Kc\beta)v + r(cK - b)}{rc(1 + \alpha v)} := \varphi_1(v),$$

$$y = \frac{b}{c},$$

$$z = \frac{b\delta(N - ne^{m\tau}) - \mu cv}{qcv + nbpe^{m\tau}} := \varphi_2(v),$$

$$\frac{\beta xv}{1 + \alpha v} = \frac{b}{c}e^{m\tau}(\delta + pz). \tag{13}$$

Since $z \geq 0$, we have $v \leq \delta b(N - ne^{m\tau})/\mu c$. This indicates that there is no biological equilibrium when $v > \delta b(N - ne^{m\tau})/\mu c$. Let F be a function defined on the closed interval $[0, \delta b(N - ne^{m\tau})/\mu c]$ as follows:

$$F(v) = \frac{\beta\varphi_1(v)v}{1 + \alpha v} - \frac{b}{c}e^{m\tau}(\delta + p\varphi_2(v)). \tag{14}$$

Clearly, $F(0) = -b(\delta + p\varphi_2(0))e^{m\tau} < 0$ and

$$F'(v) = \frac{\beta(cK - b)}{c(1 + \alpha v)^2} - \frac{b}{c}pe^{m\tau}\varphi_2'(v). \tag{15}$$

Since $\varphi_2'(v) = -bc(\mu npe^{m\tau} + q\delta(N - ne^{m\tau}))/(qcv + nbpe^{m\tau})^2$, we have $F'(v) > 0$.

When the innate immune response has not been established, we have $cy_2 - b \leq 0$. Then, we define the reproduction number for the innate immune response as follows:

$$\mathcal{R}_1^Z = \frac{cy_2}{b}, \tag{16}$$

where $1/b$ is the average life expectancy of innate immune cells, c is the rate of immune response activation, and y_2 is the number of infected tumor cells at the steady state E_2. Hence, $\mathcal{R}_1^Z$ describes the average number of innate immune cells activated by the infected tumor cells.

If $\mathcal{R}_1^Z < 1$, then $y_2 < b/c$, $v_2 < \delta b(N - ne^{m\tau})/\mu c$, and $F(\delta b(N - ne^{m\tau})/\mu c) < (\delta b/c)(\beta x_2(N - ne^{m\tau})/\mu(1 + \alpha v_2) - e^{m\tau}) = 0$. Then, there is no equilibrium when $\mathcal{R}_1^Z < 1$.

If $\mathcal{R}_1^Z > 1$, then $y_2 > b/c$, $v_2 > \delta b (N - ne^{m\tau})/\mu c$, and $F(\delta b (N - ne^{m\tau})/\mu c) > \delta b/c (\beta x_2 (N - ne^{m\tau})/\mu (1 + \alpha v_2) - e^{m\tau}) = 0$. Therefore, model (1) has a unique equilibrium with immune response $E_3 (x_3, y_3, v_3, z_3)$, where $v_3 \in (0, \delta b (N - ne^{m\tau})/\mu c)$, $x_3 = (crK\alpha - br\alpha - Kc\beta)v_3 + r(cK - b)/rc(1 + \alpha v_3)$, $y_3 = b/c$, and $z_3 = b\delta (N - ne^{m\tau}) - \mu cv_3/qcv_3 + nbpe^{m\tau}$.

By rearranging the above discussions, we have the following theorem. □

Theorem 2.

(i) *If $\mathcal{R}_0 \leq 1$, then model (1) has uniquely two equilibria that are the desired outcome therapy equilibrium $E_0 (0, 0, 0, 0)$ and the complete failure therapy equilibrium $E_1 (K, 0, 0, 0)$*

(ii) *If $\mathcal{R}_0 > 1$, then model (1) has a unique partial success therapy equilibrium without immune response*

$E_2 (x_2, y_2, v_2, 0)$ *besides E_0 and E_1, where $x_2 = \mu r + K\delta (N - ne^{m\tau}) (r\alpha - \beta) + \sqrt{\Delta}/2r$ $(N - ne^{m\tau}) (\beta e^{-m\tau} + \alpha\delta)$, $y_2 = rx_2 (K - x_2)/rx_2 + K\delta e^{m\tau}$, and $v_2 = \delta (N - ne^{m\tau})/\mu y_2$*

(iii) *If $\mathcal{R}_1^Z > 1$, then model (1) has a unique partial success therapy equilibrium with immune response $E_3 (x_3, y_3, v_3, z_3)$ besides E_0, E_1, and E_2, where $v_3 \in (0, \delta b (N - ne^{m\tau})/\mu c)$, $x_3 = (crK\alpha - br\alpha - Kc\beta)v_3 + r(cK - b)/rc(1 + \alpha v_3)$, $y_3 = b/c$, and $z_3 = b\delta (N - ne^{m\tau}) - \mu cv_3/qcv_3 + nbpe^{m\tau}$.*

3. Model Analysis and Stability

To understand the dynamics of the proposed model, we first analyze the local asymptotic stability of equilibria. Let $E(x, y, v, z)$ be an arbitrary equilibrium of model (1). Hence, the characteristic equation at E is given by

$$\begin{vmatrix} r\left(1 - \dfrac{2x + y}{K}\right) - \dfrac{\beta v}{1 + \alpha v} - \lambda & -\dfrac{rx}{K} & -\dfrac{\beta x}{(1 + \alpha v)^2} & 0 \\[3mm] \dfrac{\beta v}{1 + \alpha v}e^{-(m+\lambda)\tau} & -\delta - pz - \lambda & \dfrac{\beta x}{(1 + \alpha v)^2}e^{-(m+\lambda)\tau} & -py \\[3mm] -\dfrac{n\beta v}{1 + \alpha v} & N\delta & \dfrac{n\beta x}{(1 + \alpha v)^2} - \mu - qz - \lambda & -qv \\[3mm] 0 & cz & 0 & cy - b - \lambda \end{vmatrix} = 0. \tag{17}$$

Theorem 3. *The desired outcome therapy equilibrium $E_0 (0, 0, 0, 0)$ is unstable.*

Proof. It is not hard to see that at $E_0 (0, 0, 0, 0)$, equation (17) becomes

$$(r - \lambda)(\delta + \lambda)(\mu + \lambda)(b + \lambda) = 0. \tag{18}$$

Since $\lambda = r > 0$ is a positive root of the above equation, we deduce that E_0 is unstable. □

Theorem 4. *If $\mathcal{R}_0 < 1$, then the complete failure therapy equilibrium E_1 is locally asymptotically stable and unstable if $\mathcal{R}_0 > 1$.*

Proof. At E_1, (17) can be written as follows:

$$(r + \lambda)(b + \lambda)\big[\lambda^2 + (n\beta K + \mu + \delta)\lambda + \delta (n\beta K + \mu)\big(1 - \mathcal{R}_0 e^{-\lambda\tau}\big)\big] = 0. \tag{19}$$

Obviously, $\lambda_1 = -r$ and $\lambda_2 = -b$ are two negative roots of equation (19). Then, we consider the following transcendental equation:

$$\lambda^2 + (n\beta K + \mu + \delta)\lambda + \delta (n\beta K + \mu)\big(1 - \mathcal{R}_0 e^{-\lambda\tau}\big) = 0. \tag{20}$$

For $\tau = 0$ and $\mathcal{R}_0 < 1$, we have $\delta (n\beta K + \mu)(1 - \mathcal{R}_0) > 0$. Thus, the entire roots of (20) have negative real parts.

Afterward, we set $i\psi (\psi > 0)$ to be a purely imaginary root of (20). Then,

$$\begin{cases} -\psi^2 + \delta (n\beta K + \mu) = \delta (n\beta K + \mu)\mathcal{R}_0 \cos(\psi\tau), \\ (n\beta K + \mu + \delta)\psi = -\delta (n\beta K + \mu)\mathcal{R}_0 \sin(\psi\tau), \end{cases} \tag{21}$$

which leads to

$$\psi^4 + \big[\delta^2 + (n\beta K + \mu)^2\big]\psi^2 + \delta^2 (n\beta K + \mu)^2 \big(1 - \mathcal{R}_0^2\big) = 0. \tag{22}$$

Denote $\mathcal{S} = \psi^2$. Then, the previous equation becomes

$$\mathcal{S}^2 + \big[\delta^2 + (n\beta K + \mu)^2\big]\mathcal{S} + \delta^2 (n\beta K + \mu)^2 \big(1 - \mathcal{R}_0^2\big) = 0, \tag{23}$$

which has no positive root when $\mathcal{R}_0 < 1$. This implies that E_1 is locally asymptotically stable if $\mathcal{R}_0 < 1$. In fact, (23) having no positive roots implies that equation (20) does not exhibit any stability switch [12]. This means that the stability of E_1 for $\tau = 0$ is the same as that for $\tau \geq 0$, implying that E_1 is asymptotically stable for all $\tau \geq 0$

For $\mathcal{R}_0 > 1$, we consider the following function:

$$f(\lambda) = \lambda^2 + (n\beta K + \mu + \delta)\lambda + \delta (n\beta K + \mu)\big(1 - \mathcal{R}_0 e^{-\lambda\tau}\big). \tag{24}$$

We have $f(0) = \delta (n\beta K + \mu)(1 - \mathcal{R}_0) < 0$ and $\lim_{\lambda \rightarrow +\infty} f(\lambda) = +\infty$. Then, the equation $f(\lambda) = 0$ has at least one

positive root when $\mathcal{R}_0 > 1$. This implies that the characteristic equation (19) has at least one positive eigenvalue when $\mathcal{R}_0 > 1$. Therefore, the complete failure therapy equilibrium E_1 becomes unstable as long as $\mathcal{R}_0 > 1$.

The following result investigates the global stability of the complete failure therapy equilibrium E_1 when $\mathcal{R}_0 \le 1$. $\quad\square$

Theorem 5. *If $\mathcal{R}_0 \le 1$, then the complete failure therapy equilibrium E_1 is globally asymptotically stable for all $\tau \ge 0$.*

Proof. We consider the following functional:

$$V(t) = e^{m\tau} y(t) + \frac{e^{m\tau}}{N} v(t) + \int_{t-\tau}^{t} \frac{\beta x(s) v(s)}{1 + \alpha v(s)} ds + \frac{p e^{m\tau}}{c} z. \tag{25}$$

Taking the derivative of V along t of the solutions of (1) delivers

$$\left.\frac{dV}{dt}\right|_{(1)} = \left(1 - \frac{n e^{m\tau}}{N}\right) \frac{\beta x v}{1 + \alpha v} - \frac{\mu e^{m\tau}}{N} v - \left(\frac{q}{N} + \frac{pb}{c}\right) z e^{m\tau}. \tag{26}$$

Seeing that $\limsup_{t \to \infty} x(t) \le K$, we deduce that each ω-limit point satisfies $x(t) \le K$. Hence, it is sufficient to take solutions for which $x(t) \le K$. Thus,

$$\left.\frac{dV}{dt}\right|_{(1)} \le \frac{e^{m\tau}}{N} (n\beta K + \mu)(\mathcal{R}_0 - 1) v - \left(\frac{q}{N} + \frac{pb}{c}\right) z e^{m\tau}. \tag{27}$$

Then, $dV/dt|_{(1)} \le 0$ when $\mathcal{R}_0 \le 1$. Moreover, it is easy to prove that the largest invariant subset of $\{(x, y, v, z) \mid dV/dt = 0\}$ is the singleton $\{E_1\}$. From LaSalle's invariance principle [13], we conclude that E_1 is globally asymptotically stable as long as $\mathcal{R}_0 \le 1$. $\quad\square$

Next, we study the stability of E_2. In this case, (4) becomes

$$(c y_2 - b - \lambda)\left[\lambda^3 + a_1 \lambda^2 + a_2 \lambda + a_3 + (b_1 \lambda + b_2) e^{-\lambda \tau}\right] = 0, \tag{28}$$

where

$$a_1 = \mu + \delta + \frac{r x_2}{K} + \frac{n\beta x_2}{(1 + \alpha v_2)^2},$$

$$a_2 = \delta\mu + (\mu + \delta)\frac{r x_2}{K} + \frac{n\delta\beta x_2}{(1 + \alpha v_2)^2} + \frac{r n \beta x_2^2}{K(1 + \alpha v_2)^2} - \frac{n\beta^2 x_2 v_2}{(1 + \alpha v_2)^3},$$

$$a_3 = \frac{r\mu\delta x_2}{K} + \frac{r n \beta \delta x_2^2}{K(1 + \alpha v_2)^2} - \frac{n\beta^2 \delta x_2 v_2}{(1 + \alpha v_2)^3},$$

$$b_1 = \frac{\beta x_2}{1 + \alpha v_2}\left(\frac{r v_2}{K} - \frac{N\delta}{1 + \alpha v_2}\right)e^{-m\tau},$$

$$b_2 = \frac{\beta x_2}{1 + \alpha v_2}\left(\frac{r\mu v_2}{K} + \frac{N\beta\delta v_2}{(1 + \alpha v_2)^2} - \frac{N\delta r x_2}{K(1 + \alpha v_2)}\right)e^{-m\tau}. \tag{29}$$

Clearly, $\lambda_1 = c y_2 - b$ is a root of (28). If $\mathcal{R}_1^Z > 1$, then $\lambda_1 > 0$ and E_2 is unstable. However, $\lambda_1 < 0$ if $\mathcal{R}_1^Z < 1$. In this case, we study the roots of the following equation:

$$\lambda^3 + a_1 \lambda^2 + a_2 \lambda + a_3 + (b_1 \lambda + b_2) e^{-\lambda \tau} = 0. \tag{30}$$

The general form of this transcendental characteristic equation was investigated by Beretta and Kuang in [14].

For $\tau = 0$, (30) becomes

$$\lambda^3 + a_1 \lambda^2 + (a_2 + b_1)\lambda + a_3 + b_2 = 0. \tag{31}$$

Since $a_1 > 0$ and $a_3 + b_2 = (N - n)\beta^2 \delta x_2 v_2/(1 + \alpha v_2)^3 + r\mu(\alpha\delta + \beta)x_2 v_2/K(1 + \alpha v_2) > 0$, we deduce by applying the Routh–Hurwitz criterion that E_2 is locally asymptotically stable if $a_1(a_2 + b_1) - (a_3 + b_2) > 0$.

Let $i\vartheta (\vartheta > 0)$ be a root of (30). Then,

$$\begin{cases} a_1 \vartheta^2 - a_3 = b_1 \vartheta \sin(\vartheta\tau) + b_2 \cos(\vartheta\tau), \\ -\vartheta^3 + a_2 \vartheta = -b_1 \vartheta \cos(\vartheta\tau) + b_2 \sin(\vartheta\tau). \end{cases} \tag{32}$$

Hence,

$$\vartheta^6 + \left(a_1^2 - 2a_2\right)\vartheta^4 + \left(a_2^2 - 2a_1 a_3 - b_1^2\right)\vartheta^2 + a_3^2 - b_2^2 = 0, \tag{33}$$

which reduces to

$$g(\mathcal{S}) := \mathcal{S}^3 + q_2 \mathcal{S}^2 + q_1 \mathcal{S} + q_0 = 0, \tag{34}$$

where $\mathcal{S} = \vartheta^2$, $q_2 = a_1^2 - 2a_2$, $q_1 = a_2^2 - 2a_1 a_3 - b_1^2$, and $q_0 = a_3^2 - b_2^2$. By an analogical discussion as in [10], let $\Delta = q_2^2 - 3q_1$ and $\mathcal{S}^* = \sqrt{\Delta} - q_2/3$. Hence, we consider the following assertions:

(i_1) $q_0 \ge 0$ and $\Delta \le 0$

(i_2) $q_0 \ge 0$, $\Delta > 0$, and $\mathcal{S}^* \le 0$

(i_3) $q_0 \ge 0$, $\Delta > 0$, and $g(\mathcal{S}^*) > 0$

Therefore, we have the following result.

Theorem 6. *Assume $\mathcal{R}_0 > 1$.*

(1) If $\mathcal{R}_1^Z < 1$, $a_1(a_2 + b_1) - (a_3 + b_2) > 0$, and one of the conditions (i_1)–(i_3) holds, then the partial success therapy equilibrium without immune response E_2 is locally asymptotically stable for any time delay $\tau \ge 0$

(2) If $\mathcal{R}_1^Z > 1$, then E_2 is unstable.

Assume that equation (34) has positive roots. Without loss of generality, we assume that (34) has three positive solutions named $\mathcal{S}_1$, $\mathcal{S}_2$, and $\mathcal{S}_3$ which are ordered as follows: $\mathcal{S}_1 < \mathcal{S}_2 < \mathcal{S}_3$. It follows that equation (33) admits three positive solutions that are

$$\vartheta_1 = \sqrt{\mathcal{S}_1},$$
$$\vartheta_2 = \sqrt{\mathcal{S}_2} \text{ and } \vartheta_3 = \sqrt{\mathcal{S}_3}. \tag{35}$$

By (32), we get

$$\tau_k^j = \frac{1}{\vartheta_j} \arccos\left(\frac{b_2\left(a_1\vartheta_j^2 - a_3\right) + b_1\vartheta_j^2\left(\vartheta_j^2 - a_2\right)}{b_2^2 + b_1^2\vartheta_j^2}\right) + \frac{2k\pi}{\vartheta_j},$$

(36)

where $j = 1, 2, 3$ and $k \in \mathrm{IN}$. Therefore, $\pm i\vartheta_j$ is a pair of purely imaginary roots of (30) with $\tau = \tau_k^j$. Let

$$\tau_0 = \tau_0^{j_0} = \min_{j\in\{1,2,3\}}\left\{\tau_0^j\right\}, \vartheta_0 = \vartheta_{j_0}.$$

(37)

We set $\lambda(\tau) = \varsigma(\tau) + i\vartheta(\tau)$ to be the root of equation (30) satisfying $\varsigma(\tau_k^j) = 0$ and $\vartheta(\tau_k^j) = \vartheta_j$. Differentiating (30) with respect to τ, we get

$$\left(\frac{d\lambda}{d\tau}\right)^{-1} = \frac{3\lambda^2 + 2a_1\lambda + a_2 + b_1e^{-\lambda\tau}}{\lambda(b_1\lambda + b_2)e^{-\lambda\tau}} - \frac{\tau}{\lambda}.$$

(38)

Thus,

$$\mathrm{Re}\left(\frac{d\lambda}{d\tau}\right)^{-1}\bigg|_{\tau=\tau_k^j} = \frac{3\vartheta_j^4 + 2\left(a_1^2 - 2a_2\right)\vartheta_j^2 + a_2^2 - 2a_1a_3 - b_1^2}{b_1^2\vartheta_j^2 + b_2^2},$$

$$= \frac{g'\left(\vartheta_j^2\right)}{b_1^2\vartheta_j^2 + b_2^2}.$$

(39)

It is not difficult to find out that $g'(\vartheta_j^2) \neq 0$ for all $j = 1, 2, 3$. Then, the transversality condition holds and we get the following result.

Theorem 7. *Assume $\mathcal{R}_1^Z < 1 < \mathcal{R}_0$ and $a_1(a_2 + b_1) - (a_3 + b_2) > 0$ hold.*

If either $q_0 < 0$ or $q_0 \geq 0$, $\Delta > 0$, $\mathcal{S}^* > 0$, and $g(\mathcal{S}^*) \leq 0$, then E_2 is locally asymptotically stable for all $\tau \in [0, \tau_0)$ and becomes unstable when $\tau > \tau_0$. Moreover, model (1) undergoes a Hopf bifurcation at E_2 when $\tau = \tau_k^j$, for $j = 1, 2, 3$ and $k \in IN$.

Remark 1. Theorem 7 shows that the delay τ can cause the partial success therapy equilibrium without immune response E_2 to gain or lose its stability. In addition, periodic solutions appear when the value of this delay is equal to a critical value.

Finally, we discuss the stability of the partial success therapy equilibrium with immune response E_3 when $\mathcal{R}_1^Z > 1$. In this case, (17) becomes

$$\lambda^4 + c_3\lambda^3 + c_2\lambda^2 + c_1\lambda + c_0 + \left(d_2\lambda^2 + d_1\lambda + d_0\right)e^{-\lambda\tau} = 0,$$

(40)

where

$$c_3 = \mu + \delta + (p+q)z_3 + \frac{rx_3}{K} + \frac{n\beta x_3}{\left(1 + \alpha v_3\right)^2},$$

$$c_2 = bpz_3 + \left(\mu + \delta + (p+q)z_3 + \frac{n\beta x_3}{\left(1+\alpha v_3\right)^2}\right)\frac{rx_3}{K} + \left(\delta + pz_3\right)\left(\mu + qz_3 + \frac{n\beta x_3}{\left(1+\alpha v_3\right)^2}\right) - \frac{n\beta^2 x_3 v_3}{\left(1+\alpha v_3\right)^3},$$

$$c_1 = bpz_3\left(\left(\mu + qz_3\right) + \frac{n\beta x_3}{\left(1+\alpha v_3\right)^2}\right) + \frac{rx_3}{K}\left[bpz_3 + \left(\delta + pz_3\right)\left(\mu + qz_3 + \frac{n\beta x_3}{\left(1+\alpha v_3\right)^2}\right)\right] - \frac{n\beta^2 x_3 v_3}{\left(1+\alpha v_3\right)^3}\left(\delta + pz_3\right),$$

$$c_0 = bpz_3\left[\frac{rx_3}{K}\left(\mu + qz_3 + \frac{n\beta x_3}{\left(1+\alpha v_3\right)^2}\right) - \frac{n\beta^2 x_3 v_3}{\left(1+\alpha v_3\right)^3}\right],$$

$$d_2 = \frac{\beta x_3}{1 + \alpha v_3}\left(\frac{rv_3}{K} - \frac{N\delta}{1+\alpha v_3}\right)e^{-m\tau},$$

$$d_1 = \left[\frac{\beta N\delta x_3}{\left(1+\alpha v_3\right)^2}\left(\frac{\beta v_3}{1+\alpha v_3} - \frac{rx_3}{K}\right) + \frac{\beta x_3 v_3}{1+\alpha v_3}\left(\frac{r}{K}\left(\mu + qz_3\right) + \frac{qcz_3}{1+\alpha v_3}\right)\right]e^{-m\tau},$$

$$d_0 = \frac{\beta qcx_3 v_3 z_3}{\left(1+\alpha v_3\right)^2}\left(\frac{rx_3}{K} - \frac{\beta v_3}{1+\alpha v_3}\right)e^{-m\tau}.$$

(41)

The above equation is the same as that analyzed by Hattaf in [9]. Then, let $i\phi\,(\phi > 0)$ be a root of (41). We have

$$\begin{cases} \phi^4 - c_2\phi^2 + c_0 = \left(d_2\phi^2 - d_0\right)\cos(\phi\tau) - b_1\phi\sin(\phi\tau), \\ -c_3\phi^3 + c_1\phi = -d_1\phi\cos(\phi\tau) - \left(d_2\phi^2 - d_0\right)\sin(\phi\tau), \end{cases} \tag{42}$$

which can be reduced to

$$\begin{aligned} &\phi^8 + \left(c_3^2 - 2c_2\right)\phi^6 + \left(c_2^2 - d_2^2 + 2c_0 - 2c_1c_3\right)\phi^4 \\ &+ \left(c_1^2 - d_1^2 - 2c_0c_2 + 2d_0d_2\right)\phi^2 + c_0^2 - d_0^2 = 0. \end{aligned} \tag{43}$$

Let $u = \phi^2$. Then, (43) becomes

$$h(u) := u^4 + p_3 u^3 + p_2 u^2 + p_1 u + p_0 = 0, \tag{44}$$

where $p_3 = c_3^2 - 2c_2$, $p_2 = c_2^2 - d_2^2 + 2c_0 - 2c_1c_3$, $p_1 = c_1^2 - d_1^2 - 2c_0c_2 + 2d_0d_2$, and $p_0 = c_0^2 - d_0^2$. Clearly, if $p_0 < 0$, equation (44) admits at least one positive root. Additionally, we have

$$h'(u) = 4u^3 + 3p_3 u^2 + 2p_2 u + p_1 = 0. \tag{45}$$

According to Cardano's formula, the cubic roots of (45) can be written as follows:

$$u_1 = \sqrt[3]{-\frac{Q}{2} + \sqrt{\overline{\Delta}}} + \sqrt[3]{-\frac{Q}{2} + \sqrt{\overline{\Delta}}} - \frac{p_3}{4},$$

$$u_2 = j\sqrt[3]{-\frac{Q}{2} + \sqrt{\overline{\Delta}}} + j^2\sqrt[3]{-\frac{Q}{2} - \sqrt{\overline{\Delta}}} - \frac{p_3}{4}, \tag{46}$$

$$u_3 = j^2\sqrt[3]{-\frac{Q}{2} + \sqrt{\overline{\Delta}}} + j\sqrt[3]{-\frac{Q}{2} - \sqrt{\overline{\Delta}}} - \frac{p_3}{4},$$

where

$$\mathscr{P} = \frac{8p_2 - 3p_3^2}{16},$$

$$Q = \frac{p_3^3 - 4p_3p_2 + 8p_1}{32},$$

$$\overline{\Delta} = \left(\frac{\mathscr{P}}{3}\right)^3 + \left(\frac{Q}{2}\right)^2, \tag{47}$$

$$j = -\frac{1}{2} + i\frac{\sqrt{3}}{2}.$$

Hence, we discuss the existence of real positive roots of (44).

(i) When $\overline{\Delta} > 0$, (44) has only a real root u_1 and the other two roots are conjugate complex numbers. Thus,

$$h'(u) = 4(u - u_1)\left(u^2 - 2\mathrm{Re}(u_2)z + |u_2|^2\right). \tag{48}$$

It follows that h admits a unique strict global minimum at $u = u_1$, and it is because $u^2 - 2\mathrm{Re}(u_2)z + |u_2|^2 > 0$ for all $u \in \mathrm{IR}$.

(ii) When $\overline{\Delta} = 0$, all roots are real with $u_1 = 3Q/\mathscr{P} - p_3/4$ and $u_2 = u_3 = 3Q/2\mathscr{P} - p_3/4$. Hence,

$$h'(u) = 4(u - u_1)(u - u_2)^2. \tag{49}$$

Thus, h reaches its strict global minimum at $u = u_1$. We conclude that if $p_0 \geq 0$ and $\overline{\Delta} \geq 0$, then equation (44) has a positive root if and only if $u_1 > 0$ and $h(u_1) \leq 0$.

(iii) When $\overline{\Delta} < 0$, the entire roots are real and distinct. In this case, we have

$$h'(u) = 4(u - u_1)(u - u_2)(u - u_3). \tag{50}$$

By analogical reasoning, we deduce that if $p_0 \geq 0$ and $\overline{\Delta} < 0$, then equation (44) has positive root if and only if there exists at least one $u^* \in \{u_1, u_2, u_3\}$ verifying $u^* > 0$ and $h(u^*) \leq 0$.

A summary of the above analysis leads to the following lemma.

Lemma 1

(i) If $p_0 < 0$, then equation (44) has at least one positive root

(ii) If $p_0 \geq 0$ and $\overline{\Delta} < 0$, then equation (44) has a positive root if and only if $u_1 \geq 0$ and $h(u_1) \leq 0$

(iii) If $p_0 \geq 0$ and $\overline{\Delta} < 0$, then equation (44) has a positive root if and only if there exists at least one $u^* \in \{u_1, u_2, u_3\}$ verifying $u^* > 0$ and $h(u^*) \leq 0$.

Based on Lemma 1, we set the following conditions:

$(\mathrm{H}_1)\,p_0 < 0$

$(\mathrm{H}_2)\,p_0 \geq 0$, $\overline{\Delta} \geq 0$, $u_1 > 0$, and $h(u_1) \leq 0$

$(\mathrm{H}_3)\,p_0 \geq 0$, $\overline{\Delta} < 0$, and there exists at least one $u^* \in \{u_1, u_2, u_3\}$ verifying $u^* > 0$ and $h(u^*) \leq 0$,

If conditions (H_1)–(H_3) are not fulfilled, then equation (44) has no positive solutions. Thus, equation (40) has no purely imaginary roots. Consequently, the partial success therapy equilibrium with immune response $E_3(x_3, y_3, v_3, z_3)$ is locally asymptotically stable for all $\tau \geq 0$. In this case, the presence of Hopf bifurcation is not achievable.

Next, we assume that one of the conditions (H_1)–(H_3) is fulfilled; then equation (44) admits at least one positive solution. Let $d \in \{1, 2, 3, 4\}$ be the number of positive roots of

(44). Denote these d positive roots by u_k. Then, equation (43) has d positive solutions $\phi_k = \sqrt{u_k}$, $k = 1, 2, \ldots, d$. Therefore, from (42), we obtain

$$
\tau_\eta^k = \frac{1}{\phi_k} \arccos \left(\frac{\left(\phi_k^4 - c_2\phi_k^2 + c_0\right)\left(b_2\phi_k^2 - b_0\right) + b_1\phi_k^2\left(c_3\phi_k^4 - c_1\right)}{b_1\phi_k^2 + \left(b_2\phi_k^2 - b_0\right)^2} \right)
$$
$$
+ \frac{2\eta\pi}{\phi_k},
$$
(51)

where $k = 1, 2, \ldots, d$ and $\eta \in \text{IN}$. We deduce that $\pm i\phi_k$ is a pair of purely imaginary roots of (40) with $\tau = \tau_\eta^k$. Define

$$
\tau_0 = \tau_0^{k_0} = \min_{k \in \{1,2,\ldots,d\}} \left\{ \tau_0^k \right\}, \phi_0 = \phi_{k_0}.
$$
(52)

We set $\lambda(\tau) = \varsigma(\tau) + i\phi(\tau)$ to be the root of equation (40) such that $\varsigma(\tau_\eta^k) = 0$ and $\phi(\tau_\eta^k) = \phi_k$. Considering ς as a function of τ and differentiating both sides of (40) with respect to τ lead to

$$
\left(\frac{d\lambda}{d\tau} \right)^{-1} = \frac{4\lambda^3 + 3c_3\lambda^2 + 2c_2\lambda + c_1 + (2d_2\lambda + d_1)e^{-\lambda\tau}}{\lambda\left(d_2\lambda^2 + d_1\lambda + d_0\right)e^{-\lambda\tau}} - \frac{\tau}{\lambda}.
$$
(53)

This implies that

$$
\text{Re}\left(\frac{d\lambda}{d\tau} \right)^{-1} \bigg|_{\tau=\tau_\eta^k} = \frac{4\phi_k^6 + 3p_3\phi_k^4 + 2p_2\phi_k^2 + p_1}{b_1\phi_k^2 + \left(b_2\phi_k^2 - b_0\right)^2}, = \frac{h'\left(\phi_k^2\right)}{b_1^2\phi_k^2 + b_2^2}.
$$
(54)

Since $\text{sign}\left\{ d(\text{Re}\lambda)/d\tau \mid_{\tau=\tau_\eta^k} \right\} = \text{sign}\left\{ \text{Re}(d\lambda/d\tau)^{-1} \mid_{\tau=\tau_\eta^k} \right\}$, we obtain

$$
\text{sign}\left\{ d(\text{Re}\lambda)/d\tau \mid_{\tau=\tau_\eta^k} \right\}
$$
$$
= \text{sign}\{h'(u_k)\} = \text{sign}\left\{4\phi_k^6 + 3p_3\phi_k^4 + 2p_2\phi_k^2 + p_1\right\}.
$$
(55)

Therefore, based on the above analysis, we claim the following result.

Theorem 8.
Assume that $\mathscr{R}_1^Z > 1$.

(i) If conditions (H_1)–(H_3) are not fulfilled, then the partial success therapy equilibrium with immune response E_3 is locally asymptotically stable for all $\tau \geq 0$.

(ii) If one of the conditions (H_1)–(H_3) is fulfilled, then the partial success therapy equilibrium with immune response E_3 is locally asymptotically stable for any time delay $\tau \in [0, \tau_0)$ and becomes unstable when $\tau > \tau_0$. Furthermore, if $h'(\phi_0^2) \neq 0$, then the transversality condition holds and model (1) undergoes a Hopf bifurcation at E_3 when $\tau = \tau_0$.

Based on Lemma 4.3 in [9], we easily deduce the following theorem.

Theorem 9.
Assume that $\mathscr{R}_1^Z > 1$.

(i) If equation (44) admits only one positive and simple root u_1, then E_3 is locally asymptotically stable for $\tau \in [0, \tau_0^1)$ and becomes unstable for $\tau > \tau_0^1$. Furthermore, a Hopf bifurcation appears when $\tau = \tau_\eta^1$, $\eta \in IN$.

(ii) If equation (44) admits only two positive and simple roots u_1, u_2 which are ordered as $u_2 < u_1$, then there exist a finite number of intervals such that if the delay τ is fixed in these intervals, the equilibrium E_3 is locally asymptotically stable, while unstable if τ not belonging to ones. In this case, E_3 switches from stability to instability.

(iii) If equation (44) admits at least three positive and simple roots, then there exists a least one stability switch.

Remark 2. Theorems 8 and 9 show that when the delay τ is considered, the partial success equilibrium with immune response E_3 can lose or gain its stability and rich dynamical behaviors occur including Hopf bifurcation and stability switches.

4. Discussion and Conclusion

In this paper, we have proposed and analyzed a virological model for cancer therapy with effects of saturation, innate immune response, and delay that biologically represents the time needed for infected tumor cells to produce new virions after viral entry. We first proved the positivity and the boundedness of solutions and discussed the existence of equilibria by means of two threshold parameters that are the basic reproduction number denoted by $\mathscr{R}_0$ and the reproduction number for innate immune response labeled by $\mathscr{R}_1^Z$ which represents the average number of innate immune cells activated by damaged tumor cells. More accurately, the proposed model has uniquely (i) two equilibria, the desired outcome therapy equilibrium E_0 and the complete failure therapy equilibrium E_1 if $\mathscr{R}_0 \leq 1$; (ii) three equilibria: E_0, E_1, and the partial success therapy equilibrium without immune response E_2 if $\mathscr{R}_1^Z \leq 1 < \mathscr{R}_0$; and (iii) four equilibria: E_0, E_1, E_2, and the partial success therapy equilibrium with immune response E_3 if $\mathscr{R}_1^Z > 1$. We have demonstrated that E_0 is always unstable and E_1 is globally asymptotically stable if $\mathscr{R}_0 \leq 1$ and becomes unstable if $\mathscr{R}_0 > 1$. Additionally, the stability of E_2 and E_3, Hopf bifurcation, and stability switches are analyzed rigorously. Furthermore, our model generalizes those in [7, 10] and our analytical results show that the delay in infection with oncolytic viruses can lead to the loss or stability of both equilibria E_2 and E_3.

Data Availability

The data used to support the findings of this study are available from the corresponding author upon request.

Conflicts of Interest

The authors declare that they have no conflicts of interest.

References

[1] E. Kelly and S. J. Russell, "History of oncolytic viruses: genesis to genetic engineering," *Molecular Therapy*, vol. 15, no. 4, pp. 651–659, 2007.

[2] T. C. Liau, E. Galanis, and D. Kirn, "Clinical trial results with oncolytic virotherapy: a century of promise, a decade of progress," *Journal of Nature Clinical Practice Oncology*, vol. 4, pp. 101–117, 2007.

[3] S. J. Russel, K. W. Pengl, and J. C. Bell, "Oncolytic virotherapy," *Journal of Nature Biotechnology*, vol. 30, pp. 658–670, 2012.

[4] J. Malinzi, P. Sibanda, and H. Mambili-Mamboundou, "Analysis of virotherapy in solid tumor invasion," *Mathematical Biosciences*, vol. 263, pp. 102–110, 2015.

[5] A. Nguyen, L. Ho, and Y. Wan, "Chemotherapy and oncolytic virotherapy: advanced tactics in the war against cancer," *Frontiers in Oncology*, vol. 4, p. 145, 2014.

[6] E. Binz and L. M. Ulrich, "Chemovirotherapy: combining chemotherapeutic treatment with oncolytic virotherapy," *Oncolytic Virotherapy*, vol. 4, pp. 39–48, 2015.

[7] T. A. Phan and J. P. Tian, "The role of the innate immune system in oncolytic virotherapy," *Computational and Mathematical Methods in Medicine*, vol. 2017, pp. 1–17, 2017.

[8] K. S. Kim, S. Kim, and I. H. Jung, "Hopf bifurcation analysis and optimal control of treatment in a delayed oncolytic virus dynamics," *Mathematics and Computers in Simulation*, vol. 149, pp. 1–16, 2018.

[9] K. Hattaf, "Global stability and Hopf bifurcation of a generalized viral infection model with multi-delays and humoral immunity," *Physica A: Statistical Mechanics and Its Applications*, vol. 545, Article ID 123689, 2020.

[10] A. Nouni, K. Hattaf, and N. Yousfi, "Dynamics of a mathematical model for cancer therapy with oncolytic viruses," *Communications in Mathematical Biology and Neuroscience*, vol. 1, no. 6, pp. 1–12, 2019.

[11] J. Hale and S. M. Verduyn Lunel, *Introduction to Functional Differential Equations*, Springer-Verlag, New York, NY, USA, 1993.

[12] H. I. Freedman and Y. Kuang, "Stability switches in linear scalar neutral delay equations," *Funkcialaj Ekvacioj*, vol. 34, pp. 187–209, 1991.

[13] J. P. LaSalle, "The stability of dynamical systems," in *Proceedings of the Regional Conference Series in Applied Mathematics*, SIAM, Philadelphia, PA, USA, July 1976.

[14] E. Beretta and Y. Kuang, "Geometric stability switch criteria in delay differential systems with delay dependent parameters," *SIAM Journal on Mathematical Analysis*, vol. 33, no. 5, pp. 1144–1165, 2002.

WILEY | Hindawi

Research Article

On Some Properties of the Hofstadter–Mertens Function

Pavel Trojovský [ID]

Department of Mathematics, Faculty of Science, University of Hradec Králové, Rokitanského 62, Hradec Králové, Czech Republic

Correspondence should be addressed to Pavel Trojovský; pavel.trojovsky@uhk.cz

Many mathematicians have been interested in the study of recursive sequences. Among them, a class of "chaotic" sequences are named "meta-Fibonacci sequences." The main example of meta-Fibonacci sequence was introduced by Hofstadter, and it is called the Q-sequence. Recently, Alkan–Fox–Aybar and the author studied the pattern induced by the connection between the Q-sequence and other known sequences. Here, we continue this program by studying a "Mertens' version" of the *Hofstadter sequence*, defined (for $x > 0$) by $x \mapsto \sum_{n \leq x} \mu(n) Q(n)$, where $\mu(n)$ is the Möbius function. In particular, as we shall see, this function encodes many interesting properties which relate prime numbers to "meta-sequences".

1. Introduction

The set of the integer sequences, denoted by $\mathbb{Z}^\infty$, is in the main stream of the mathematical studies. For example, the problems associated with the set of prime numbers are central topics in mathematics and in many recent applications (including modern cryptography) are based on these sequences. Another very famous numerical sequence is the sequence of Fibonacci numbers $(F_n)_{n \geq 0}$ defined by the recurrence $F_{n+2} = F_n + F_{n+1}$ (for $n \geq 2$), with initial values $F_0 = 0$ and $F_1 = 1$. The Fibonacci sequence is a binary recurrence; i.e., each term is the sum of the two preceding ones. Binary means order 2, so for an order k sequence, we need to know the previous k terms (in some combinations).

There are classes of sequences which are not linear (like the Fibonacci sequence). For instance, the sequence $(a_n)_{n \geq 0}$ defined by the quadratic recurrence $a_{n+1} = a_n^2 + c$, with $a_n = 0$ (where c is a given complex number), is a standard example of fractal sequence (connected to Mandelbrot's set). However, besides being nonlinear, it still has order 1.

Probably the first class of recursive sequences without a fixed order, was proposed, in 1979, by Hofstadter and Gödel [1]. In fact, they defined $(Q(n))_{n \geq 1}$ by the self-recurrence relation as follows:

$$Q(n) = Q(n - Q(n - 1)) + Q(n - Q(n - 2)), \quad (1)$$

with initial values $Q(1) = Q(2) = 1$. The term "self-recurrence" is the key point here. Because we must first know the value of $\max\{Q(n - 1), Q(n - 2)\}$ in order to calculate the value of $Q(n)$, the prefix "meta" means that this kind of sequence transcends, in some sense (maybe because of the nonexistence of a fixed order), the usual examples (i.e., it is "beyond" the standard recurrent sequences). The first terms of $Q(n)$ are

$$1, 1, 2, 3, 3, 4, 5, 5, 6, 6, 6, 8, 8, 8, 10, 9, 10, \ldots, \quad (2)$$

and the graph of $Q(n)$ in the interval $[1; 1, 500, 000]$ is plotted in Figure 1.

At first glance, the "self-definition" of $Q(n)$ appears to be a very strange definition. Paradoxically, so far, we do not know even if $Q(n)$ exists for all positive integers n (this is confirmed for $n < 12 \cdot 10^9$) [2]).

Many mathematicians worked on conditional results related to the *Hofstadter sequence* (i.e., $Q(n)$) under the assumption of its well definition. For example, Golomb [3] was the first to prove that $\lim_{n \to \infty} Q(n)/n = 1/2$, provided that this limit exists. A much weaker version of this result would be enough to ensure that the *Hofstadter sequence* is well defined. In fact, it suffices that $Q(n) \leq n + 1$, for all $n \geq 1$ (the limit says that $Q(n)$ grows as $n/2$).

By knowing the growth of $Q(n)$, namely, $Q(n) \approx n/2$, Pinn [4] developed the study of generations by paying
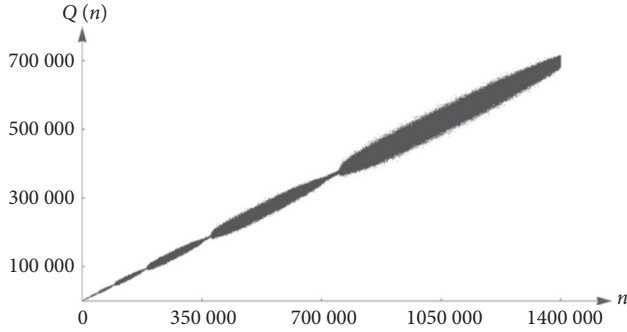
Figure 1: *Hofstadter Q-sequence* for (n) from 1 to 1,500,000.

Figure 2: $H(n) = C(n) - Q(n)$ for n from 1 to 1,500,000.

attention to the Q-graph. For him, these generations are the intervals $[a,b]$ such that the partial graph $\{(x, Q(x)): x \in [a,b]\}$ contains a complete "sausages" pattern as in Figure 1.

In 2017, Alkan et al. [5] made a very interesting discovery by studying the sequence $H(n) := C(n) - Q(n)$ (named by them as *Hofstadter* chaotic heart sequence, see its "heart fractal-like structure" in Figure 2), where C(n) is the Hofstadter–Conway $10,000 sequence is defined by the following recurrence:

$$C(n) = C(C(n-1)) + C(n - C(n-1)), \qquad (3)$$

with initial values $C(1) = C(2) = 1$ (in contrast with $Q(n)$, and it was proved that this sequence is well defined on $\mathbb{Z}_{>0}$).

Furthermore, we recall the *Möbius function* $\mu(n)$ which is defined by

$$\mu(n) = \begin{cases} 1, & \text{if } n = 1, \\ (-1)^N, & \text{if } n \text{ is a product of } N \text{ distinct primes}, \\ 0, & \text{if } N \text{ has one or more repeated prime factors.} \end{cases} \qquad (4)$$

A few values of this function are

$$1, -1, -1, 0, -1, 1, -1, 0, 0, 1, -1, 0, -1, 1, 1, 0, -1, 0, -1, 0, \ldots. \qquad (5)$$

This function plays an important role in number theory and combinatorics (mainly due its unpredictable behavior). Its *accumulation (or summation) function* denoted by $M(x)$ (and called the *Mertens function*) is defined by $M(x) := \sum_{n \leq x} \mu(n)$ (here the sum is taken over all positive integers smaller or equal to x).

The *Mertens function* slowly grows in positive and negative directions both on the average and in peak value, oscillating in an apparently chaotic manner passing through zero when n has the following values:

$$2, 39, 40, 58, 65, 93, 101,$$
$$145, 149, 150, 159, 160, \qquad (6)$$
$$163, 164, 166, 214, 231, \ldots.$$

We point out the stronger relation between $M(x)$ and some important number theoretic statements:

(i) The *Prime Number theorem* (which says that $\pi(x)\log x/x$ tends to 1 as $x \longrightarrow \infty$) is equivalent to $M(x) = o(x)$ (here $\pi(x)$ is the *prime counting function*, namely, the number of prime numbers belonging to $[1, x]$)

(ii) The *Riemann Hypothesis* is equivalent to $M(x) = O(x^{(1/2)+\varepsilon})$, for all $\varepsilon > 0$ (see [6, Theorem 14.25]), where, as usual, O and o are the standard *Big-O* and *Little-o* Landau notations

Recall that, we say $f(x) = O(g(x))$ if there exists a positive constant C, such that $|f(x)| \leq C|g(x)|$ for all sufficiently large x (the same meaning as $f \ll g$ and $f(x) = o(g(x))$ if $\lim_{x \longrightarrow \infty} f(x)/g(x) = 0$). Also, we denote $f \sim g$, if $f(x)/g(x)$ tends to 1 as $x \longrightarrow \infty$ (f and g are said to be *asymptotically equivalent*).

In the same spirit than by Alkan et al. [5], in a very recent paper, the author of [7] studied the relationship between the functions $Q(n)$ and $\mu(n)$, by defining $B(n) := Q(n) - n\mu(n)$. In this paper, we continue this program by introducing and analyzing the accumulation function of $\mu(n)Q(n)$ which gives relations between meta-Fibonacci sequences, prime factorization, and random walks.

Throughout the paper, we shall use the familiar notation $[a, b] = \{a, a+1, \ldots, b\}$, for integers $a < b$.

2. Hofstadter–Mertens Function

Here, we intend to consider the behavior of the accumulation function of $\mu(n)Q(n)$, denoted by $M_Q(x)$, which we call *Hofstadter–Mertens function* and it is defined as follows.

Definition 1. Let $M_Q(x) = \sum_{n \leq x} \mu(n)Q(n)$, where $Q(n)$ denotes the nth term of Hofstadter sequence and $\mu(n)$ is the Möbius function.

A few values of the sequence $(M_Q(n))_{n \geq 1}$ are

$$1, 0, -2, -2,$$
$$-5, -1, -6, -6, -6, 0, -6, -6, \qquad (7)$$
$$-14, -6, 4, 4, -6, -6, -17, \ldots.$$

We note the apparently chaotic behavior of $M_Q(x)$ which passes through zero (i.e., $M_Q(x) \leq 0$ and $M_Q(x+1) > 0$) when x takes the following integer values:

$$2, 10, 16, 22, 28, 36, 41, 66, 69, 102, 130, 137, 169, 240, 250, 257, 262, 265, \ldots.$$
$$(8)$$

Also, its structure seems to be chaotic and its shape seems to be as a growing "electrocardiogram" (see Figure 3).

Now, we shall split our study into four points: growth, generational structure, pseudo-periodicity, and statistical viewpoint.

In all what follows, we shall suppose that $Q(n)$ is well defined and that $Q(n)/n$ tends to 1/2 as $n \longrightarrow \infty$. We shall quote this as "Hypothesis (H)."

2.1. Growth.

It is almost unnecessary to stress that one of the first properties to study in the direction of a better comprehension of the behavior of a "chaotic" function is its growth (for large time). In fact, the structure of such a function is strongly reflected in its growth properties. For this reason, this section will be devoted to this kind of study.

By the Hypothesis (H) (in particular, $Q(n) = O(n)$) together with the fact that $|\mu(n)| \in \{0, 1\}$, we deduce that

$$M_Q(x) = O(x^2). \qquad (9)$$

However, this upper bound can be sharpened with the aid of some analytic number theory facts. For example, we know that $M(x) = o(x)$ and by Hypothesis (H), we can write $Q(n) = (n/2)(1 + o(1))$. This allows us to invoke a very useful formula due to Abel which makes an interplay between a discrete sum and an integral (continuous sum).

2.2. Abel's Summation Formula.

Let $(a_n)_n$ be a sequence of real numbers, and define its partial sum $A(x) := \sum_{n \leq x} a_n$. For a real number $x > 1$, let f be a continuously differentiable function on $[1, x]$. Then,

$$\sum_{n \leq x} a_n f(n) = A(x) f(x) - \int_1^x A(t) f'(t) \, dt. \qquad (10)$$

Before applying the previous formula, observe that $M_Q(x)$ can be rewritten as

$$M_Q(x) = \frac{1}{2} \sum_{n \leq x} n\mu(n)(1 + o(1)) = \frac{1}{2} \left(\sum_{n \leq x} n\mu(n) + \sum_{n \leq x} o(n) \right). \qquad (11)$$

Note that, by the properties of Landau's symbols, $\sum_{n \leq x} o(n) = o(\sum_{n \leq x} n) = o(x^2)$ and now, in order to obtain an estimate to $\sum_{n \leq x} n\mu(n)$, we are in the position to apply Abel's Summation Formula with the choice of $a_n := \mu(n)$ and $f(t) = t$. Thus,
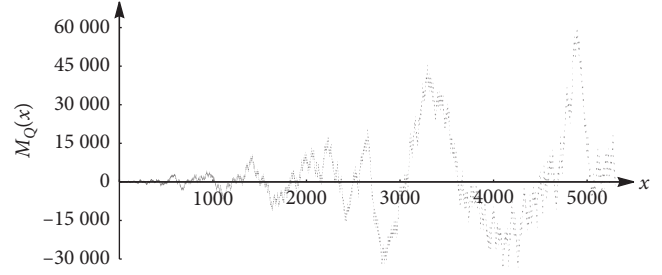
FIGURE 3: $M_Q(x) = \sum_{n < x} \mu(n) Q(n)$ for $x \in [1; 5,000]$.

$$\sum_{n \leq x} n\mu(n) = xM(x) - \int_1^x M(t) \, dt. \qquad (12)$$

By the prime number theorem, we have $M(x) = o(x)$ and then

$$\sum_{n \leq x} n\mu(n) = o(x^2) - \int_1^x o(t) \, dt. \qquad (13)$$

Again, by the properties of Landau's symbols, we have $\int_1^x o(t) \, dt = o(\int_1^x t \, dt) = o(x^2)$ and so we arrive at the following fact.

Fact 1. It holds that

$$M_Q(x) = o(x^2). \qquad (14)$$

We remark that since the Riemann Hypothesis (RH) is equivalent to $M(x) = O(x^{(1/2)+\varepsilon})$, then, by proceeding along the same lines as before, we deduce the following fact.

Fact 2. By assuming that the Riemann Hypothesis is true, then, for all $\varepsilon > 0$, it holds that

$$M_Q(x) = O(x^{(3/2)+\varepsilon}). \qquad (15)$$

Remark 1. Note that in Figure 4, the bound $x^{(3/2)}$ (red colored) seems to be very huge as compared to $|M_Q(x)|$. However, we point out that a similar feeling happens by plotting a similar graphic to $M(x)$ and $x^{(1/2)}$. In fact, this leads to the "very probable" conjecture raised by Mertens: $|M(x)| < \sqrt{x}$, for all $x > 0$. However, this conjecture was proved to be false (see [8]) for some (nonexplicit) counter examples of astronomical order about $10^{10^{40}}$.

2.3. Generational Structure.

The growth behavior of the graphical structure of $M_Q(n)$ brings a complex fractal-like structure. In fact, these kinds of patterns are commonly called "generational structure" of a meta-Fibonacci sequence (for more information about these structures for other meta-Fibonacci sequences, we refer the reader to [9–11]). In our case, these "generations" are the repeated "zigzag" pattern. More precisely, with Pinn's terminology, it is possible to partition the set of positive integers as

$$\mathbb{Z}_{>0} = \bigcup_{g \geq 0} G(g), \qquad (16)$$

FIGURE 4: Graph of $M_Q(n)$ (black colored), for n from 1 to 25,000 between the bounds $\pm x^{(3/2)}$ (red color dashed line).

FIGURE 5: Graph of $M_Q(x)$ (gray colored) and the disposal of endpoints of a generation (interval generation in black color).
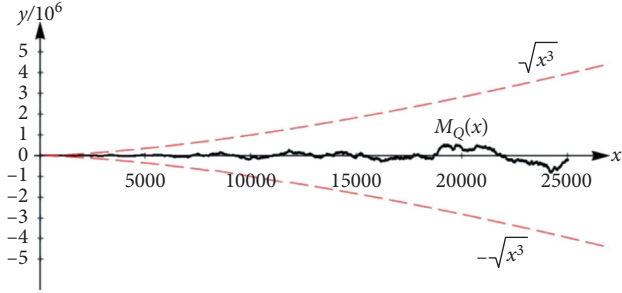
where $G(g)$ is a finite interval of natural numbers which is known as the gth *generation* of the sequence. In our case, each generation $G(g) = [x_0(g), x_1(g)]$ will be in such a way that (see Figure 5)

   (i) $M_Q(x_0(g)) < 0$

   (ii) $x_1(g) = \min\{t > x_0(g) + 1 : M_Q(t) < 0\}$

In an extensive empirical/heuristical study (see Figure 6), we were not able to find a pattern for $x_0(g)$ and $x_1(g)$. The main reason may lie in the chaotic behavior of $\mu(n)$ (related to random walks, for example). However, it is possible to deduce that $x_1(g) - x_0(g)$ can be made arbitrarily large. That is, we have the following fact.

Fact 3. For all positive integers N, there is an interval $G(g)$ with length strictly larger than N.

In the next section, we shall see that a kind of periodicity of $M_Q(x)$ is responsible for the veracity of this fact.

We point out that most of these findings are empirical observations, since virtually speaking, nothing has been proved rigorously about the Q-sequence, so far (as previously mentioned).

2.4. Pseudo-Periodicity. A function $f: \mathbb{R} \longrightarrow \mathbb{R}$ is said to be periodic if there exists a positive integer T such that $f(x + T) = f(x)$, for all $x \in \mathbb{R}$ (in other words, the function repeats its values in regular intervals or periods). The most important examples of periodic functions are the trigonometric functions, which repeat over intervals of 2π radians. Periodic functions are used throughout science to describe oscillations, waves, and other phenomena that exhibit periodicity. Any function that is not periodic is called *aperiodic*.

Clearly, the Hofstadter–Mertens function is aperiodic. However, we can define another kind of periodicity.

Definition 2. A function $f: \mathbb{R} \longrightarrow \mathbb{R}$ is said to be meta-periodic if for any positive integer T, there exist infinitely many positive values of x, such that $f(x + T) = f(x)$. Let T be a positive integer, and let $p_1 < p_1 <, \ldots, < p_T$ be the first T prime numbers. We have that the congruence system
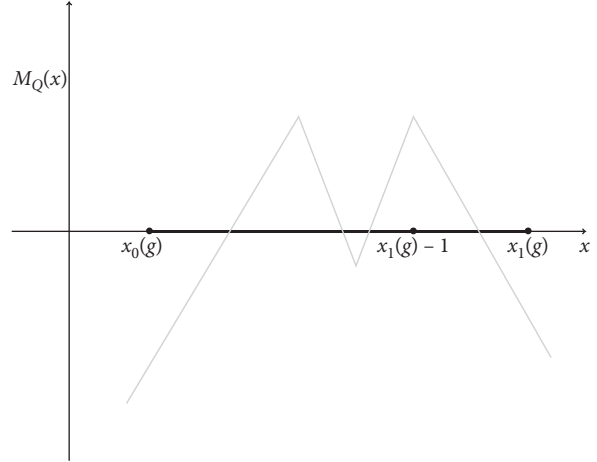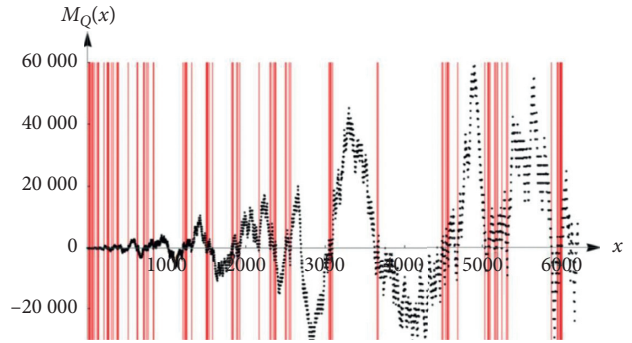
FIGURE 6: $M_Q(n)$ for n from 1 to 6000 with its first 101 "generations" separated by vertical lines.

$$\begin{cases} x \equiv -1 \pmod{p_1^2}, \\ x \equiv -2 \pmod{p_2^2}, \\ \quad\quad \vdots \\ x \equiv -T \pmod{p_T^2} \end{cases} \tag{17}$$

has infinitely many solutions in x (in a residue class modulo $(p_1 p_2, \ldots, p_T)^2$), say $(n_k)_{k \geq 0}$, by the *Chinese remainder theorem*. Clearly, for a particular solution $x = n_0$, we have that $p_i^2 \mid n_0 + i$ and so $\mu(n_0 + i) = 0$, for all $i \in [1, T]$. Thus, one has $\mu(n_0) = \cdots = \mu(n_0 + T) = 0$. In particular, we have

$$M_Q(n_k + T) = M_Q(n_k), \tag{18}$$

for all $k \geq 0$. Thus, we have the following fact.

Fact 4. The Hofstadter–Mertens function is meta-periodic. For instance, for some values of T, we have the following:

   (i) For $T = 2$, we have the family of solutions $n \equiv 7 \pmod{36}$

   (ii) For $T = 3$, we have the family of solutions $n \equiv 547 \pmod{900}$

   (iii) For $T = 5$, we have the family of solutions $n \equiv 1308247 \pmod{5336100}$

2.5. Statistical Viewpoint. Now, we wish to study the behavior of $M_Q(x)$ in a statistical vein. For this, our method will be based on a process that appeared in OEIS A283360 (see also its *Link* section) for the behavior that keeps the main characteristic of Q-sequence with deviations of noise in generations. Here, we define $q(n)$ as the remainder after division of $\sum_{k=1}^{n} M_Q(k)$ by n. So, for $n \in [1, 20]$, $q(n)$ attains the following values:

$$0, 1, 2, 1, 2, 3, 6, 3, 0, 3, 0, 9, 12, 11, 5, 13, 11, 9, 15, 3. \quad (19)$$

Now, we define $q^*(n) = |q(n + 1) - q(n)|$ and Figure 7 is the scatter plot of $M_Q(n)$ and $q^*(n)$ for n from 1 to 10000.

Figure 8 shows the evaluation (in a statistical viewpoint) of the *standard deviation* (SD), *mean* (arithmetic mean), and *median* of values of $M_Q(n)$ in the interval $[1, m]$, for $2 \leq m \leq 5000$.

3. Hofstadter–Mertens Function × Riemann Zeta Function

We close this study by comparing $M_Q(x)$ and the Riemann zeta function $\zeta(s) = \sum_{n \geq 1} 1/n^s$ (for $\Re(s) > 1$). We know that $\zeta(s)$ converges for all $\Re(s) > 1$ and admits an analytic continuation (via Abel Summation Formula) for $\Re(s) \geq 1$ except for a simple pole at $s = 1$, with residue 1 (in fact, Riemann extended this continuation for all complex planes but $s = 1$).

The zeta function is only one example of the called *Dirichlet series* which, for an arithmetic function $f: \mathbb{N} \longrightarrow \mathbb{R}$, is defined by

$$D(f, s) := \sum_{n \geq 1} \frac{f(n)}{n^s}. \quad (20)$$

Many properties of prime numbers are encoded by Dirichlet's series and its Euler's product. For example, for the Riemann zeta function, we have

$$\zeta(s) = \prod_{p} \left(1 - p^{-s}\right)^{-1}, \quad (21)$$

where the product is taken over all prime numbers. We know the huge importance of primes in mathematics and even in real life (as in cryptography). So, among the attempts made in this direction, we were able to provide the following fact.

Fact 5. We have that

$$\sum_{n \geq 1} \frac{\mu(n) Q(n)}{n^s} = \frac{1}{\zeta(s)} \sum_{n \geq 1} \frac{\psi(n)}{n^s}, \quad (22)$$

where

$$\psi(n) \sim \frac{(-1)^{\omega(n)}}{2} \frac{\phi(n)}{n} \prod_{p|n} p. \quad (23)$$

Here, as usual, $\omega(n)$ denotes the number of distinct prime factors of n and $\varphi(n) = \#\{k \in [1, n] : \gcd(k, n) = 1\}$ is the *Euler totient function*.
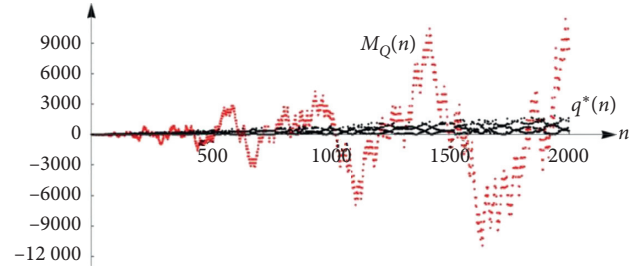
FIGURE 7: The scatter plot of $M_Q(n)$ (red colored) and $q^*(n)$ (black colored) for n from 1 to 2,000.
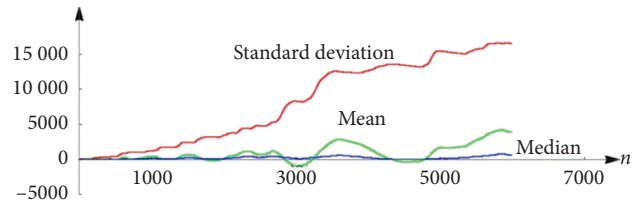
FIGURE 8: Standard deviation, mean, and median of $M_Q(n)$.

In order to prove this fact, we recall the *Dirichlet convolution* between two Dirichlet's series.

Definition 3. Let f and g be arithmetic functions; then, the Dirichlet convolution of f and g, denoted by f^*g is defined by

$$f^*g(n) := \prod_{d|n} f(d) g\left(\frac{n}{d}\right). \quad (24)$$

A well-known fact is that $D(f, s) \cdot D(g, s) = D(f^*g, s)$. Thus, let us consider $f(n) = 1$ (for all n), i.e., $D(f, s) = \zeta(s)$ and then,

$$D(\mu(n) Q(n), s) \cdot \zeta(s) = D(\mu(n) Q(n)^* 1, s) = \sum_{n \geq 1} \frac{\psi(n)}{n^s}, \quad (25)$$

where $\psi(n) = (\mu(n) Q(n)^* 1)(n) = \sum_{d|n} \mu(n) Q(n)$. Since, by Hypothesis (H), $Q(n)) \sim n/2$, then $\psi(n) \sim (1/2) \sum_{d|n} d\mu(d)$. Note that

$$\sum_{d|n} d\mu(d) = (-1)^{\omega(n)} \phi(\text{rad}(n)), \quad (26)$$

where $\text{rad}(n) = \sum_{p|n} p$ (where p is a prime) is called the *radical* of n (the proof of (26) follows from the fact that the left-hand side and the right-hand side, in formula (26), represent arithmetic multiplicative functions and so it is enough to compare them when n is a prime power). Now, we use $\phi(\text{rad}(n))/\text{rad}(n) = \phi(n)/n$ to conclude Fact 5.

4. Conclusion

In this paper, we continue the fruitful program started by Hofstadter, Golomb, Pinn, Alkan, Fox, and Aybar (among others) to study the behavior of meta-Fibonacci sequences, mainly the Q-sequence. Here, we studied the sequence

$M_Q(n)$ which is defined as the accumulation function of the product between the Q-sequence and the *Möbius function* (we call $M_Q(n)$ as *Hofstadter–Mertens function*). The sequence $M_Q(n)$ is studied with emphasis on its chaotic behavior. We split the text into four parts. We started by growing properties of $M_Q(n)$ and its relation with the *Riemann hypothesis* (here, we used some analytic tools). Then, we present some data regarding its "generational structures" together with some other facts. In the third part, we worked on the pattern repetition of $M_Q(x)$ by showing that it satisfies a kind of "meta-periodicity." We finish by mentioning some statistical viewpoints of the Hofstadter–Mertens function, such as its mean, median, and standard deviation (in a large scale). In the final section, we still present some theories of Dirichlet series related to $\mu(n)Q(n)$ which could have some theoretical interest in detection of primes or problems related to the *Riemann zeta function*.

Data Availability

The data calculated by the software Mathematica for Figures 1, 2, 3, 4, 6, 7, and 8 used to support the findings of this study are included within the supplementary information files.

Conflicts of Interest

The author declares that there are no conflicts of interest regarding the publication of this paper.

Supplementary Materials

The data of Figures 1, 2, 3, 4, 6, 7, and 8 are in separate files Figure 1.dat, Figure 2.dat, Figure 3.dat, Figure 4.dat, Figure 6.dat, Figure 7.dat, and Figure 8.dat. (*Supplementary Materials*)

References

[1] D. R. Hofstadter and E. Gödel, *Bach: An Eternal Golden Braid*, Basic Books, New York, NY, USA, 1979.

[2] A. Isgur, R. Lech, S. Moore, S. Tanny, Y. Verberne, and Y. Zhang, "Constructing new families of nested recursions with slow solutions," *SIAM Journal on Discrete Mathematics*, vol. 30, no. 2, pp. 1128–1147, 2016.

[3] S. W. Golomb, *Discrete Chaos: Sequences Satisfying "Strange" Recursions*, https://oeis.org/A005185/a005185 1.pdf, In press, 1991.

[4] K. Pinn, "Order and chaos in Hofstadter's $Q(n)$ sequence," *Complexity*, vol. 4, no. 3, pp. 41–46, 1999.

[5] A. Alkan, N. Fox, and O. O. Aybar, "On Hofstadter heart sequences," *Complexity*, vol. 2017, Article ID 2614163, 8 pages, 2017.

[6] E. C. Titchmarsh, *The Theory of the Riemann Zeta-Function*, University of Oxford, Oxford, UK, 1951.

[7] P. Trojovský, "On some properties of a meta-Fibonacci sequence connected to hofstadter sequence and möbius function," *Chaos, Solitons & Fractals*, vol. 134, Article ID 109708, 2020.

[8] A. M. Odlyzko and H. J. J. Te Riele, "Disproof of the Mertens conjecture," *Journal für die reine und angewandte Mathematik (Crelles Journal)*, vol. 1985, no. 357, pp. 138–160, 1985.

[9] A. Alkan, "On a generalization of Hofstadter's Q-sequence: a family of chaotic generational structures," *Complexity*, vol. 2018, Article ID 8517125, 8 pages, 2018.

[10] A. Alkan, "On a conjecture about generalized Q-recurrence," *Open Mathematics*, vol. 16, no. 1, pp. 1490–1500, 2018.

[11] B. Dalton, M. Rahman, and S. Tanny, "Spot-based generations for meta-fibonacci sequences," *Experimental Mathematics*, vol. 20, no. 2, pp. 129–137, 2011.

WILEY | Hindawi

Research Article

Computational and Numerical Solutions for $(2 + 1)$-Dimensional Integrable Schwarz–Korteweg–de Vries Equation with Miura Transform

Raghda A. M. Attia,[1,2] **S. H. Alfalqi,**[3] **J. F. Alzaidi,**[3] **Mostafa M. A. Khater** **,**[1,4] **and Dianchen Lu** [1]

[1]*Department of Mathematics, Faculty of Science, Jiangsu University, Zhenjiang 212013, China*
[2]*Department of Basic Science, Higher Technological Institute, 10th of Ramadan 44634, Egypt*
[3]*Department of Mathematics, Faculty of Science and Arts in Mahayil Asir, King Khalid University, Abha, Saudi Arabia*
[4]*Department of Mathematics, El Obour Institutes, Cairo 11828, Egypt*

Correspondence should be addressed to Mostafa M. A. Khater; mostafa.khater2024@yahoo.com

This paper investigates the analytical, semianalytical, and numerical solutions of the $(2 + 1)$–dimensional integrable Schwarz–Korteweg–de Vries (SKdV) equation. The extended simplest equation method, the sech-tanh method, the Adomian decomposition method, and cubic spline scheme are employed to obtain distinct formulas of solitary waves that are employed to calculate the initial and boundary conditions. Consequently, the numerical solutions of this model can be investigated. Moreover, their stability properties are also analyzed. The solutions obtained by means of these techniques are compared to unravel relations between them and their characteristics illustrated under the suitable choice of the parameter values.

1. Introduction

The Korteweg–de Vries (KdV) equation is a seminal model in fluid mechanics. This model was introduced by Boussinesq in 1877 and reintroduced by Diederik Korteweg and Gustav de Vries in 1895. The KdV has the following formula [1–9]:

$$\mathcal{Q}_t + \mathcal{U}_{xxx} - 6\mathcal{U}\mathcal{U}_x = 0, \tag{1}$$

where $\mathcal{U} = \mathcal{U}(x, t)$ characterizes the weakly nonlinear shallow water waves. Equation (1) can be written in many distinct forms and combined with other models. One of them is the Schwarz–Korteweg–de Vries (SKdV) equation given by

$$\mathcal{Q}_t + \mathcal{Q}_x \left[\left(\frac{\mathcal{Q}_{xx}}{\mathcal{Q}_x} \right) - \frac{1}{2} \left(\frac{\mathcal{Q}_{xx}}{\mathcal{Q}_x} \right)^2 \right] = 0, \tag{2}$$

where $\mathcal{Q} = \mathcal{Q}(x, t)$ is the unknown function. The SKdV was derived by Krichever and Novikov [10] and Weiss [11, 12].

In this paper, we study the $(2 + 1)$-dimensional integrable generalization of SKdV as follows:

$$\mathcal{U}_t + \frac{1}{4}\mathcal{U}_{xxy} - \frac{\mathcal{U}_x \mathcal{U}_{xy}}{2\mathcal{U}} - \frac{\mathcal{U}_{xx}\mathcal{U}_y}{4\mathcal{U}} + \frac{\mathcal{U}_x^2 \mathcal{U}_y}{2\mathcal{U}^2} - \frac{\mathcal{U}_x}{8} \int \left(\frac{\mathcal{U}_x^2}{\mathcal{U}^2} \right)_y \mathrm{d}x = 0. \tag{3}$$

Equation (3) was derived by Toda and Yu [13]. Using the following transformation on equation (3),

$$\begin{aligned}
\mathcal{U} &= \mathcal{S}_x, \\
\mathcal{S} &= e^{\mathcal{F}}, \\
\mathcal{F}_x &= \mathcal{U}, \\
\mathcal{F}_t &= \mathcal{R},
\end{aligned} \tag{4}$$

where $\mathcal{S} = \mathcal{S}(x,t), \mathcal{F} = \mathcal{F}(x,t), \mathcal{U} = \mathcal{U}(x,t)$, and $\mathcal{R} = \mathcal{R}(x,t)$ are the unknown functions, we obtain

$$\begin{cases} 4\mathcal{U}^2\mathcal{R}_x - 4\mathcal{U}\mathcal{U}_x\mathcal{R} + \mathcal{U}^2\mathcal{U}_{xxy} - \mathcal{U}\mathcal{U}_{xx}\mathcal{U}_y - 3\mathcal{U}\mathcal{U}_x\mathcal{U}_{xy} + 3\mathcal{U}_x^2\mathcal{U}_y - \mathcal{U}^4\mathcal{U}_y = 0, \\ \mathcal{U}_t - \mathcal{R}_x = 0. \end{cases} \tag{5}$$

This equation is obtained from the study by Bruzón et al. [14–16]. Using the Miura transform [17–19] on equation (5) as

$$\begin{aligned} \mathcal{B}_x &= \frac{\mathcal{U}_{xx}}{4\mathcal{U}} - \frac{3\mathcal{U}_x^2}{8\mathcal{U}^2} - \frac{\mathcal{U}^2}{8}, \\ \mathcal{B}_y &= -\frac{\mathcal{R}}{\mathcal{U}}, \end{aligned} \tag{6}$$

we obtain [20, 21]

$$4\mathcal{B}_{xt} + \mathcal{B}_{xxxy} + 8\mathcal{B}_{xy}\mathcal{B}_x + 4\mathcal{B}_y\mathcal{B}_{xx} = 0. \tag{7}$$

If we adopt the wave transformation

$$\begin{aligned} \mathcal{B}(x,y,t) &= \mathcal{B}(\mathfrak{Z}), \\ \mathfrak{Z} &= \rho x + \delta y + ct, \end{aligned} \tag{8}$$

then we convert equation (7) into an ordinary differential equation (NLODE). The integration of the obtained NLODE with zero constant of integration leads to

$$4c\mathcal{B}' + \rho^2\delta\mathcal{B}''' + 6\rho\delta\mathcal{B}'^2 = 0. \tag{9}$$

If we consider the substitution $\mathcal{B}' = \mathcal{F}$, then it results in

$$4c\mathcal{F} + \rho^2\delta\mathcal{F}'' + 6\rho\delta\mathcal{F}^2 = 0. \tag{10}$$

Having these ideas in mind, this paper is organized as follows: Section 2 presents the two methods and derives the solutions of the SKdV equation. Section 5 represents the solutions for several numerical values of the parameters. Additionally, their stability and properties are also discussed. Finally, Section 6 summarises the main conclusions.

2. Explicit Solutions

In this section, we apply two analytical techniques for deriving the solutions of the $(2 + 1)$-dimensional integrable SKdV model. We adopt the extended simplest equation method and the sech-tanh method to obtain various distinct formulas of solitary wave solutions of equation (3). For further details about the two methods, see [22–26].

2.1. Extended Simplest Equation. According to the homogeneous balance rule between the highest derivative and the nonlinear term in equation (9), we obtain $n = 2$. Thus, the general solution of equation (10) is given by

$$\mathcal{F}(\mathfrak{Z}) = \sum_{i=-n}^{n} a_i\mathcal{C}(\mathfrak{Z})^i = a_2\mathcal{C}(\mathfrak{Z})^2 + a_1\mathcal{C}(\mathfrak{Z}) + \frac{a_{-2}}{\mathcal{C}(\mathfrak{Z})^2} + \frac{a_{-1}}{\mathcal{C}(\mathfrak{Z})} + a_0, \tag{11}$$

where $a_i (i = -2, \ldots, 2)$ are arbitrary constants. Additionally, $\mathcal{C}(\mathfrak{Z})$ satisfies the following ordinary differential equation:

$$\mathcal{C}'(\mathfrak{Z}) = \alpha + \lambda\mathcal{C}(\mathfrak{Z}) + \mu\mathcal{C}(\mathfrak{Z})^2, \tag{12}$$

where β, α, and μ are the arbitrary constants. Substituting equations (11) and (12) into (9) and collecting all terms of $\mathcal{C}^i(\mathfrak{Z})$ $(i = -4, -3, \ldots, 3, 4)$, we get a system of algebraic equations. Solving this system, we obtain two families of solutions.

Family 1

$$\begin{aligned} a_0 &\longrightarrow \frac{1}{6}\left(-2\alpha\mu\rho - \lambda^2\rho\right), \\ a_1 &\longrightarrow 0, \\ a_2 &\longrightarrow 0, \\ a_{-1} &\longrightarrow -\alpha\lambda\rho, \\ a_{-2} &\longrightarrow -\alpha^2\rho, \\ c &\longrightarrow \frac{1}{4}\left(\delta\lambda^2\rho^2 - 4\alpha\delta\mu\rho^2\right). \end{aligned} \tag{13}$$

Family 2

$$\begin{aligned} a_0 &\longrightarrow \frac{1}{6}\left(-2\alpha\mu\rho - \lambda^2\rho\right), \\ a_1 &\longrightarrow -\lambda\mu\rho, \\ a_2 &\longrightarrow -\mu^2\rho, \\ a_{-1} &\longrightarrow 0, \\ a_{-2} &\longrightarrow 0, \\ c &\longrightarrow \frac{1}{4}\left(\delta\lambda^2\rho^2 - 4\alpha\delta\mu\rho^2\right). \end{aligned} \tag{14}$$

From these two families, the solitary wave solutions of equation (7) can be obtained.

According to Family 1, we have the following expressions.

2.1.1. When $\lambda = 0$. For $\alpha\mu > 0$, we obtain

$$\mathcal{F}_1(x, y, t) = -\frac{\alpha\mu\rho}{3} - \frac{\lambda^2\rho}{6} - \alpha\mu\rho \cot^2\left(\frac{1}{4}\sqrt{\alpha\mu}\left(\delta\rho^2 t\left(\lambda^2 - 4\alpha\mu\right) + 4\rho x + 4\delta y + 4\vartheta\right)\right)$$
$$- \lambda\rho\sqrt{\alpha\mu}\cot\left(\frac{1}{4}\sqrt{\alpha\mu}\left(\delta\rho^2 t\left(\lambda^2 - 4\alpha\mu\right) + 4\rho x + 4\delta y + 4\vartheta\right)\right), \tag{15}$$

$$\mathcal{F}_2(x, y, t) = -\frac{\alpha\mu\rho}{3} - \frac{\lambda^2\rho}{6} - \alpha\mu\rho \tan^2\left(\frac{1}{4}\sqrt{\alpha\mu}\left(\delta\rho^2 t\left(\lambda^2 - 4\alpha\mu\right) + 4\rho x + 4\delta y + 4\vartheta\right)\right)$$
$$- \lambda\rho\sqrt{\alpha\mu}\tan\left(\frac{1}{4}\sqrt{\alpha\mu}\left(\delta\rho^2 t\left(\lambda^2 - 4\alpha\mu\right) + 4\rho x + 4\delta y + 4\vartheta\right)\right). \tag{16}$$

For $\alpha\mu < 0$, we obtain

$$\mathcal{F}_3(x, y, t) = \alpha\mu\rho \coth^2\left(\frac{1}{4}\sqrt{-\alpha\mu}\left(\rho\left(4x - 4\alpha\delta\mu\rho t\right) + 4\delta y\right) \mp \frac{\log(\vartheta)}{2}\right) - \frac{\alpha\mu\rho}{3}, \tag{17}$$

$$\mathcal{F}_4(x, y, t) = \alpha\mu\rho \tanh^2\left(\frac{1}{4}\sqrt{-\alpha\mu}\left(\rho\left(4x - 4\alpha\delta\mu\rho t\right) + 4\delta y\right) \mp \frac{\log(\vartheta)}{2}\right) - \frac{\alpha\mu\rho}{3}. \tag{18}$$

When $4\alpha\mu > \lambda^2$, we obtain

$$\mathcal{F}_5(x, y, t) = -\frac{\alpha\mu\rho}{3} - \frac{4\alpha^2\mu^2\rho}{\left(\lambda - \sqrt{4\alpha\mu - \lambda^2}\tan\left((1/8)\sqrt{4\alpha\mu - \lambda^2}\left(\rho\left(\delta\rho t\left(\lambda^2 - 4\alpha\mu\right) + 4x\right) + 4\delta y + 4\vartheta\right)\right)\right)^2}$$
$$- \frac{\lambda^2\rho}{6} + \frac{2\alpha\lambda\mu\rho}{\lambda - \sqrt{4\alpha\mu - \lambda^2}\tan\left((1/8)\sqrt{4\alpha\mu - \lambda^2}\left(\rho\left(\delta\rho t\left(\lambda^2 - 4\alpha\mu\right) + 4x\right) + 4\delta y + 4\vartheta\right)\right)}, \tag{19}$$

$$\mathcal{F}_6(x, y, t) = -\frac{\alpha\mu\rho}{3} - \frac{4\alpha^2\mu^2\rho}{\left(\lambda - \sqrt{4\alpha\mu - \lambda^2}\cot\left((1/8)\sqrt{4\alpha\mu - \lambda^2}\left(\rho\left(\delta\rho t\left(\lambda^2 - 4\alpha\mu\right) + 4x\right) + 4\delta y + 4\vartheta\right)\right)\right)^2}$$
$$- \frac{\lambda^2\rho}{6} + \frac{2\alpha\lambda\mu\rho}{\lambda - \sqrt{4\alpha\mu - \lambda^2}\cot\left((1/8)\sqrt{4\alpha\mu - \lambda^2}\left(\rho\left(\delta\rho t\left(\lambda^2 - 4\alpha\mu\right) + 4x\right) + 4\delta y + 4\vartheta\right)\right)}. \tag{20}$$

According to Family 2, we have the following expressions.

$$\mathscr{F}_7(x,y,t) = -\frac{\alpha\mu\rho}{3} - \frac{\lambda^2\rho}{6} - \alpha\mu\rho\tan^2\left(\frac{1}{4}\sqrt{\alpha\mu}\left(\delta\rho^2t\left(\lambda^2 - 4\alpha\mu\right) + 4\rho x + 4\delta y + 4\vartheta\right)\right)$$

$$- \lambda\rho\sqrt{\alpha\mu}\tan\left(\frac{1}{4}\sqrt{\alpha\mu}\left(\delta\rho^2t\left(\lambda^2 - 4\alpha\mu\right) + 4\rho x + 4\delta y + 4\vartheta\right)\right), \tag{21}$$

$$\mathscr{F}_8(x,y,t) = -\frac{\alpha\mu\rho}{3} - \frac{\lambda^2\rho}{6} - \alpha\mu\rho\cot^2\left(\frac{1}{4}\sqrt{\alpha\mu}\left(\delta\rho^2t\left(\lambda^2 - 4\alpha\mu\right) + 4\rho x + 4\delta y + 4\vartheta\right)\right)$$

$$- \lambda\rho\sqrt{\alpha\mu}\cot\left(\frac{1}{4}\sqrt{\alpha\mu}\left(\delta\rho^2t\left(\lambda^2 - 4\alpha\mu\right) + 4\rho x + 4\delta y + 4\vartheta\right)\right). \tag{22}$$

For $\alpha\mu < 0$, we obtain

$$\mathscr{F}_9(x,y,t) = \alpha\mu\rho\tanh^2\left(\frac{1}{4}\sqrt{-\alpha\mu}\left(\rho(4x - 4\alpha\delta\mu\rho t) + 4\delta y\right) \mp \frac{\log(\vartheta)}{2}\right) - \frac{\alpha\mu\rho}{3}, \tag{23}$$

$$\mathscr{F}_{10}(x,y,t) = \alpha\mu\rho\coth^2\left(\frac{1}{4}\sqrt{-\alpha\mu}\left(\rho(4x - 4\alpha\delta\mu\rho t) + 4\delta y\right) \mp \frac{\log(\vartheta)}{2}\right) - \frac{\alpha\mu\rho}{3}. \tag{24}$$

When $\alpha = 0$: For $\lambda > 0$, we get

$$\mathscr{F}_{11}(x,y,t) = -\frac{\lambda^2\mu^2\rho\exp\left((1/2)\lambda\left(\rho\left(\delta\lambda^2\rho t + 4x\right) + 4\delta y + 4\vartheta\right)\right)}{6\left(\mu e^{(1/4)\delta\lambda^3\rho^2t + \lambda\rho x + \delta\lambda y + \lambda\vartheta} - 1\right)^2}$$

$$- \frac{2\lambda^2\mu\rho e^{(1/4)\lambda\rho\left(\delta\lambda^2\rho t + 4x\right) + \delta\lambda y + \lambda\vartheta}}{3\left(\mu e^{(1/4)\delta\lambda^3\rho^2t + \lambda\rho x + \delta\lambda y + \lambda\vartheta} - 1\right)^2}$$

$$- \frac{\lambda^2\rho}{6\left(\mu e^{(1/4)\delta\lambda^3\rho^2t + \lambda\rho x + \delta\lambda y + \lambda\vartheta} - 1\right)^2}. \tag{25}$$

For $\lambda < 0$, we obtain

$$\mathscr{F}_{12}(x,y,t) = -\frac{\mu^4\rho\exp\left((1/2)\lambda\left(\rho\left(\delta\lambda^2\rho t + 4x\right) + 4\delta y + 4\vartheta\right)\right)}{\left(\mu e^{(1/4)\delta\lambda^3\rho^2t + \lambda\rho x + \delta\lambda y + \lambda\vartheta} + 1\right)^2}$$

$$- \frac{\lambda^2\rho}{6\left(\mu e^{(1/4)\delta\lambda^3\rho^2t + \lambda\rho x + \delta\lambda y + \lambda\vartheta} + 1\right)^2}$$

$$- \frac{\lambda^2\mu^2\rho\exp\left((1/2)\lambda\left(\rho\left(\delta\lambda^2\rho t + 4x\right) + 4\delta y + 4\vartheta\right)\right)}{6\left(\mu e^{(1/4)\delta\lambda^3\rho^2t + \lambda\rho x + \delta\lambda y + \lambda\vartheta} + 1\right)^2}$$

$$+ \frac{\lambda\mu^2\rho e^{1/4\lambda\rho\left(\delta\lambda^2\rho t + 4x\right) + \delta\lambda y + \lambda\vartheta}}{\left(\mu e^{(1/4)\delta\lambda^3\rho^2t + \lambda\rho x + \delta\lambda y + \lambda\vartheta} + 1\right)^2}$$

$$- \frac{\lambda^2\mu\rho e^{(1/4)\lambda\rho\left(\delta\lambda^2\rho t + 4x\right) + \delta\lambda y + \lambda\vartheta}}{3\left(\mu e^{(1/4)\delta\lambda^3\rho^2t + \lambda\rho x + \delta\lambda y + \lambda\vartheta} + 1\right)^2}$$

$$+ \frac{\lambda\mu^3\rho\exp\left(1/2\lambda\left(\rho\left(\delta\lambda^2\rho t + 4x\right) + 4\delta y + 4\vartheta\right)\right)}{\left(\mu e^{(1/4)\delta\lambda^3\rho^2t + \lambda\rho x + \delta\lambda y + \lambda\vartheta} + 1\right)^2}. \tag{26}$$

2.1.2. When $\lambda = 0$. For $\alpha\mu > 0$, we obtain

When $4\alpha\mu > \lambda^2$, we obtain

$$\mathscr{F}_{13}(x,y,t) = \frac{2\alpha\mu\rho}{3} - \frac{\lambda^2\rho}{6} + \frac{1}{4}\lambda^2\rho\sec^2$$

$$\left(\frac{1}{8}\sqrt{4\alpha\mu - \lambda^2}\left(\delta\rho^2t\left(\lambda^2 - 4\alpha\mu\right) + 4\rho x + 4\delta y + 4\vartheta\right)\right)$$

$$- \alpha\mu\rho\sec^2\left(\frac{1}{8}\sqrt{4\alpha\mu - \lambda^2}\left(\delta\rho^2t\left(\lambda^2 - 4\alpha\mu\right) + 4\rho x + 4\delta y + 4\vartheta\right)\right), \tag{27}$$

$$\mathscr{F}_{14}(x,y,t) = \frac{2\alpha\mu\rho}{3} - \frac{\lambda^2\rho}{6} + \frac{1}{4}\lambda^2\rho\csc^2$$

$$\left(\frac{1}{8}\sqrt{4\alpha\mu - \lambda^2}\left(\delta\rho^2t\left(\lambda^2 - 4\alpha\mu\right) + 4\rho x + 4\delta y + 4\vartheta\right)\right)$$

$$- \alpha\mu\rho\csc^2\left(\frac{1}{8}\sqrt{4\alpha\mu - \lambda^2}\left(\delta\rho^2t\left(\lambda^2 - 4\alpha\mu\right) + 4\rho x + 4\delta y + 4\vartheta\right)\right). \tag{28}$$

2.2. Sech-Tanh Method. The general solution of equation (10) according to the sech-tanh method and calculated value of balance is given by

$$\mathscr{F}(\mathfrak{Z}) = \sum_{i=1}^{n}\operatorname{sech}^{i-1}(\mathfrak{Z})\left(a_i\operatorname{sech}(\mathfrak{Z}) + b_i\tanh(\mathfrak{Z})\right) + a_0$$

$$= \operatorname{sech}(\mathfrak{Z})\left(a_2\operatorname{sech}(\mathfrak{Z}) + b_2\tanh(\mathfrak{Z})\right)$$

$$+ a_1\operatorname{sech}(\mathfrak{Z}) + a_0 + b_1\tanh(\mathfrak{Z}), \tag{29}$$

where $a_0, a_1, a_2, b_1,$ and b_2 are the arbitrary constants. Substituting equation (29) into (10) and collecting all terms of $\operatorname{sech}(\mathfrak{Z}), \operatorname{sech}^2(\mathfrak{Z}), \operatorname{sech}^3(\mathfrak{Z}), \tanh(\mathfrak{Z}), \tanh(\mathfrak{Z})\operatorname{sec}h^2(\mathfrak{Z}),$ and $\tanh(\xi)\operatorname{sech}(\mathfrak{Z})$, we obtain a system of algebraic equations. Solving this system, we obtain

$$a_0 \longrightarrow \frac{2\sqrt{c}}{3\sqrt{\delta}},$$

$$a_1 \longrightarrow 0,$$

$$a_2 \longrightarrow -\frac{\sqrt{c}}{\sqrt{\delta}},$$

$$b_1 \longrightarrow 0,$$ \hfill (30)

$$b_2 \longrightarrow 0,$$

$$\rho \longrightarrow -\frac{\sqrt{c}}{\sqrt{\delta}}, \quad \text{where } (c > 0, \delta > 0).$$

Consequently, the explicit solution of equation (7) is given by

$$\mathscr{F}_{15}(x, y, t) = \frac{\sqrt{c}\left(2 - 3\mathrm{sech}^2(ct + \rho x + \delta y)\right)}{3\sqrt{\delta}}. \tag{31}$$

3. Stability Investigation

We now examine the stability property for $(2+1)$-dimensional integrable SKdV model with the Miura transformation by means of an Hamiltonian system. The momentum $\mathfrak{H}$ in the Hamiltonian system is given by

$$\mathfrak{H} = \frac{1}{2}\int_{-\mathscr{I}}^{\mathscr{I}} \mathscr{B}^2(\mathfrak{Z})\mathrm{d}\mathfrak{Z}, \tag{32}$$

where $\mathscr{B}(\mathfrak{Z})$ is the solution of the model. Consequently, the condition for stability of the solutions can be formulated as

$$\frac{\partial \mathfrak{H}}{\partial c} > 0, \tag{33}$$

where c is the wave velocity. The momentum in the Hamiltonian system for equations (18) and (31) are given, respectively, by

$$\mathfrak{H} = \frac{1}{c}\Big(3200c - \mathrm{sech}^2(10c + 26) - \mathrm{sech}^2(10c + 34) + \mathrm{sech}^2(26 - 10c) + \mathrm{sech}^2(34 - 10c) - 4\log\big((e^{52} - 1)$$

$$\times \sinh(10c) + (1 + e^{52})\cosh(10c)\big) - 4\log\big((e^{68} - 1)\sinh(10c) + (1 + e^{68})\cosh(10c)\big) + 4\log\big((1 + e^{52})\cosh(10c) \tag{34}$$

$$-(e^{52} - 1)\sinh(10c)\big) + 4\log\big((1 + e^{68})\cosh(10c) - (e^{68} - 1)\sinh(10c)\big)\Big),$$

$$\mathfrak{H} = \frac{1}{72}\Big(4\big(100c + \log(e^{7-5c} + e^{5c}) + \log(e^{23-5c} + e^{5c}) - \log(e^{-5c} + e^{5c+7}) - \log(e^{-5c} + e^{5c+23})\big)$$

$$-\mathrm{sech}^2\Big(5c + \frac{7}{2}\Big) - \mathrm{sech}^2\Big(5c + \frac{23}{2}\Big) + \mathrm{sech}^2\Big(\frac{7}{2} - 5c\Big) + \mathrm{sech}^2\Big(\frac{23}{2} - 5c\Big)\Big). \tag{35}$$

And thus,

$$\left.\frac{\partial \mathfrak{H}}{\partial c}\right|_{c=72} = 2.37146 \times 10^{-298} > 0, \tag{36}$$

$$\left.\frac{\partial \mathfrak{H}}{\partial c}\right|_{c=9} = 5.55556 > 0. \tag{37}$$

We conclude that this solution is stable on the interval $x \in [-5, 5], t \in [-5, 5]$. This result shows the ability of the solutions for their application. Using the same steps, we can check the stability property of all other obtained solutions.

4. Semianalytical and Numerical Solutions

This section applies semianalytical and numerical schemes for deriving the solutions of the $(2+1)$-dimensional integrable SKdV model. The Adomian decomposition method and cubic b-spline schemes are employed to the method to investigate the accuracy of the obtained analytical solutions. Also, this study aims to give a comparison between both used analytical schemes. For further details about the two methods, see [27–30].

4.1. Adomian Decomposition Method. Applying this scheme gives equation (10) in the following form:

$$\sum_{j=0}^{\infty} \mathscr{F}_j(\mathfrak{Z}) = \mathscr{F}(0) + \mathscr{F}'(0)\mathfrak{Z} - \frac{4c}{\rho^2\delta}\mathscr{L}^{-1}\left(\sum_{j=0}^{\infty} \mathscr{F}_j(\mathfrak{Z})\right) - \frac{6}{\rho}\mathscr{L}^{-1}\left(\sum_{j=0}^{\infty} A_j\right). \tag{38}$$

Thus, with respect to equation (18) and the following conditions $\alpha = -1, a_0 = 4, a_{-1} = 0, a_{-2} = -3, c = 72, \delta = 2, \lambda = 0, \mu = 4,$ and $\rho = 3$, we obtain

$$\mathscr{F}_0 = -2,$$

$$\mathscr{F}_1 = 12\mathfrak{Z}^2,$$

$$\mathscr{F}_2 = -8\mathfrak{Z}^4, \tag{39}$$

$$\mathscr{F}_3 = 8\mathfrak{Z}^4 - \frac{16\mathfrak{Z}^6}{3}.$$

Consequently, the semianalytical solution of equation (10) is written in the following form:

(a)

(b)

(c)
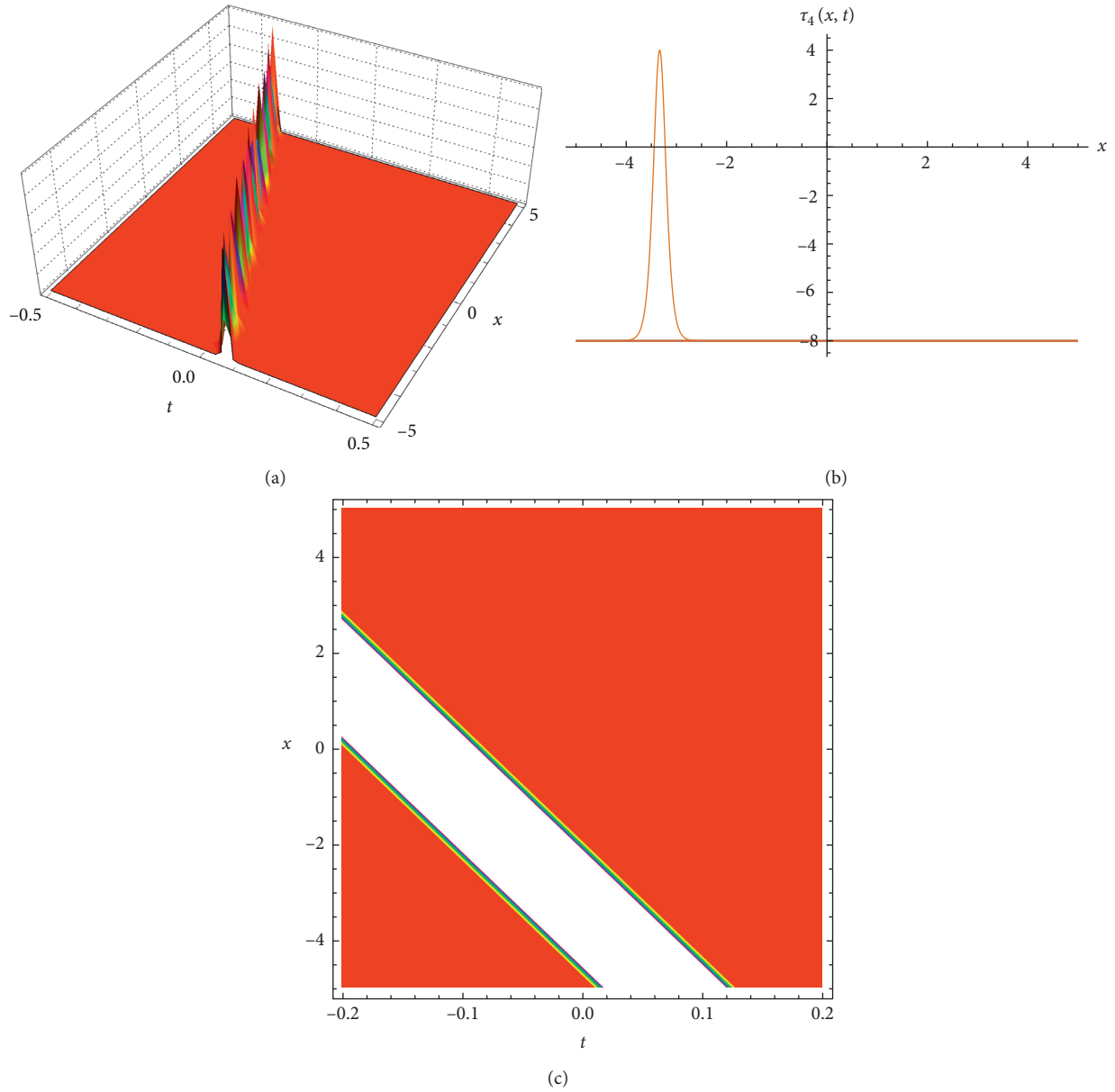
FIGURE 1: Solitary wave in three different forms of equation (18).

$$\mathcal{F} = -\frac{16\mathfrak{Z}^6}{3} + 12\mathfrak{Z}^2 - 2 + \cdots. \tag{40}$$

However, with respect to equation (31) and the following conditions $a_0 = 1, a_1 = 0, a_2 = -(3/2), b_1 = 0, b_2 = 0, c = 9, \delta = 4,$ and $\rho = -(3/2)$, we obtain

$$\mathcal{F}_0 = -\frac{1}{2},$$

$$\mathcal{F}_1 = \frac{3\mathfrak{Z}^2}{2},$$

$$\mathcal{F}_2 = -\mathfrak{Z}^4, \tag{41}$$

$$\mathcal{F}_3 = \frac{13\mathfrak{Z}^6}{30} - \frac{\mathfrak{Z}^4}{2}.$$

Consequently, the semianalytical solution of equation (10) is written in the following form:

$$\mathcal{F} = \frac{13\mathfrak{Z}^6}{30} - \frac{3\mathfrak{Z}^4}{2} + \frac{3\mathfrak{Z}^2}{2} - \frac{1}{2} + \cdots. \tag{42}$$

4.2. Cubic B-Spline Scheme. Employing the cubic B-spline scheme to evaluate the numerical solutions of equation (10). Using same initial and boundary conditions with respect to the obtained solutions (18) and (31), yields

5. Discussion

This section illustrates several of the results for $\mathcal{F}(x, y, t)$ to highlight the properties of the $(2 + 1)$-dimensional integrable SKdV model with Miura transformation. In the

(a)

(b)

(c)
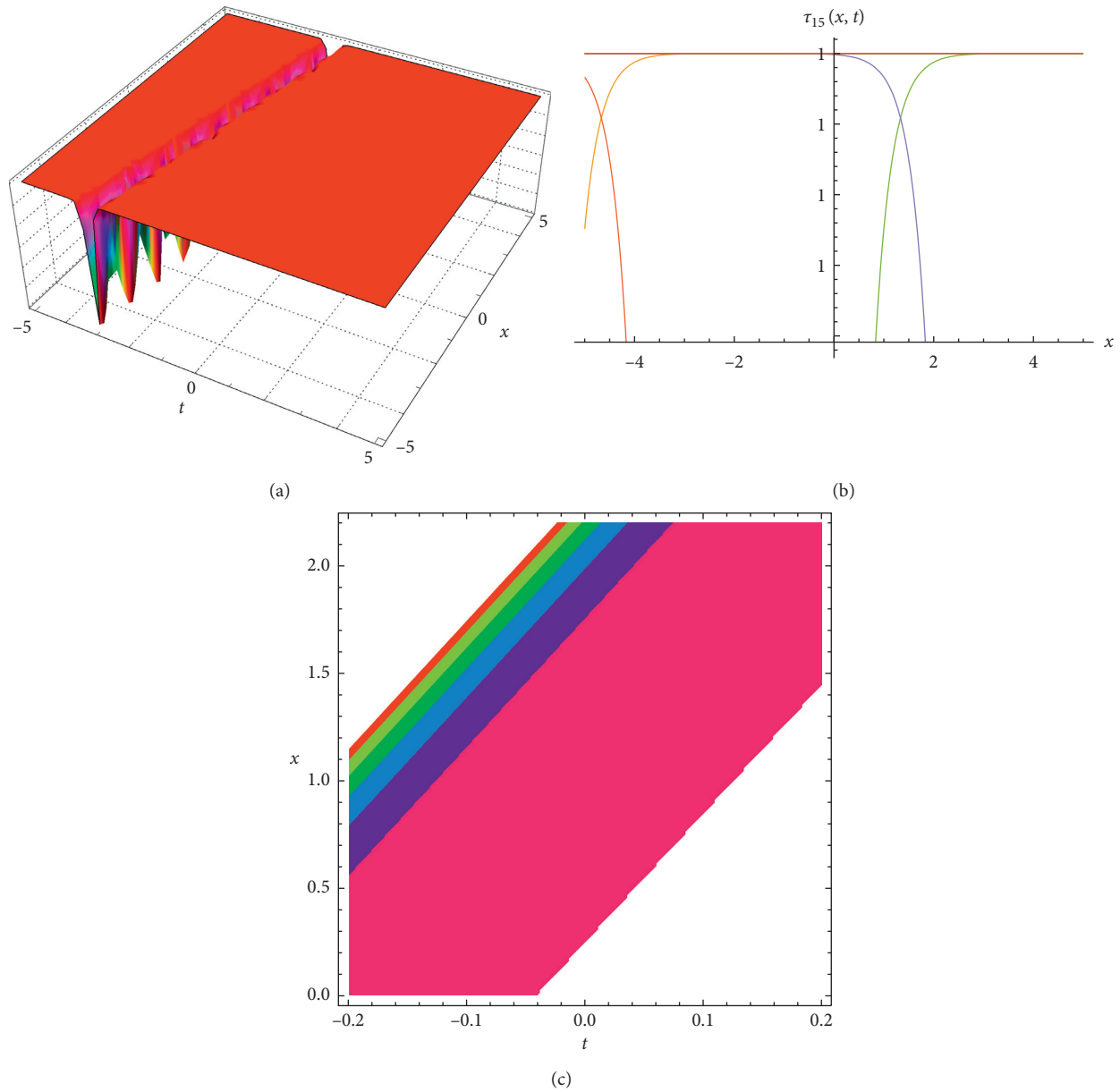
FIGURE 2: Solitary wave in three different forms of equation (31).

follow-up, we fix the value of y to characterize these solutions and the interpretation is based on three different types of representations (three- and two-dimensional charts and contour plot). In the following steps, the physical interpretation of the represented figures is discussed:

(i) Figure 1 shows the bright solitary for (18) in the three-dimensional plot (a) to illustrate the perspective view of the solution, the two-dimensional plot (b) to present the wave propagation pattern of

the wave along x- axis, and the contour plot (c) to explain the overhead view of the solution when $\alpha = -1, a_0 = 4, a_{-1} = 0, a_{-2} = -3, c = 72, \delta = 2, \lambda = 0, \mu = 4,$ and $\rho = 3$

(ii) Figure 2 shows the dark solitary for (31) in the three-dimensional plot (a) to illustrate the perspective view of the solution, the two-dimensional plot (b) to present the wave propagation pattern of the wave along the x-axis, and the contour plot (c) to explain the overhead view of the solution when

(a)

(b)

(c)

FIGURE 3: Exact and numerical solutions of equation (10) according to the obtained analytical solution via the extended simplest equation method.

$a_0 = 1, a_1 = 0, a_2 = -(3/2), b_1 = 0, b_2 = 0, c = 9, \delta = 4$, and $\rho = -(3/2)$

(iii) Figure 3 illustrates the exact and semianalytical obtained solutions, respectively, by the extended simplest equation method and Adomian decomposition method

(iv) Figure 4 illustrates the exact and semianalytical obtained solutions, respectively, by the sech-tanh expansion method and Adomian decomposition method

(v) Figure 5 illustrates the exact and numerical obtained solutions, respectively, via the sech-tanh expansion method and cubic B-spline scheme

(a)

(b)

(c)

Figure 4: Exact and numerical solutions of equation (10) according to the obtained analytical solution via the sech-tanh expansion method.

(vi) Figure 6 illustrates the exact and numerical obtained solutions, respectively, via the sech-tanh expansion method and cubic B-spline scheme

Now, we shall show the accuracy of our obtained solution and explain the comparison between the two employed analytical schemes:

(a)

(b)

(c)
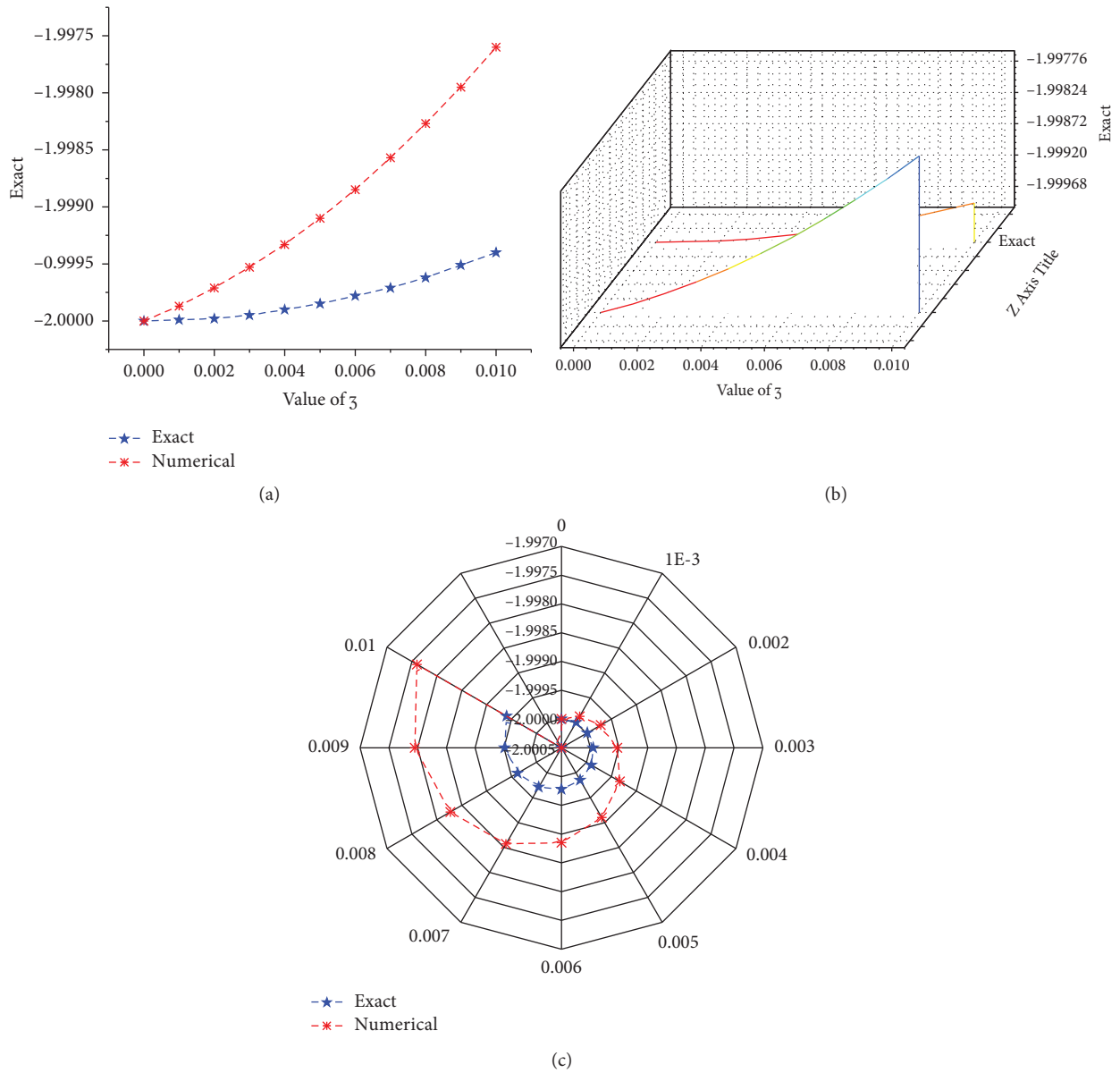
FIGURE 5: Exact and numerical solutions of equation (10) according to the obtained analytical solution via the extended simplest equation method.

(vii) Tables 1 and 2 show calculated values of the exact, semianalytical, and numerical solutions with different values of ζ. These values show the accuracy of the obtained analytical solutions via the sech-tanh expansion method over the obtained analytical solutions via the extended simplest equation method where the absolute values of error in the sech-tanh method is smaller that those obtained by the extended simplest equation method. Figure 7 explains the absolute value of error in 1 and 2.

(a)

(b)

(c)
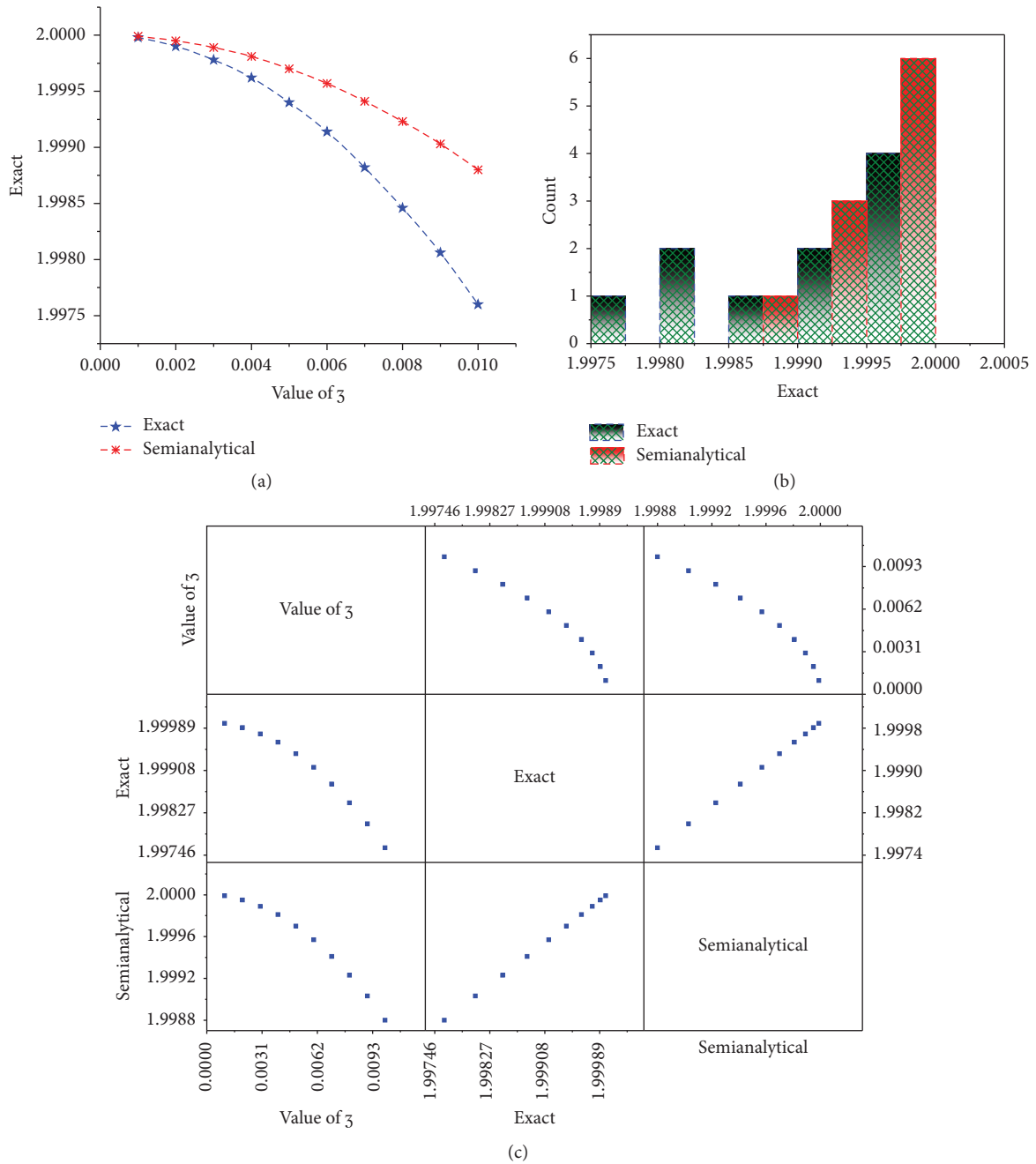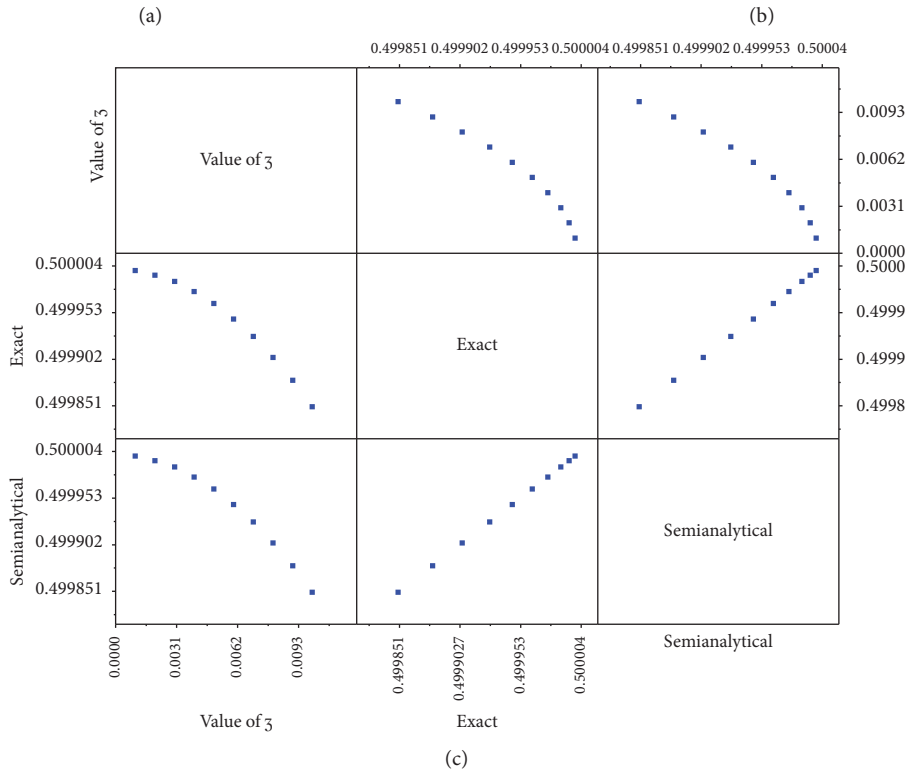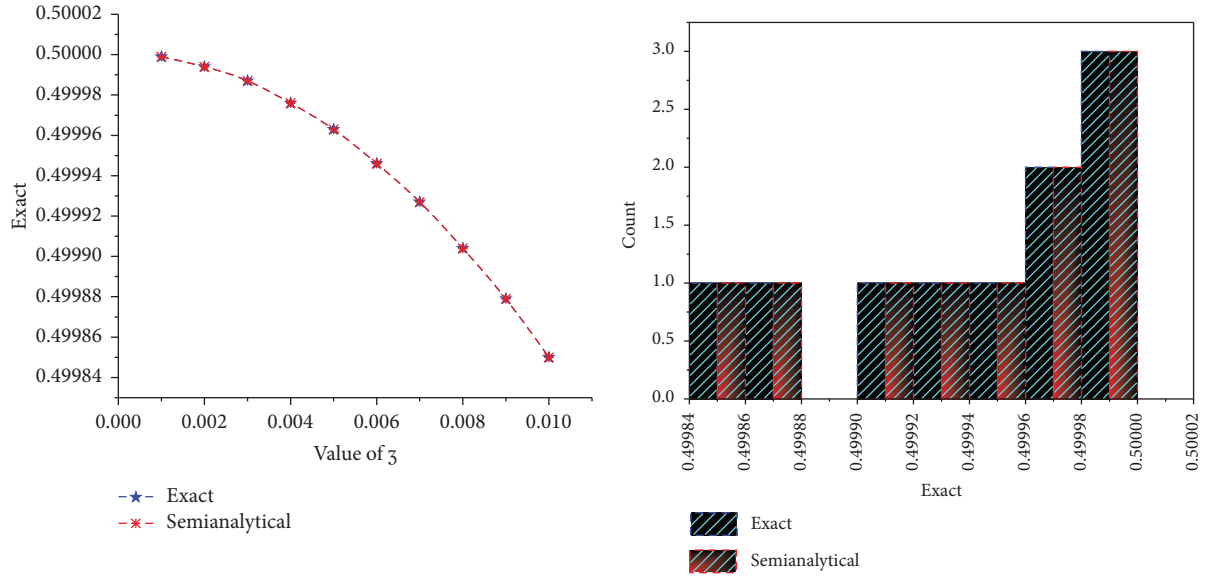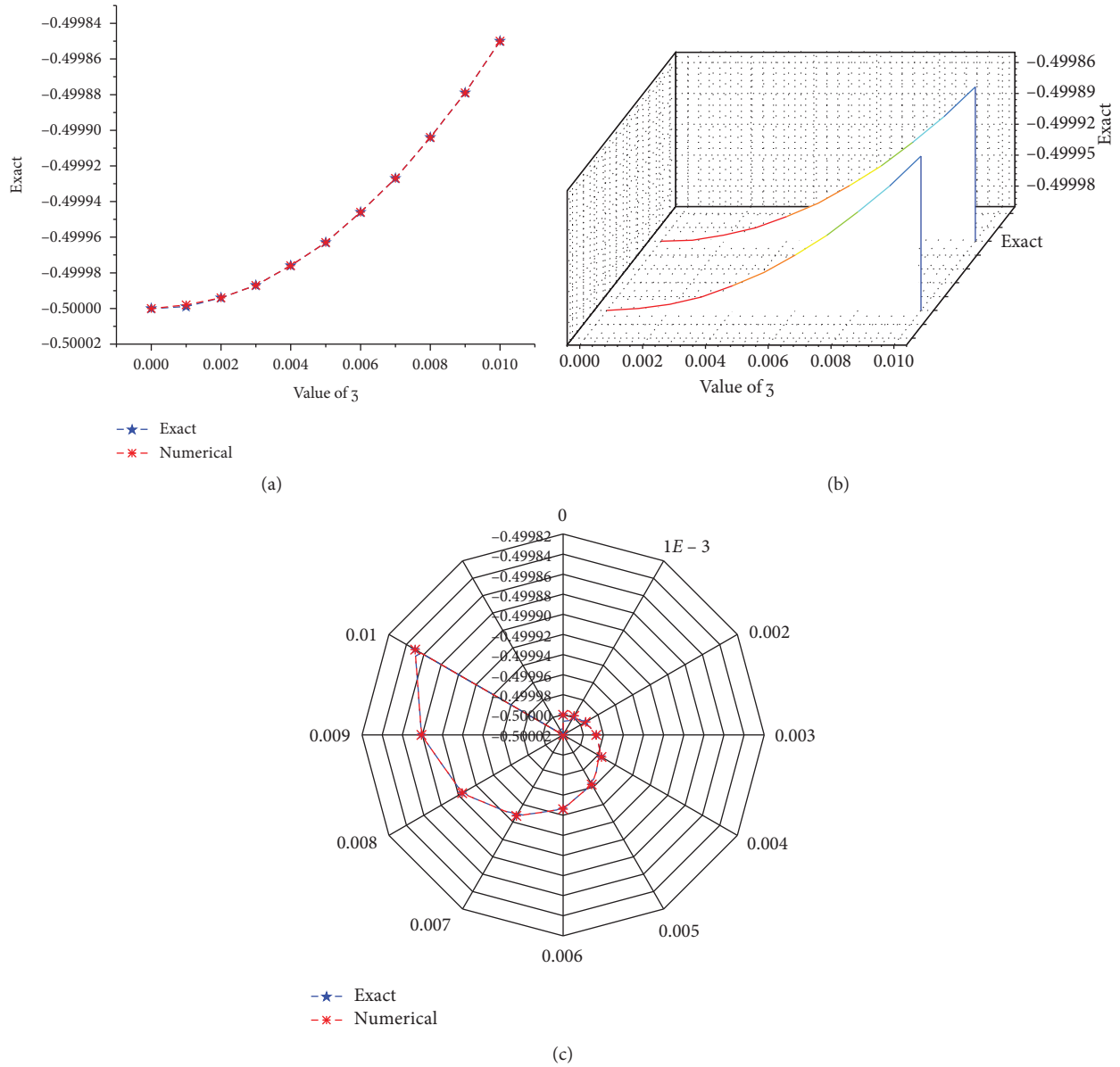
FIGURE 6: Exact and numerical solutions of equation (10) according to the obtained analytical solution via the sech-tanh expansion method.

TABLE 1: Exact, semianalytical, and absolute values of error with different values of $\mathfrak{Z}$ with respect to the obtained solution via extended simplest equation method (18) and sech-tanh method (31) via the Adomian decomposition method.

Value of 3	Ext. Sim Eq. method		Sech-tanh method		Absolute error	
	Exact	Approximate	Exact	Approximate	First scheme	Second scheme
0.001	1.99998	1.99999	0.499999	0.499999	$1.19999E{-}05$	4.99711×10^{-13}
0.002	1.9999	1.99995	0.499994	0.499994	0.000047999	7.99988×10^{-12}
0.003	1.99978	1.99989	0.499987	0.499987	0.000107995	4.05003×10^{-11}
0.004	1.99962	1.99981	0.499976	0.499976	0.000191984	1.28001×10^{-10}
0.005	1.9994	1.9997	0.499963	0.499963	0.00029996	3.12502×10^{-10}
0.006	1.99914	1.99957	0.499946	0.499946	0.000431917	6.48006×10^{-10}
0.007	1.99882	1.99941	0.499927	0.499927	0.000587846	1.20052×10^{-9}
0.008	1.99846	1.99923	0.499904	0.499904	0.000767738	2.04804×10^{-9}
0.009	1.99806	1.99903	0.499879	0.499879	0.00097158	3.28057×10^{-9}
0.01	1.9976	1.9988	0.49985	0.49985	0.00119936	5.00013×10^{-9}

Table 2: Exact, numerical, and absolute value of error with different value of ʒ with respect to the obtained solution via the extended simplest equation method (18) and sech-tanh method (31) via the cubic B-spline scheme.

Value of ʒ	Ext. Sim Eq. Method		Sech-tanh method		Absolute error	
	Exact	Numerical	Exact	Numerical	First scheme	Second scheme
0	−2	−2	−0.5	−0.5	0	0
0.001	−1.99999	−1.99987	−0.499999	−0.499998	0.00012596	8.99958×10^{-12}
0.002	−1.99998	−1.99971	−0.499994	−0.499994	0.000263919	1.59986×10^{-11}
0.003	−1.99995	−1.99953	−0.499987	−0.499987	0.000413876	2.09974×10^{-11}
0.004	−1.9999	−1.99933	−0.499976	−0.499976	0.000575829	2.39971×10^{-11}
0.005	−1.99985	−1.9991	−0.499963	−0.499963	0.000749778	2.49963×10^{-11}
0.006	−1.99978	−1.99885	−0.499946	−0.499946	0.000935721	2.39959×10^{-11}
0.007	−1.99971	−1.99857	−0.499927	−0.499927	0.00113366	2.09953×10^{-11}
0.008	−1.99962	−1.99827	−0.499904	−0.499904	0.00134358	1.59955×10^{-11}
0.009	−1.99951	−1.99795	−0.499879	−0.499879	0.0015655	8.99764×10^{-12}
0.01	−1.9994	−1.9976	−0.49985	−0.49985	0.0017994	0

(a)

(b)
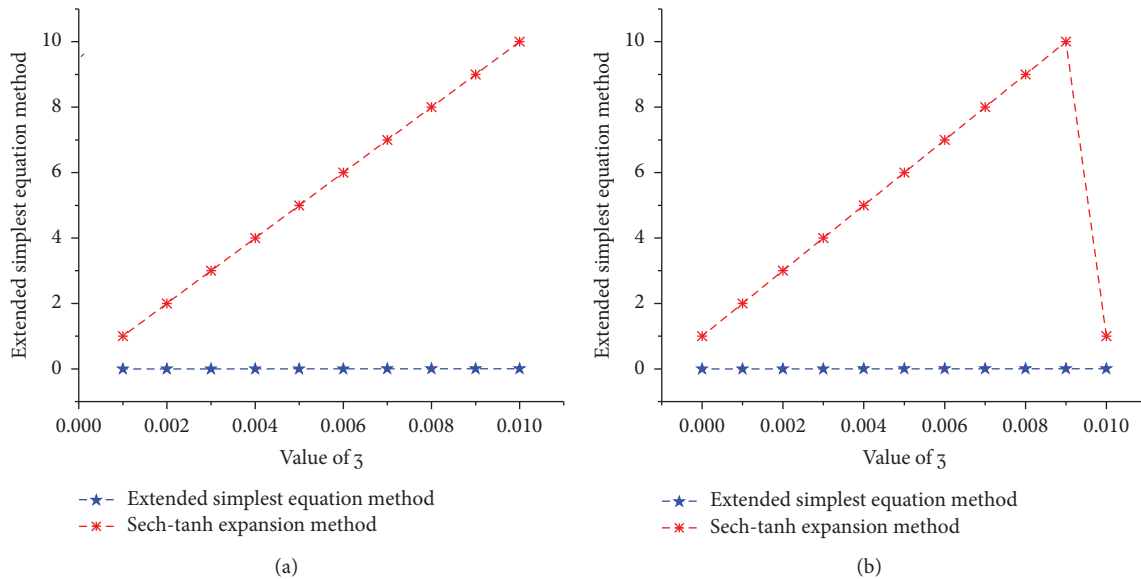
Figure 7: Absolute value of error via the Adomian decomposition method (a) and cubic B-spline scheme (b) based on the shown value in Tables 1 and 2.

6. Conclusion

In this paper, the extended simplest equation and sech-tanh expansion methods have been successfully implemented on the $(2 + 1)$-dimensional integrable SKdV model with Miura transform. Moreover, the stability properties of the solutions have also been tackled. The Adomian decomposition method and cubic B-spline scheme have also employed to investigate the semi-analytical and numerical solutions, and the two show the accuracy of the obtained analytical solutions. The rigor of the obtained solutions that have been obtained by the sech-tanh expansion method has been discussed. The solutions were represented by allowing a physical interpretation and better interpretation of their properties. In summary, this paper studied the SKdV and found relevant solutions that provide new interpretations of the real-world phenomena.

Data Availability

Data sharing is not applicable for this article as no datasets were generated or analyzed during the current study.

Conflicts of Interest

The authors declare that there are no conflicts of interest.

Authors' Contributions

All authors conceived the study, participated in its design and coordination, drafted the manuscript, participated in the sequence alignment, and read and approved the final manuscript.

Acknowledgments

References

[1] A. Seadawy, "Stability analysis of traveling wave solutions for generalized coupled nonlinear KdV equations," *Applied Mathematics & Information Sciences*, vol. 10, no. 1, pp. 209–214, 2016.

[2] M. S. Osman and A.-M. Wazwaz, "An efficient algorithm to construct multi-soliton rational solutions of the (2+1)-dimensional KdV equation with variable coefficients," *Applied Mathematics and Computation*, vol. 321, pp. 282–289, 2018.

[3] A.-M. Wazwaz and S. A. El-Tantawy, "A new integrable ($$3+1$$ 3+1)-dimensional KdV-like model with its multiple-soliton solutions," *Nonlinear Dynamics*, vol. 83, no. 3, pp. 1529–1534, 2016.

[4] C. B. Jackson, C. Østerlund, G. Mugar, K. D. Hassman, and K. Crowston, "Motivations for sustained participation in crowdsourcing: case studies of citizen science on the role of talk," in *Proceedings of the 2015 48th Hawaii International Conference on System Sciences*, pp. 1624–1634, IEEE, Kauai, HI, USA, January 2015.

[5] A. H. Bhrawy, E. H. Doha, S. S. Ezz-Eldien, and M. A. Abdelkawy, "A numerical technique based on the shifted legendre polynomials for solving the time-fractional coupled KdV equations," *Calcolo*, vol. 53, no. 1, pp. 1–17, 2016.

[6] A. R. Seadawy, "The generalized nonlinear higher order of KdV equations from the higher order nonlinear Schrödinger equation and its solutions," *Optik*, vol. 139, pp. 31–43, 2017.

[7] A. El-Ajou, O. A. Arqub, and S. Momani, "Approximate analytical solution of the nonlinear fractional KdV-Burgers equation: a new iterative algorithm," *Journal of Computational Physics*, vol. 293, pp. 81–95, 2015.

[8] S. Lou and F. Huang, "Alice-Bob physics: coherent solutions of nonlocal KdV systems," *Scientific Reports*, vol. 7, no. 1, p. 869, 2017.

[9] W.-Q. Hu and S.-L. Jia, "General propagation lattice Boltzmann model for variable-coefficient non-isospectral KdV equation," *Applied Mathematics Letters*, vol. 91, pp. 61–67, 2019.

[10] I. M. Krichever and S. P. Novikov, "Holomorphic bundles over algebraic curves and non-linear equations," *Russian Mathematical Surveys*, vol. 35, no. 6, pp. 53–79, 1980.

[11] J. Weiss, "The Painlevé property for partial differential equations. II: Bäcklund transformation, Lax pairs, and the Schwarzian derivative," *Journal of Mathematical Physics*, vol. 24, no. 6, pp. 1405–1413, 1983.

[12] J. Weiss, "The Painlevé property and Bäcklund transformations for the sequence of Boussinesq equations," *Journal of Mathematical Physics*, vol. 26, no. 2, pp. 258–269, 1985.

[13] K. Toda and S.-J. Yu, "The investigation into the Schwarz-Korteweg-de Vries equation and the Schwarz derivative in (2+1) dimensions," *Journal of Mathematical Physics*, vol. 41, no. 7, pp. 4747–4751, 2000.

[14] M. S. Bruzón, M. L. Gandarias, C. Muriel, J. Ramírez, and F. R. Romero, "Traveling-wave solutions of the Schwarz–Korteweg–de Vries equation in 2+1 dimensions and the Ablowitz–Kaup–Newell–Segur equation through symmetry reductions," *Theoretical and Mathematical Physics*, vol. 137, no. 1, pp. 1378–1389, 2003.

[15] J. Ramírez, J. L. Romero, M. S. Bruzón, and M. L. Gandarias, "Multiple solutions for the Schwarzian Korteweg-de Vries equation in (2+1) dimensions," *Chaos, Solitons & Fractals*, vol. 32, no. 2, pp. 682–693, 2007.

[16] N. A. Kudryashov and A. Pickering, "Rational solutions for Schwarzian integrable hierarchies," *Journal of Physics A: Mathematical and General*, vol. 31, no. 47, pp. 9505–9518, 1998.

[17] A. Nakamura, "The Miura transform and the existence of an infinite number of conservation laws of the cylindrical KdV equation," *Physics Letters A*, vol. 82, no. 3, pp. 111-112, 1981.

[18] C. E. Kenig and Y. Martel, "Global well-posedness in the energy space for a modified KP II equation via the Miura transform," *Transactions of the American Mathematical Society*, vol. 358, no. 6, pp. 2447–2488, 2006.

[19] J. Mas and E. Ramos, "The constrained KP hierarchy and the generalised Miura transformation," *Physics Letters B*, vol. 351, no. 1-3, pp. 194–199, 1995.

[20] M. Senthil Velan and M. Lakshmanan, "Lie symmetries, Kac-Moody-Virasoro algebras and integrability of certain (2+1)-dimensional nonlinear evolution equations," *Journal of Nonlinear Mathematical Physics*, vol. 5, no. 2, pp. 190–211, 1998.

[21] H. Ma and Y. Bai, "New solutions of the Schwarz-Korteweg-de Vries equation in 2+1 dimensions with the Gauge transformation," *International Journal of Nonlinear Science*, vol. 17, no. 1, pp. 41–46, 2014.

[22] M. Khater, R. Attia, and D. Lu, "Modified auxiliary equation method versus three nonlinear fractional biological models in present explicit wave solutions," *Mathematical and Computational Applications*, vol. 24, no. 1, 2019.

[23] M. M. Khater, D. Lu, and R. A. Attia, "Dispersive long wave of nonlinear fractional Wu-Zhang system via a modified auxiliary equation method," *AIP Advances*, vol. 9, no. 2, p. 25003, 2019.

[24] R. Attia, D. Lu, and M. Khater, "Chaos and relativistic energy-momentum of the nonlinear time fractional Duffing equation," *Mathematical and Computational Applications*, vol. 24, no. 1, p. 10, 2019.

[25] H. M. Baskonus, D. A. Koç, and H. Bulut, "Dark and new travelling wave solutions to the nonlinear evolution equation," *Optik*, vol. 127, no. 19, pp. 8043–8055, 2016.

[26] F. Dusunceli, "New exponential and complex traveling wave solutions to the Konopelchenko-Dubrovsky model," *Advances in Mathematical Physics*, vol. 2019, Article ID 7801247, 9 pages, 2019.

[27] Z. Odibat, "An optimized decomposition method for nonlinear ordinary and partial differential equations," *Physica A: Statistical Mechanics and Its Applications*, vol. 541, p. 123323, 2020.

[28] H. O. Bakodah, A. A. Al Qarni, M. A. Banaja, Q. Zhou, S. P. Moshokoa, and A. Biswas, "Bright and dark Thirring optical solitons with improved Adomian decomposition method," *Optik*, vol. 130, pp. 1115–1123, 2017.

[29] A. T. Ali, M. M. A. Khater, R. A. M. Attia, A.-H. Abdel-Aty, and D. Lu, "Abundant numerical and analytical solutions of the generalized formula of Hirota-Satsuma coupled KdV system," *Chaos, Solitons & Fractals*, vol. 131, p. 109473, 2020.

[30] M. M. Khater, C. Park, A.-H. Abdel-Aty, R. A. Attia, and D. Lu, "On new computational and numerical solutions of the modified Zakharov–Kuznetsov equation arising in electrical engineering," *Alexandria Engineering Journal*, vol. 59, no. 3, pp. 1099–1105, 2020.

WILEY | Hindawi

Research Article
Complexity Analysis of a Four-Dimensional Energy-Economy-Environment Dynamic System

Shuai Jin[1] and Liuwei Zhao [ID][1,2]

[1]School of Management, Jiangsu University, Zhenjiang, Jiangsu 212013, China
[2]School of Business, Jiangsu University of Technology, Changzhou, Jiangsu 213001, China

Correspondence should be addressed to Liuwei Zhao; 136901672@qq.com

A novel four-dimensional energy, economic, and environmental (3E) under energy reduction constraints chaotic system is proposed. The acquisition of environmental quality data is the key to this paper. During the course of the study, we used Bayesian estimation algorithm to calibrate the environmental quality. Based on the official data, the Levenberg–Marquardt backpropagation neural network method was optimized by genetic algorithm to effectively identify the parameters in the 3E system. The research results show that although increasing energy reduction inputs can improve environmental quality, the effect on energy intensity and overall stability of the system is not obvious. When polluting input in the ecological environment system affects its maximum capacity, the environmental system collapses (i.e., the ecological system can no longer purify the environment through the self-circulation process and will eventually die out). Therefore, it is necessary to correctly grasp the ecological environment protection and the relationship between economic developments and explore synergies to promote ecological priorities and green development new ideas.

1. Introduction

In the context of the rapid development of the global economy, China has become one of the largest economy groups; however, there are obvious contradictions between rapid economic growth with energy use and the protection of the environment. There are mutual influences and mutual checks and balances among energy systems, economic systems, and environmental systems. Therefore, to achieve coordinated development of energy, economic, and environmental system has become an important part of achieving development goals of the region. Economy-energy-environment system has come into being 3E system, which is used for analyzing the comprehensive development level of economy, energy, and environment for a region, thus using the result data to judge the degree of coordination among economy, energy, and environment and make a new plan.

New elements have been continuously created as the evolution of 3E systems has not followed the linear mechanism, which has made the world even more diversified and

complicated. Thus, it is fair to say that the nonlinear evolution model has become the prerequisite that has gradually enriched and complicated the 3E system. It is the new elements coming from the nonlinear mechanism that has supported the evolution and complicated the elements. Accordingly, the information that follows suits has continued to increase and accumulate, which has ensured the sustainable development. The complicated nonlinear mechanism generally lies in the elements outside and inside of the environment system, which has stabilized the structure, organization, and the conditioning mechanism for the system, to stimulate and confine the revolution of the whole system.

Presently, we have seen massive research on nonlinear model's complexity. For instance, Zhao et al. believe that there are many species in the environmental system; there are complex relationships among species, such as parasitism, symbiosis, and natural enemies. There are direct or indirect connections among all species, which constitute a complex ecological network. Because the environmental system has the characteristics of nonlinearity, self-organization,

nonnegotiability, dynamics, openness, multilevel, self-similarity, and so on, it is a typical complex system, and it is a large system with many elements, levels, and complex relationships. If we want to solve the current environmental problems facing mankind, we must apply complexity theory to environmental problems making the structure of environmental system more reasonable and the balance of environment, economy, and society rebuilt [1]. Fang believes that structural complexity is one of the most fundamental problems of dynamic complexity of ecosystems. The development and application of dynamic system theory are helpful to understand the complexity of ecosystem. It is pointed out that structural complexity and dynamic complexity are interrelated. Simple dynamic models of ecosystem show that simple structural systems can produce very complex and unpredictable dynamic behavior in some cases. However, the ecosystems with complex structures may not necessarily produce complex dynamic behaviors [2]. Development and application of the dynamics system would help enhance the understanding of 3E system's complexity. The research would also help indicate that complexity between structure and dynamics are interrelated. The 3E system's simple dynamic model indicated that simple structure system would generate complicated and unpredictable dynamic behavior. However, the complied ecosystem would not necessarily lead to complicated dynamic behavior [3]. We can make basic judgment on current researches on 3E system's internal connectivity and interaction from multiple perspectives. Some of the researches are based on the samples from the time series and applied from cointegration and causal tests, discussing the relationship between energy and economy. Scholars all around the world have consensus about the interaction of the two, believing that consumption of energy and economic growth has been highly correlated for the long time and yet exhibits notable regional difference [4, 5]. Regarding the relationship between energy and environment, some scholars believe that increase in energy output and consumption are the main culprit behind the degradation of environment [6, 7]. It is worth noting that most of the researches on the topic are based on Kuznets curve, while the conclusions that follow suit are divergent. On the one hand, the supporters aim to figure out the internal motivations [8–10] that form the EKC from the perspective of economic growth, trade, and policies. They have come to the roughly similar conclusion: the quality of environment would be improved in tandem with economic development following its degradation. On the other hand, the skeptics of the EKC believe that the relationship between economy and environment could include U-shape, N-shape, or synchronous curves [11–13].

Some other researches are based on the comprehensive discussion regarding the 3E system. However, the scholars have chosen different research timing and methods, mainly including measurement and evaluation of the 3E system's coordination [14], application of dynamic CGE model [15], the endogenous growth model [16], and the relationships and correlations among outputs of 3E based on the analysis of the econometric model [17]. Current literature has basic consensus of the conclusion regarding the coordination analysis of the 3E system, believing that China's coordination remains at a lower level. Meanwhile, Wei et al. have included demographic system into their researches, leading to a dynamically open yet more complicated system, in order to build up multipurpose planning and an integrated model reflecting a check-and-balance relationship [18]. The research comes with a novel angel.

Currently, environmental protection still falls behind social and economic development. Pollutions caused by multistages, multifields, and multitypes have been continually mounting, yet the environmental carrying capacity has (nearly) reached its limit. Hence, the worsening environmental problems have not been radically resolved. In the process of handling the issues, people have been gradually aware that improvement of the environmental quality hinges on well-managed resources, resolved environmental problems, and control of pollutants' emission. Good environmental quality is related to the sustainable development of the economy and society. It is an important breakthrough to adjust the economic structure and achieve economic growth. It is conducive to promoting economic competition and promoting the development of green development and environmental industries. Accordingly, various scholars have embarked on research on energy reduction. For instance, Löschel and Otto have built up a dynamic balance model to study the relationships among the variables including carbon dioxide emission, energy consumption, speed of technological innovation, and economic development. His conclusion suggests that decision-makers prudently design the carbon dioxide emission cut policies [19]. Erdmenger and his team detailed the measures for Germany to reach its CO_2 emission target by 40% and carbon emission cut by 224 mn MT [20]. Xu and his team adopt the AIM and CGE models to evaluate sulfur dioxide control's impact on the pollutant and CO_2 emission cut locally. They believe that China could enjoy the benefits from carbon emission via control over sulfur dioxide emission [21]. Cullende and Allood found through research that efficiency is a very important role in carbon emission reduction. The scale of the energy flow is an important indicator to evaluate potential return from the efficiency. Estimating the global energy flow's scale and complexity could bring about the maximum energy efficiency return [22]. Prasad studied the impact of renewable energy policies in 39 states on CO_2 reduction. They discovered that, after 19 states' introduction of Fund for the Public Interest, or something similar to "carbon tax," CO_2 emission has seen notable and stable decline [23]. Fang established a three-dimensional system for energy conservation and emission reduction and obtained energy-saving attractions. Meanwhile, they evaluate the performance of energy saving and emission cut [24–27]; more research is needed [28, 29].

In recent years, BP neural network has attracted more and more attention in the field of artificial intelligence. Many nonlinear methods have been proposed to predict the trend of energy and economy, such as BP neural network [30–34]. BP neural network has unique advantages in economic fields such as economic analysis [35–38] and time series prediction. If the computation amount allows, any number of many-to-many mappings can be fitted with a smaller fitting error. The strong coupling relationship among the factors in the prediction system

is an interwoven and interactive relationship, which can be expressed by the connection weights and thresholds between nodes in each layer. Compared with the traditional multiple regression prediction method, this expression has better fitting ability and precision. BP neural network has strong nonlinear function approximation ability and has been widely used in time series analysis and financial forecasting. BP neural network has the ability to fit the function and determine the weights and thresholds between neurons through learning process [39]. Therefore, we depended on the official statistics and measured data of the China Statistical Yearbook to predict the future trend of 3E.

In the process of enhancing environment governance, we have seen more complicated environmental issues for which it is more difficult to find solutions. With that, we see even more difficulties and complexity for the various projects to further strengthen environment governance and environmental quality improvement. Presently, industrialization, urbanization, and modernization have propelled energy demand at a growth stage. Ongoing consumption increase in fossil fuels with high pollution and high carbon emission has impeded the sustainable development for the environment. Therefore, we need to fully realize the dynamic complexity of the 3E system and the lag of environmental protection, in order to reduce the damage more effectively and rationally to the ecological environment system and make the economy sustainable.

With the rapid development of environmental protection, the gradual improvement of social-environmental awareness, and the increasing competition in the industry, the environmental governance network is a complex adaptive system formed by the game and interest coordination and self-organization under the market operation mechanism. Therefore, the research on 3E systems needs to pay more attention to the complexity brought by multisystem interaction. In general, 3E is increasingly showing the dynamic complexity of the system. Therefore, it is necessary to study how the three systems of the main body establish an effective coordination strategy mechanism and study the environmental governance network and economy based on such microbehavior and game characteristics. Develop a macrointegrated structure and a mechanism for the formation of good performance, in particular, the emergence of the overall structure and performance of 3E systems and the systematic analysis between environmental and economic systems. In the meantime, judging from the current research that concerns the impact of environmental governance and environmental governance system engineering and diving deeply into current study, we believe that the following aspects need to be enhanced and perfected. Study the following issues: First, based on the research foundation of the relationship of the dual systems, we need to integrate the 3E into the system analysis, by developing theoretical analyses based on the multiple systems' coordination and development angles. Secondly, we need to study the evaluation pattern of the 3E's complexity. Thirdly, the official data are used to identify the 3E system parameters and the evolution of the 3E system analyzed. It is under such current situation that the 3E system's variation pattern would be of significance to the system's sustainable development.

This study makes a series of significant contributions to the research of the 3E's complexity:

First, this study considers the inclusion of energy reduction constraints on the 3E system proposed and gets a new four-dimensional system, which is more in line with the actual situation and the current development needs.

Second, this study deviates from the leading research on energy-economy-environment systems research that focuses primarily on environmental impact analysis [40], global environmental development [41], eco-industrial systems planning [42, 43], dynamic assessment of urban economy-resource-environment systems [44], and economic and environmentally sustainable development [45]. Here, through the stability analysis of dynamic 3E system by system complexity theory, the gap in methodology commonly used in 3E system research is bridged. The results provide a practical policy prescription for effective pollution control.

Third, based on the official data, the Levenberg-Marquardt backpropagation neural network method was optimized by genetic algorithm to effectively identify the parameters in the 3E system, which is more conducive to better research on the interaction between various elements of the 3E system.

This paper is organized as follows. In Section 2, we construct a 3E system with energy-constrained constraints and theoretically analyze the system through the theory of complexity and use numerical simulation to demonstrate the various dynamic behaviors of the four-dimensional system. In Section 3, the genetic algorithm is used to optimize the LM-BP neural network method to identify and confirm the system parameters of the four-dimensional system. In Section 4, an in-depth analysis of the changes in key parameters of the system is carried out to study the stability and dynamic complexity of the system. Finally, the main conclusions of this study are given.

2. Model Construct and Theoretical Analysis

2.1. Model Construct. In the paper, we consider the inclusion of energy reduction constraints on the 3E system proposed by Zhao et al. [1] and get a new four-dimensional system, which is more in line with the actual situation and the current development needs. Energy, economy, and environment (3E) system containing energy reduction constraints is given in the following form:

$$
\begin{cases}
\dot{x} = a_1 x \left(\dfrac{y}{M} - 1 \right) - a_2 y + a_3 z + a_4 w, \\[2mm]
\dot{y} = -b_1 x + b_2 y \left(\dfrac{1-y}{F} \right) + b_3 z \left(\dfrac{1-z}{E} \right) - b_4 w, \\[2mm]
\dot{z} = c_1 x \left(\dfrac{x}{N} - 1 \right) - c_2 y - c_3 z - c_4 w, \\[2mm]
\dot{w} = d_1 x - d_2 y + d_3 z \left(\dfrac{1-z}{H} \right) + d_4 w \left(\dfrac{y}{P} - 1 \right),
\end{cases}
\tag{1}
$$

where $x(t)$, $y(t)$, $z(t)$, are $w(t)$, respectively, the level of energy conservation and emission reduction, pollution emission, economic growth (GDP), and environmental quality in period t, a_i, b_i, c_i, d_i ($i = 1, 2, 3, 4$), M, F, E, N, H, and P are normal numbers, $t \in I$, and I is an economic cycle. (Table 1)

In system (1), $\dot{x}$ represents the change level of energy saving and emission reduction in t period; $\dot{y}$ represents the level of change in pollution emissions in t period; $\dot{z}$ represents the growth level of economic growth in the t period; $\dot{w}$ represents the change level of environmental quality in t period. When the impact of pollution exceeds the maximum capacity of the ecological environment (that $\dot{w} > 0$), it means that the ecological environment is deteriorating. In this case, the ecosystem cannot rely on self-regulation to repair. Therefore, when this situation continues, the ecological environment will eventually be sold out; when $\dot{w} \le 0$, it means that the environmental quality has reached a dynamic balance or gradually improved, and only under this condition can the ecological environment be the basis of human social development [46–48].

By system (1), energy intensity can be launched; the form of energy intensity is as follows:

$$\text{energy intensity} = \frac{\text{A economic cycle energy consumption}}{\text{GDP within an economic cycle}}. \tag{2}$$

Next, we will analyze the dynamics of 3E system containing energy reduction constraints. By calculation, the Jacobian matrix of the system (1) can be obtained as follows:

$$
J = \begin{bmatrix}
\left(\dfrac{y}{M} - 1\right)a_1 & \dfrac{xa_1}{M} - a_2 & a_3 & a_4 \\[2ex]
-b_1 & \dfrac{(F - 2y)b_2}{F} & \dfrac{(E - 2z)b_3}{E} & -b_4 \\[2ex]
-\dfrac{(N - 2x)c_1}{N} & -c_2 & -c_3 & -c_4 \\[2ex]
d_1 & -d_2 + \dfrac{wd_4}{P} & \dfrac{(H - 2z)d_3}{H} & \left(\dfrac{y}{P - 1} - 1\right)d_4
\end{bmatrix}. \tag{3}
$$

The six real equilibrium points of the 3E system (1) are, respectively, $O(0, 0, 0, 0)$, $S_1(x_1, y_1, z_1, w_1)$, $S_2(x_2, y_2, z_2, w_2)$, $S_3(x_3, y_3, z_3, w_3)$, $S_4(x_4, y_4, z_4, w_4)$, and $S_5(x_5, y_5, z_5, w_5)$. The Jacobian matrix of system (1) at equilibrium point $O(0, 0, 0, 0)$ is of the following form:

$$
J_0 = \begin{bmatrix}
-a_1 & -a_2 & a_3 & a_4 \\
-b_1 & b_2 & b_3 & -b_4 \\
-c_1 & -c_2 & -c_3 & -c_4 \\
d_1 & -d_2 & d_3 & -d_4
\end{bmatrix}. \tag{4}
$$

So the characteristic polynomial of $J(O)$ is as follows:

$$f(\lambda) = \lambda^4 + A\lambda^3 + B\lambda^2 + C\lambda + D = 0, \tag{5}$$

where

$$
\begin{aligned}
A = {}& a_1 - b_2 + c_3 + d_4, \\
B = {}& a_3c_1 - a_2b_1 + b_3c_2 - b_2c_3 - a_4d_1 + b_4d_2 + c_4d_3 - b_2d_4 + c_3d_4 + a_1(c_3 + d_4 - b_2), \\
C = {}& a_1b_3c_2 - a_1b_2c_3 + a_4b_2d_1 - a_4c_3d_1 - a_4b_1d_2 + a_1b_4d_2 + b_4c_3d_2 - b_3c_4d_2 \\
& + a_4c_1d_3 + b_4c_2d_3 + a_1c_4d_3 - b_2c_4d_3 - a_1b_2d_4 + b_3c_2d_4 + a_1c_3d_4 - b_2c_3d_4 \\
& + a_3(c_4d_1 + c_1d_4 - b_2c_1 - b_1c_2) - a_2(b_3c_1 - b_4d_1 + b_1(c_3 + d_4)), \\
D = {}& a_2b_4c_3d_1 - a_2b_3c_4d_1 + a_1b_4c_3d_2 - a_1b_3c_4d_2 - a_2b_4c_1d_3 + a_1b_4c_2d_3 - a_2b_1c_4d_3 - a_1b_2c_4d_3 \\
& - a_4(b_3c_2d_1 - b_2c_3d_1 + b_3c_1d_2 + b_1c_3d_2 + b_2c_1d_3 + b_1c_2d_3) - a_2b3c_1d_4 + a_1b_3c_2d_4 \\
& - a2b_1c_3d_4 - a_1b_2c_3d_4 + a_3(b_4c_2d_1 - b_2c_4d_1 + b_4c_1d_2 + b_1c_4d_2 - b_2c_1d_4 - b_1c_2d_4).
\end{aligned}
\tag{6}
$$

System (1) is a very complex dynamic system, when a_i, b_i, c_i, d_i, M, F, E, N, H, and P values are different, system (1) performance is complex, and dynamic behavior is also different. In this study, we set the following: $a_1 = 0.09$, $a_2 = 0.025$, $a_3 = 0.012$, $a_4 = 0.165$, $b_1 = 0.422$, $b_2 = 0.2$, $b_3 = 0.8$, $b_4 = 0.4$, $c_1 = 0.035$, $c_2 = 0.008$, $c_3 = 0.075$, $c_4 = 0.078$, $d_1 = 0.121$, $d_2 = 0.035$, $d_3 = 0.0145$, $d_4 = 0.775$, $M = 0.9$, $F = 1.6$, $E = 2.95$, $N = 0.35$, $H = 1.25$, and $P = 2.4$.

By calculation, four eigenvalues of the Jacobian matrix $J(O)$ are $\lambda_1 = 0.2236$, $\lambda_2 = -0.7845$, and $\lambda_{3,4} = -0.0895 \pm 0.0706i$. Because $\lambda_i < 1$ ($i = 1, 2, 3, 4$), we know that the equilibrium $O(0, 0, 0, 0)$ is unstable.

Let c_2 be any value, so we can obtain the following characteristic equation:

$$
\begin{aligned}
f(\lambda) = {}& \lambda^4 + 0.74\lambda^3 + (0.8c_2 - 0.0683)\lambda^2 \\
& + (0.6927c_2 - 0.0297)\lambda - 0.0026 + 0.036c_2 = 0.
\end{aligned}
\tag{7}
$$

Let $p_1 = 0.74$, $p_2 = 0.8c_2 - 0.0683$, $p_3 = 0.6927c_2 - 0.0297$, and $p_4 = 0.036c_2 - 0.0026$. According to the Routh-Hurwitz criterion, we can obtain the following conditions: $p_1 = 0.74 > 0$, $p_1p_2 - p_3 > 0$, and $p_1p_2p_3 - p_4p_1^2 - p_3^2 > 0$. By calculation, when

TABLE 1: The specific meanings of each parameter are explained.

Parameter	Explanation ($t \in I$, I is an economic cycle)
a_1	The development coefficient of energy saving and emission reduction $x(t)$
a_2	The inhibition coefficient of pollution emission $y(t)$ on energy saving and emission reduction $x(t)$
a_3	The influence coefficient of $z(t)$ input of economic growth on energy saving and emission reduction $x(t)$
a_4	The influence coefficient of $w(t)$ input of environmental quality on energy saving and emission reduction $x(t)$
b_1	The influence coefficient of the development of energy saving and emission reduction $x(t)$ on pollution emission $y(t)$
b_2	The development rate elasticity coefficient of pollution emission $y(t)$
b_3	The influence coefficient of economic growth $z(t)$ on pollution emission $y(t)$
b_4	The inhibition coefficient of environmental quality $w(t)$ on pollution emission $y(t)$
c_1	The influence coefficient of the development of energy saving and emission reduction $x(t)$ on economic growth
c_2	The influence coefficient of pollution emission $y(t)$ on economic growth $z(t)$
c_3	The restraint factor of investment in energy saving and emission reduction $x(t)$ on economic growth $z(t)$
c_4	The restraint factor of investment in improving environmental quality $w(t)$ on economic growth $z(t)$
d_1	The influence coefficient of the development of energy saving and emission reduction $x(t)$ on the improvement of environmental quality $w(t)$
d_2	The inhibition coefficient of pollution emission $y(t)$ on environmental quality $w(t)$
d_3	The influence coefficient of economic growth $z(t)$'s investment on improving environmental quality $w(t)$
d_4	The speed coefficient of ecological environment self-repair without external intervention
M	The peak value of the impact of pollution emission $y(t)$ on energy saving and emission reduction $x(t)$
F	The peak value of pollution emission $y(t)$ in an economic cycle
E	The peak value of economic growth $z(t)$ in an economic cycle
N	The peak value of the impact of energy saving and emission reduction $x(t)$ on economic growth $z(t)$ in an economic cycle
H	The peak value of the impact of economic growth $z(t)$ on environmental quality $w(t)$ in an economic cycle
P	The maximum amount of pollution that can be contained by the ecological environment

$0 < c_2 < 0.0575$, that equilibrium point $O(0, 0, 0, 0)$ is unstable.

Now, bring the parameter values set above to system (1). By calculation, we get the equilibrium points: $S_1 (-1.4149, 0.534, 3.7951, -0.5030)$, $S_2 (1.35, 0.5868, 1.4901, 0.2367)$, $S_3 (1.0838, 0.6617, 0.7819, 0.2)$, $S_4 (0.8185, 2.5042, 0.7327, -0.4697)$, and $S_5 (1.2523, 2.5109, 2.2876, -1.0085)$. A similar approach shows the eigenvalue of the equilibrium point S_1: $\lambda_1 = -0.7309$, $\lambda_2 = -0.4548$, and $\lambda_{3,4} = 0.2696 \pm 0.2758i$; the eigenvalue of the equilibrium point S_2: $\lambda_1 = -0.0314$, $\lambda_2 = 0.0665$, and $\lambda_{3,4} = -0.0783 \pm 0.1974i$; the eigenvalue of the equilibrium point S_3: $\lambda_1 = -0.5057$, $\lambda_2 = -0.0189$, and $\lambda_{3,4} = 0.2068 \pm 0.3074i$; the eigenvalue of the equilibrium point S_4: $\lambda_1 = 0.0232$, $\lambda_2 = 0.1221$, and $\lambda_{3,4} = -0.1191 \pm 0.0801i$; the eigenvalue of the equilibrium point S_5: $\lambda_1 = -0.3009$, $\lambda_2 = 0.1127$, and $\lambda_{3,4} = 0.0519 \pm 0.1578i$. At the equilibrium point $S_1 (-1.4149, 0.534, 3.7951, -0.5030)$ $3.7951, -0.5030)$, $x(t)$ is negative and energy intensity is about 0.14. Environmental quality $w(t)$ has reached dynamic equilibrium or gradually improved, which is an ideal state:

$$\nabla V = \frac{\partial \dot{x}}{\partial x} + \frac{\partial \dot{y}}{\partial y} + \frac{\partial \dot{z}}{\partial z} + \frac{\partial \dot{w}}{\partial w} = \left(-1 + \frac{y}{M}\right)a_1 + \frac{(F - 2y)b_2}{F}$$

$$- c_3 + \left(-1 + \frac{y}{P}\right)d_4$$

$$= b_2 - a_1 - c_3 - d_4 + y\left(\frac{a_1}{M} - \frac{2b_2}{F} + \frac{d_4}{P}\right).$$

(8)

When $(a_1/M) - (2b_2/F) + (d_4/P) = 0$ and $b_2 - a_1 - c_3 - d_4 < 0$, system (1) is dissipative.

2.2. System Simulation Analysis. Numerical simulation analysis of the system allows us to more intuitively see the complex dynamic behavior of the system, which plays a very important role in the evolution and stability of the research system. Next, we will carry out dynamic simulation analysis of the 3E system under the energy reduction constraint and select the initial value of the system [0.015, 0.758, 1.83, 1.5].

As can be seen from Figure 1, the evolution trajectory of the system (1) enters an irregular chaotic state, and the shape of the three-dimensional attractor diagram composed of different parameters is also different.

In addition, Figure 2 gives system (1) mixed phase diagram of a two-dimensional plane in different sections. It can be seen from Figure 2 that the irregular evolution trajectories of system (1) under different cross sections are not the same, which also shows that the chaotic motion is irregular and disordered. The generation of mixed behavior in the 3E system will have a great impact on the stability of the system and also cause problems in the normal operation of the system. The time series diagram of system (1) ($x(t)$, $y(t)$, $z(t)$, and $w(t)$) is given in Figure 3.

Figure 4 shows bifurcation diagram and corresponding Lyapunov exponential diagram of the variable $c_2 \in [0.006, 0.014]$ change of the four-dimensional system (1). From Figure 4, we find that the four-dimensional system (1) has very complex dynamic behavior. As we all know, the Lyapunov exponential is generally used to determine whether the system is stable. If the maximum Lyapunov exponent of the system is greater than 0, it can be explained that the system produces mixed chaotic behavior, which is a full manifestation of unstable evolution. In this study, the degree of complexity of the four-dimensional 3E systems under the constraints of energy reduction is self-evident. If the maximum Lyapunov exponent of the system is greater
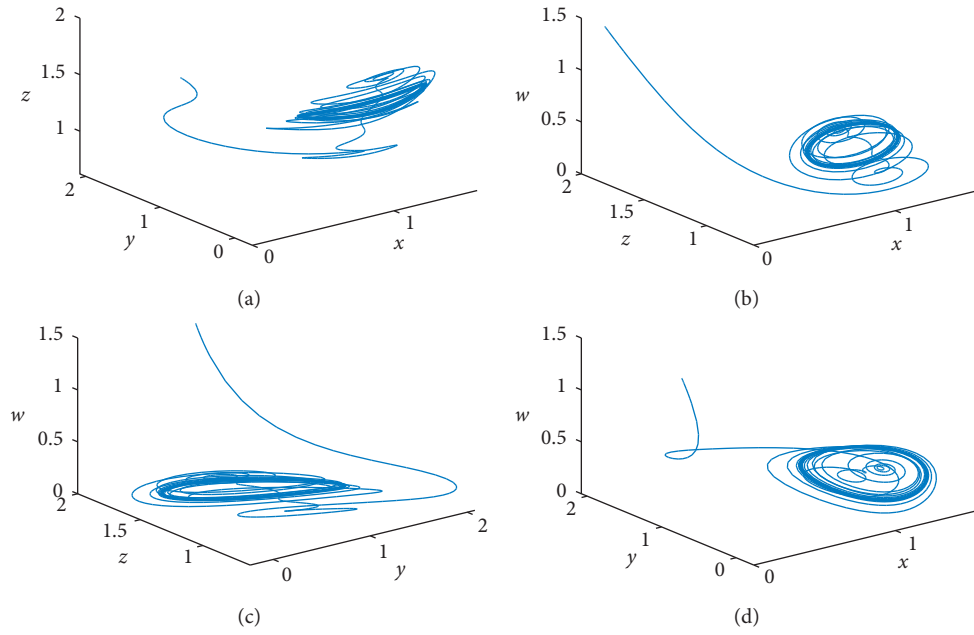
FIGURE 1: Three-dimensional spatial chaotic attractor phase diagram of system (1).
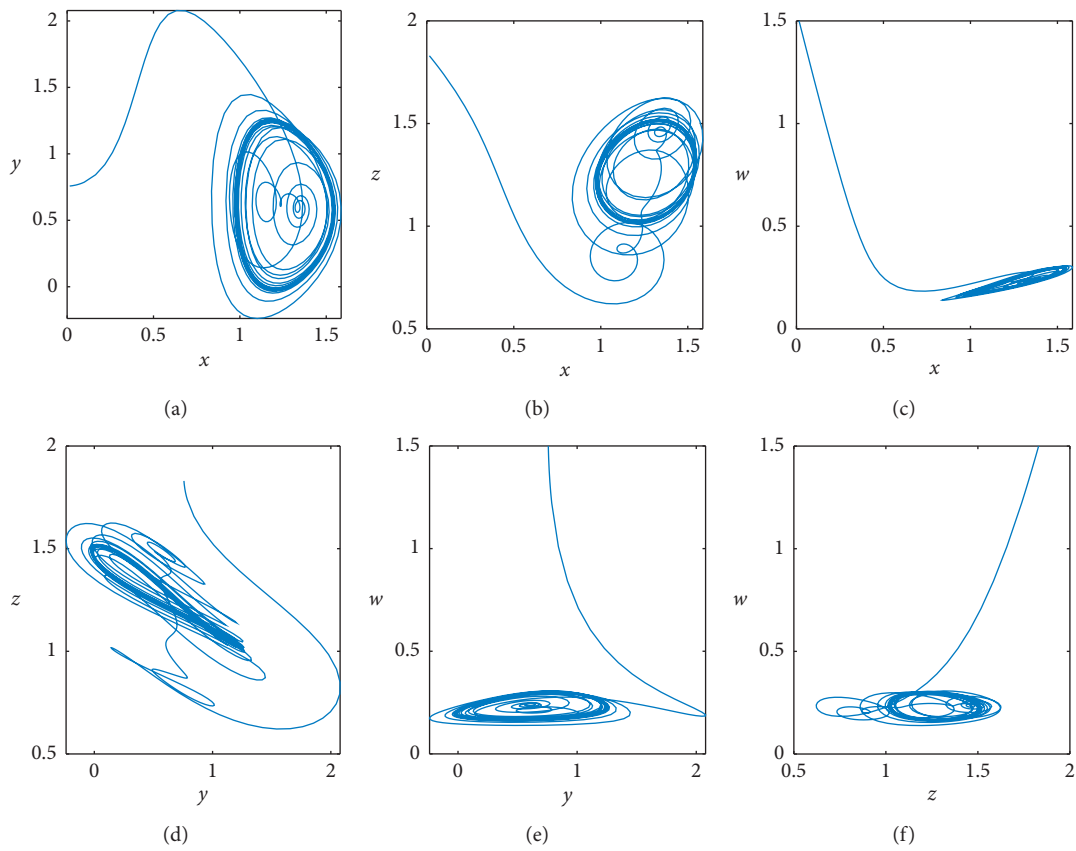
FIGURE 2: Two-dimensional plane chaotic attractor phase diagram of system (1).

than or equal to zero, we can determine the occurrence of bifurcation in the four-dimensional system. Behavior is more likely to develop into a chaotic trend.

Impact of initial state on the evolution trend of the complex four-dimensional dynamical system (1): Figure 5 shows the sensitive dependence of complex four-dimensional
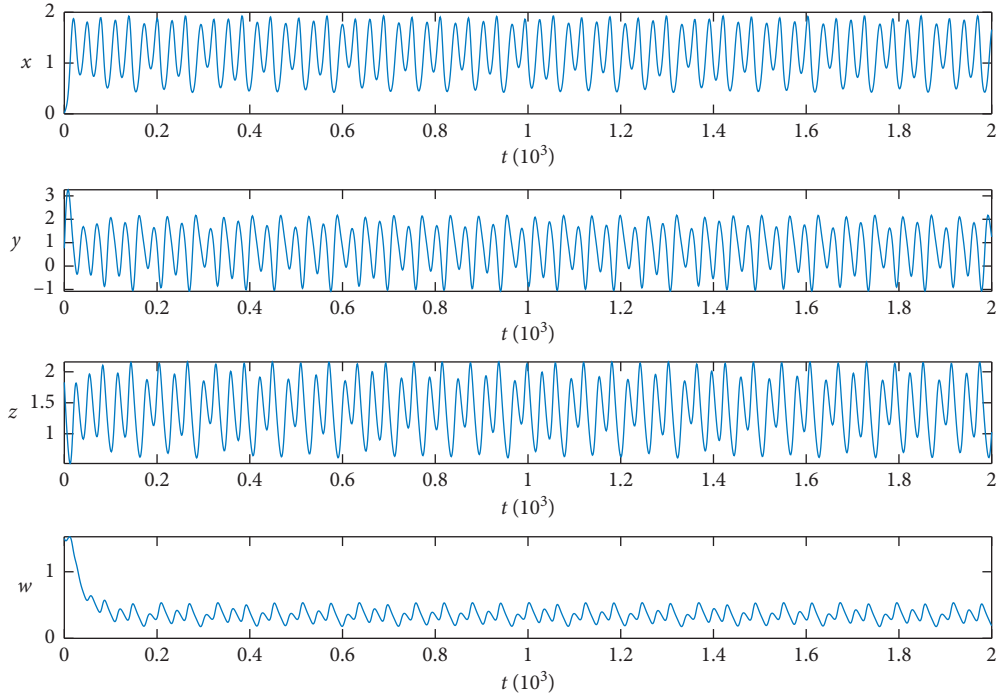
FIGURE 3: System (1) time sequences diagram.

(a)

(b)
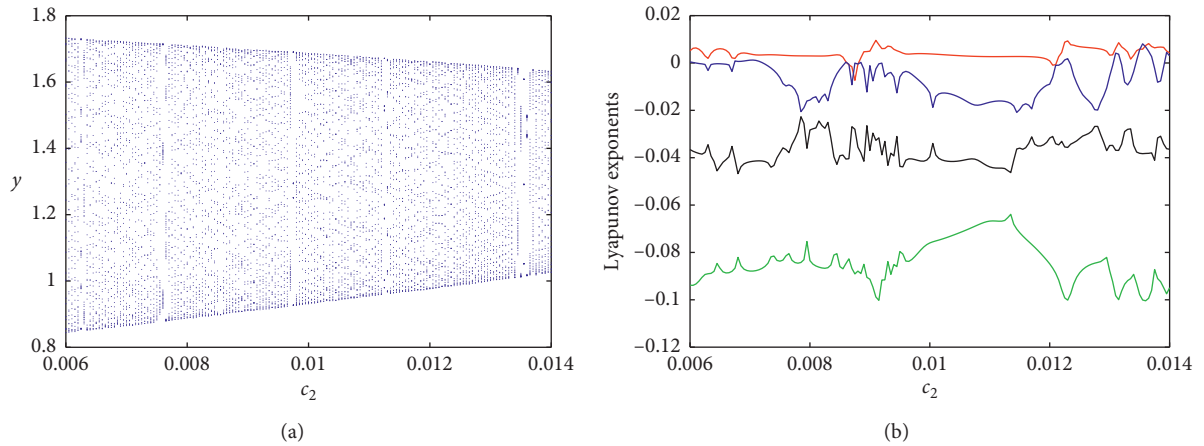
FIGURE 4: With $c_2 \in [0.006, 0.014]$ change system (1): (a) bifurcation diagram; (b) Lyapunov exponential diagram of corresponding (a).

system (1) on initial conditions. The sensitivity of system (when losing stability) with $(x, y, z, w) = (0.015, 0.758, 1.83.1.5)$, $(x_1, y, z, w) = (0.014, 0.758, 1.83.1.5)$, and $(x_2, y, z, w) = (0.016, 0.758, 1.83.1.5)$ and a small change in the initial conditions may cause a large change in the whole four-dimensional system, which indicates that the system is sensitive to the initial state. From Figure 5, we can also know that the initial values vary greatly in the trajectories of the deviated system (1). Although the initial states are indistinguishable, the initial values will be quickly established after several iterations, which is also an important symbol of chaotic motion.

3. System Parameter Identification

3.1. Data Gathering. On the basis of complex interactions, a four-dimensional dynamic system that integrates, restricts, and promotes energy conservation, energy, economy, and environment is established. In this study, the determination of the parameters of the four-dimensional dynamic system is of great significance to the actual research. Because the environment, energy intensity, and economic growth are affected by the changes of these variables, based on the official statistics and measured data of the China Statistical Yearbook, genetic optimization of the optimized LM-BP neural network method

FIGURE 5: System (1) sensitivity analysis.

TABLE 2: Statistics on energy reduction, energy consumption, GDP, and environment in China.

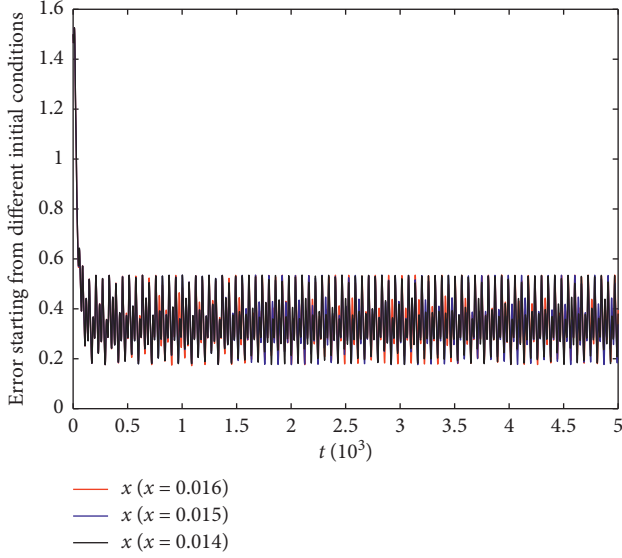| Year	x	y	z	w
2000	1.9626	1.0455	1.1085	0.9837
2001	3.6786	1.1066	1.2228	0.9595
2002	2.2791	1.2064	1.3482	0.9347
2003	1.2699	1.4020	1.5283	0.8747
2004	2.3033	1.6382	1.8062	0.7741
2005	1.9352	1.8594	2.0813	0.7242
2006	2.0778	2.0380	2.4509	0.6403
2007	3.9437	2.2156	3.0307	0.5455
2008	6.5583	2.2808	3.5976	0.4752
2009	3.2830	2.3912	3.8997	0.4061
2010	3.3307	2.5656	4.6020	0.3693
2011	3.6871	2.7534	5.4243	0.3565
2012	4.0130	2.8608	6.0326	0.3210
2013	3.9274	2.9659	6.6068	0.2817
2014	4.2167	3.0292	7.2151	0.2575
2015	4.2893	3.0583	7.6813	0.2322
2016	4.5925	3.1004	8.2872	0.2159
2017	4.6121	3.1942	9.2297	0.2147

is used to obtain the actual parameters of the four-dimensional system, to further analyze the evolutionary relationship between energy consumption, energy, economic growth, and the environment of the 3E system.

In this paper, we mainly use the calculation method of energy reduction that is now common in the world to calculate the amount of skill emission reduction [18]. The principal component analysis method based on the covariance matrix is used to calculate the environmental quality index [1] to represent the data of the environmental change. Data on energy consumption and economic growth are mainly derived from China's official statistical yearbook. In addition, in order to make the environmental quality index positive during the research process, we also use the logarithmic logic model for data standardization. All the data in Table 2 is a standardized process based on the 1999 data. The final data is as follows.

3.2. Model Validation. The LM-BP neural network method optimized by genetic algorithm has a good application in the parameter identification of nonlinear systems [1], and it has good identification accuracy, which makes this method widely used in nonidentification of linear system parameters. After system (1) is discretized, the difference equation of the following form is obtained:

$$
\begin{cases}
x(k+1) = x(k) + T\left[a_1 x(k)\left(\dfrac{y}{M-1}\right) - a_2 y + a_3 z + a_4 w\right], \\[2mm]
y(k+1) = y(k) + T\left[-b_1 x + b_2 y\left(\dfrac{1-y}{F}\right) + b_3 z\left(\dfrac{1-z}{E}\right) - b_4 w\right], \\[2mm]
z(k+1) = z(k) + T\left[c_1 x\left(\dfrac{x}{N-1}\right) - c_2 y - c_3 z - c_4 w\right], \\[2mm]
w(k+1) = w(k) + T\left[d_1 x - d_2 y + d_3 z\left(\dfrac{1-z}{H}\right) + d_4 w\left(\dfrac{y}{P-1}\right)\right].
\end{cases}
\tag{9}
$$

In this study, we used the former $n - 1$ group of data as the input data of the LM-BP neural network optimized by the genetic algorithm and the post $n - 1$ data as the output data of the LM-BP neural network optimized by the genetic algorithm. In addition, the data needs to be normalized in $\overline{x_i} = (x_i - x_{min})/(x_{max} - x_{min})$ form. All other parameters will be set to random number and the identified error control 10^{-6}. Finally, the identified system parametersare as shown in Table 3.

The data of 1980 is selected as the initial value of system [0.00000085, 0.658, 1.73, 1.1211], and the true validity of the identification parameters is further verified. The evolution trajectory of the system is shown in Figures 6 and 7. It can be seen from the phase diagram of the evolutionary trajectory of the system that the evolution trajectory of the system is multicycle and can always be in a stable mode. This explains the true effectiveness of the system from the side, which is also in line with the real situation.

4. System Parameter Analysis

In order to fully understand the stability of the above four-dimensional system (1), as well as the changes and impacts of energy intensity, how to effectively reduce energy intensity, stabilize economic development, improve the quality of ecological environment, and seek for high-quality, sustainable development models and strategies, and suggestions for the coordinated development of energy, economy, and environment, therefore, it is necessary to conduct an in-depth analysis of some key parameters of the four-dimensional system (1).

In Figures 8(a) and 8(b), we can find that although increasing the investment in energy saving and emission reduction can effectively improve the environmental quality, the effect on reducing energy intensity is not obvious. Over time, the amplitudes of the evolutionary fluctuations of energy intensity and environmental quality oscillate around

a_1	a_2	a_3	a_4	b_1	b_2	b_3	b_4	c_1	c_2	c_3	c_4	d_1	d_2	d_3	d_4	M	F	E	N	H	P
0.1277	0.2338	0.1992	0.0115	0.1896	0.4325	0.3818	0.0141	0.7582	0.5265	0.5834	0.0534	0.0591	0.0191	0.2567	0.5892	0.6523	0.5816	0.6437	0.5573	0.6943	0.7121

TABLE 3: System (1) identifies the actual parameters.
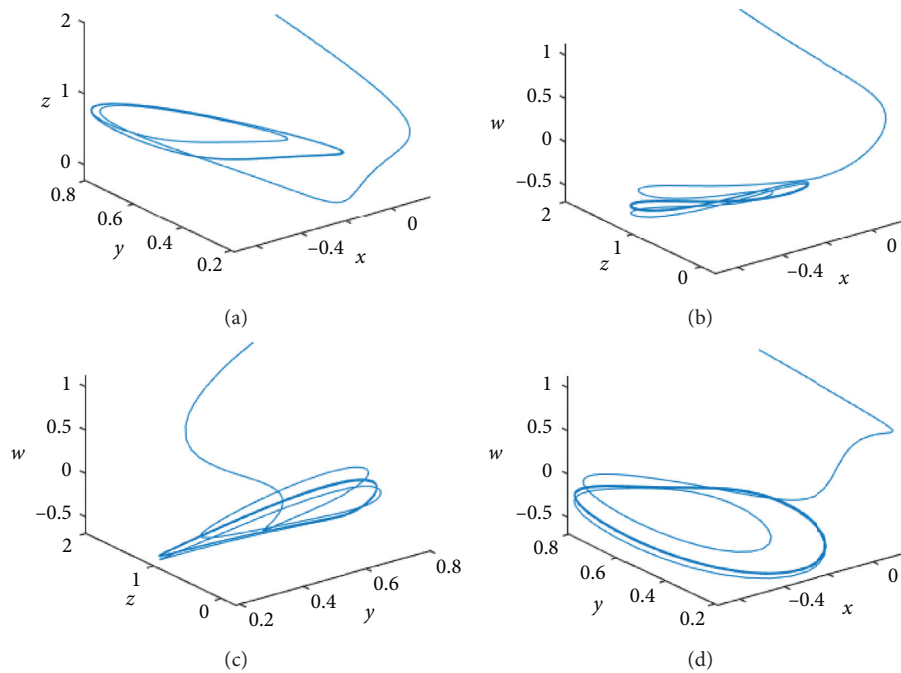
Figure 6: Three-dimensional spatial phase diagram of system (1) with identified parameters.
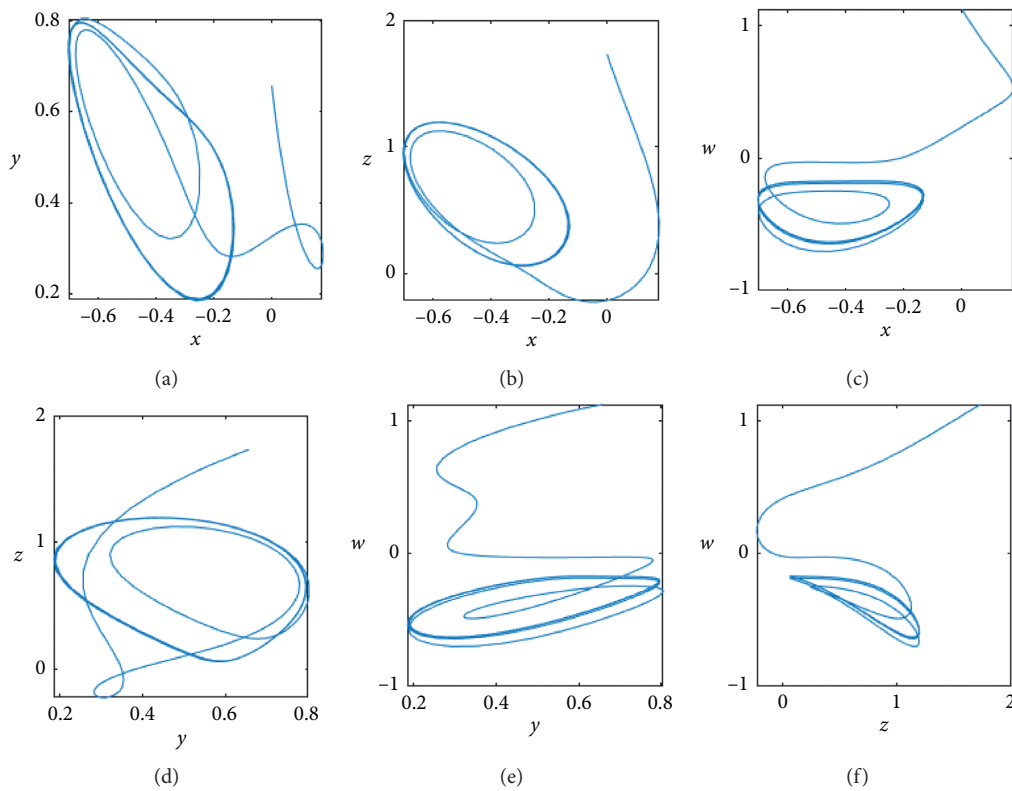
Figure 7: Two-dimensional plane phase diagram of system (1) with identified parameters.

a certain value. In a relatively short period of time, the improvement of environmental quality is also very obvious, but in the long run, the environment is still deteriorating

with the decline in the discount rate of energy-saving and emission-reduction inputs. The oscillating amplitude of energy intensity will decrease significantly with the increase

(a)

(b)
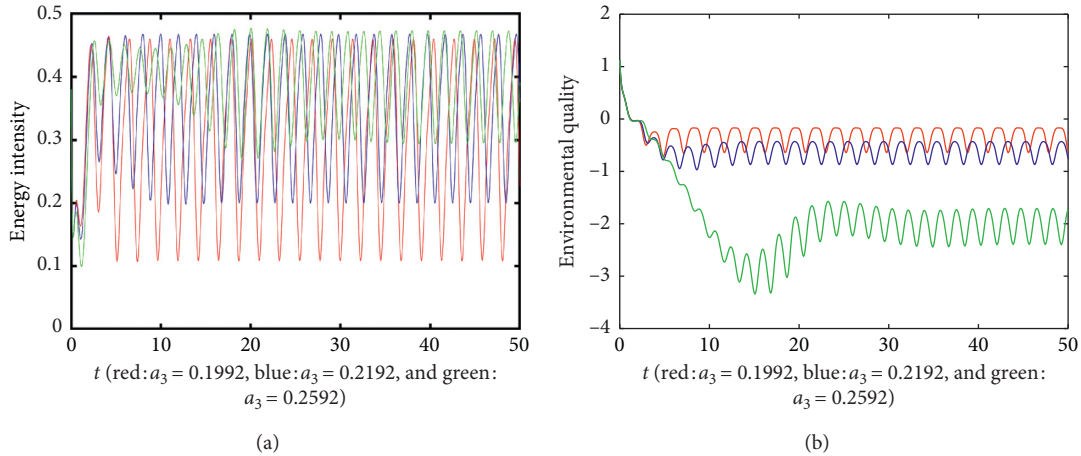
FIGURE 8: The parameters a_3 on the influence of system (1).

of energy-saving and emission-reduction input, but there is no obvious effect on the peak energy intensity. Therefore, it is not obvious that the effect of reducing the energy intensity and improving the stability of environmental quality by simply increasing the investment in energy saving and emission reduction is not obvious.

From Figures 9(a) and 9(b), we can find that when the peak value of pollution emissions $F = 0.5816$, the evolution trajectories of energy intensity and environmental quality show fluctuations around a certain central value over time. This phenomenon will be very unfavorable to the improvement of environmental quality in controlling pollution emissions (i.e., the inability to effectively reflect the energy reduction policies); when $F = 0.4816$, with the passage of time, energy intensity and environmental quality are still fluctuating up and down at a certain central value but will gradually shrink with the magnitude of evolutionary fluctuations, and the maximum peak of energy intensity is also significantly smaller than before. It also has a significant impact on the evolution of environmental quality. In the long run, the central value of the shock is decreasing, the amplitude of the shock is decreasing, and eventually it tends to be stable. After the pollution emission peak is lowered again $F = 0.3816$, the energy intensity and environmental quality evolve to a stable value at a relatively fast rate, and the peak value of the energy intensity and the center value of the oscillation are reduced again before comparison. Therefore, it can be better explained that effective control of the peak arrival time of pollution emissions can be used as an important decision for pollution emission control and energy intensity reduction.

From Figure 9(b), we can also find that the advance of the peak of pollution emissions makes the environmental system take the risk ahead, and the threat level is greatly increased. The reason for this phenomenon is that the peak of pollution discharge exceeds the self-purification speed of the natural environment system during the self-circulation process, so that the accumulation of pollutants in the ecological environment system reaches the maximum capacity, and the self-purification ability of the environmental system

is weakened. In a relatively short period of time, the ecological environment system is extremely deteriorated. Therefore, how to effectively and reasonably control the peak of pollution emission is very important for controlling the stability of 3E system and improving the environmental quality.

By comparing Figure 10(a), it can be found that, in the short term, the environmental capacity of the ecosystem has no significant effect on the stability of the evolution of the 3E system. As the environmental capacity decreases, over time, the evolution of environmental quality shows an upward trend of fluctuations and fluctuations around a certain central value; when the capacity of the ecosystem falls to the limit (i.e., the pollution effect exceeds the ecological environment), the system collapses (i.e., the ecological environment disappears, and the ecosystem can no longer rely on self-regulation to repair the ecological environment). As a result, this situation continues and the ecological environment is eventually sold out. It is confirmed that the ecological environment system has a certain bearing capacity, and the effect that the ecosystem will not be in operation or self-purification after the limit value can be exceeded is not significant.

From Figure 10(b), we can find that the effect of simply increasing the economic investment in the environment to improve the environmental quality is not obvious, it does not increase the economic investment as expected, and the environment can be effectively improved. From the evolutionary trajectory of the system, it can be seen that the evolutionary trajectory of the system revolves around central value fluctuation and oscillation amplitude over time. This phenomenon shows that the effects of economic input in the process of environmental governance are not significant enough. Therefore, in order to improve the quality of the ecological environment and promote the rapid development of the economy, we need more measures to use more means and technologies to promote stable economic growth and management of the ecological environment. It is necessary to correctly grasp the ecological environment protection and the relationship between economic developments, explore
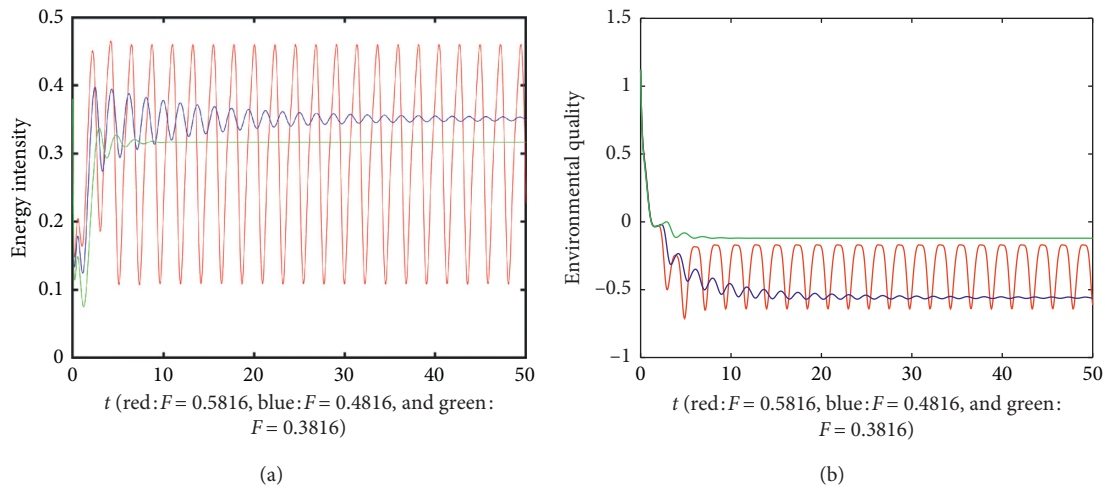
(a)

(b)

FIGURE 9: The parameters F on the influence of system (1).
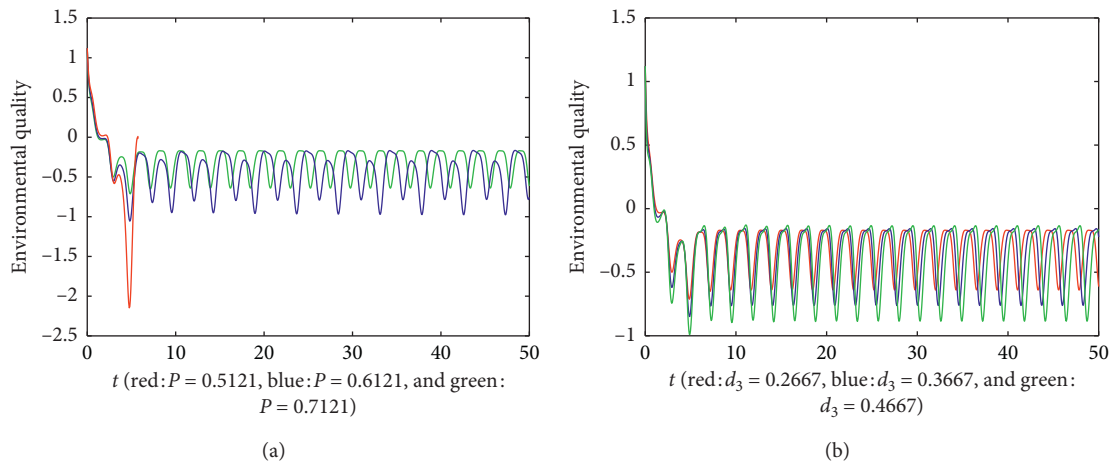

(a)

(b)

FIGURE 10: The different parameters P and d_3 on the influence of system (1).

synergies to promote ecological priorities and green development new ideas, and ultimately achieve a "win-win" environment and economy.

5. Conclusion

In this study, the energy, economic, and environmental (3E) four-dimensional system model of energy conservation constraints was first established. The Bayesian estimation method is used to correct the environmental quality variables to obtain the environmental quality data needed for the research. In addition, based on the Chinese statistical yearbook data, the Levenberg–Marquardt BP neural network method optimized by genetic algorithm is used to energy, economy, and environment under energy conservation constraints. The parameters in the four-dimensional system model are effectively identified. Finally, the system science analysis theory and complex system dynamics theory are used to analyze the stability and complex dynamics of the

model and explore the influence of some key parameters in the four-dimensional system on the evolution stability of the system. The main conclusions are as follows:

(1) Although increasing the investment in energy reduction can effectively improve the environmental quality; in a relatively short period of time, the improvement of environmental quality is also very obvious, but in the long run, the environment is still deteriorating with the decline in the discount rate of energy reduction inputs.

(2) It can be better explained that effective control of the peak arrival time of pollution emissions can be used as an important decision for pollution emission control and energy intensity reduction; therefore, how to effectively and reasonably control the peak of pollution emissions is of great significance for controlling the stability of energy, economy, and environment system under the constraint of energy

reduction, regulating energy intensity, and improving environmental quality and sustainable development.

(3) As the environmental capacity decreases, over time, the evolution of environmental quality shows an upward trend of fluctuations and fluctuations around a certain central value; when the capacity of the ecosystem falls to the limit, the system collapses. In order to improve the quality of the ecological environment and promote the rapid development of the economy, we need more measures to use more means and technologies to promote stable economic growth and management of the ecological environment.

Therefore, it is necessary to correctly grasp the ecological environment protection and the relationship between economic developments and explore synergies to promote ecological priorities and green development new ideas.

Data Availability

The numerical simulations data used to support the findings of this study were supplied by the corresponding author under license and so cannot be made freely available. Requests for access to these data should be made to the corresponding author (e-mail address: 136901672@qq.com).

Conflicts of Interest

The authors declare no conflicts of interest.

Acknowledgments

References

[1] L. Zhao, C. Otoo, and A. Otoo, "Stability and complexity of a novel three-dimensional environmental quality dynamic evolution system," *Complexity*, vol. 2019, Article ID 3941920, 11 pages, 2019.

[2] G. Fang, L. Tian, M. Sun, and M. Fu, "Analysis and application of a novel three-dimensional energy-saving and emission-reduction dynamic evolution system," *Energy*, vol. 40, no. 1, pp. 291–299, 2012.

[3] R. K. Upadhyay, S. R. K. Iyengar, and V. Rai, "Stability and complexity in ecological systems," *Chaos, Solitons & Fractals*, vol. 11, no. 4, pp. 533–542, 2000.

[4] J. Asafu-Adjaye, "The relationship between energy consumption, energy prices and economic growth: time series evidence from Asian developing countries," *Energy Economics*, vol. 22, no. 6, pp. 615–625, 2000.

[5] G. Hondroyiannis, S. Lolos, and E. Papapetrou, "Energy consumption and economic growth: assessing the evidence from Greece," *Energy Economics*, vol. 24, no. 4, pp. 319–336, 2002.

[6] S. Wang, J. Xu, and C. Qiu, "Bounds testing for energy consumption and environmental pollution," *China Population, Resources and Environment*, vol. 20, no. 4, pp. 69–73, 2010.

[7] L. I. Guozhang, J. Jiang, and C. Zhou, "Relation between total factor energy efficiency and environmental pollution," *China Population, Resources and Environment*, vol. 20, no. 4, pp. 50–56, 2010.

[8] R. López, "The environment as a factor of production: the effects of economic growth and trade liberalization," *Journal of Environmental Economics and Management*, vol. 27, no. 2, pp. 163–184, 1994.

[9] A. Grainger, "The forest transition: an alternative approach," *Area*, vol. 3, pp. 242–251, 1998.

[10] M. Shahbaz, N. Khraief, G. S. Uddin, and I. Ozturk, "Environmental Kuznets curve in an open economy: a bounds testing and causality analysis for Tunisia," *Renewable & Sustainable Energy Reviews*, vol. 34, pp. 325–336, 2014.

[11] J. Andreoni and A. Levinson, "The simple analytics of the environmental Kuznets curve," *Journal of Public Economics*, vol. 80, no. 2, pp. 269–286, 2001.

[12] E. Magnani, "The Environmental Kuznets Curve: development path or policy result?" *Environmental Modelling & Software*, vol. 16, no. 2, pp. 157–165, 2001.

[13] A. K. Bello and O. M. Abimbola, "Does the level of economic growth influence environmental quality in Nigeria: a test of environmental Kuznets curve (EKC) hypothesis?" *Pakistan Journal of Social Sciences*, vol. 7, no. 4, pp. 325–329, 2010.

[14] C. Liu, D. Duan, R. Yu et al., "Spatial-temporal structure of coupling of the economy resources-environment system in Wuhan metropolitan area," *China Population, Resources and Environment*, vol. 24, no. 5, pp. 145–152, 2014.

[15] Z. Guo, Y. Zheng, and X. Zhang, "Analysis of the energy-environment-economy system in China based on dynamic CGE model," *Journal of Systems Engineering*, vol. 29, no. 5, pp. 581–591, 2014.

[16] L. Zheng and Q. Zhu, "Vertical technological progress, industrial structure change and sustainable economic growth under energy and environment constraints," *Journal of Finance and Economics*, vol. 7, pp. 49–60, 2013.

[17] Z. L. Zhang, B. Xue, X. P. Chen, and C. Y. Lu, "Evolutionary mechanism analysis of energy-economy-environment system in China: based on Haken model," *Ecological Economy (Chinese Version)*, vol. 31, no. 1, pp. 14–17, 2015.

[18] Y.-M. Wei, R. Zeng, and Y. Fan, "A multi objective goal programming model for Beijing's coordination development of population, resources, environment and economy," *System Engineering-Theory and Practice*, vol. 22, no. 2, pp. 74–83, 2002.

[19] A. Löschel and V. M. Otto, "Technological uncertainty and cost effectiveness of CO_2 emission reduction," *Energy Economics*, vol. 31, no. 31, pp. S4–S17, 2009.

[20] C. Erdmenger, H. Lehmann, K. Müschen, J. Tambke, S. Mayr, and K. Kuhnhenn, "A climate protection stategy for Germany-40% reduction of CO_2 emission by 2020 compared to 1990," *Energy Policy*, vol. 37, pp. 158–165, 2009.

[21] Y. Xu and T. Masui, "Local air pollutant emission reduction and ancillary carbon benefits of SO_2 control policies: application of AIM/CGE model to China," *European Journal of Operational Research*, vol. 198, no. 1, pp. 315–325, 2009.

[22] J. M. Cullende and J. M. Allood, "The efficient use of energy: tracing the global flow of energy from fuel to service," *Energy Policy*, vol. 38, no. 1, pp. 75–81, 2010.

[23] M. Prasad and S. Munch, "State-level renewable electricity policies and reductions in carbon emissions," *Energy Policy*, vol. 45, no. 45, pp. 237–242, 2012.

[24] G. Fang, L. Tian, M. Fu, and M. Sun, "The impacts of carbon tax on energy intensity and economic growth - a dynamic evolution analysis on the case of China," *Applied Energy*, vol. 110, pp. 17–28, 2013.

[25] G. Fang, L. Tian, M. Fu, M. Sun, Y. He, and L. Lu, "How to promote the development of energy-saving and emission-reduction with changing economic growth rate-a case study of China," *Energy*, vol. 143, no. 143, pp. 732–745, 2018.

[26] G. Fang, L. Tian, M. Fu et al., "The effect of energy construction adjustment on the dynamical evolution of energy-saving and emission-reduction system in China," *Applied Energy*, vol. 196, pp. 180–189, 2017.

[27] G. Fang, L. Tian, M. Fu, M. Sun, R. Du, and M. Liu, "Investigating carbon tax pilot in YRD urban agglomerations-Analysis of a novel ESER system with carbon tax constraints and its application," *Applied Energy*, vol. 194, pp. 635–647, 2017.

[28] X. Li, J. Du, and H. Long, "A comparative study of Chinese and foreign green development from the perspective of mapping knowledge domains," *Sustainability*, vol. 10, no. 12, p. 4357, 2018.

[29] X. Fan, Y. Zhang, and J. Yin, "Evolutionary analysis of a three-dimensional carbon price dynamic system," *Sustainability*, vol. 11, no. 1, p. 116, 2019.

[30] J.-Z. Wang, J.-J. Wang, Z.-G. Zhang, and S.-P. Guo, "Forecasting stock indices with back propagation neural network," *Expert Systems with Applications*, vol. 38, no. 11, pp. 14346–14355, 2011.

[31] M. A. Boyacioglu and D. Avci, "An adaptive network-based fuzzy inference system (ANFIS) for the prediction of stock market return: the case of the istanbul stock exchange," *Expert Systems with Applications*, vol. 37, no. 12, pp. 7908–7912, 2010.

[32] C.-H. Cheng, T.-L. Chen, and L.-Y. Wei, "A hybrid model based on rough sets theory and genetic algorithms for stock price forecasting," *Information Sciences*, vol. 180, no. 9, pp. 1610–1629, 2010.

[33] E. Hadavandi, H. Shavandi, and A. Ghanbari, "Integration of genetic fuzzy systems and artificial neural networks for stock price forecasting," *Knowledge-Based Systems*, vol. 23, no. 8, pp. 800–808, 2010.

[34] A. Bagheri, H. Mohammadi Peyhani, and M. Akbari, "Financial forecasting using ANFIS networks with quantum-behaved particle swarm optimization," *Expert Systems with Applications*, vol. 41, no. 14, pp. 6235–6250, 2014.

[35] X. Liu and X. Ma, "Based on BP neural network stock prediction," *Journal of Curriculum and Teaching*, vol. 1, no. 1, pp. 45–50, 2012.

[36] A. S. Babu and S. K. Reddy, "Exchange Rate Forecasting using ARIMA, neural network and fuzzy neuron," *Journal of Stock & Forex Trading*, vol. 4, no. 3, pp. 1–5, 2015.

[37] A. Murkute and T. Sarode, "Forecasting market price of stock using artificial neural network," *International Journal of Computer Applications*, vol. 124, no. 12, pp. 11–15, 2015.

[38] Q. Ye and L. Wei, "The prediction of stock price based on improved wavelet neural network," *Open Journal of Applied Sciences*, vol. 5, no. 4, pp. 115–120, 2015.

[39] L. Zhang, F. Wang, B. Xu, W. Chi, Q. Wang, and T. Sun, "Prediction of stock prices based on LM-BP neural network and the estimation of overfitting point by RDCI," *Neural Computing and Applications*, vol. 30, no. 5, pp. 1425–1444, 2018.

[40] M. Marzouk and S. Azab, "Environmental and economic impact assessment of construction and demolition waste disposal using system dynamics," *Resources, Conservation and Recycling*, vol. 82, pp. 41–49, 2014.

[41] D. H. Meadows, J. Randers, and D. L. Meadows, *The Limits to Growth: The 30-Year Update*, Chelsea Green Pub, White River Junction, VT, USA, 2004.

[42] P. P.-J. Yang and O. B. Lay, "Applying ecosystem concepts to the planning of industrial areas:a case study of Singapore's Jurong Island," *Journal of Cleaner Production*, vol. 12, no. 8–10, pp. 1011–1023, 2004.

[43] Y. Fang, R. P. Côté, and R. Qin, "Industrial sustainability in China: practice and prospects for eco-industrial development," *Journal of Environmental Management*, vol. 83, no. 3, pp. 315–328, 2007.

[44] D. Guan, W. Gao, W. Su, H. Li, and K. Hokao, "Modeling and dynamic assessment of urban economy-resource-environment system with a coupled system dynamics- geographic information system model," *Ecological Indicators*, vol. ll, no. 5, pp. 1333–1344, 201l.

[45] S. F. Zhan, X. C. Zhang, C. Ma, and W. P. Chen, "Dynamic modelling for ecological and economic sustainability in a rapid urbanizing region," *Procedia Environmental Sciences*, vol. 13, pp. 242–251, 2012.

[46] I. Musu and M. Lines, "Endogenous growth and environmental preservation,""Endogenous growth and environmental preservation," in *Environmental Economics: Proceeding of European Economic Association at Oxford*, G. Boero and A. Silberston, Eds., St Martins Press, London, UK, 1995.

[47] D. Fullerton and S. Kim, "Environmental investment and policy with dissortional taxes and endogenous growth," *Journal of Environmental Economics and Management*, vol. 56, no. 2, pp. 141–154, 2008.

[48] J.-h. Chen, C. Lai, and J. Y. shieh, "Anticipated environment policy and transitional dynamics in endogenous growth model," *Environmental and Resource Economics*, vol. 25, no. 2, pp. 233–254, 2003.

WILEY | Hindawi

Research Article

Exact Solutions of Damped Improved Boussinesq Equations by Extended (G'/G)-Expansion Method

Kai Fan [ID]^{1,2,3,4} **and Cunlong Zhou** [ID]^{1,2,3}

^{1}*Engineering Research Center of Heavy Machinery Ministry of Education, Taiyuan University of Science and Technology,*
 Taiyuan 030024, China
^{2}*Mechanical Engineering College, Taiyuan University of Science and Technology, Taiyuan 030024, China*
^{3}*Shanxi Provincial Key Laboratory of Metallurgical Device Design Theory and Technology,*
 Taiyuan University of Science and Technology, Taiyuan 030024, China
^{4}*Applied Science College, Taiyuan University of Science and Technology, Taiyuan 030024, China*

Correspondence should be addressed to Kai Fan; 2014279@tyust.edu.cn and Cunlong Zhou; zcunlong@tyust.edu.cn

With the help of the auxiliary function method, we solved the improved Boussinesq (IBq) equation with fluid dynamic damping and the modified IBq (IMBq) equation with Stokes damping, and we obtained their three types of travelling wave exact solutions, which is an extension service of the numerical simulation and the existence of a solution. From the waveform diagram of IBq equation with hydrodynamic damping, it can be seen that when the propagation velocity of kink wave changes, the amplitude also changes significantly, and it is also found that the kink isolated waveform is significantly asymmetric due to the increase of damping coefficient v, which may be of some value in explaining some physical phenomena. In addition, the symbolic computing software maple makes our computing work easier.

1. Introduction

There are various kinds of nonlinear phenomena in nature, most of which can be described by nonlinear evolution equations. It is well known that the Boussinesq (Bq) equation, which describes the propagation model of long wave in shallow water, is one of them and has the following two basic forms:

$$u_{tt} - u_{xx} + \delta u_{xxxx} = \left(u^2\right)_{xx}, \tag{1}$$

$$u_{tt} - u_{xx} - u_{xxtt} = \left(u^2\right)_{xx}, \tag{2}$$

where u represents displacement and subscripts x and t represent partial derivatives concerning x and t, respectively. Equations (1) and (2) were first deduced by Boussinesq [1, 2]. If the coefficient δ of the fourth derivative of (1) is greater than zero, (1) is linearly stable and can be used to describe the transverse vibration of small nonlinear elastic beam,

which is called the "good" Bq equation [3]. When δ is less than zero, it is called the "bad" Bq equation because of its linear instability [4]. Equation (2) is also an important model to approximate the propagation of long waves in shallow water, which is called the IBq equation. The exact solution of Bq equation can be obtained by [5–7]. Makhankov derived the IBq equation from the fluid dynamics equations of the plasma, which had a modified equation called IMBq equation [8], as shown in (3). In recent years, there have been many papers on the dynamics of solitons in plasma [9–12].

$$u_{tt} - u_{xx} - u_{xxtt} = \left(u^3\right)_{xx}. \tag{3}$$

Equations (2) and (3) differ only in terms of nonlinear forces. Equation (2) can also be used to describe the kinetic and thermodynamic properties of anharmonic monatomic and diatomic chains [13]. In literature [14], lattice soliton dynamics of a single atomic chain under damping and

external forces are studied. The IBq equation with hydro-dynamic damping term and the IMBq equation with Stokes damping term are obtained, respectively, under the conditions of the third and fourth anharmonic potentials. The IBq equation with hydrodynamical damping term is shown in (3), and the IMBq equation with Stokes damping term is shown in (4). Arévalo et al. [14] obtained the solitary wave solution of (4) with bell-shaped shape through numerical simulation. Naranmandula [15] also obtained an equation similar to (4) when studying the propagation of one-dimensional longitudinal wave in nonlinear microstructural solid and simulated the influence of microstructural effect on the evolution of kinked isolated wave by finite difference method:

$$u_{tt} - u_{xx} - u_{xxtt} - \nu u_{xxt} = \left(u^2\right)_{xx}, \tag{4}$$

$$u_{tt} - u_{xx} - u_{xxtt} + \nu u_t = \left(u^3\right)_{xx}. \tag{5}$$

In 2012, Wang and Xu studied the global existence of small amplitude solutions of the Cauchy problem of (4) in Sobolev space [16]. In 2013, Wang and Xu studied the global existence of small amplitude solutions of the Cauchy problem of (5) in Sobolev space [17]. In 2015, Chen gives sufficient conditions of the blow-up of the solution of the Cauchy problem of (5) in Sobolev space [18]. In order to better grasp the model represented by (4) and (5), it is necessary to obtain their exact travelling wave solutions. With the development of computer technology, many scholars interested in nonlinear science have studied the exact solutions of nonlinear evolution equations and used different methods to solve different equations, such as the Riccati-Bernoulli sub-ODE method [19], the Exp-function method [20], the modified Exp-function method [21, 22], the Exp $(-\phi)$-expansion method [23], the tanh-coth method [24–26], the homogeneous balance method [27], the improvement of (G'/G)-expansion method [28–30], the formal linearization method [31], the first integral method [32], $(1/G')$-expansion and modified Kudryashov methods [33], and the (G'/G)-expansion method [34–38].

Through searching the whole network, we find that there are many articles on Bq equation and also many articles on the existence of solutions to Cauchy problems of (4) and (5). In this paper, by means of the extended (G'/G)-expansion method, some exact travelling wave solutions of (4) and (5) are obtained, and some individual solutions are briefly presented and discussed, especially kink soliton solutions assigned to parameters. In the case of an extended (G'/G)-expansion, the integral constants of the equation should not be set directly to zero, which may result in the loss of arbitrary constants in the final expression [38, 39]. Although there is no uniform solution for all nonlinear partial differential equations, different methods may not yield different solutions [40] because these solutions may only be expressed differently or they may be different particular solutions belonging to the same general solution. In addition, some of the different approaches are equivalent [41, 42].

2. Summary of the Extended (G'/G)-Expansion Method

Consider a generalized nonlinear evolution equation

$$P\left(u, u_x, u_t, u_{tt}, u_{xt}, u_{xx}, \ldots\right) = 0, \tag{6}$$

where u is an unsolved function, and it has two independent variables, x and t.

The steps of the extended (G'/G)-expansion method to solve (6) are listed as follows:

(i) *Step 1.* Under the transformation,

$$u(x, t) = U(\xi), \xi = x - ct. \tag{7}$$

We translate (6) to the ordinary differential equation (ODE)

$$P\left(U, -cU', U', c^2U'', -cU'', U'', \ldots\right) = 0. \tag{8}$$

(i) *Step 2.* If the form of (8) allows, we can integrate it once but do not set the integral constant to zero, which will help simplify the following calculation. The travelling wave solution of (8) is proposed as follows:

$$U(\xi) = \sum_{i=0}^{m} a_i \left(\frac{G'}{G}\right)^i + \sum_{i=1}^{m} b_i \left(\frac{G'}{G}\right)^{-i}, \tag{9}$$

where a_i and b_i $(i = 1, 2, \ldots, m)$ are undetermined constants. G is a function of ξ. In combination with the form of (9), the highest derivative term and the nonlinear term in (8) are balanced by the homogeneous equilibrium principle, and the value of the positive integer m in (9) can be obtained. The G appearing in (8) is the solution of the second-order differential equation

$$G'' + \lambda G' + \mu G = 0, \tag{10}$$

where λ and μ will be determined later.

(iii) *Step 3.* Substitute (9) and (7) into (8), use the ordinary differential (10) concerning (G'/G) to combine the same power terms of (G'/G), and then set the coefficients of all powers of (G'/G) to zero; we get a nonlinear algebraic system of equations concerning the unknowns $a_i, b_i, \lambda, \mu,$ and c.

(iv) *Step 4.* Using the computational software Maple programming, we can solve the algebraic equations in step 3. By substituting the obtained results into (9) and using the general solutions of (10) in different situations, multiple exact solutions of different types of (6) can be obtained.

The general solutions of (10) are given as

$$
\left(\frac{G\prime}{G}\right) = \begin{cases} \dfrac{\sqrt{\lambda^2-4\mu}}{2}\left(\dfrac{C_1\sinh\left(\left(\sqrt{\lambda^2-4\mu}/2\right)\xi\right)+C_2\cosh\left(\left(\sqrt{\lambda^2-4\mu}/2\right)\xi\right)}{C_1\cosh\left(\left(\sqrt{\lambda^2-4\mu}/2\right)\xi\right)+C_2\sinh\left(\left(\sqrt{\lambda^2-4\mu}/2\right)\xi\right)}\right)-\dfrac{\lambda}{2}, & \lambda^2-4\mu>0, \\[3em] \dfrac{\sqrt{4\mu-\lambda^2}}{2}\left(\dfrac{-C_1\sin\left(\left(\sqrt{4\mu-\lambda^2}/2\right)\xi\right)+C_2\cos\left(\left(\sqrt{4\mu-\lambda^2}/2\right)\xi\right)}{C_1\cos\left(\left(\sqrt{4\mu-\lambda^2}/2\right)\xi\right)+C_2\sin\left(\left(\sqrt{4\mu-\lambda^2}/2\right)\xi\right)}\right)-\dfrac{\lambda}{2}, & \lambda^2-4\mu<0, \\[3em] \dfrac{C_2}{C_1+C_2\xi}-\dfrac{\lambda}{2}, & \lambda^2-4\mu=0. \end{cases}
\tag{11}
$$

These results can further be written in some more simplified forms depending upon the conditions on the ratio of C_1 and C_2 as

$$
\left(\frac{G'}{G}\right) = \begin{cases} \dfrac{\sqrt{\lambda^2-4\mu}}{2}\tanh\left(\dfrac{\sqrt{\lambda^2-4\mu}}{2}\xi+\xi_0\right)-\dfrac{\lambda}{2}, \lambda^2-4\mu>0, \tanh(\xi_0)=\dfrac{C_2}{C_1}, \left|\dfrac{C_2}{C_1}\right|<1, \\[2.5em] \dfrac{\sqrt{\lambda^2-4\mu}}{2}\coth\left(\dfrac{\sqrt{\lambda^2-4\mu}}{2}\xi+\xi_0\right)-\dfrac{\lambda}{2}, \lambda^2-4\mu>0, \coth(\xi_0)=\dfrac{C_2}{C_1}, \left|\dfrac{C_2}{C_1}\right|>1, \\[2.5em] \dfrac{\sqrt{4\mu-\lambda^2}}{2}\cot\left(\dfrac{\sqrt{4\mu-\lambda^2}}{2}\xi+\xi_0\right)-\dfrac{\lambda}{2}, \lambda^2-4\mu<0, \cot(\xi_0)=\dfrac{C_2}{C_1}, \\[2.5em] \dfrac{C_2}{C_1+C_2\xi}-\dfrac{\lambda}{2}, \lambda^2-4\mu=0. \end{cases}
\tag{12}
$$

3. Exact Solutions of (3) and (4)

3.1. The IBq Equation with Hydrodynamical Damping

$$
u_{tt}-u_{xx}-u_{xxtt}-vu_{xxt}=\left(u^2\right)_{xx},
\tag{13}
$$

where v is the damping constant of internal friction (we call this type of friction hydrodynamical).

We apply (7) to (13), we integrate once concerning ξ, we set the integration constant to M, and then we can convert (12) to nonlinear ODE:

$$
\left(c^2-1\right)U'-c^2U'''+cvU''-2UU'=M.
\tag{14}
$$

At equilibrium, the highest nonlinear term in (14), and the highest derivative term in (14), we get m equal to 2. Therefore, the exact solution of (14) in the form of (9) can be written as follows:

$$
U(\xi)=a_0+a_1\frac{G'}{G}+a_1\left(\frac{G'}{G}\right)^2+b_1\frac{G}{G'}+b_2\left(\frac{G}{G'}\right)^2.
\tag{15}
$$

Substitute (15) into (14), use the ordinary differential (10) concerning (G'/G) to combine the same power terms of (G'/G), and then let the coefficients be equal to zero; we get a nonlinear algebraic system of equations concerning the unknowns $a_0, a_1, a_2, b_1, b_2, c,$ and M:

$$\left(\frac{G}{G'}\right)^5: \quad -24c^2\mu^3b_2 - 4\mu b_2^2 = 0,$$

$$\left(\frac{G}{G'}\right)^4: \quad -6c^2\mu^3b_1 - 54c^2\mu^2\lambda b_2 + 6c\mu^2 v b_2 - 6\mu b_1 b_2 - 4\lambda b_2^2 = 0,$$

$$\left(\frac{G}{G'}\right)^3: \quad -12c^2\mu^2\lambda b_1 - 38c^2\mu\lambda^2 b_2 - 40c^2\mu^2 b_2 + 2c\mu^2 v b_1 + 10c\mu v\lambda b_2 + 2c^2\mu b_2 - 4\mu a_0 b_2 - 2\mu b_1^2 - 6\lambda b_1 b_2 - 2\mu b_2 - 4b_2^2 = 0,$$

$$\left(\frac{G}{G'}\right)^2: \quad -7c^2\mu\lambda^2 b_1 - 8c^2\lambda^3 b_2 - 8c^2\mu^2 b_1 - 52c^2\mu\lambda b_2 + 3c\mu v\lambda b_1$$
$$+ 4cv\lambda^2 b_2 + c^2\mu b_1 + 2c^2\lambda b_2 + 8c\mu v b_2 - 2\mu a_0 b_1 - 2\mu a_1 b_2 - 4\lambda a_0 b_2 - 2\lambda b_1^2 - \mu b_1 - 2\lambda b_2 - 6b_1 b_2 = 0,$$

$$\frac{G}{G'}: \quad -c^2\lambda^3 b_1 - 8c^2\mu\lambda b_1 - 14c^2\lambda^2 b_2 + cv\lambda^2 b_1 - 16c^2\mu b_2 + c^2\lambda b_1$$
$$+ 2c\mu v b_1 + 6cv\lambda b_2 + 2c^2 b_2 - 2\lambda a_0 b_1 - 2\lambda a_1 b_2 - \lambda b_1 - 4a_0 b_2 - 2b_1^2 - 2b_2 = 0,$$

$$\left(\frac{G}{G'}\right)^0: \quad b_1 c^2 - 2a_0 b_1 + 2a_2 b_1\mu + cva_1\lambda\mu - c^2 b_1\lambda^2 - 2c^2\mu b_1 - 6c^2\lambda b_2$$
$$+ 2c^2 a_1\mu^2 - c^2\mu a_1 + 2a_0 a_1\mu + 2cvb_2 + \mu a_1 + c^2 a_1\lambda^2\mu + 6c^2 a_2\lambda\mu^2 - 2a_1 b_2 + cvb_1\lambda + 2cva_2\mu^2 - b_1 - M = 0,$$

$$\frac{G'}{G}: \quad 14c^2\mu\lambda^2 a_2 + c^2\lambda^3 a_1 + 16c^2\mu^2 a_2 + 8c^2\mu\lambda a_1 + 6c\mu v\lambda a_2 + cv\lambda^2 a_1 - 2c^2\mu a_2$$
$$- c^2\lambda a_1 + 2c\mu va_1 + 4\mu a_0 a_2 + 2\mu a_1^2 + 2\lambda a_0 a_1 + 2\lambda a_2 b_1 + 2\mu a_2 + \lambda a_1 = 0,$$

$$\left(\frac{G'}{G}\right)^2: \quad 8c^2\lambda^3 a_2 + 52c^2\mu\lambda a_2 + 7c^2\lambda^2 a_1 + 4cv\lambda^2 a_2 + 8c^2\mu a_1 - 2c^2\lambda a_2 + 8c\mu va_2$$
$$+ 3cv\lambda a_1 - c^2 a_1 + 6\mu a_1 a_2 + 4\lambda a_0 a_2 + 2\lambda a_1^2 + 2\lambda a_2 + 2a_0 a_1 + 2a_2 b_1 + a_1 = 0,$$

$$\left(\frac{G'}{G}\right)^3: \quad 38c^2\lambda^2 a_2 + 40c^2\mu a_2 + 12c^2\lambda a_1 + 10cv\lambda a_2 - 2c^2 a_2 + 2cva_1 + 4\mu a_2^2 + 6\lambda a_1 a_2 + 4a_0 a_2 + 2a_1^2 + 2a_2 = 0,$$

$$\left(\frac{G'}{G}\right)^4: \quad 54c^2\lambda a_2 + 6c^2 a_1 + 6cva_2 + 4\lambda a_2^2 + 6a_1 a_2 = 0,$$

$$\left(\frac{G'}{G}\right)^5: \quad 24c^2 a_2 + 4a_2^2 = 0.$$

$$(16)$$

Using symbolic computation software maple, the solution of this system is obtained as follows:

$$
\left\{
\begin{aligned}
a_0 &= \frac{1}{150} \frac{\left[180v^2\lambda^4 + 324\mu v^2\lambda^2 + 144\mu^2 v^2 + 54v^2\lambda^2 - 1050\lambda^4 + 48\mu v^2 - 600\mu\lambda^2 + 4v^2 - 225\lambda^2\right]}{\lambda^2\left(14\lambda^2 + 8\mu + 3\right)}, \\[2mm]
a_1 &= \frac{4}{25} \frac{v^2\left(6\lambda^2 + 6\mu + 1\right)}{\lambda\left(14\lambda^2 + 8\mu + 3\right)}, \\[2mm]
a_2 &= \frac{2}{25} \frac{v\left(210c\lambda^3 + 120c\mu\lambda + 12v\lambda^2 + 45c\lambda + 12\mu v + 2v\right)}{\lambda^2\left(14\lambda^2 + 8\mu + 3\right)}, \\[2mm]
b_1 &= \frac{4}{25} \frac{\mu v\left(210c\lambda^3 + 120c\mu\lambda + 6v\lambda^2 + 45c\lambda + 6\mu v + v\right)}{\lambda\left(14\lambda^2 + 8\mu + 3\right)}, \\[2mm]
b_2 &= \frac{2}{25} \frac{\mu^2 v\left(210c\lambda^3 + 120c\mu\lambda + 12v\lambda^2 + 45c\lambda + 12\mu v + 2v\right)}{\lambda^2\left(14\lambda^2 + 8\mu + 3\right)},
\end{aligned}
\right. \tag{17}
$$

$$
M = -\frac{4}{125} \frac{c\mu v\left(\begin{array}{l}1050c^2\lambda^6 + 2700c^2\mu\lambda^4 - 1050cv\lambda^5 + 1200c^2\mu^2\lambda^2 - 825c^2\lambda^4 - 5220c\mu v\lambda^3 + 120v^2\lambda^4 - 150c^2\mu\lambda^2 \\ - 2640c\mu^2 v\lambda - 225cv\lambda^3 - 225c^2\lambda^2 - 990c\mu v\lambda - 120\mu^2 v^2 + 44v^2\lambda^2 + 4\mu v^2 + 4v^2\end{array}\right)}{\lambda^2\left(14\lambda^2 + 8\mu + 3\right)}. \tag{18}
$$

Substituting the values from (17) and using the general solutions of (10) in different situations, multiple exact solutions of different types of (13) can be obtained.

(i) *Case 1*. When $\lambda^2 - 4\mu > 0$, the solution of the hyperbolic form of equation (13) is as follows:

$$
\begin{aligned}
U_1(\xi) &= \frac{1}{150} \frac{\left[180v^2\lambda^4 + 324\mu v^2\lambda^2 + 144\mu^2 v^2 + 54v^2\lambda^2 - 1050\lambda^4 + 48\mu v^2 - 600\mu\lambda^2 + 4v^2 - 225\lambda^2\right]}{\lambda^2\left(14\lambda^2 + 8\mu + 3\right)} \\[2mm]
&+ \frac{4}{25} \frac{v^2\left(6\lambda^2 + 6\mu + 1\right)}{\lambda\left(14\lambda^2 + 8\mu + 3\right)}\left[-\frac{\lambda}{2} + \eta_1\left(\frac{C_1\sinh\left(\eta_1\xi\right) + C_2\cosh\left(\eta_1\xi\right)}{C_1\cosh\left(\eta_1\xi\right) + C_2\sinh\left(\eta_1\xi\right)}\right)\right] \\[2mm]
&+ \frac{2}{25} \frac{v\left(210c\lambda^3 + 120c\mu\lambda + 12v\lambda^2 + 45c\lambda + 12\mu v + 2v\right)}{\lambda^2\left(14\lambda^2 + 8\mu + 3\right)}\left[-\frac{\lambda}{2} + \eta_1\left(\frac{C_1\sinh\left(\eta_1\xi\right) + C_2\cosh\left(\eta_1\xi\right)}{C_1\cosh\left(\eta_1\xi\right) + C_2\sinh\left(\eta_1\xi\right)}\right)\right]^2 \\[2mm]
&+ \frac{4}{25} \frac{\mu v\left(210c\lambda^3 + 120c\mu\lambda + 6v\lambda^2 + 45c\lambda + 6\mu v + v\right)}{\lambda\left(14\lambda^2 + 8\mu + 3\right)}\left[-\frac{\lambda}{2} + \eta_1\left(\frac{C_1\sinh\left(\eta_1\xi\right) + C_2\cosh\left(\eta_1\xi\right)}{C_1\cosh\left(\eta_1\xi\right) + C_2\sinh\left(\eta_1\xi\right)}\right)\right]^{-1} \\[2mm]
&+ \frac{2}{25} \frac{\mu^2 v\left(210c\lambda^3 + 120c\mu\lambda + 12v\lambda^2 + 45c\lambda + 12\mu v + 2v\right)}{\lambda^2\left(14\lambda^2 + 8\mu + 3\right)}\left[-\frac{\lambda}{2} + \eta_1\left(\frac{C_1\sinh\left(\eta_1\xi\right) + C_2\cosh\left(\eta_1\xi\right)}{C_1\cosh\left(\eta_1\xi\right) + C_2\sinh\left(\eta_1\xi\right)}\right)\right]^{-2},
\end{aligned} \tag{19}
$$

where $\xi = x - ct$, $\eta_1 = (1/2)\sqrt{\lambda^2 - 4\mu}$, and C_1 and C_2 are free constants.

In particular, if $C_1 \neq 0$ and $C_2 = 0$, then $U_1(\xi)$ becomes

$$
\begin{aligned}
\overline{U}_1(\xi) = {} & \frac{1}{150} \frac{\left[180v^2\lambda^4 + 324\mu v^2\lambda^2 + 144\mu^2 v^2 + 54v^2\lambda^2 - 1050\lambda^4 + 48\mu v^2 - 600\mu\lambda^2 + 4v^2 - 225\lambda^2\right]}{\lambda^2\left(14\lambda^2 + 8\mu + 3\right)} \\[2mm]
& + \frac{4}{25} \frac{v^2\left(6\lambda^2 + 6\mu + 1\right)}{\lambda\left(14\lambda^2 + 8\mu + 3\right)} \left[-\frac{\lambda}{2} + \eta_1 \tanh\left(\eta_1\xi\right)\right] \\[2mm]
& + \frac{2}{25} \frac{v\left(210c\lambda^3 + 120c\mu\lambda + 12v\lambda^2 + 45c\lambda + 12\mu v + 2v\right)}{\lambda^2\left(14\lambda^2 + 8\mu + 3\right)} \left[-\frac{\lambda}{2} + \eta_1 \tanh\left(\eta_1\xi\right)\right]^2 \\[2mm]
& + \frac{4}{25} \frac{\mu v\left(210c\lambda^3 + 120c\mu\lambda + 6v\lambda^2 + 45c\lambda + 6\mu v + v\right)}{\lambda\left(14\lambda^2 + 8\mu + 3\right)} \left[-\frac{\lambda}{2} + \eta_1 \tanh\left(\eta_1\xi\right)\right]^{-1} \\[2mm]
& + \frac{2}{25} \frac{\mu^2 v\left(210c\lambda^3 + 120c\mu\lambda + 12v\lambda^2 + 45c\lambda + 12\mu v + 2v\right)}{\lambda^2\left(14\lambda^2 + 8\mu + 3\right)} \left[-\frac{\lambda}{2} + \eta_1 \tanh\left(\eta_1\xi\right)\right]^{-2}.
\end{aligned}
\tag{20}
$$

Again using (12), the general solutions for $U_1(\xi)$ in simplified forms are written as

$$
\begin{aligned}
U_{11}(\xi) = {} & \frac{1}{150} \frac{\left[180v^2\lambda^4 + 324\mu v^2\lambda^2 + 144\mu^2 v^2 + 54v^2\lambda^2 - 1050\lambda^4 + 48\mu v^2 - 600\mu\lambda^2 + 4v^2 - 225\lambda^2\right]}{\lambda^2\left(14\lambda^2 + 8\mu + 3\right)} \\[2mm]
& + \frac{4}{25} \frac{v^2\left(6\lambda^2 + 6\mu + 1\right)}{\lambda\left(14\lambda^2 + 8\mu + 3\right)} \left[-\frac{\lambda}{2} + \eta_1 \tanh\left(\eta_1\xi + \xi_0\right)\right] \\[2mm]
& + \frac{2}{25} \frac{v\left(210c\lambda^3 + 120c\mu\lambda + 12v\lambda^2 + 45c\lambda + 12\mu v + 2v\right)}{\lambda^2\left(14\lambda^2 + 8\mu + 3\right)} \left[-\frac{\lambda}{2} + \eta_1 \tanh\left(\eta_1\xi + \xi_0\right)\right]^2 \\[2mm]
& + \frac{4}{25} \frac{\mu v\left(210c\lambda^3 + 120c\mu\lambda + 6v\lambda^2 + 45c\lambda + 6\mu v + v\right)}{\lambda\left(14\lambda^2 + 8\mu + 3\right)} \left[-\frac{\lambda}{2} + \eta_1 \tanh\left(\eta_1\xi + \xi_0\right)\right]^{-1} \\[2mm]
& + \frac{2}{25} \frac{\mu^2 v\left(210c\lambda^3 + 120c\mu\lambda + 12v\lambda^2 + 45c\lambda + 12\mu v + 2v\right)}{\lambda^2\left(14\lambda^2 + 8\mu + 3\right)} \left[-\frac{\lambda}{2} + \eta_1 \tanh\left(\eta_1\xi + \xi_0\right)\right]^{-2},
\end{aligned}
\tag{21}
$$

when $|C_2/C_1| < 1$ and $\tanh(\xi_0) = C_2/C_1$;

$$
\begin{aligned}
U_{12}(\xi) = \frac{1}{150} & \frac{\left[180v^2\lambda^4 + 324\mu v^2\lambda^2 + 144\mu^2 v^2 + 54v^2\lambda^2 - 1050\lambda^4 + 48\mu v^2 - 600\mu\lambda^2 + 4v^2 - 225\lambda^2\right]}{\lambda^2\left(14\lambda^2 + 8\mu + 3\right)} \\[2mm]
& + \frac{4}{25} \frac{v^2\left(6\lambda^2 + 6\mu + 1\right)}{\lambda\left(14\lambda^2 + 8\mu + 3\right)} \left[-\frac{\lambda}{2} + \eta_1 \coth(\eta_1\xi + \xi_0)\right] \\[2mm]
& + \frac{2}{25} \frac{v\left(210c\lambda^3 + 120c\mu\lambda + 12v\lambda^2 + 45c\lambda + 12\mu v + 2v\right)}{\lambda^2\left(14\lambda^2 + 8\mu + 3\right)} \left[-\frac{\lambda}{2} + \eta_1 \coth(\eta_1\xi + \xi_0)\right]^2 \\[2mm]
& + \frac{4}{25} \frac{\mu v\left(210c\lambda^3 + 120c\mu\lambda + 6v\lambda^2 + 45c\lambda + 6\mu v + v\right)}{\lambda\left(14\lambda^2 + 8\mu + 3\right)} \left[-\frac{\lambda}{2} + \eta_1 \coth(\eta_1\xi + \xi_0)\right]^{-1} \\[2mm]
& + \frac{2}{25} \frac{\mu^2 v\left(210c\lambda^3 + 120c\mu\lambda + 12v\lambda^2 + 45c\lambda + 12\mu v + 2v\right)}{\lambda^2\left(14\lambda^2 + 8\mu + 3\right)} \left[-\frac{\lambda}{2} + \eta_1 \coth(\eta_1\xi + \xi_0)\right]^{-2},
\end{aligned}
\tag{22}
$$

when $|C_2/C_1| > 1$ and $\coth(\xi_0) = C_2/C_1$.

(ii) *Case 2.* When $\lambda^2 - 4\mu < 0$, the solution of the trigonometric form of (13) is as follows:

$$
\begin{aligned}
U_2(\xi) = \frac{1}{150} & \frac{\left[180v^2\lambda^4 + 324\mu v^2\lambda^2 + 144\mu^2 v^2 + 54v^2\lambda^2 - 1050\lambda^4 + 48\mu v^2 - 600\mu\lambda^2 + 4v^2 - 225\lambda^2\right]}{\lambda^2\left(14\lambda^2 + 8\mu + 3\right)} \\[2mm]
& + \frac{4}{25} \frac{v^2\left(6\lambda^2 + 6\mu + 1\right)}{\lambda\left(14\lambda^2 + 8\mu + 3\right)} \left[-\frac{\lambda}{2} + \eta_2\left(\frac{-C_1\sin(\eta_2\xi) + C_2\cos(\eta_2\xi)}{C_1\cos(\eta_2\xi) + C_2\sin(\eta_2\xi)}\right)\right] \\[2mm]
& + \frac{2}{25} \frac{v\left(210c\lambda^3 + 120c\mu\lambda + 12v\lambda^2 + 45c\lambda + 12\mu v + 2v\right)}{\lambda^2\left(14\lambda^2 + 8\mu + 3\right)} \left[-\frac{\lambda}{2} + \eta_2\left(\frac{-C_1\sin(\eta_2\xi) + C_2\cos(\eta_2\xi)}{C_1\cos(\eta_2\xi) + C_2\sin(\eta_2\xi)}\right)\right]^2 \\[2mm]
& + \frac{4}{25} \frac{\mu v\left(210c\lambda^3 + 120c\mu\lambda + 6v\lambda^2 + 45c\lambda + 6\mu v + v\right)}{\lambda\left(14\lambda^2 + 8\mu + 3\right)} \left[-\frac{\lambda}{2} + \eta_2\left(\frac{-C_1\sin(\eta_2\xi) + C_2\cos(\eta_2\xi)}{C_1\cos(\eta_2\xi) + C_2\sin(\eta_2\xi)}\right)\right]^{-1} \\[2mm]
& + \frac{2}{25} \frac{\mu^2 v\left(210c\lambda^3 + 120c\mu\lambda + 12v\lambda^2 + 45c\lambda + 12\mu v + 2v\right)}{\lambda^2\left(14\lambda^2 + 8\mu + 3\right)} \left[-\frac{\lambda}{2} + \eta_2\left(\frac{-C_1\sin(\eta_2\xi) + C_2\cos(\eta_2\xi)}{C_1\cos(\eta_2\xi) + C_2\sin(\eta_2\xi)}\right)\right]^{-2},
\end{aligned}
\tag{23}
$$

where $\xi = x - ct, \eta_2 = (1/2)\sqrt{4\mu - \lambda^2}$, and C_1 and C_2 are free constants.

(iii) *Case 3.* When $\lambda^2 - 4\mu = 0$, the solution to (13), in rational functional form, is as follows:

$$
\begin{aligned}
U_3(\xi) = &\frac{1}{150} \frac{\left[180v^2\lambda^4 + 324\mu v^2\lambda^2 + 144\mu^2 v^2 + 54v^2\lambda^2 - 1050\lambda^4 + 48\mu v^2 - 600\mu\lambda^2 + 4v^2 - 225\lambda^2\right]}{\lambda^2\left(14\lambda^2 + 8\mu + 3\right)} \\[2mm]
&+ \frac{4}{25} \frac{v^2\left(6\lambda^2 + 6\mu + 1\right)}{\lambda\left(14\lambda^2 + 8\mu + 3\right)} \left[-\frac{\lambda}{2} + \frac{C_2}{C_1 + C_2\xi}\right] \\[2mm]
&+ \frac{2}{25} \frac{v\left(210c\lambda^3 + 120c\mu\lambda + 12v\lambda^2 + 45c\lambda + 12\mu v + 2v\right)}{\lambda^2\left(14\lambda^2 + 8\mu + 3\right)} \left[-\frac{\lambda}{2} + \frac{C_2}{C_1 + C_2\xi}\right]^2 \\[2mm]
&+ \frac{4}{25} \frac{\mu v\left(210c\lambda^3 + 120c\mu\lambda + 6v\lambda^2 + 45c\lambda + 6\mu v + v\right)}{\lambda\left(14\lambda^2 + 8\mu + 3\right)} \left[-\frac{\lambda}{2} + \frac{C_2}{C_1 + C_2\xi}\right]^{-1} \\[2mm]
&+ \frac{2}{25} \frac{\mu^2 v\left(210c\lambda^3 + 120c\mu\lambda + 12v\lambda^2 + 45c\lambda + 12\mu v + 2v\right)}{\lambda^2\left(14\lambda^2 + 8\mu + 3\right)} \left[-\frac{\lambda}{2} + \frac{C_2}{C_1 + C_2\xi}\right]^{-2},
\end{aligned}
\tag{24}
$$

where $\xi = x - ct$ and C_1, C_2 are free constants.

3.2. The IMBq Equation with Stokes Damping

$$
u_{tt} - u_{xx} - u_{xxtt} + vu_t = \left(u^3\right)_{xx}, \tag{25}
$$

where v is a nonnegative number. We apply (7) to (25), we integrate it once concerning ξ, we set the constant to M, and then we can convert (25) to the nonlinear ODE:

$$
\left(c^2 - 1\right)U' - c^2 U''' - cvU - 3U^2 U' = M. \tag{26}
$$

At equilibrium, the highest nonlinear term $U^2 U'$ in (26), and the highest derivative term U''' in (26), we get m equal to 1. Therefore, the exact solution of (26) in the form of (9) can be written as follows:

$$
U(\xi) = a_0 + a_1\frac{G\prime}{G} + b_1\frac{G}{G'}. \tag{27}
$$

Substitute (27) into (26), use the ordinary differential (10) concerning (G'/G) to combine the same power terms of (G'/G), and then let the coefficients be equal to zero; we get a nonlinear algebraic system of equations concerning the unknowns a_0, a_1, b_1, c, and M:

$$
\left(\frac{G}{G\prime}\right)^5: \quad -24c^2\mu^3 b_2 - 4\mu b_2^2 = 0,
$$

$$
\left(\frac{G}{G\prime}\right)^4: \quad -6c^2\mu^3 b_1 - 54c^2\mu^2\lambda b_2 + 6c\mu^2 v b_2 - 6\mu b_1 b_2 - 4\lambda b_2^2 = 0,
$$

$$
\left(\frac{G}{G\prime}\right)^3: \quad -12c^2\mu^2\lambda b_1 - 38c^2\mu\lambda^2 b_2 - 40c^2\mu^2 b_2 + 2c\mu^2 v b_1 + 10c\mu v\lambda b_2 + 2c^2\mu b_2 - 4\mu a_0 b_2 - 2\mu b_1^2 - 6\lambda b_1 b_2 - 2\mu b_2 - 4b_2^2 = 0,
$$

$$
\begin{aligned}
\left(\frac{G}{G\prime}\right)^2: \quad &-7c^2\mu\lambda^2 b_1 - 8c^2\lambda^3 b_2 - 8c^2\mu^2 b_1 - 52c^2\mu\lambda b_2 + 3c\mu v\lambda b_1 + 4cv\lambda^2 b_2 + c^2\mu b_1 + 2c^2\lambda b_2 + 8c\mu v b_2 \\
&- 2\mu a_0 b_1 - 2\mu a_1 b_2 - 4\lambda a_0 b_2 - 2\lambda b_1^2 - \mu b_1 - 2\lambda b_2 - 6b_1 b_2 = 0,
\end{aligned}
$$

$$\frac{G}{G'}: \; -c^2\lambda^3 b_1 - 8c^2\mu\lambda b_1 - 14c^2\lambda^2 b_2 + cv\lambda^2 b_1 - 16c^2\mu b_2 + c^2\lambda b_1 + 2c\mu v b_1 + 6cv\lambda b_2 + 2c^2 b_2 - 2\lambda a_0 b_1 - 2\lambda a_1 b_2$$

$$-\lambda b_1 - 4a_0 b_2 - 2b_1^2 - 2b_2 = 0,$$

$$\left(\frac{G}{G'}\right)^0: \; b_1 c^2 - 2a_0 b_1 + 2a_2 b_1 \mu + cva_1\lambda\mu - c^2 b_1\lambda^2 - 2c^2\mu b_1 - 6c^2\lambda b_2 + 2c^2 a_1\mu^2 - c^2\mu a_1 + 2a_0 a_1\mu + 2cvb_2$$

$$+ \mu a_1 + c^2 a_1\lambda^2\mu + 6c^2 a_2\lambda\mu^2 - 2a_1 b_2 + cvb_1\lambda + 2cva_2\mu^2 - b_1 - M = 0,$$

$$\frac{G'}{G}: \; 14c^2\mu\lambda^2 a_2 + c^2\lambda^3 a_1 + 16c^2\mu^2 a_2 + 8c^2\mu\lambda a_1 + 6c\mu v\lambda a_2 + cv\lambda^2 a_1 - 2c^2\mu a_2 - c^2\lambda a_1 + 2c\mu v a_1$$

$$+ 4\mu a_0 a_2 + 2\mu a_1^2 + 2\lambda a_0 a_1 + 2\lambda a_2 b_1 + 2\mu a_2 + \lambda a_1 = 0,$$

$$\left(\frac{G'}{G}\right)^2: \; 8c^2\lambda^3 a_2 + 52c^2\mu\lambda a_2 + 7c^2\lambda^2 a_1 + 4cv\lambda^2 a_2 + 8c^2\mu a_1 - 2c^2\lambda a_2 + 8c\mu v a_2 + 3cv\lambda a_1 - c^2 a_1 + 6\mu a_1 a_2$$

$$+ 4\lambda a_0 a_2 + 2\lambda a_1^2 + 2\lambda a_2 + 2a_0 a_1 + 2a_2 b_1 + a_1 = 0,$$

$$\left(\frac{G'}{G}\right)^3: \; 38c^2\lambda^2 a_2 + 40c^2\mu a_2 + 12c^2\lambda a_1 + 10cv\lambda a_2 - 2c^2 a_2 + 2cva_1 + 4\mu a_2^2 + 6\lambda a_1 a_2 + 4a_0 a_2 + 2a_1^2 + 2a_2 = 0,$$

$$\left(\frac{G'}{G}\right)^4: \; 54c^2\lambda a_2 + 6c^2 a_1 + 6cva_2 + 4\lambda a_2^2 + 6a_1 a_2 = 0,$$

$$\left(\frac{G'}{G}\right)^5: \; 24c^2 a_2 + 4a_2^2 = 0.$$

$$(28)$$

Using symbolic computation software maple, the solution of this system is obtained as follows:

Case 1: $\left\{a_0 = -I, a_1 = 0, b_1 = -\dfrac{-Icv + M}{c^2\lambda^2 + 2c^2\mu - c^2 - 2}\right\},$

$$(29)$$

Case 2: $\left\{a_0 = I, a_1 = 0, b_1 = -\dfrac{Icv + M}{c^2\lambda^2 + 2c^2\mu - c^2 - 2}\right\},$ (30)

where I is the imaginary unit. Substituting the values from (29) and using the general solutions of (10) in different situations, multiple exact solutions of different types of (25) can be obtained.

(i) *Case 1.* When $\lambda^2 - 4\mu > 0$, the solution to (25), in hyperbolic functional form, is as follows:

$$U_1(\xi) = -I - \frac{-Icv + M}{c^2\lambda^2 + 2c^2\mu - c^2 - 2}\left[-\frac{\lambda}{2} + \eta_1\left(\frac{C_1\sinh(\eta_1\xi) + C_2\cosh(\eta_1\xi)}{C_1\cosh(\eta_1\xi) + C_2\sinh(\eta_1\xi)}\right)\right]^{-1},$$

$$(31)$$

where $\xi = x - ct$, $\eta_1 = (1/2)\sqrt{\lambda^2 - 4\mu}$, and C_1, C_2 are free constants.

In particular, if $C_1 \neq 0$ and $C_2 = 0$, then $U_1(\xi)$ becomes

$$\overline{U}_1(\xi) = -I - \frac{-Icv + M}{c^2\lambda^2 + 2c^2\mu - c^2 - 2}\left[\frac{\lambda}{2} + \eta_1\tanh(\eta_1\xi)\right]^{-1}.$$

$$(32)$$

Again using (12), the general solutions for $U_1(\xi)$ in simplified forms are written as

$$U_{11}(\xi) = -I - \frac{-Icv + M}{c^2\lambda^2 + 2c^2\mu - c^2 - 2}\left[\frac{\lambda}{2} + \eta_1\tanh(\eta_1\xi + \xi_0)\right]^{-1},$$

$$(33)$$

when $|C_2/C_1| < 1$ and $\tanh(\xi_0) = C_2/C_1$;

$$U_{12}(\xi) = -I - \frac{-Icv + M}{c^2\lambda^2 + 2c^2\mu - c^2 - 2}\left[\frac{\lambda}{2} + \eta_1\coth(\eta_1\xi + \xi_0)\right]^{-1},$$

$$(34)$$

when $|C_2/C_1| > 1$ and $\coth(\xi_0) = C_2/C_1$.

(ii) *Case 2.* When $\lambda^2 - 4\mu < 0$, the solution to (25), in trigonometric functional form, is as follows:

$$U_2(\xi) = -I - \frac{-Icv + M}{c^2\lambda^2 + 2c^2\mu - c^2 - 2}\left[\frac{\lambda}{2} + \eta_2\left(\frac{-C_1\sin(\eta_2\xi) + C_2\cos(\eta_2\xi)}{C_1\cos(\eta_2\xi) + C_2\sin(\eta_2\xi)}\right)\right]^{-1}, \tag{35}$$

where $\xi = x - ct, \eta_2 = (1/2)\sqrt{4\mu - \lambda^2}$, and C_1, C_2 are free constants.

(iii) *Case 3.* When $\lambda^2 - 4\mu = 0$, the solution to (25), in rational functional form, is as follows:

$$U_3(\xi) = -I - \frac{-Icv + M}{c^2\lambda^2 + 2c^2\mu - c^2 - 2}\left[-\frac{\lambda}{2} + \frac{C_2}{C_1 + C_2\xi}\right]^{-1}, \tag{36}$$

$$U_1(\xi) = I - \frac{Icv + M}{c^2\lambda^2 + 2c^2\mu - c^2 - 2}\left[-\frac{\lambda}{2} + \eta_1\left(\frac{C_1\sinh(\eta_1\xi) + C_2\cosh(\eta_1\xi)}{C_1\cosh(\eta_1\xi) + C_2\sinh(\eta_1\xi)}\right)\right]^{-1}, \tag{37}$$

where $\xi = x - ct, \eta_1 = (1/2)\sqrt{\lambda^2 - 4\mu}$, and C_1, C_2 are free constants.

In particular, if $C_1 \neq 0$ and $C_2 = 0$, then $U_1(\xi)$ becomes

$$\overline{U}_1(\xi) = I - \frac{Icv + M}{c^2\lambda^2 + 2c^2\mu - c^2 - 2}\left[-\frac{\lambda}{2} + \eta_1\tanh(\eta_1\xi)\right]^{-1}. \tag{38}$$

Again using (12), the general solutions for $U_1(\xi)$ in simplified forms are written as

$$U_{11}(\xi) = I - \frac{Icv + M}{c^2\lambda^2 + 2c^2\mu - c^2 - 2}\left[-\frac{\lambda}{2} + \eta_1\tanh(\eta_1\xi + \xi_0)\right]^{-1}, \tag{39}$$

where $\xi = x - ct$ and C_1, C_2 are arbitrary constants.

Substituting the values from (30) and using the general solutions of (10) in different situations, multiple exact solutions of different types of (25) can be obtained.

(i) *Case 1.* When $\lambda^2 - 4\mu > 0$, the solution to (25), in hyperbolic functional form, is as follows:

when $|C_2/C_1| < 1$ and $\tanh(\xi_0) = C_2/C_1$;

$$U_{12}(\xi) = I - \frac{Icv + M}{c^2\lambda^2 + 2c^2\mu - c^2 - 2}\left[-\frac{\lambda}{2} + \eta_1\coth(\eta_1\xi + \xi_0)\right]^{-1}, \tag{40}$$

when $|C_2/C_1| > 1$ and $\coth(\xi_0) = C_2/C_1$.

(ii) *Case 2.* When $\lambda^2 - 4\mu < 0$, the solution to (25), in trigonometric functional form, is as follows:

$$U_2(\xi) = I - \frac{Icv + M}{c^2\lambda^2 + 2c^2\mu - c^2 - 2}\left[-\frac{\lambda}{2} + \eta_2\left(\frac{-C_1\sin(\eta_2\xi) + C_2\cos(\eta_2\xi)}{C_1\cos(\eta_2\xi) + C_2\sin(\eta_2\xi)}\right)\right]^{-1}, \tag{41}$$

where $\xi = x - ct, \eta_2 = (1/2)\sqrt{4\mu - \lambda^2}$, and C_1, C_2 are arbitrary constants.

(iii) *Case 3.* When $\lambda^2 - 4\mu = 0$, the solution to (25), in rational functional form, is as follows:

$$U_3(\xi) = I - \frac{Icv + M}{c^2\lambda^2 + 2c^2\mu - c^2 - 2}\left[-\frac{\lambda}{2} + \frac{C_2}{C_1 + C_2\xi}\right]^{-1}, \tag{42}$$

where $\xi = x - ct$ and C_1, C_2 are free constants.

4. Discussion

In [14], the damped IBq (14) is derived and the local waveform of its numerical solution is obtained. The local two-dimensional display of the numerical solution is a bell-shaped waveform, similar to the local figure of the two-dimensional figure obtained by taking time as a constant in Figure 1. Figure 1 is a three-dimensional diagram of the trigonometric solution (23). It is well known that numerical solutions may miss some solutions of the equation, as shown in Figure 2, which is a kinked type of isolated wave and is not mentioned in [14]. As can be seen from Figure 2, when we
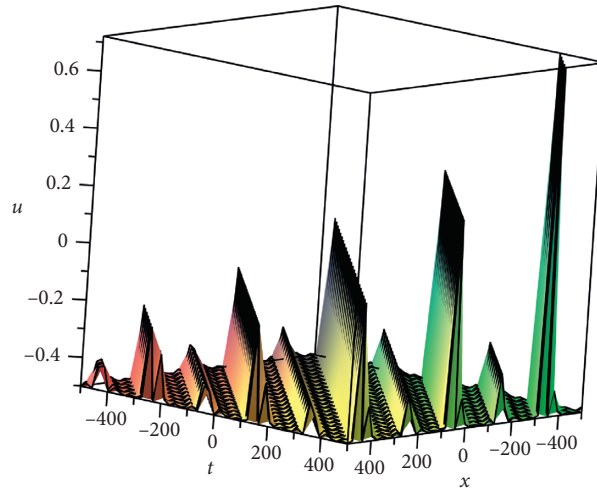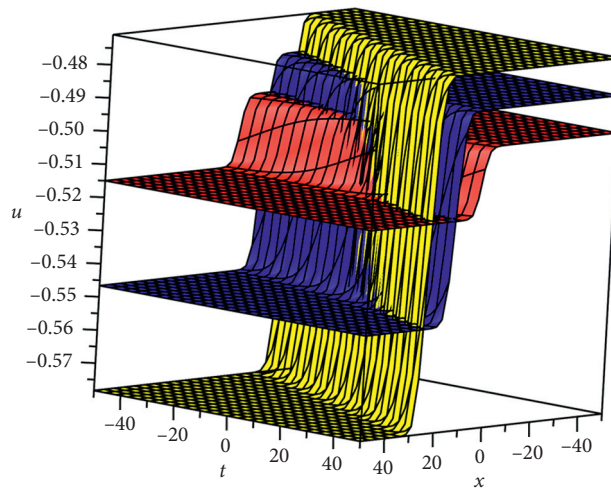
FIGURE 1: 3D graph of solution (23) when $\lambda = \sqrt{2}, \mu = 1.5, c = 1, v = 0.001,$ and $C_1 = C_2 = 1$.

Solution (18) red: $c = 0.1$, blue: $c = 0.3$, and yellow: $c = 0.5$

FIGURE 2: 3D graph of solution (19) when $\lambda = \sqrt{2}, \mu = 0.3, v = 0.1,$ and $C_2 = 0$.

change the value of wave velocity c and increase gradually, the propagation direction of kinked isolated wave follows the change, and the amplitude of waveform increases gradually. Mathematically, the value of c can be used to modulate the kinked isolated waveform represented by this equation.

In [15], the authors deduce a damped equation similar to (14) and use a numerical method (finite difference method) to find a kinked isolated wave. The equation derived in [15] is (43), and it is also concluded that when the dissipation coefficient β_1 is much larger than the dispersion coefficient β_2, the kinked isolated wave will have asymmetric characteristics:

$$u_{tt} - u_{xx} + u_{xxxx} - \beta_2 u_{xxtt} - \beta_1 u_{xxt} = \left(u^2 \right)_{xx}. \qquad (43)$$

Using (7), we apply the travelling wave transformation to (13) and (43), integrate once, and then assume that $\beta_1 = v$

and $\beta_2 = 1 + c^{-2}$; we get the same (14). The waveform of the kinked isolated wave obtained from (14) varies with the damping coefficient v, as shown in Figure 3. As can be seen from Figure 3, with the increase of v, the precise kink solitary wave solution waveform obtained by the extended (G'/G)-expansion also shows the asymmetric characteristics of waveform and becomes more and more obvious. It is shown that the exact solution is helpful to verify the numerical solution.

It can be seen from solution (17) of the algebraic system of (14) that $a_0, a_1, a_2, b_1,$ and b_2 are expressed by other parameters. When we want to find an expression for wave velocity c, we can also find a solution in the following form. The difference is that, in the expression for solution (17), the wave velocity is arbitrary, and here the coefficient a_2 is arbitrary:
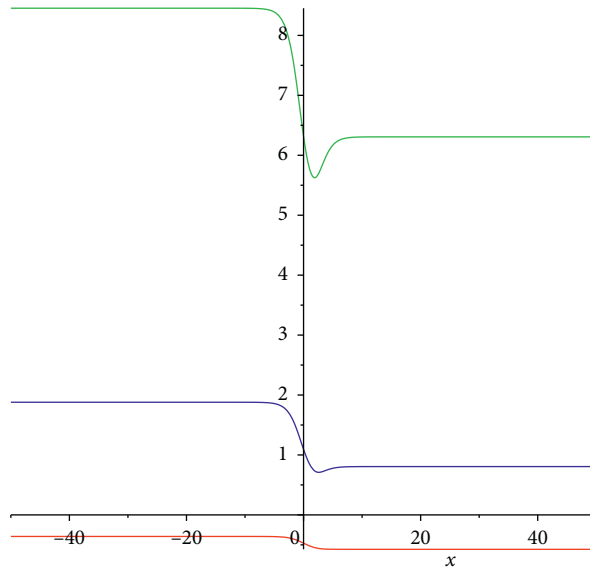
Solution (18) red: $v = 1$, blue: $v = 5$, and green: $v = 10$

FIGURE 3: The two-dimensional representation of solution (19) when $\lambda = \sqrt{2}, \mu = 0.3, c = 0.1, t = 10$, and $C_2 = 0$.

$$
\left\{
\begin{aligned}
c &= -\frac{1}{30} \frac{-350\lambda^4 a_2 - 200\mu\lambda^2 a_2 + 24v^2\lambda^2 + 24\mu v^2 - 75\lambda^2 a_2 + 4v^2}{\left(14\lambda^2 + 8\mu + 3\right)v\lambda}, \\[2mm]
a_0 &= \frac{1}{150} \frac{\left[180v^2\lambda^4 + 324\mu v^2\lambda^2 + 144\mu^2 v^2 + 54v^2\lambda^2 - 1050\lambda^4 + 48\mu v^2 - 600\mu\lambda^2 + 4v^2 - 225\lambda^2\right]}{\lambda^2\left(14\lambda^2 + 8\mu + 3\right)}, \\[2mm]
a_1 &= \frac{4}{25} \frac{v^2\left(6\lambda^2 + 6\mu + 1\right)}{\lambda\left(14\lambda^2 + 8\mu + 3\right)}, \\[2mm]
b_2 &= \mu^2 a_2 \\[2mm]
b_1 &= -\frac{2}{25} \frac{\left(-350\lambda^4 a_2 - 200\mu\lambda^2 a_2 + 12v^2\lambda^2 + 12\mu v^2 - 75\lambda^2 a_2 + 2v^2\right)\mu}{\left(14\lambda^2 + 8\mu + 3\right)\lambda}.
\end{aligned}
\right.
\tag{44}
$$

When we use solution (44), the arbitrary constant M also contains an expression for a_2, which is too long to display here. For solutions (29) and (30) of the second algebraic system, the expressions are simple, and the expressions of arbitrary constants M and wave velocity c can be easily solved from them.

In the extended (G'/G)-expansion method, when the coefficients b_i $(i = 1, 2, \ldots, m)$ are set to 0, it is reduced to the (G'/G)-expansion method, which is the same idea as the simplest equation method reduced to the tanh method [43]. We think superficially that the extended (G'/G)-expansion method fuses the solutions of two Ricatti equations in a certain form. In other words, the extended (G'/G)-expansion method decomposes the solutions of nonlinear partial differential equation into the solutions of two Ricatti equations. A brief explanation is given as follows.

If $G = G(\xi)$ is the solution of the second-order differential equation

$$
G'' + \lambda G\prime + \mu G = 0,
\tag{45}
$$

we can get

$$\left(\frac{G'(\xi)}{G(\xi)}\right)' = \frac{G''(\xi)G(\xi) - (G'(\xi))^2}{G^2(\xi)} = -\left(\frac{G'}{G}\right)^2 - \lambda\left(\frac{G'}{G}\right) - \mu,$$

$$(46)$$

$$\left(\frac{G(\xi)}{G'(\xi)}\right)' = \frac{(G'(\xi))^2 - G(\xi)G''(\xi)}{(G\prime(\xi))^2} = 1 + \frac{G(\lambda G' + \mu G)}{(G')^2}$$

$$= 1 + \lambda\left(\frac{G}{G'}\right) + \mu\left(\frac{G}{G'}\right)^2.$$

$$(47)$$

It can be seen from (46) and (47) that when G satisfies (45), (G'/G) and (G/G') each satisfy a generalized Ricatti equation, and the derivative results of (G'/G) and (G/G') can be converted into the polynomial form of (G'/G) or (G/G'), which is the basis for collecting coefficients to obtain an algebraic system of equations.

5. Conclusion

With the help of the auxiliary function method, we solved two damped generalized IBq equations and we obtained their three types of travelling wave exact solutions, which is an extension work of the numerical solution and the existence of a solution. From the waveform of solution (19), it can be seen that the waveform of the kink wave can be modulated by changing the value of c. It is found that, for the hydrodynamic damping IBq equation, the varying damping coefficient v makes the waveform of the kinked isolated wave represented by (19) appear obviously asymmetric, which is consistent with the conclusion obtained by numerical method in [15]. In addition, the role of maple in our work should not be overlooked to make our computing work easier.

Data Availability

No data were used to support this study.

Conflicts of Interest

The authors declare that they have no conflicts of interest.

Authors' Contributions

All authors read and approved the final manuscript.

Acknowledgments

References

[1] J. Boussinesq, "Théorie des ondes et des remous qui se propagent le long d'un canal rectangulaire horizontal en communiquant au liquide contenu dans ce canal des vitesses sensiblement pareilles de la surface au fond," *Journal de Mathématiques Pures et Appliquées*, vol. 17, no. 2, pp. 55–108, 1872.

[2] J. Boussinesq, "Essai sur la théorie des eaux courantes," *Mém. Acad. Sci. Inst. Nat. France*, vol. 23, no. 1, pp. 1–680, 1877.

[3] V. Varlamov, "Eigenfunction expansion method and the long-time asymptotics for the damped Boussinesq equation," *Discrete & Continuous Dynamical Systems—A*, vol. 7, no. 4, pp. 675–702, 2001.

[4] T. Hatice, N. Polat, and A. Ertaş, "Global existence and decay of solutions for the generalized bad Boussinesq equation," *Applied Mathematics—A Journal of Chinese Universities*, vol. 28, no. 3, pp. 253–268, 2013.

[5] A.-M. Wazwaz, "Compactons and solitary wave solutions for the Boussinesq wave equation and its generalized form," *Applied Mathematics and Computation*, vol. 182, no. 1, pp. 529–535, 2006.

[6] S. T. Mohyud, M. A. Noor, and A. Waheed, "Exp-function method for generalized traveling solutions of good Boussinesq equations," *Journal of Applied Mathematics and Computing*, vol. 30, no. 1-2, pp. 439–445, 2009.

[7] G. Forozani and M. Ghorveei Nosrat, "Solitary solution of modified bad and good Boussinesq equation by using of tanh and extended tanh methods," *Indian Journal of Pure and Applied Mathematics*, vol. 44, no. 4, pp. 497–510, 2013.

[8] V. G. Makhankov, "Dynamics of classical solitons (in nonintegrable systems)," *Physics Reports*, vol. 35, no. 1, pp. 1–128, 1978.

[9] P. Chatterjee, R. Ali, and A. Saha, "Analytical solitary wave solution of the dust ion acoustic waves for the damped forced korteweg-de Vries equation in superthermal plasmas," *Zeitschrift für Naturforschung A*, vol. 73, no. 2, pp. 151–159, 2018.

[10] R. Ali, A. Saha, and P. Chatterjee, "Analytical electron acoustic solitary wave solution for the forced KdV equation in superthermal plasmas," *Physics of Plasmas*, vol. 24, no. 12, Article ID 122106, 2017.

[11] B. Yan, P. Prasad, S. Mukherjee, A. Saha, and S. Banerjee, "Dynamical complexity and multistability in a novel lunar wake plasma system," *Complexity*, vol. 2020, Article ID 5428548, 2020.

[12] A. Saha and J. Tamang, "Effect of q-nonextensive hot electrons on bifurcations of nonlinear and supernonlinear ion-acoustic periodic waves," *Advances in Space Research*, vol. 63, no. 5, pp. 1596–1606, 2019.

[13] P. Rosenau, "Dynamics of nonlinear mass-spring chains near the continuum limit," *Physics Letters A*, vol. 118, no. 5, pp. 222–227, 1986.

[14] E. Arévalo, Y. Gaididei, and F. G. Mertens, "Soliton dynamics in damped and forced Boussinesq equations," *The European Physical Journal B*, vol. 27, no. 1, pp. 63–74, 2002.

[15] S. S. Naranmandula, "The evolution of bell and Kink isolated waves in microstructured solids," *Chinese Journal of Theoretical and Applied Mechanics*, vol. 44, no. 1, pp. 117–122, 2012.

[16] S. Wang and H. Xu, "On the asymptotic behavior of solution for the generalized IBq equation with hydrodynamical damped term," *Journal of Differential Equations*, vol. 252, no. 7, pp. 4243–4258, 2012.

[17] S. Wang and H. Xu, "On the asymptotic behavior of solution for the generalized IBq equation with Stokes damped term," *Zeitschrift für angewandte Mathematik und Physik*, vol. 64, no. 3, pp. 719–731, 2013.

[18] X. Y. Chen, "Global existence of solution of cauchy problem for a generalized IMBq equation with weak damping," *Acta Mathematica Scientia*, vol. 35, no. 1, pp. 68–82, 2015.

[19] M. A. E. Abdelrahman and O. Moaaz, "New exact solutions to the dual-core optical fibers," *Indian Journal of Physics*, vol. 94, no. 5, pp. 705–711, 2020.

[20] J. Manafian and M. Lakestani, "Optical solitons with Biswas-Milovic equation for Kerr law nonlinearity," *European Physical Journal Plus*, vol. 130, no. 4, pp. 1–12, 2015.

[21] M. Shakeel, M. A. Iqbaol, Q. Din, Q. M. Hassan, and K. Ayub, "New exact solutions for coupled nonlinear system of ion sound and Langmuir waves," *Indian Journal of Physics*, vol. 96, no. 5, pp. 885–894, 2020.

[22] M. Jahani and J. Manafian, "Improvement of the Exp-function method for solving the BBM equation with time-dependent coefficients," *European Physical Journal Plus*, vol. 131, no. 3, pp. 1–12, 2016.

[23] M. G. Hafez, M. N. Alam, and M. A. Akbar, "Traveling wave solutions for some important coupled nonlinear physical models via the coupled Higgs equation and the Maccari system," *Journal of King Saud University—Science*, vol. 27, no. 2, pp. 105–112, 2015.

[24] N. H. Abdel-All, M. A.-A. Abdel-Razek, and A.-A. K. Seddeek, "Expanding the tanh-function method for solving nonlinear equations," *Applied Mathematics*, vol. 2, no. 9, pp. 1096–1104, 2011.

[25] M. A. Akbar, N. H. M. Ali, and S. T. Mohyud-Din, "Assessment of the further improved (G'/G)-expansion method and the extended tanh-method in probing exact solutions of nonlinear PDEs," *Springer Plus*, vol. 2, no. 1, pp. 2–9, 2013.

[26] Ö. F. Gözükızıl and Ş. Akçağıl, "The tanh-coth method for some nonlinear pseudoparabolic equations with exact solutions," *Advances in Difference Equations*, vol. 143, no. 1, pp. 2–18, 2013.

[27] A. S. Abdel, E. S. Osman, and M. Khalfallah, "The homogeneous balance method and its application to the Benjamin-Bona-Mah-oney(BBM) equation," *Applied Mathematics and Computation*, vol. 217, no. 4, pp. 1385–1390, 2010.

[28] M. Jalil, F. A. Mehdi, M. Khalilian, and R. S. Jeddi, "Application of the generalized (G'/G)-expansion method for nonlinear PDEs to obtaining soliton wave solution," *Optik—International Journal for Light and Electron Optics*, vol. 135, pp. 395–406, 2017.

[29] Z. Zhang, J. Huang, J. Zhong et al., "The extended (G'/G)-expansion method and travelling wave solutions for the perturbed nonlinear Schrödinger's equation with Kerr law nonlinearity," *Pramana*, vol. 82, no. 6, pp. 1011–1029, 2014.

[30] J. Pang, C.-q. Bian, and L. Chao, "A new auxiliary equation method for finding travelling wave solutions to KdV equation," *Applied Mathematics and Mechanics*, vol. 31, no. 7, pp. 929–936, 2010.

[31] M. Mirzazadeh and M. Eslami, "Exact multisoliton solutions of nonlinear Klein–Gordon equation in $1 + 2$ dimensions," *European Physical Journal Plus*, vol. 128, no. 11, pp. 1–92, 2013.

[32] N. Taghizadeh and M. Mirzazadeh, "The first integral method to some complex nonlinear partial differential equations," *Journal of Computational and Applied Mathematics*, vol. 235, no. 16, pp. 4871–4877, 2011.

[33] N. A. Muhammad, M. H. Syed, A. Saha et al., "Exact solutions, conservation laws, bifurcation of nonlinear and supernonlinear traveling waves for Sharma–Tasso–Olver equation," *Nonlinear Dynamics*, vol. 94, no. 3, pp. 1791–1801, 2018.

[34] M. Mirzazadeh and M. E. Dark, "Optical solitons of Biswas–Milovic equation with dual-power law nonlinearity," *European Physical Journal Plus*, vol. 130, no. 1, pp. 1–7, Article ID 4, 2015.

[35] M. E. Elsayed and A. N. Abdul-Ghani, "Solitons and other exact solutions for variant nonlinear Boussinesq equations," *Optik—International Journal for Light and Electron Optics*, vol. 139, pp. 166–177, 2017.

[36] A. Malik, F. Chand, H. Kumar, and S. C. Mishra, "Exact solutions of some physical models using the (G'/G)-expansion method," *Pramana*, vol. 78, no. 4, pp. 513–529, 2012.

[37] D. M. Mothibi and C. M. Khalique, "On the exact solutions of a modified Kortweg de Vries type equation and higher-order modified Boussinesq equation with damping term," *Advances in Difference Equations*, vol. 166, no. 1, pp. 1–7, 2013.

[38] M. Wang, X. Li, and J. Zhang, "The (G'/G)-expansion method and travelling wave solutions of nonlinear evolution equations in mathematical physics," *Physics Letters A*, vol. 372, no. 4, pp. 417–423, 2008.

[39] N. A. Kudryashov, "Seven common errors in finding exact solutions of nonlinear differential equations," *Communications in Nonlinear Science and Numerical Simulation*, vol. 14, no. 9-10, pp. 3507–3529, 2009.

[40] N. A. Kudryashov, "On "new travelling wave solutions" of the KdV and the KdV-burgers equations," *Communications in Nonlinear Science and Numerical Simulation*, vol. 14, no. 5, pp. 1891–1900, 2009.

[41] N. A. Kudryashov, "A note on the G'/G-expansion method," *Applied Mathematics and Computation*, vol. 217, no. 4, pp. 1755–1758, 2010.

[42] N. A. Kudryashov and N. B. Loguinova, "Be careful with the Exp-function method," *Communications in Nonlinear Science and Numerical Simulation*, vol. 14, no. 5, pp. 1881–1890, 2009.

[43] N. A. Kudrayshov, "Simplest equation method to look for exact solutions of nonlinear differential equations," *Chaos, Solitons & Fractals*, vol. 24, no. 5, pp. 1217–1231, 2005.